

Lecture Notes in Mechanical Engineering

Eswaraiah Chinthapudi
Suddhasatwa Basu
Bhaskar Narayan Thorat *Editors*

Sustainable Chemical, Mineral and Material Processing


Select Proceedings of 74th Annual
Session of Indian Institute of Chemical
Engineers (CHEMCON-2021)

 Springer

Lecture Notes in Mechanical Engineering


Series Editors

Fakher Chaari, National School of Engineers, University of Sfax, Sfax, Tunisia

Francesco Gherardini , Dipartimento di Ingegneria “Enzo Ferrari”, Università di Modena e Reggio Emilia, Modena, Italy

Vitalii Ivanov, Department of Manufacturing Engineering, Machines and Tools, Sumy State University, Sumy, Ukraine

Editorial Board

Francisco Cavas-Martínez , Departamento de Estructuras, Construcción y Expresión Gráfica Universidad Politécnica de Cartagena, Cartagena, Murcia, Spain

Francesca di Mare, Institute of Energy Technology, Ruhr-Universität Bochum, Bochum, Nordrhein-Westfalen, Germany

Mohamed Haddar, National School of Engineers of Sfax (ENIS), Sfax, Tunisia

Young W. Kwon, Department of Manufacturing Engineering and Aerospace Engineering, Graduate School of Engineering and Applied Science, Monterey, CA, USA

Justyna Trojanowska, Poznan University of Technology, Poznan, Poland

Lecture Notes in Mechanical Engineering (LNME) publishes the latest developments in Mechanical Engineering—quickly, informally and with high quality. Original research reported in proceedings and post-proceedings represents the core of LNME. Volumes published in LNME embrace all aspects, subfields and new challenges of mechanical engineering. Topics in the series include:

- Engineering Design
- Machinery and Machine Elements
- Mechanical Structures and Stress Analysis
- Automotive Engineering
- Engine Technology
- Aerospace Technology and Astronautics
- Nanotechnology and Microengineering
- Control, Robotics, Mechatronics
- MEMS
- Theoretical and Applied Mechanics
- Dynamical Systems, Control
- Fluid Mechanics
- Engineering Thermodynamics, Heat and Mass Transfer
- Manufacturing
- Precision Engineering, Instrumentation, Measurement
- Materials Engineering
- Tribology and Surface Technology

To submit a proposal or request further information, please contact the Springer Editor of your location:

China: Ms. Ella Zhang at ella.zhang@springer.com

India: Priya Vyas at priya.vyas@springer.com

Rest of Asia, Australia, New Zealand: Swati Meherishi at swati.meherishi@springer.com

All other countries: Dr. Leontina Di Cecco at Leontina.dicecco@springer.com

To submit a proposal for a monograph, please check our Springer Tracts in Mechanical Engineering at <https://link.springer.com/bookseries/11693> or contact Leontina.dicecco@springer.com

Indexed by SCOPUS. All books published in the series are submitted for consideration in Web of Science.

Eswaraiah Chinthapudi · Suddhasatwa Basu ·
Bhaskar Narayan Thorat
Editors

Sustainable Chemical, Mineral and Material Processing

Select Proceedings of 74th Annual Session
of Indian Institute of Chemical Engineers
(CHEMCON-2021)

 Springer

Editors

Eswaraiah Chinthapudi
Council of Scientific and Industrial
Research
CSIR-Institute of Minerals and Materials
Technology
Bhubaneswar, Odisha, India

Suddhasatwa Basu
Department of Chemical Engineering
Indian Institute of Technology Delhi
New Delhi, India

Bhaskar Narayan Thorat
Institute of Chemical Technology Mumbai
ICT – IOC Campus
Bhubaneswar, Odisha, India

ISSN 2195-4356

ISSN 2195-4364 (electronic)

Lecture Notes in Mechanical Engineering

ISBN 978-981-19-7263-8

ISBN 978-981-19-7264-5 (eBook)

<https://doi.org/10.1007/978-981-19-7264-5>

© The Editor(s) (if applicable) and The Author(s), under exclusive license to Springer Nature Singapore Pte Ltd. 2023

This work is subject to copyright. All rights are solely and exclusively licensed by the Publisher, whether the whole or part of the material is concerned, specifically the rights of translation, reprinting, reuse of illustrations, recitation, broadcasting, reproduction on microfilms or in any other physical way, and transmission or information storage and retrieval, electronic adaptation, computer software, or by similar or dissimilar methodology now known or hereafter developed.

The use of general descriptive names, registered names, trademarks, service marks, etc. in this publication does not imply, even in the absence of a specific statement, that such names are exempt from the relevant protective laws and regulations and therefore free for general use.

The publisher, the authors, and the editors are safe to assume that the advice and information in this book are believed to be true and accurate at the date of publication. Neither the publisher nor the authors or the editors give a warranty, expressed or implied, with respect to the material contained herein or for any errors or omissions that may have been made. The publisher remains neutral with regard to jurisdictional claims in published maps and institutional affiliations.

This Springer imprint is published by the registered company Springer Nature Singapore Pte Ltd. The registered company address is: 152 Beach Road, #21-01/04 Gateway East, Singapore 189721, Singapore

Preface

We are pleased to bring out these select proceedings on the theme “Sustainable Chemical, Mineral and Material Processing” presented in Indian Chemical Engineering Congress (CHEMCON-2021) held at CSIR—Institute of Minerals & Materials Technology, Bhubaneswar, Odisha, India during 26th–30th December 2021. CHEMCON-2021 is an annual conference which is in continuation of the series of Chemical Engineering Congress held every year in various parts of India.

More than 400 papers were presented by researchers across the globe during CHEMCON-2021 and nearly 24 quality papers were selected for publication in the proceedings after peer review process. The three important aspects of engineering have been covered in this book are Chemical Engineering, Mineral Engineering and Materials Engineering. The chapters in the proceedings are incorporated under three sub-themes, i.e. Chemical Processing, Mineral Processing and Materials Processing to attract the target-specific audience. We expect that these proceedings will be helpful to the students, researchers, industrial consultants and also policymakers in decision-making.

Bhubaneswar, India
Bhubaneswar, India
Mumbai, India

Dr. Eswaraiah Chinthapudi
Prof. Suddhasatwa Basu
Prof. Bhaskar Narayan Thorat

Contents

Chemical Processing

Simulated Natural Gas Hydrate Storage: Experimental and Modeling Approach	3
Bhavikkumar Mahant, Omkar Singh Kushwaha, and Rajnish Kumar	
Engineering Aspects on the Design and Realization of Medical Oxygen Concentrator for Oxygen Therapy	17
Sakshi Singhal, Janardan Singh, Yalisala Lakshman, V. Chitra, N. Saravanan, R. Muraleekrishnan, and S. A. Ilangoan	
Numerical Investigation on the Effect of the Shape of Cavities on the Melting Process of Latent Heat Thermal Storage Material Paraffin Wax	29
Debasree Ghosh, Chandan Guha, and Joyjeet Ghose	
The Study of Wind Speed and Various Leak Size Repercussion on Toxic Chlorine Leakage from Tonner Using 3D Computational Fluid Dynamics (CFD) Analysis Technique	45
Govind K. Patil, Jitendra B. Naik, Nikita K. Patil, Prakash Dandawate, and Sagar R. Pardeshi	
Design of a Centralized PI Controller for Three-Tank Hybrid System Based on Optimization Methods	65
N. Rajasekhar, V. S. V. Bhanukiran, T. K. Radhakrishnan, and N. Samsudeen	
Novel Systems for Utilization of Cold Energy of Liquefied Natural Gas at Regasification Terminal	83
Niteen R. Yeole	
Ionic Mass Transfer in Electrolyte–Kerosene Flow Systems	97
K. Ashok Kumar, G. V. S. Sarma, and K. V. Ramesh	

Application of Epoxidized Vegetable Oil for Improving Rheological Properties of Crude Oil	109
Biswadeep Pal, Sampa Guin, and Tarun Kumar Naiya	
Quaternary Recycling Studies for Desalination Membrane Management	121
M. Srija, S. Bhandari, and T. L. Prasad	
Mineral Processing	
Kaolin: An Alternate Resource of Alumina	135
Sonidarshani Routray, Barsha Dash, Abdul R. Sheik, C. K. Sarangi, and Kali Sanjay	
Effect of Rheology on Filtration of a Brecciated Limestone Ore Slurry	145
Md. Serajuddin, Amit Bhai Patel, Sulekha Mukhopadhyay, and K. Anand Rao	
Integrated Approach for Extraction of Molybdenum and Silica from an Unexploited Nigerian Molybdenite Rich Ore	163
Adeyemi Christianah, Santosh Deb Barma, Mamata Mohapatra, Alafara A. Baba, and Suddhasatwa Basu	
A Comparative Study on Flotation of Coal Using Eco-Friendly Single Reagent and Conventional Dual-Reagent System	175
N. Vasumathi, M. Sai Kumar, D. S. V. Abhishek, T. V. Vijaya Kumar, and S. J. Gopalkrishna	
Beneficiation Aspects to Improve the Quality of Bauxite Mining Waste PLK Rock	189
Satyasish Rout, Santosh Deb Barma, Rahul Kumar Soni, Prasanta Kumar Baskey, C. Eswaraiah, and Danda Srinivas Rao	
Study on Flotation of Sillimanite Using Plant-Based Collector	203
N. Vasumathi, K. Chennakesavulu, I. Cassandra Austen, M. Sai Kumar, T. V. Vijaya Kumar, and Ajita Kumari	
Flotation of Low-Grade Graphite Ore Using Collector Derived from Low-Density Polyethylene Waste	213
M. Sai Kumar, K. Rashid Sulthan, N. Vasumathi, Ajita Kumari, and T. V. Vijaya Kumar	
Material Processing	
Micromorphology and Pore Size Evaluation of Biomass Chars During Pyrolysis	227
R. Shivakumar and Samita Maitra	

Characterization of Indigenous Clay-Based Ceramic Water Purifiers Mostly Available in Tripura and Its Performance Evaluation	237
Aritrika Saha, Harjeet Nath, and Rahul Das	
Magnetic and LPG Sensing Properties of Nickel Ferrite Nanoparticles Derived from Metallurgical Wastes	257
K. J. Sankaran, U. Balaji, and R. Sakthivel	
Catalytic Behavior of Noble Metal Nanoparticle-Metal Oxide Assemblies: An Effect of Interfacial Ligands	265
Simantini Nayak and Yatendra S. Chaudhary	
Optimization of Nickel Loading of Ni-Al₂O₃ Catalyst for Syngas Production by Tri-Reforming of Methane	277
Satyam Gupta and Goutam Deo	
Preparation of SiC from Rice Husk: Past, Present, and Future	287
Saroj Kumar Singh, Sudarsan Raj, and Debiduta Debasish	
Synthesis and Characterization of a Novel Nanocarbon Derived Nanoporous Al₂O₃ Powder as a Potential Adsorbent for Treatment of Wastewater	295
K. Sarath Chandra, D. Suharika, Debasish Sarkar, G. V. S. Sarma, and K. V. Ramesh	
Rice Husk-Derived Silica Nanoparticles Using Optimized Titrant Concentration for the One-Step Nanofluid Preparation	303
Prashant Kumar and Sudipto Chakraborty	

About the Editors

Dr. Eswaraiah Chinthapudi obtained his B.Tech. in Chemical Engineering from S.V. University, Tirupati, and subsequently received his M.Tech. and Ph.D. in Chemical Engineering from Indian Institute of Technology Kharagpur and Indian Institute of Technology Madras, respectively. Prior to joining CSIR-IMMT as a scientist, he worked as a project officer at IIT Madras in a BHEL sponsored project. He worked as a CSIR-Quick Hire Fellow during the year 2006–2007 at CSIR-IMMT. Currently, he is a senior principal scientist in the Mineral Processing Department at CSIR-IMMT, Bhubaneswar, and a professor of Engineering Sciences, AcSIR. He has more than 15 years of R&D and teaching experience in the area of mineral processing. During his tenure, he has been involved in several projects as a project leader/team member and made commendable contributions to the mineral and metallurgical process industries. He has developed several beneficiation processes for low-grade ore fines and slimes, which has led the industries to produce the quality of raw materials required for steel production. He has published over 50 research articles in national/international journals and conferences to his credit. His area of specialization is advanced particulate processing, modelling, and simulation. In recognition of his outstanding contributions in particulate processing, he has been awarded several prestigious awards from various organizations/professional societies. He is a fellow of the Indian Institute of Chemical Engineers (FIChE), a fellow of the Institution of Engineers (India) (FIE), and a member of several professional societies. He was awarded Indian National Science Academy (INSA) Fellowship to work at CSIRO, Brisbane, Australia, for one year. He also worked as a senior researcher at the University of Lorraine, Nancy, France, for 12 months. Currently, he is working on an energy-efficient dry beneficiation process development to treat the low-grade ores, slimes. He has significant exposure and experience in equipment design. He designed and developed an indigenous advanced computer monitored twin-pendulum device, a unique facility in India for online determination of actual breakage energy during grinding. At present, Dr. Eswaraiah and his team are designing an indigenous energy-efficient stirred mill to treat the Indian low-grade ores.

Prof. Suddhasatwa Basu completed Ph.D./M.S. in Chemical Engineering from the Indian Institute of Science, Bangalore, after obtaining B.Tech. in Chemical Engineering from Calcutta University. He worked for five years as a research fellow and as a visiting faculty at the University of Alberta, Edmonton, Canada. Prior to taking over as the director of CSIR-IMMT, he was an associate dean (research development) and a former head of Chemical Engineering Department at the Indian Institute of Technology (IIT) Delhi. He has vast work experience in developing energy materials and their application to energy conversion and storage devices, e.g., fuel cells, supercapacitors and batteries, electrolyser for hydrogen generation by water splitting, and CO₂ reduction to organics. He worked on Oil-Sands Extraction at Alberta, Canada, specializing in slurry transport and separation of oil and sands. Earlier, he also worked on Colloids and Interfacial Phenomena, particularly on demulsification and removal dye from wastewater. He has published over 200 papers in high-impact journals (H-index 38), holds 7 patents, successfully transferred 2 technologies to various industries, and completed Rs 20 Crore worth of projects at IIT Delhi. He is a fellow of Indian Academy Engineering, National Academy of Science of India, fellow of Royal Soc. Chem. U.K., fellow of International Association of Advanced Materials, received Herdillia Award - Excellence in Basic Research in Chemical Engineering, Dr. A. V. Rama Rao Foundation's Research Award in Chemical Engineering/Technology. He is an editor/associate editor/editorial board member of several international journals published by Willey, Springer, Elsevier, and ACS.

Prof. Bhaskar N. Thorat completed graduate and postgraduate degree in Chemical Engineering from ICT-Mumbai. He later received his Doctorate in Chemical Engineering from ICT-Mumbai under the guidance of Padmabhushan Professor J. B. Joshi. He worked under multiple renowned mentors, namely Prof. Arun S. Mujumdar, Prof. M. M. Sharma, and Prof. G. D. Yadav. He started his career at National Chemical Laboratory, Pune, as a scientist. Then, he worked as a senior lecturer in Chemical Engineering at ICT, Mumbai, and was later appointed as a professor of Chemical Engineering Department at the Institute of Chemical Technology/UDCT, Mumbai (2006–2018). Meanwhile, he also served as the head of Department, Dept. of Chemical Engineering from 2015–2018, at the Institute of Chemical Technology, Mumbai. Since August 2018, he has been appointed as the director of a newly established Odisha off-campus of ICT, supported by the Indian Oil Corporation (IOC). He has over 30 years of experience in developing grass root and sustainable technologies based on the fundamentals of chemical engineering products and allied branches. He has had more than 250 consultancy assignments in the last 20 years. He has authored more than 200 papers in peer-reviewed journals and international proceedings and has co-authored and edited more than 10 monographs. He also holds more than 10 patents, with 100% commercialization. He is a fellow of the Royal Society of Chemistry and Indian Chemical Society. He received the Lifetime Achievement Award for Outstanding Contribution to Drying and Dehydration, 2019, by Taylor and Francis. He also received several renowned awards such as NOCIL AWARD for excellence

in the design of new equipment and process in 2015, Gunther Oertel Startup Innovation Award for Microbutor Innovation in 2017, Bill and Melinda Gates Foundation Award of USD 260,000 for Innovative Dryers in 2013, etc.

Chemical Processing

Simulated Natural Gas Hydrate Storage: Experimental and Modeling Approach



Bhavikkumar Mahant, Omkar Singh Kushwaha, and Rajnish Kumar

1 Introduction

There is observed a substantial growth and advancement in the research and development towards the gas hydrate based storage and transportation of greenhouse gases such as methane and carbon dioxide, including the innovative ways to utilize the hydrogen along with the methane [1, 2]. Recently, it has been observed that the gas hydrate research trend includes investigations on hydrogen gas based gas hydrates [3]. While it requires an enormous amount of time to gain the maturity and confidence to develop sustainable technology for hydrogen gas hydrates, the world is focusing on the scale-up opportunities for natural gas hydrate (NGH) as an energy source. All the research studies in this direction add up the important data for a better understanding of the various types of gas hydrates either based on the gas composition, simulated requirements, or application based research [1].

Natural gas has emerged as a primary energy source in many applications worldwide due to its contribution to lowering pollution and high energy conversion. In order to store and transport, the world has well established supply chain of liquefied natural gas (LNG) across the continents [4]. However, it is facing a significant amount of challenges during the small-scale transportation of natural gas. Although compressed natural gas (CNG) technology is accountable for major small-scale transportation, CNG has inherent safety and operational challenges [4]. Many times, accidents occurred due to CNG technology, resulting in catastrophic to human lives and establishments. Other than that, the past findings suggested that CNG is not as economical as LNG and NGH in order to transport natural gas to more than 2000 km

B. Mahant (✉) · O. S. Kushwaha · R. Kumar
Department of Chemical Engineering, Indian Institute of Technology Madras, Chennai 600036,
Tamil Nadu, India
e-mail: ch19d752@smail.iitm.ac.in

[4]. To troubleshoot the mentioned challenges of CNG technology, NGH is under research for better storage and transportation in the form of natural gas [5].

Gas hydrates are compounds that are formed in the presence of water and gas at moderately high pressure and low temperature. The major limitation of gas hydrate formation is the slow formation rate due to the mass transfer limitation at the interface of gas and liquid [6]. The reported solution to the mass transfer limitation is to use the kinetic hydrate promoters (KHPs), which can increase the formation rate by surface modification, and thermodynamic hydrate promoters (THPs), which are responsible for shifting the phase equilibria by taking part in the gas hydrate formation process [7, 8]. The major class of KHPs includes surfactant molecules that can be an effective solution; however, they have very high foam generation and are not perfectly biodegradable [8, 9]. Hence, in order to further exploit gas hydrate technology for the storage and transport of other gases, particularly natural gas, a set of organic di-acids were used as additives.

In the present work, the storage and modeling studies on simulated natural gas (SNG) hydrates were done in a similar reactor setup as described by Kushwaha et al. 2019 [10]. The additives, namely oxalic acid and succinic acid, were selected based on the data analyzed on the basis of solubility and nonpolar gas diffusion inferences. The present study reports the observations on the storage capacity of the SNG in a designed reactor setup that can open up the opportunities to utilize the novel gas hydrate promoters, which have not formed the high foam generation and are biodegradable in nature.

The gas hydrate research has been using various types of modeling approaches to predict the gas hydrate formation conditions apart from the empirical equations. Artificial neural network (ANN) and adaptive neuro-fuzzy inference systems (ANFIS) were employed to understand the impact of model prediction on gas hydrate formation [11]. ANN and ANFIS application in the methane gas hydrate formation were studied and elaborated in the previously published results [12]. A detailed study on an ionic liquid solution on methane gas hydrate with the help of ANFIS was demonstrated by Ghiasi et al., 2021. That provides the basis for predicting the modeling data for methane gas hydrate apart from the affluence of pure water to form gas hydrate [13].

The novelty of the study is to extract the properties of both the chemical additives to give their impact on the hydrogen bonding present in the gas hydrate water cages. The chemical di-acids can mitigate the major bottleneck of high foam generation by using conventional surfactants. Other than that, both di-acids are biological compounds and completely biodegradable, which can conserve the environment. In oxalic acid, only have -COOH group present in its molecular structure, which can initiate the forming of hydrogen bonds in between the water cages. The highly present hydrogen bond in oxalic acid makes the process of gas hydrate formation slower. While, in succinic acid (COOH-CH₂-CH₂-COOH) has the presence of hydrophobic sites in terms of -CH₂, which increases the dissolution of nonpolar gas and makes faster the process of gas hydrate promotion. Therefore, due to the molecular arrangements of given di-acids, the promotion or inhibition of gas hydrate formation.

Table 1 Composition of simulated natural gas (SNG)

S. no.	Gas component	Composition (mol %)
1	Methane	88.4
2	Ethane	4.80
3	Propane	3.45
4	n-butane+iso-butane	1.94
5	Carbon dioxide	1.41

2 Material and Methods

2.1 Materials

All the chemicals used in this study for the SNG gas hydrate formation were LR grade. Any kind of further treatment was not applied to the chemicals. High purity (purity 99%) oxalic acid and succinic acid were obtained from SRL Pvt. Ltd, India. Milli—Q water was used throughout the study to make a solution and pure water. The SNG gas with the composition mentioned in Table 1 was supplied by the Indo Gas agency, India.

2.2 Methods

2.2.1 Experimental Setup

The experimental setup with an SS-316 jacketed crystallizer of 140 cm³ with polycarbonate windows was used to conduct the experiments, as shown in Fig. 1. The crystallizer was fitted with a pressure transducer (Wika, range 0–16 MPa) and a temperature sensor (RTD-Pt 100). The temperature was maintained by an external temperature control unit supplied by Siskin Profichill, India. A magnetic stirrer, Remi-make (1 ML), was used to rotate the liquid-gas mixture inside the crystallizer. The controller and data acquisition system (PPI) was used to acquire the pressure and temperature data, which was further analyzed using data processing and a computational unit.

2.2.2 Experimental Procedure

The crystallizer was cleaned with the soap solution and acetone and then rinsed with Milli-Q water. The chemicals were dissolved in the required amount of Milli-Q water for making an aqueous solution. The stirring was done to the aqueous solution to get a clear homogeneous solution. 50 ml of the aqueous solution was transferred to the crystallizer, and a magnetic pellet was placed inside it. The crystallizer was sealed, and the coolant (ethylene glycol+water) was circulated inside the jacket to attain

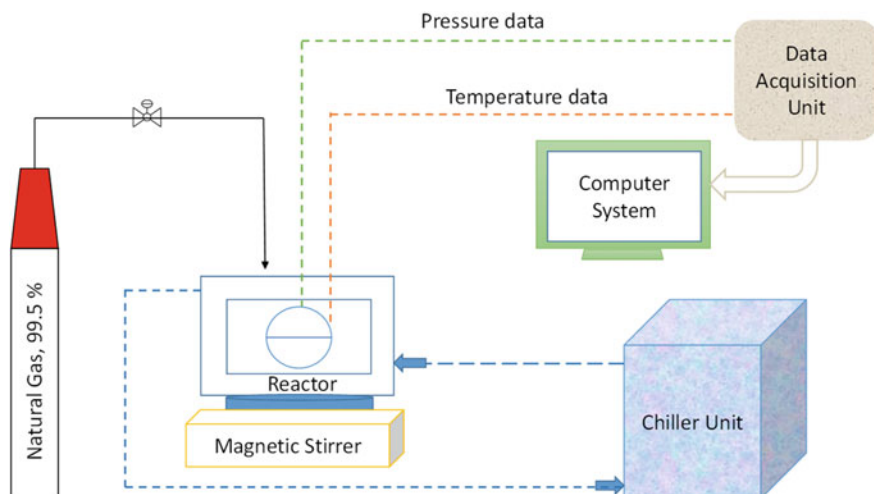


Fig. 1 Experimental setup for simulated natural gas storage in gas hydrate

the temperature of 274.15 K. The simulated natural gas (SNG) was flushed through the reactor after attaining the desired temperature. The natural gas was then charged ~ 3 MPa, which was higher than the hydrate forming three-phase equilibrium pressure of natural gas. For the molar calculations used in this study, the initial data of the gas dissolution has been avoided. Therefore, the natural gas magnetic stirrer was started with a fixed speed of 350 RPM after charging. The end of the hydrate formation process was marked as shown in the stability of the pressure and temperature, and this was taken as the sign of saturation. For each system, three individual fresh, experimental runs were performed. The results are reported considering standard deviations obtained from the experimental data.

2.2.3 Theory and Calculations

The gas hydrate formation process is categorized mainly into two parts: (1) Induction Period and (2) Growth Period. The induction time is known as the time taken for the nucleation of the first solid hydrate crystal. The nucleation has been followed by hydrate growth, where the hydrate formation takes place very quickly and consistently, which results in a sharp pressure decline. The present study includes induction time as the time until a sudden pressure drop was observed with the simultaneous increase in the temperature [6, 7].

The gas trapped or the amount of gas enclathrated in the cages is calculated by taking the difference between moles of gas injected in the crystallizer and the moles of gas present in the gas phase [14] at any given time “ t ” by using Eq. (1).

$$(\Delta n_{h,\downarrow})_t = \left(\frac{V_r P}{zRT} \right)_{t=0} - \left(\frac{V_r P}{zRT} \right)_{t=t} \quad (1)$$

where,

V_r Volume of the gaseous phase in the reactor,

P Pressure in the reactor,

T Temperature in the reactor,

R Universal gas constant,

z Compressibility factor, calculations based on Pitzer's correlation.

The hydrate formation rate is calculated by the forward difference formula as given in Eq. (2).

$$\left(\frac{d(\Delta n_{h,\downarrow})_t}{dt} \right) = \frac{(\Delta n_{h,\downarrow})_{t=0} - (\Delta n_{h,\downarrow})_{t=t}}{\Delta t} \quad (2)$$

For the gas hydrate processes, the water to hydrate conversion [6] gives an idea of the efficiency of the reaction, which can be obtained by using Eq. (3).

$$\text{Conversion of water to hydrate (mole\%)} = \frac{\Delta n_{h,\downarrow} \times \text{Hydration Number}}{n_{\text{water}}} \times 100 \quad (3)$$

where,

n_{water} moles of water

Hydration number 6.2 for structure (I) and 5.75 for structure (II).

2.2.4 Artificial Neural Network (ANN) Modeling

The artificial neural network is a mathematical model structured by the functions of neurons, which has applications in the approximation and prediction of experimental processes [15]. The network has computational units in such a way that mimics the biological structure of the human brain [15, 16]. To optimize the proposed model better, there are multiple numbers of connections within and between the layers in terms of weights used for storage and learning the information [15, 16].

ANN network for the current study had been developed in order to cater to the requirements of the gas hydrate formation process in Matlab R2021a, which is represented in Fig. 2. Three input parameters that include time, pressure, and temperature were considered in the input layer. The data were processed in the hidden layers and converted the result in mole consumption as methane as the output layer [16, 17]. The proposed results obtained from the ANN model were further investigated in order to test the model with the experimental results. The weight and biases data from the ANN model were extracted in order to develop a mathematical representation of the ANN model. Substitute all the input data which were collected from the

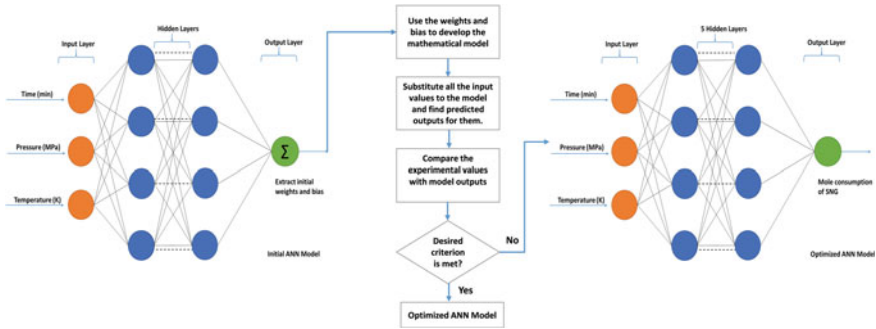


Fig. 2 Schematic diagrams of ANN model used in the study of methane gas hydrate formation in the presence of di-acids

experimental conditions and calculate the output from it. The predicted results from the mathematical ANN model were compared with the experimental results to check the consistency of the results.

2.2.5 Adaptive Neuro-Fuzzy Inference System (ANFIS) Modeling

Jang developed the ANFIS model by considering it a new type of the ANN model [18]. The ANFIS is based on the system of the Takagi-Sugeno fuzzy inference system. It is an adaptive learning based model, which is the main difference between ANFIS and fuzzy logic (FL) based model [18].

ANFIS has the neural network block, which can be able to learn from the input data of the model. The Neuro-Fuzzy tool available in the Matlab R2021a was used to perform the ANFIS study. The Sugeno type ANFIS model was used for the current study with a hybrid optimization method [13]. The structure of the ANFIS model used for methane gas hydrate is shown in Fig. 3.

3 Results and Discussion

3.1 Mole Consumption Analysis of SNG for Gas Hydrate Formation

The experimental data were analyzed in order to understand the kinetics of natural gas hydrate formation in a comparative manner. Figure 4 represents the mole consumption profiles in the presence of the additives in two concentrations.

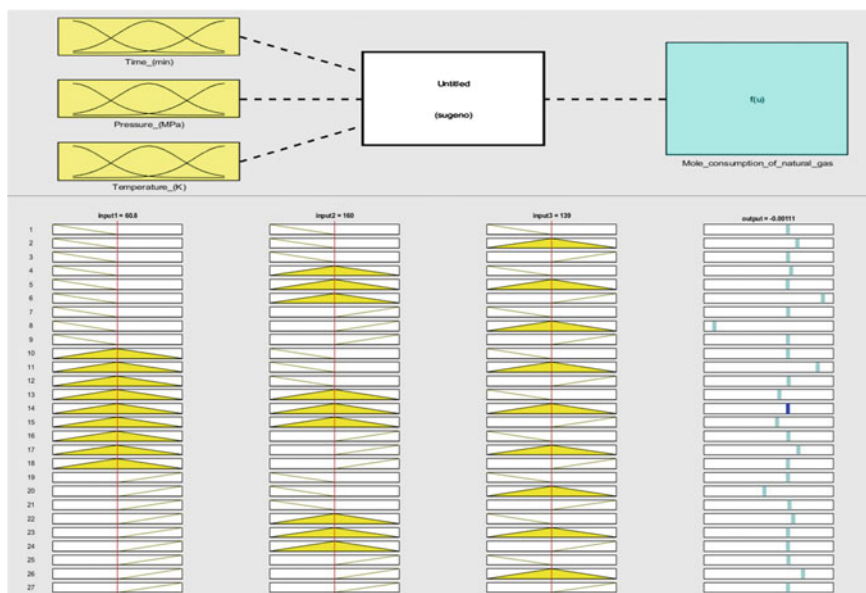


Fig. 3 Snapshot of ANFIS interface developed in Matlab R2021a for natural gas hydrate mole consumption

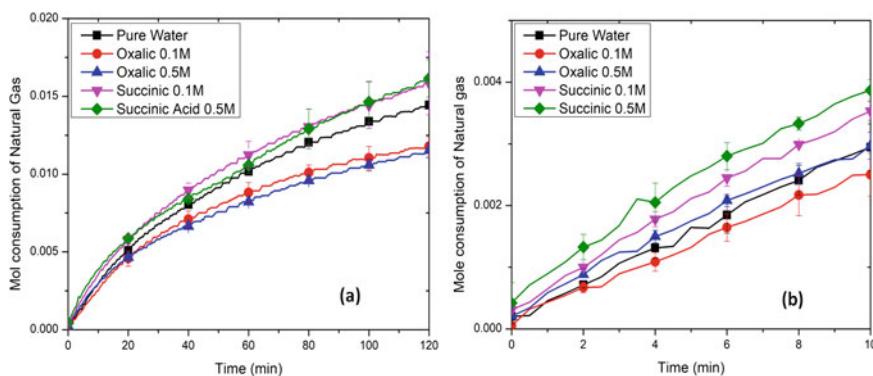


Fig. 4 Mole consumption comparison of SNG during the formation of natural gas hydrates in pure water and different additives systems in **a** 0.1 M and **b** 0.5 M concentrations

It is evident from Fig. 4a, which represents the SNG uptake profiles for 120 min. The data includes oxalic and succinic acid systems with 0.1 M and 0.5 M concentrations. Gas hydrate experiments include gas dissolution, gas hydrate nucleation section, and gas hydrate growth phase [7, 8]. In the current results, the origin of the graph represents the natural gas hydrate nucleation inside the crystallizer. Here, it is evident that the highest SNG uptake was observed in the case of succinic acid

systems (SAS) with the concentration of 0.5 M, having high similarity with the results of 0.1 M. Thus, succinic acid showed a higher kinetic promotion of the gas uptake during hydrate formation.

On the other hand, oxalic acid exhibited the opposite trend to succinic acid results by showing inhibiting behavior during the natural gas hydrate formation. The 0.1 M concentration of the oxalic acid system showed relatively less inhibition during the gas hydrate formation than the 0.5 M oxalic acid system. This result explains that the higher the concentration of oxalic acid system, the more inhibition effect was attended.

The analysis of the uptake profiles for the initial 10 min is represented in Fig. 4b. The initial gas hydrate formation kinetics of 10 min is significant and can further provide insights into gas hydrate nucleation and the initial growth phase of gas hydrate. The results revealed consistent behavior of succinic acid, whereas the mixed observations in the case of water and oxalic acid were found, which showed relatively low kinetics to that of succinic acid systems.

As shown in Fig. 4a, the oxalic acid was clear, inhibiting the gas hydrate formation for a more extended period. While in the results of the first 10 min in Fig. 4b, the results of oxalic acid and water were shown mixed behavior of promotion and inhibition of gas hydrate. The major reason behind this is the helping nature of oxalic acid to form hydrogen bonds with water cages and aiding the gas hydrate formation process in the initial phase. The 0.1 M oxalic acid can make less hydrogen bonding, reduce the cage formation behavior of water, and make it a gas hydrate inhibitor. At the same time, the higher concentration of 0.5 M oxalic acid has a higher amount of hydrogen bonding, which enhances the cage formation behavior of water and temporarily promotes gas hydrate formation. Ultimately, oxalic acid inhibits the gas hydrate in the long run.

3.2 Gas Uptake and Induction Time of Natural Gas Hydrate Formation

The gas uptake profile demonstrated the continuous and good conversion of SNG into SNG gas hydrate based on the availability of water and gas in the reactor system. Additionally, the natural gas uptake data follows a similar trend to the SNG mole consumption data, thus projecting that the oxalic acid system results in a lower conversion of SNG to SNG hydrates. It is shown in Fig. 5a that the succinic acid system with both concentrations provides a higher gas uptake in comparison to water. The analysis of SNG gas uptake in this section concludes that the presented process has the potential to convert a good quantity of SNG into SNG gas hydrates.

The SNG mole consumption and gas uptake profiles are influenced by the induction time. The induction time of all additive systems, oxalic acid, succinic acid, and pure water are duly represented in Fig. 5b. Thus, representing the effect of additive concentration on the induction time during the gas hydrate formation process. The oxalic acid systems have an induction time of 35–45% higher than the pure water

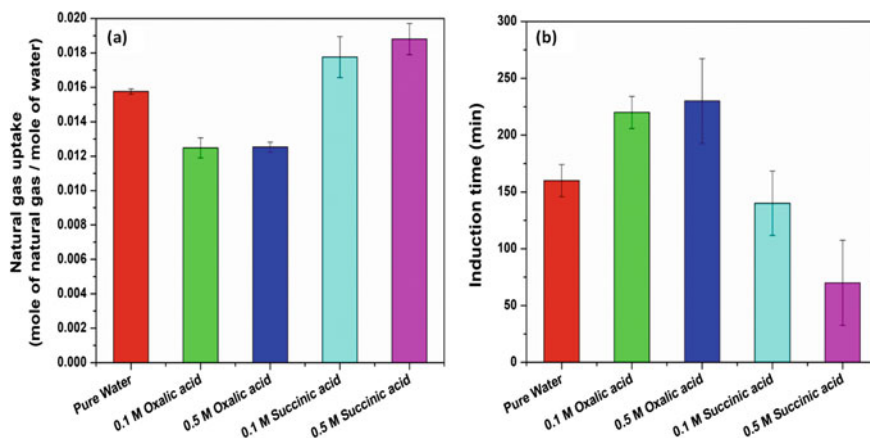


Fig. 5 **a** Comparison of SNG gas uptake derived from the mole of natural gas consumed per mole of water. **b** Comparison of induction time of SNG gas hydrate formation in the presence of the various system

system, distinguishing it as the prominent gas hydrate inhibitor for the formation of SNG gas hydrate. At the same time, the succinic acid systems have shown relatively lower induction times in the range of 10–60% compared to the pure water system.

Overall, the experimental findings for the gas uptake and the induction time explain the impact of using di-acids as non-foaming additives with the water on the formation of SNG gas hydrates. The results showed that oxalic acid has inhibition behavior during the gas hydrate formation, while succinic acid is responsible for the promotion effect during the gas hydrate formation.

3.3 ANN Modeling of Natural Gas Consumption in the Gas Hydrate

The gas uptake profiles give a better understanding of the moles of gas consumed during the hydrate formation process. Figure 6 gives a comparative analysis of the profiles obtained from the moles of gas consumed during the experiment and the moles of gas consumed predicted by the ANN modeling. The ANN model data followed the experimental results perfectly well in the linear regression analysis of them, having an R^2 value of more than 0.95. Figure 6a explains the result achieved for 0.1 mol % oxalic acid solution for SNG gas hydrate formation. The predicted model fits the experimental value at a significantly better value. Figure 6b explains the same details for 0.5 mol % oxalic acid solution and has an excellent agreement between model and experimental value. Oxalic acid has a linear profile with significant inhibition for SNG mole consumption, resulting in the accurate ANN model prediction.

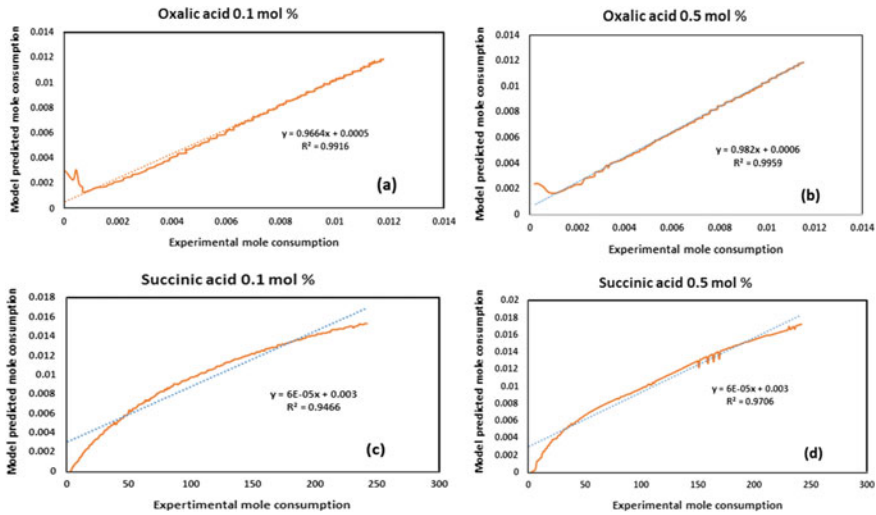


Fig. 6 Comparison of ANN based prediction of SNG mole consumption with experimental mole consumption **a** oxalic acid 0.1 M, **b** oxalic acid 0.5 M, **c** succinic acid 0.1 M, **d** succinic acid 0.5 M

Figure 6c provides the detail of fitting between ANN modeled values with experimental value for 0.1 mol % succinic acid solution. The model data follows the experimental values very well, as shown. Figure 6d gives the same detail for 0.5 mol % succinic acid solution, which is better fitting than the fitting of 0.1 mol %. The major reason for less accurate fitting for succinic acid is the sharp increase in the SNG mole consumption by acting as a gas hydrate promotor. Results concluded that ANN could provide a better understanding of the experimental values by using mathematical modeling.

3.4 ANFIS Modeling of Natural Gas Consumption in the Gas Hydrate

In this study, ANFIS, along with ANN, was employed to better understand SNG gas hydrate formation with the help of robust modeling tools. Although ANN has most of the features to include all the randomized effects during the experimental study, ANFIS can provide the fuzzification of the data that can reduce the time consuming approach of ANN modeling. ANFIS has another important characteristic for exhibiting the clustering of the data used for the ANN study. ANFIS can provide the inner structural details of the system on which the modeling study was performed. [12]. In the ANFIS finding, the training of a maximum 1000 epoch was performed in order to remove the inconsistency and increase the regression coefficient to compare respective modeling and experimental result.

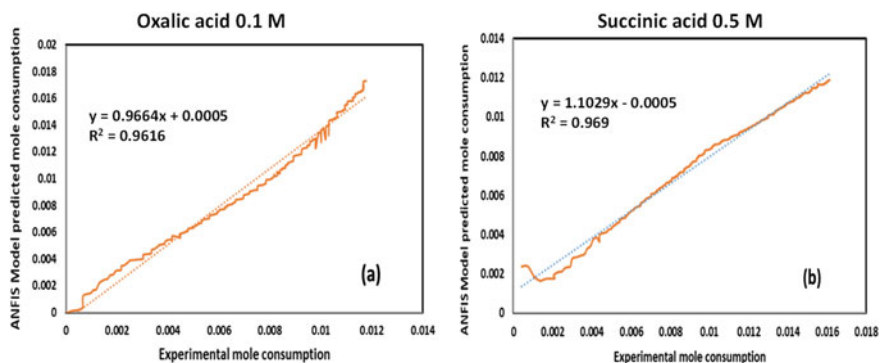


Fig. 7 Comparison of ANFIS based prediction of SNG mole consumption with experimental mole consumption **a** oxalic acid 0.1 M, **b** succinic acid 0.5 M

The modeling data was extracted from the ANFIS interface in Matlab. The extracted data were further used for the linear regression analysis, and it turned out that the R^2 value of the regression was more than 0.96 for all of the cases. The results in Fig. 7a explain the data predictability for the oxalic acid system, and the same is explained for the succinic acid system in Fig. 7b. The ANFIS data can be used to check the data consistency and scrutinization in future studies, thus enabling the other di-acids to be scrutinized on a comparative model with the current additive systems in further studies.

4 Conclusion

A comparative investigation of the gas hydrate based gas uptake of SNG in the presence of simple di-acids was conducted, which revealed a better gas uptake in the case of succinic acid molecules with a high affinity towards nonpolar gases giving a synthetic natural gas uptake order of SAS > Water system > OAS. The di-acids can act as the kinetic gas hydrate promotor or inhibitor without foaming, unlike the conventional kinetic hydrate promotors like surfactants. The nature of di-acids is biodegradable, which can provide the basis for the sustainable scale-up of the given process. The ANN modeling on the experimental output of gas consumption has been found to give a much better fit for the gas uptake profiles having high accuracy than the experimental analysis. ANN modeling is also helpful in understanding the gas promotion or inhibition effect for similar kinds of chemical additives. ANFIS model was also constructed in order to study the internal parameters and data structure with lower time requirements. The results from the ANFIS data also well followed the experimental results and proved the study in a more meaningful way. That will be useful to screen the suitable chemical additive with low dependence on experimental study. Thus, a further study on higher acids may give more insights.

Therefore, based on the experimental findings in this work, the authors have explored the formation of natural gas hydrates using the simulated gas composition by using a gas hydrate based process. Thus, using these additives, an economical process may be further developed for various applications such as the separation of the gases from the mixture of gases, gas storage, desalination, and energy transportation. This work also gives deeper insights into the economically feasible way for the storage of methane enriched gas mixtures under controlled conditions. The experimental observations are found to be well supported by computer aided programs (AI tools). This study further opens the doors for further exploration of the gas hydrates for their chemical nature and structural details in the presence of non-foaming organic additives.

Acknowledgements The authors would like to thank the facilities provided by the Indian Institute of Madras for carrying out the research. Bhavikkumar acknowledges the Prime Minister Research Fellowship from the Ministry of Education, Government of India.

References

1. Hassanpouryouzband A, Joonaki E, Farahani MV, Takeya S, Ruppel C, Yang J, Tohidi B (2020) Gas hydrates in sustainable chemistry. *Chemical Soc Rev* 49(15):5225–5309
2. Mahant B, Linga P, Kumar R (2021) Hydrogen economy and role of hythane as a bridging solution: a perspective review. *Energy Fuels* 35(19):15424–15454
3. Ghosh D, Devi P, Kushwaha OS, Kumar R, Kumar P (2020) In operando generation and storage of hydrogen by coupling monolithically integrated photoelectrochemical cell with clathrate hydrates molecular storage. *ACS Appl Energy Mater* 3(7):6834–6844
4. Hao W, Wang J, Fan S, Hao W (2008) Evaluation and analysis method for natural gas hydrate storage and transportation processes. *Energy Convers Manage* 49(10):2546–2553
5. Kanda H (2006) Economic study on natural gas transportation with natural gas hydrate (NGH) pellets. In: *Proceedings of 23rd world gas conference*, Amsterdam, pp 1990–2000
6. Sloan Jr ED, Koh CA (2007) *Clathrate hydrates of natural gases*, 3rd edn. CRC Press
7. Kushwaha OS, Meshram SB, Bhattacharjee G, Kumar R (2019) Molecular insights about gas hydrate formation. In: *Advances in spectroscopy: molecules to materials*. Springer, Singapore, pp 311–322
8. Meshram SB, Sardar H, Kushwaha OS, Sangwai J, Kumar R (2021) A systematic molecular investigation on sodium dodecyl benzene sulphonate (SDBS) as a low dosage hydrate inhibitor (LDHI) and the role of Benzene Ring in the structure. *J Mol Liq* 337:116374
9. Choudhary N, Kushwaha OS, Bhattacharjee G, Chakrabarty S, Kumar R (2020) Macro and molecular level insights on gas hydrate growth in the presence of Hofmeister salts. *Ind Eng Chem Res* 59(47):20591–20600
10. Meshram SB, Kushwaha OS, Reddy PR, Bhattacharjee G, Kumar R (2019) Investigation on the effect of oxalic acid, succinic acid and aspartic acid on the gas hydrate formation kinetics. *Chin J Chem Eng* 27(9):2148–2156
11. Mehrizadeh M (2021) Prediction of gas hydrate formation using empirical equations and data-driven models. *Mater Today Proc* 42:1592–1598
12. Foroozesh J (2013) Application of Artificial Intelligence (AI) modeling in kinetics of methane hydrate growth. *Am J Anal Chem* 4(11):616
13. Ghiasi MM, Mohammadi AH, Zendejboudi S (2021) Modeling stability conditions of methane Clathrate hydrate in ionic liquid aqueous solutions. *J Mol Liq* 325:114804

14. Smith JM, Van Nas HC, Abbott M (2004) Introduction to chemical engineering thermodynamics. McGraw-Hill
15. Mohammadi AH, Richon D (2008) A mathematical model based on artificial neural network technique for estimating liquid water–hydrate equilibrium of water–hydrocarbon System. *Ind Eng Chem Res* 47(14):4966–4970
16. Ghavipour M, Ghavipour M, Chitsazan M, Najibi SH, Ghidary SS (2013) Experimental study of natural gas hydrates and a novel use of neural network to predict hydrate formation conditions. *Chem Eng Res Des* 91(2):264–273
17. Rebai N, Hadjadj A, Benmounah A, Berrouk AS, Boualleg SM (2019) Prediction of natural gas hydrates formation using a combination of thermodynamic and neural network modeling. *J Petrol Sci Eng* 182:106270
18. Jang JS (1993) ANFIS: adaptive-network-based fuzzy inference system. *IEEE Trans Syst Man Cybern* 23(3):665–685

Engineering Aspects on the Design and Realization of Medical Oxygen Concentrator for Oxygen Therapy



Sakshi Singhal, Janardan Singh, Yalisala Lakshman, V. Chitra, N. Saravanan, R. Muraleekrishnan, and S. A. Ilangovan

1 Introduction

Medical Oxygen Concentrator (MOC) is a portable standalone medical device used for continuous generation of medical grade oxygen to support patients with respiratory illness or for oxygen therapy. In the present scenario of COVID-19 pandemic, treatment of seriously ill patients depends on Oxygen supply and ventilator support. There is a wide scarcity for oxygen cylinders especially in rural areas. In this situation, an effective functional relief could be medical oxygen concentrators that are mobile, handy and available in short time. Oxygen concentrators are highly reliable but units are costly in the open market. The technology is currently limited to very few countries. Under this scenario, a portable and affordable Medical Oxygen Concentrator is the need of the hour. Considering the above, VSSC, ISRO has realized an Engineering Model (EM) of portable medical oxygen concentrator which is capable of generating oxygen (conc. > 82%) continuously @10 LPM as per World Health Organization standards [1]. It works on the principle of Pressure Swing Adsorption (PSA) which is commonly used for the production of enriched oxygen from air [2–4]. Nitrogen from compressed air is removed by adsorption-desorption cycles in two zeolite columns operating in tandem, resulting in enriched oxygen in the product stream. The MOC was tested extensively as per WHO/ISO norms by ISRO.

Major components of MOC include a series of filters, oil free air compressor, PSA columns, medical grade zeolite, solenoid valves, oxygen accumulator, sensors for oxygen, pressure & flow, flowmeter and humidifier. PSA columns, oxygen accumulator and heat exchanger are designed and fabricated in-house for realizing the engineering model of MOC. Zeolites are microporous, aluminosilicate minerals

S. Singhal (✉) · J. Singh · Y. Lakshman · V. Chitra · N. Saravanan · R. Muraleekrishnan · S. A. Ilangovan
Vikram Sarabhai Space Centre, Thiruvananthapuram 695022, Kerala, India
e-mail: sakshi_singhal@vssc.gov.in

commonly used as adsorbent materials. Medical grade Zeolite of particle size 0.4–0.9 mm is used in this unit. These selectively adsorb nitrogen from air under pressure and provide high purity oxygen. The effect of air flow rate, cycle time and column pressure on oxygen purity was studied thoroughly and operating conditions are optimized. This paper provides an overview of engineering aspects of sub-systems, selection of instruments involved in realizing the MOC.

The major objective of this study was to indigenously design, develop and demonstrate the technology for enrichment of oxygen from air stream by means of a portable Medical Oxygen Concentrator at an affordable cost to meet the oxygen demands of our country.

The developed oxygen concentrator is unique in itself as it is capable of catering the needs of enriched oxygen continuously for two patients at a time. The unit is additionally equipped with adequate safety precautions including safety relief valves between compressor and the PSA column, between oxygen accumulator and delivery to a patient. It also monitors and displays various parameters such as concentration of oxygen, flowrate and delivery pressure. The unit also has various alarm warnings for low/high flow, low/high pressure, low concentration of oxygen and start-up alarm. This will help facilitate the user to be cautious in case, any malfunctioning occurs in the unit. It also has an hour meter to display the total run time of the unit.

2 Material and Methods

2.1 Major Components

Following are the major sub-systems used in MOC and its functions (Table 1).

2.2 Major Sub-Systems

2.2.1 Oil Free Air Compressor

As per WHO norms, the inlet air to PSA columns should be free from oil contaminants. Hence, oil free air compressor is selected for MOC. The capacity of Oil free air compressor is calculated from Eqs. (1) and (2) [5, 6] based on the amount of inlet air flowrate required to generate 10 LPM of oxygen at the outlet.

$$\dot{W} = Z_1 \times T_1 \times \frac{n}{(n-1)} \times \left[\left(\frac{P_2}{P_1} \right)^{\left(\frac{n}{n-1} \right)} - 1 \right] \quad (1)$$

$$T_2 = T_1 \times \left(\frac{P_2}{P_1} \right)^m; m = \left(\frac{\gamma - 1}{\gamma \eta_p} \right); n = \frac{1}{(1 - m)} \quad (2)$$

Table 1 Major components of MOC with their basic functions

Component	Function
Gross particle filter	To remove the impurities present in air (dust and other particles > 10 μ)
High efficiency particulate arrestance (HEPA) filter	To remove 99.99% of bacteria present in the air
Oil free air compressor with noise filter	To push air into the machine and forward it to the zeolite beds and noise filter is provided to meet the sound levels specified as per WHO norms (<40 dB)
Exhaust fan	To remove the heat generated inside the cabinet
Zeolite	Micro porous mineral; Have the ability to trap Nitrogen
PSA column	Filled with zeolite where oxygen separation takes place based on the principle of pressure swing adsorption
Valves (solenoid/SRV and check valve)	To divert air flow on swing mode between the two zeolite beds/To maintain supply pressure of air input and oxygen output
Oxygen accumulator	To maintain sufficient oxygen volume
Sensors (oxygen purity, pressure, flow)	To measure and monitor the parameters for display
Flow meter	To maintain the set oxygen flow (in LPM)
Humidifier	Bubble type, to humidify the oxygen to the patients
Pressure regulator	To regulate the pressure of oxygen at the outlet of the oxygen accumulator
LCD display	To display oxygen purity (%), flow rate (L/min), operating pressure (kPa) and alarms

where,

- \dot{W} Work done by compressor per mole
- T_1 Inlet temperature of air
- Z_1 Compressibility factor
- γ Ratio of specific heat (C_p/C_v)
- m Polytropic temperature exponent
- T_2 Outlet temperature of the air
- P_1 Inlet pressure of the air
- P_2 Outlet Pressure of the air
- η_p Efficiency of Air Compressor.

2.2.2 Heat Exchanger

Warm air from the air compressor is passed through coil type heat exchanger, which is then cooled using air drawn from the ambient under forced convection using a fan. The quantity of heat to be removed and heat transfer area is calculated using the following equations [5, 6]

$$\dot{Q} = m_{Air} \times C_{Air} \times \Delta T_{Air} = U A \Delta T \quad (3)$$

$$\frac{1}{U_i} = \frac{1}{h_i} + r_i \frac{\ln \frac{r_o}{r_i}}{k} + \frac{r_i}{r_o h_o} \quad (4)$$

where,

- \dot{Q} Heat duty of air cooler
- U_i Overall heat transfer coefficient based on inner tube
- U Overall heat transfer coefficient
- ΔT Temperature difference across heat exchanger
- A Heat transfer area
- r_i Tube inner radius
- r_o Tube outer radius
- h_i Tube inside heat transfer coefficient
- h_o Tube outside heat transfer coefficient.

2.2.3 PSA Column

PSA column for oxygen separation from air was designed assuming a constant flow pattern, one dimensional model [5–8] as given below:

$$(1 - \epsilon_b) \rho_P \frac{\partial q}{\partial t} = k_m \bar{a} (C - C^*) \quad (5)$$

$$k_m \bar{a} = \left[\frac{1}{k_c \bar{a}} + \frac{d_p^2}{60 D_e m (1 - \epsilon_p) \rho_P} \right]^{-1} \quad (6)$$

$$Sh = 2.0 + 1.1 Re^{0.6} Sc^{1/3} \quad (7)$$

$$D_e = \frac{\epsilon_p}{\tau} \left(\frac{1}{D} + \frac{1}{D_k} \right) \quad (8)$$

$$D_k = 9.7 \times 10^3 r_p \sqrt{\frac{T}{M}} \quad (9)$$

where,

- ϵ_b Bed porosity
- ρ_p Particle density of adsorbent
- q quantity of gas adsorbed/kg of adsorbent
- $k_m \bar{a}$ Effective mass Transfer Coefficient
- C Concentration of gas at the bulk
- C^* Concentration that can remain in equilibrium with adsorbent having adsorbate
- ϵ_p Pellet porosity
- k_c Mass transfer coefficient
- τ Tortuosity factor
- D_e Effective diffusivity
- D_k Knudsen diffusivity
- r_p Pore radius

Sequence of steps followed in the realization of PSA column is summarized in Fig. 1.

Adsorption of nitrogen over zeolite molecules is considered to follow Langmuir's isotherm as per Eq. (10).

$$q = q_m \frac{Kp}{1+Kp} \tag{10}$$

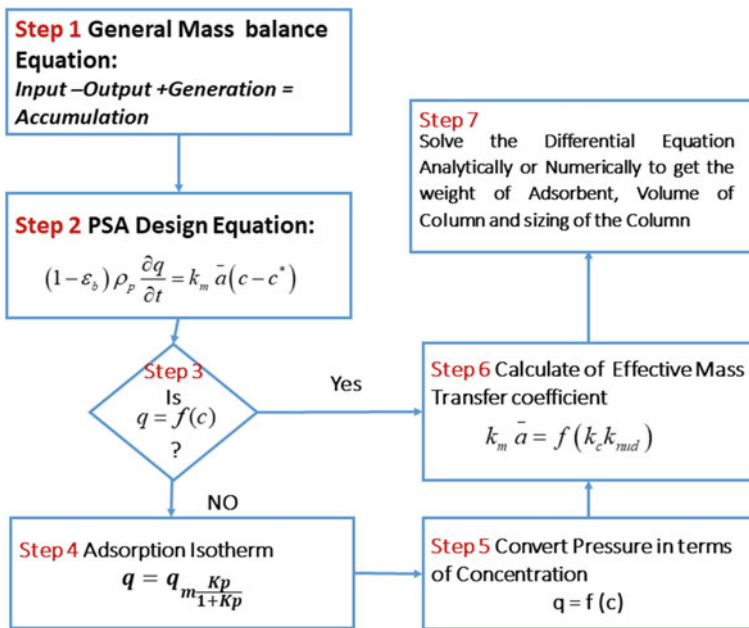
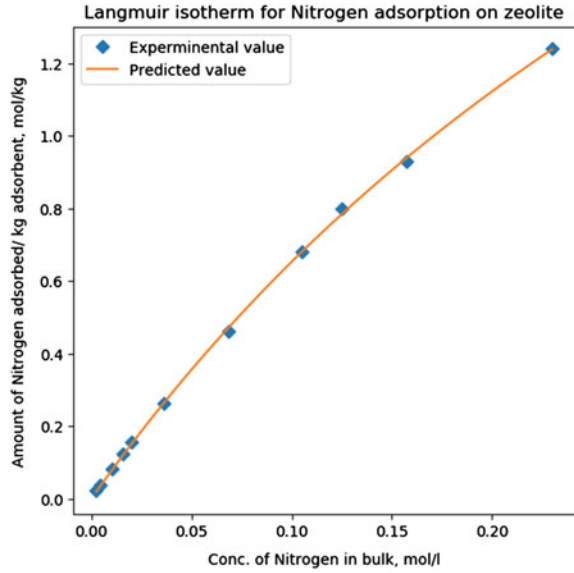


Fig. 1 PSA column realization sequence

Fig. 2 Experimental and predicted Langmuir isotherm for adsorption of nitrogen molecules on zeolite



where,

- qm maximum quantity of gas adsorbed per kg of adsorbent
- K adsorption equilibrium constant
- p partial pressure of adsorbate.

The experimental values of q versus C as reported in the literature is compared with the predicted values to generate a suitable isotherm equation and the result is shown in Fig. 2.

The pressure drop across PSA column was calculated using Ergun equation.

$$\frac{\Delta P}{L} = \left[\left(\frac{150 \times u \times \mu_g \times (1 - \varepsilon_b)}{(\phi_s \times d_p)^2 \times \varepsilon_b^3} \right) + \left(\frac{1.75 \times \rho_g \times u^2}{\phi_s \times d_p \times \varepsilon_b^3} \right) \right] \quad (11)$$

where,

- L length of the Bed
- ϕ_s Sphericity of the adsorbent
- ε_b Bed porosity
- μ_g Air viscosity
- ρ_g Air density
- u Velocity
- ΔP Pressure drop
- d_p Particle diameter

2.3 Realization of MOC

Oil free air compressor capacity, PSA column design including height of packing, diameter of bed, quantity of Zeolite, packing configuration etc. are designed from first principles. Photo of the MOC realized is shown in Fig. 3. A heat exchanger is also designed for effective removal of heat from compressed air. PSA column operates by swinging pressure between two columns through sequential operation of solenoid valves. The outlet from PSA column is connected to oxygen accumulator followed by bacterial filter, flow meter and humidifier. An LED display is mounted in the unit to display the values of discharge pressure, oxygen flowrate and oxygen concentration to the user. Considering the safety aspects, various alarms and interlocks are introduced into the unit which will alert the user for variation in flow, pressure and oxygen purity.

Table 2 gives the details on materials used for realization of sub-systems of MOC.

Fig. 3 Medical oxygen concentrator



Table 2 Material of construction for realized sub-systems of MOC

Sub-system	Material of construction
External cabinet	Polypropylene sheet
Structural framework	GI coated MS square tube
Base plate	Powder coated MS
Internal support	Polypropylene sheet
Heat exchanger	Aluminium coil
PSA column and oxygen tank	Aluminium alloy (Al 6063)

3 Results and Discussion

3.1 Effect of Air Flow Rate on Oxygen Concentration

Air has a composition of Nitrogen (79%) and Oxygen (20.8%). The inlet air flow rate to the PSA columns and its adsorption efficiency decides the required outlet flow rate of oxygen with maximum % purity. The selection of compression with discharge air flowrate is an important factor for rating the capacity of oxygen concentrator. From the theoretical studies, a suitable air compressor with a discharge flow rate of 135 lpm was selected and by varying the inlet flow rate from 110 to 130 lpm, the outlet concentration of oxygen @ 10 lpm constant output was studied. From the studies, it was observed that oxygen concentration >82% @ 10 lpm was obtained for an inlet air flowrate ranging from 115 to 125 LPM (Fig. 4).

Fig. 4 Air flow rate versus oxygen concentration

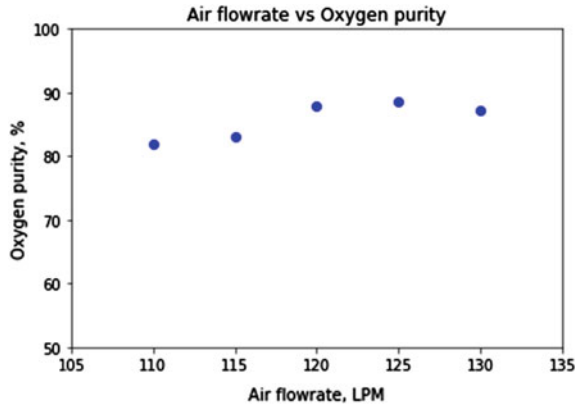
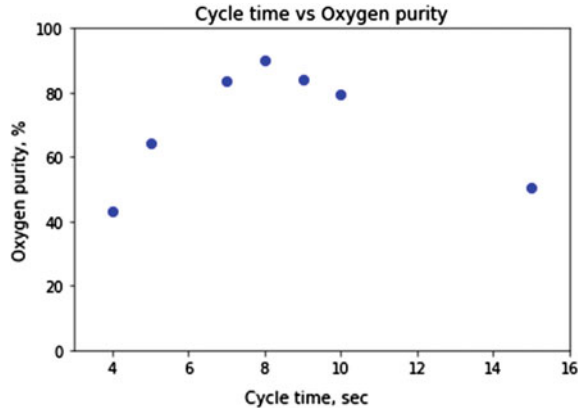


Fig. 5 Cycle time versus oxygen concentration



3.2 Effect of Cycle Time on Oxygen Concentration

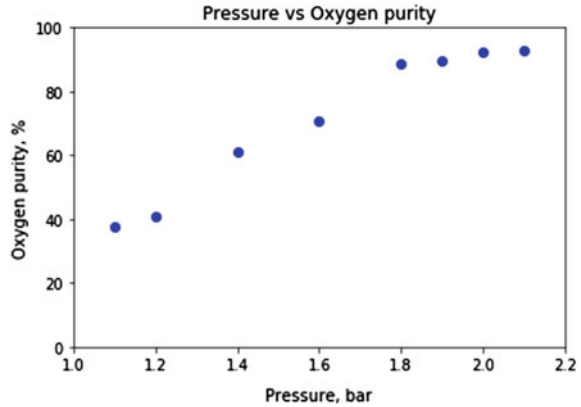
In the PSA columns adsorption (pressurisation) and desorption (depressurisation) phenomena occurs. During adsorption time, the oxygen molecules pass through and Nitrogen molecules adsorbs on the zeolites due to the quadrupole effect phenomena. Cycle time refers to the total time involved in the generation of oxygen from adsorption. The cycle time is an important factor for the generation of high purity oxygen at rated capacity, here refers to 10 lpm outlet flowrate. The cycle time studies with the manipulation of timings in the programmed software from 4 to 15 s was studied.

From Fig. 5, it is observed that oxygen concentration $>82\%$ was obtained for a cycle time in the range of 7–9 s.

3.3 Effect of Pressure on Oxygen Concentration

In general, the adsorption of gas molecules occurs at high pressure. The pressure inside the PSA columns plays a significant role in the adsorption of nitrogen molecules onto the zeolite bed. A compressor with a maximum discharge pressure of 3 bar was selected to operate the PSA column max 2.5 bar. The pressure inside the PSA columns increases with the increase in the cycle time. The optimum pressure to be operated inside the PSA column is to be studied for maximum concentration of oxygen at rated flow. It was noted that PSA column pressure of 1.8–2.2 bar is essential for effective adsorption of nitrogen over zeolites to achieve maximum oxygen purity at a flowrate of 10 LPM (Fig. 6).

Fig. 6 Column pressure versus oxygen concentration



4 Conclusion

Oxygen concentrators are highly reliable but units are costly in the open market. Under this pandemic COVID-19 scenario, VSSC (ISRO) has undertaken quick efforts to design and develop a portable Medical Oxygen Concentrator at an affordable cost. SHWAAS is capable of supplying enriched oxygen continuously @ 10 LPM adequate for two patients at a time. The working principle involves Pressure Swing Adsorption (PSA) which is commonly used for the production of oxygen from air. The major features of the developed unit are summarized in Table 3.

The unit has successfully undergone various functional and safety tests identified including alarm checks for start-up period; low oxygen concentration; low/high flow; power supply failure; high air temperature; flow measurement accuracy test, and temperature sensitivity test (15 °C and 40 °C), endurance test (40 °C and 95% RH

Table 3 Major features of MOC

Parameter	Value
Rated power	550–600 W
Operating voltage	220 V/50 Hz
Oxygen flow	0.5–10 LPM
Oxygen concentration	85% minimum
Outlet oxygen pressure	50–70 kPa
Alarm	Power failure, low and high pressure, low purity
Noise	≤60 dB
Net weight	43 kg
Dimensions	600 mm H × 500 mm L × 400 mm W
LCD display	Oxygen concentration, flow rate, pressure

for 48 h), fire propagation tests, power efficiency test, protective earth testing (all conductive parts are connected to earth), software testing, EMI & ESD Tests.

An indigenous technology for producing medical grade oxygen (82% min) was successfully demonstrated through an Engineering Model of Medical Oxygen Concentrator complying with ISO/WHO norms to support the nation during this prevailing COVID-19 pandemic situation. This technology can be used for the commercial production of medical oxygen concentrators as part of Aatmanirbhar Bharat.

Acknowledgements The authors would like to thank Director, Vikram Sarabhai Space Centre for encouraging and supporting this societal activity during the prevailing situation of COVID-19 pandemic.

References

1. Technical specifications for oxygen concentrators (2015) WHO Medical device technical series. World Health Organization, Switzerland
2. Ackley MW (2019) Medical oxygen concentrators: a review of progress in air separation technology. *Adsorption* 25(8):1437–1474
3. Rao VR, Farooq S et al (2010) Design of a two-step pulsed pressure-swing adsorption-based oxygen concentrator. *AIChE J* 56(2):354–370
4. Santos JC et al (2007) High-purity oxygen production by pressure swing adsorption. *Ind Eng Chem Res* 46(2):591–599
5. Green Don W, Robert H Perry (ed) (2008) Perry's chemical engineers' handbook, 7th edn. McGraw- Hill, United States of America
6. Sinnott R (2005) Coulson & Richardson's chemical engineering, 3rd edn, vol 6. Chemical engineering design. Butterworth-Heinemann, Burlington, MA
7. Cavenati S, Grande CA, Rodrigues AE (2004) Adsorption equilibrium of methane, carbon dioxide, and nitrogen on zeolite 13X at high pressures. *J Chem Eng Data* 49:1095–1101
8. Treybal RE (1980) Mass transfer operations, 3rd edn. McGraw- Hill Book Co., Singapore

Numerical Investigation on the Effect of the Shape of Cavities on the Melting Process of Latent Heat Thermal Storage Material Paraffin Wax



Debasree Ghosh, Chandan Guha, and Joyjeet Ghose

Abbreviations

PCM	Phase change material
LHTES	Latent heat thermal energy storage
TES	Thermal energy storage
VOF	Volume-of-fluid
H	Height of the rectangular cavity
W	Width of the rectangular cavity
V	Volume of the cavity
A	Area of the cavity
A_{mushy}	Mushy zone constant
C_p	Specific heat constant (J/kg.K)
C_{pl}	Specific heat constant of liquid PCM (J/kg.K)
g	Gravitational acceleration (m/s^2)
h	Enthalpy of fluid mixture in computational cell (J/kg)
L	Latent heat of solid–liquid phase change (J/kg)
mf	Melt fraction of PCM in heat exchanger
S_i	Momentum source
t	Time (Second)
T	Temperature (K)

D. Ghosh (✉)

Chemical Engineering, Birla Institute of Technology, Ranchi 835215, Jharkhand, India
e-mail: dghosh@bitmesra.ac.in

C. Guha

Chemical Engineering, Jadavpur University, Kolkata 700032, West Bengal, India

J. Ghose

Production and Industrial Engineering, Birla Institute of Technology, Ranchi 835215, Jharkhand, India

T_w	Cavity wall temperature (K)
T_s	Solidus temperature of PCM (K)
T_l	Liquidus temperature of PCM (K)
u_i	Velocity component in i th node (m/s)
α	The volume fraction of PCM in the computational domain
α_D	Thermal diffusivity (m^2/s)
α_{air}	Volume fraction of air in the computational cell
ρ	Density of fluid mixture in the computational cell (Kg/m^3)
k	Thermal conductivity of fluid mixture in the computational cell (W/m.K)
μ	Viscosity of fluid mixture in the computational cell (Kg. m/s)
γ	Liquid fraction of PCM
St	Stefan number
Nu	Nusselt number
Fo	Fourier number

1 Introduction

Conventional fossil fuels are decreasing rapidly due to uncontrolled use. The combustion of fossil fuels has adversely affected the global atmosphere. To overcome this situation, the use of eco-friendly and renewable energy sources is to be encouraged. Abundantly available free solar energy can be used to meet the energy gap. Nowadays, the available solar energy is effectively harvested and stored for a long period; phase change materials (PCMs) are the medium to store the solar energy in form of latent thermal energy. The domestic energy requirement can be partially fulfilled with this stored thermal energy. Control of room temperature and water heaters are the most common use of such latent heat energy storage. The higher phase change enthalpy, lower volume change during phase change, higher energy density, and non-toxic behavior are the advantageous features of the process. PCMs are also induced in the air-conditioning system, in-car radiators, industrial waste energy recovery systems, catering services, and electronic equipment for maintaining low temperatures [1–4]. The PCM heat storage material undergoes a phase transition process during charging or discharging in latent heat thermal energy storage systems (LHTES). The phase change process from solid to liquid or liquid to solid normally occurs at constant temperature or within a small range between solidus and liquidus temperature. The proper design of LHTES is required for the smooth running of the system. In the case of temperature control of building, the LHTES should be designed so that the charging daytime must be the charging time and nighttime is the discharging time. This is very important to maximize latent heat storage and minimize the sensible heat transfer for designing a highly efficient thermal energy storage unit. Especially, in cold countries, day is shorter than night; therefore, higher discharging time compared to charging time will make the process more effective. Ghosh et al. have shown that solidification or discharging time is much higher than

melting or charging time [5]. Numerical simulation of the solid-liquid phase change process is useful for the proper selection of PCM and cavity size for optimizing the phase change time. Assis et al. studied the charging and discharging of paraffin wax in a spherical cavity [6, 7]. They used enthalpy-porosity with volume-of-fluid for solid-liquid and PCM-air interface. The correlation among melt fraction and Stefan number, Fourier number, and Grashof number is calculated for both melting and solidification processes in a spherical cavity. A similar study is presented by Ghosh and Guha for the melting of PCM in the rectangular cavity [8]. Ghosh et al. also studied the effect of flow rate and temperature high-temperature-fluid on charging of PCM in PCM heat exchanger [9]. The study proposed the empirical equations to predict the melt fraction as a function of Fourier number, Stefan number, and Reynolds number. Tian et al. used four fins in a rectangular cavity to improve the melting process [10]. The fins used are made of different materials. They studied the effect of contact area and thermo-physical properties of fin material on the melting of PCM. Nimrodi et al. observed that for long vertical pipes the melting process is no more symmetric around the vertical axis [11]. The ratio of height to diameter is 50 in their study. The melting and solidification for different PCMs with different boundary conditions are available in literature [3, 12–15]. Bhatt and Kumar studied the effect of the size of PCM nanoparticles [16]. Therefore, the literature available considered spherical and cylindrical cavities for LHTES. Since the thermal conductivity of PCMs is very low, micro-encapsulation and extended surface or fins are used to improve the phase change process [6, 7, 17–22].

It is observed from the literature that researchers have studied different LHTES units with various thermal and physical conditions. The main challenge is to maximize thermal efficiency by minimizing sensible heat transfer. In the case of minimum sensible heat transfer, the phase change process is very slow. The use of PCMs in thermal energy storage systems has been presented over recent years. It is one of the most effective processes in energy storage. PCMs used in thermal energy storage (TES) systems have high phase change enthalpy with no additional subcooling or hysteresis and have proper cycling stability. The design of thermal energy storage systems requires knowledge of the thermo-physical properties of PCM and operating conditions. The experimental and simulation studies of those parameters are expensive and time-consuming tasks. The use of empirical equations can reduce this task. Therefore, a detailed numerical study on the phase change process will be helpful to design an effective LHTES more economically and safely. The effects of shape and area of the latent heat thermal storage units are significant to control the phase change process. Therefore, the objective of this study is as follows:

- (i) To study the effect of cavity shape and area on the melting time of PCM shown through numerical simulation.
- (ii) To propose empirical correlation for phase change studies under different operating constraints.

2 Material and Methods

2.1 Computational Domain

The numerical approach is very important to predict the melting phenomena inside a cavity. During the melting process, heat is supplied to the solid which is kept in a cavity. The temperature of PCM becomes constant or varies within a small range of temperature at the time of phase. Therefore, the progress of the process is not accurately measurable during experimentation. Numerical simulation is the process that analyzes the process at each time step. The heat required for melting is the same for the same mass of PCM, but the melting time is not the same for various cavity shapes and thermal boundary conditions. The phase change process considered in this study is symmetric about the vertical axis; therefore, the melting processes are studied using an axisymmetric model. This model helps to reduce the simulation time. Commercial software ANSYS-Fluent is used for numerical simulation of the melting process. The air and the molten PCM are assumed to be incompressible Newtonian fluids, and laminar flows are considered in both phases. A density-temperature relation is used for air: $\rho = 1.2 \times 10^{-5}T^2 - 0.01134T + 3.4978$ [6, 7, 22].

2.2 Mathematical Modeling

Solid-liquid phase change processes need special attention during simulation. This is because the physical properties change significantly. Viscosity is one such property. This viscosity term distinguishes the solid and fluid phases. In the solid phase, the heat transfer occurs by conduction only. The mechanism of conduction says that in this mode of heat transfer, molecules vibrate only about their equilibrium position, and no permanent displacement of molecules is observed. On the other hand, in the convection-driven heat transfer process in the fluid phase, the molecules of fluid start moving after overcoming the intermolecular force of attraction. These characteristics need some source terms in basic conservation equations. This source term differentiates solid and liquid phases. The model used in this simulation of the melting process is called the enthalpy-porosity model. The overview of the model is discussed as follows:

- The model is used for laminar, incompressible fluid, or PCM.
- An axisymmetric and unsteady flow is assumed within the cavity. It is also assumed that both solid and liquid phases are homogeneous and isotropic.
- The enthalpy-porosity model applies to both the melting and solidification of pure metal or binary alloys.
- The phase change should occur at a constant temperature or within a range of temperature.

- The solid-liquid interface is not tracked explicitly. In this model, the solid-liquid interface is treated as the porous mushy zone where the porosity of the pure liquid phase is one and that of the solid phase is zero.
- A suitable source term is introduced to the momentum equation to calculate the effect of pressure drop due to the presence of solid material.
- In this work, the multiphase volume-of-fluid (VOF) model is used to locate the non-penetrating PCM and air phase.

The governing equations are explained as follows.

2.2.1 Governing Equations

Continuity equation:

$$\frac{\partial \alpha}{\partial t} + u_i \frac{\partial \alpha}{\partial x_i} = 0 \quad (1)$$

α represents the volume fraction of PCM in the computational domain. If $\alpha = 0$, the cell does not contain any PCM and $\alpha = 1$ implies the cell is filled only with PCM. The cell is filled with a mixture of PCM and other fluids if α value varies from zero to one. More specifically, the value of α is one at the solid/liquid PCM interface, and at the PCM-air interface, the value of α varies between zero and one. The volume fraction Eq. (1) is applicable for PCM (secondary phase) not for the air (primary phase); the volume fraction of air will be computed based on the following constraint:

$$\alpha_{air} = 1 - \alpha \quad (2)$$

Momentum equation:

$$\frac{\partial}{\partial t}(\rho u_i) + \frac{\partial}{\partial x_i}(\rho u_j u_i) = \mu \frac{\partial^2 u_i}{\partial x_j \partial x_j} - \frac{\partial p}{\partial x_j} + (\rho - \rho_{ref})g + S_i \quad (3)$$

ρ_{ref} is the density of cell at the reference temperature T_{ref} .

Energy balance equation:

$$\frac{\partial}{\partial t}(\rho h) + \frac{\partial}{\partial x_i}(\rho u_i h) = \frac{\partial}{\partial x_i} \left(k \frac{\partial T}{\partial x_i} \right) \quad (4)$$

where k and μ represent the thermal conductivity and dynamic viscosity, ρ denotes the density, S_i is the momentum source term, u_i signifies the velocity component, x_i is a cartesian coordinate, and the specific enthalpy of both the air and PCM is denoted by h in the specified region. Equations (3) and (4) are valid for air, PCM, and their

interface. The Thermo-physical properties like density, thermal conductivity, and viscosity are calculated as follows:

$$\left. \begin{aligned} \rho &= \alpha \rho_{PCM} + (1 - \alpha) \rho_{air} \\ k &= \alpha k_{PCM} + (1 - \alpha) k_{air} \\ \mu &= \alpha \mu_{PCM} + (1 - \alpha) \mu_{air} \end{aligned} \right\} \quad (5)$$

where

$$\left. \begin{aligned} \rho_{PCM} &= \gamma \rho_{PCM,liq} + (1 - \gamma) \rho_{PCM,solid} \\ k_{PCM} &= \gamma k_{PCM,liq} + (1 - \gamma) k_{PCM,solid} \\ \mu_{PCM} &= \mu_{PCM,liq} \end{aligned} \right\} \quad (6)$$

Also, the expression for the change in enthalpy is defined as $h = h_{ref} + \int_{T_{ref}}^T C_p dT + h_{ref}$. h_{ref} is enthalpy at reference temperature T_{ref} . The specific enthalpy of melting (latent heat of the material) is denoted by L , and γ represents the liquid fraction during the phase change which occurs over a range of temperatures and defined by the following relations:

γ is defined as follows:

$$\left. \begin{aligned} \gamma &= 0 \text{ at } T < T_s \\ \gamma &= \frac{T - T_s}{T_l - T_s}, \text{ at } T_s < T < T_l \\ \text{and } \gamma &= 1 \text{ at } T > T_l \end{aligned} \right\} \quad (7)$$

The porosity term in the momentum source term is compared to flow through porous media defined with the help of the Carman-Kozeny equation. The mathematical form of the source term is defined as follows [6, 7]:

$$S_i = -A_{mushy} \frac{(1 - \gamma)^2}{\gamma^3 + \varepsilon} u_i \quad (8)$$

A_{mushy} in Eq. (8) is called the mushy zone constant. This mushy zone constant refers to the damping nature of the phase change process. Therefore, the enthalpy of the control volume is calculated using the energy balance equation given in Eq. (4), and the melt fraction or liquid fraction is calculated using Eq. (7). The calculated liquid fraction is updated in momentum Eq. (3), or more specifically, the liquid fraction value is updated in the source term defined in Eq. (8). The negative sign refers to that it is a sink term. As already mentioned, the solid phase is static, and it needs velocity suppression in the solid phase and this sink term is satisfying that criteria.

2.2.2 Numerical Scheme

The enthalpy-porosity model described above is solved in ANSYS-Fluent commercial software. The commercial software package has three main parts: preprocessor, solver, and post-processing. In the preprocessor, the geometry or computation domain is defined. The computational domain for the current study is shown in Fig. 1. The appropriate grid generation is done to obtain accurate results from the simulation. Grid-independency is shown in the previous research article by Ghosh et al. [8, 22]. The properties of PCM are given in Table 1. In this study, the finite volume method is applied for discretization. The control volume is considered as a staggered grid to store the properties of variables. The scalar properties are stored at the ordinary node and velocities are stored at the face-centered node [23]. The details of the numerical scheme used for discretization are given in Table 2.

2.2.3 Initial and Boundary Conditions

The initial temperature of PCM is assumed to be 1 K less than the solidus temperature of PCM. This condition minimizes the sensible heat transfer and maximizes latent heat transfer. The wall of the cavity is kept at a constant temperature and the temperature higher than the liquidus temperature. In this study, the temperature of the cavity wall varies from 310 to 320 K. The cavity is made of glass.

3 Results and Discussion

A detailed study on the melting of PCM (RT27) in a spherical cavity and rectangular cavity is presented by Ghosh and Guha [8, 22]. A similar study is presented for a 60 mm diameter spherical cavity. It is also mentionable that a glass cavity is taken for this numerical simulation. Experimentation on melting of PCM in 80 mm diameter spherical cavity is carried out to validate the numerical model considered for study [22]. The cavity is 85% filled with paraffin wax (RT27) and a water bath is used to maintain a constant wall temperature of 320 K. The initial temperature of the PCM is 300 K. The digital image analysis technique is used to calculate the melt fraction from the captured digital images. Experimental images obtained are compared with simulated density contours available using the enthalpy-porosity model with the VOF model. The deviation between experimental and simulated results is mainly due to improper identification of the mushy zone from the image captured. In the mushy region if the liquid fraction or melt fraction is lower, the zone looks like a solid phase.

The data presented in Fig. 2 shows that the time required for complete melting is lowest for the highest cavity wall temperature (320 K and $St = 0.18$) and it is around 34 min. The time required for the same is highest for the lowest cavity wall temperature which is approximately 72 min. For an increase in temperature from 310 to 315 K, the melting time is reduced by 35%, and for an increase in temperature

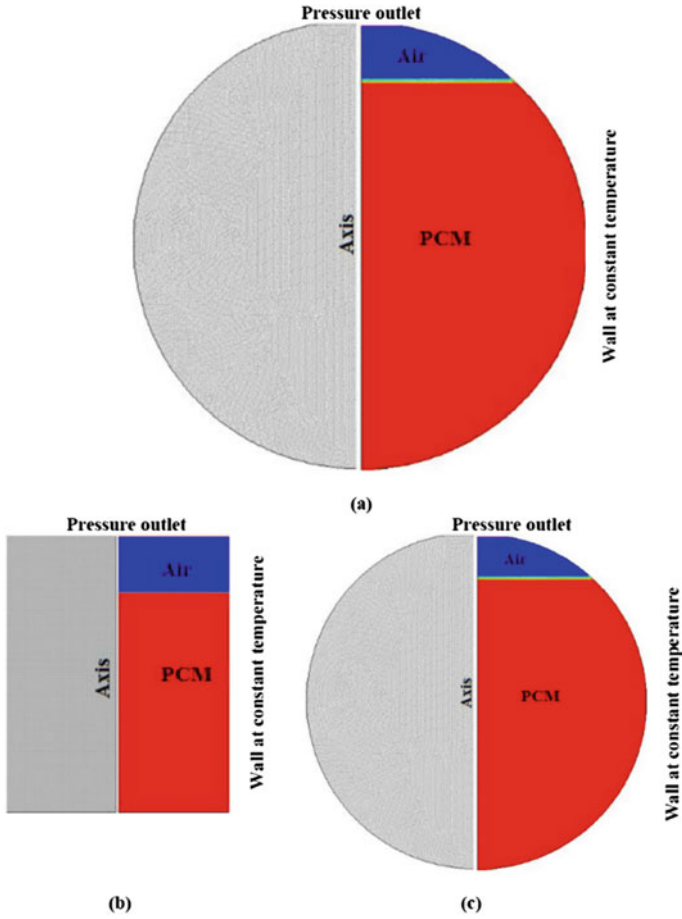


Fig. 1 Computational domain. **a** Spherical cavity (80 mm diameter), **b** rectangular cavity (50 mm \times 40 mm), **c** spherical cavity (60 mm diameter)

Table 1 Thermo-physical properties of paraffin wax (RT27)

Density	870 kg/m ³ (solid phase) 760 kg/m ³ (liquid phase)
Specific heat	1800 J/kg.K
Thermal conductivity	0.15 W/m.K
Viscosity	3.42×10^{-3} kg/m.s
Solidus temperature	301 K
Liquidus temperature	303 K
Latent heat of fusion	179 kJ/kg

Table 2 Discretization scheme

Equations	Discretization scheme
Pressure-velocity coupling equations	SIMPLE
Pressure equations	PRESTO
Momentum equations	First-order upwind
Volume fraction equations	Geo-construct
Energy equations	First-order upwind

from 310 to 315 K, the melting time is reduced by 25%. Therefore, a very high cavity wall temperature may not minimize the melting time very much. The high-temperature difference in control volume causes sensible heat transfers and makes the phase change process slower. An important parameter in heat transfer study is heat flux. Figure 3 shows the variation of volume-average heat flux during melting in a 60 mm diameter spherical cavity. The variation of heat flux shows similar variation for high cavity temperature as discussed in melting in 80 mm diameter cavity [22]. The nonlinear nature of heat flux variation decreases as the cavity wall temperature decreases and it is almost linear for cavity wall temperature 310 K. The reason is, in this case, the conductivity and thermal diffusivity of the cavity are very low, and for lower cavity wall temperature, the temperature gradient is also very low. These lower values of a driving force and higher thermal resistance make the heat transfer or phase change process slower.

In this paper, a comparative study of melting is also presented to discuss the effect of cavity shape on phase change. The results obtained are presented in Table 3. In the first case, the melting in an axisymmetric rectangular cavity and spherical cavity is

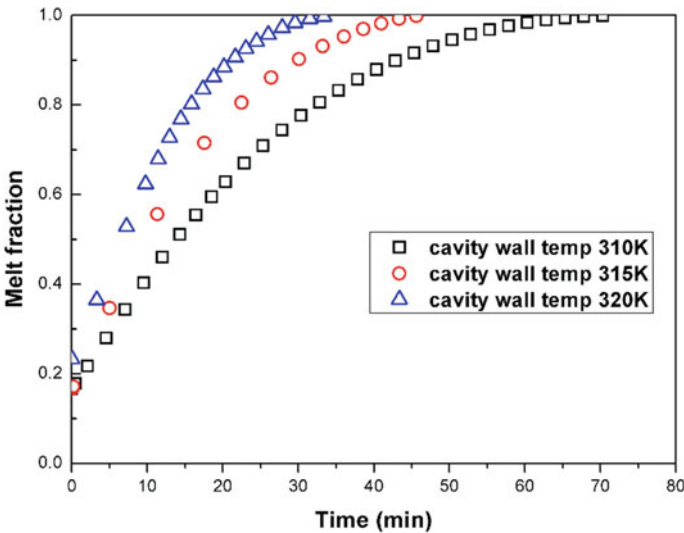


Fig. 2 Melt fraction (air+liquid PCM) for different wall temperatures in glass cavity

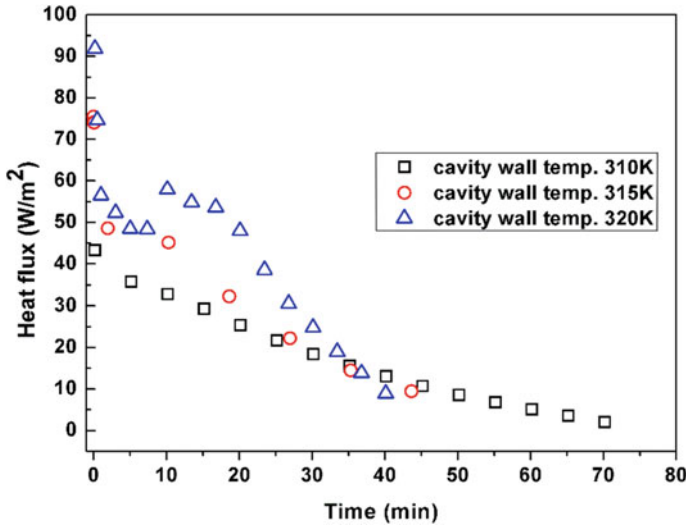


Fig. 3 Variation of heat flux for different wall temperatures in glass cavity

compared. The aspect ratio along the direction of fluid flow for a rectangular cavity is 1.25 (H/W) higher than the spherical cavity. From the preliminary knowledge of convection heat transfer, it has been seen that with the increase in the above-mentioned aspect ratio, the Nusselt number or convection heat transfer effect is increasing. It is also observed that for the same volume of the cavity, the convection heat transfer is higher in the spherical cavity. Therefore, to check the rapidness of the melting phase change process for the same boundary and operating condition, a higher aspect ratio for a rectangular cavity is considered compared to a spherical cavity. The size of the rectangular cavity is 50 mm \times 40 mm ($H \times W$) and the diameters of spherical cavities are 80 mm and 60 mm. All the cavities are made of glass ($k = 0.81$ W/m. K). The heights of PCM are 80% of the total height in the rectangular cavity and 85% of the diameter in the spherical cavity. The volume and area considered are presented in Table 3.

The volume and area are higher in the case of a spherical cavity. The thermal boundary considered is the same in both cavities. Figures 4 and 5 present the variation of melt fraction (Liq. PCM+air) for constant cavity wall temperatures of 315 K and 320 K. The initial temperature of PCM is 300 K or 1 K less than the mean melting temperature. One interesting observation is that though the size of the cavity and the amount of PCM taken are different, the time of complete melting is very close though the PCM contents are different in three cavities. The initial solid fractions of PCM in the rectangular cavity are 0.8 and that of the spherical cavity is 0.85. After 24 min, the melt fraction is the same in both the cavity. The mechanism of phase change is close contact melting. Figure 6 shows the contour of melting fractions with time for spherical cavities (80 mm and 60 mm diameter) and rectangular cavity for 320 K cavity wall temperature. In a rectangular cavity, the shape of un-melt shows

Table 3 Effect of shape on melting

<i>Shape of cavity</i>				
Rectangular		Spherical		Spherical
<i>Size of cavity</i>				
50 mm × 40 mm (H × W)		60 mm diameter		80 mm diameter
<i>Aspect ratio (H/W)</i>				
1.25		1		1
<i>Area of cavity (A) (m²)</i>				
0.0088		0.011304		0.02
<i>Height of PCM in the cavity</i>				
80% of cavity height/40 mm		85% of cavity height/51 mm		85% of cavity height/70 mm
<i>Volume (V) (m³)</i>				
0.0000628		0.000113		0.000268
<i>Initial volume fraction of PCM in cavity</i>				
0.8		0.85		0.85
<i>Cavity wall temperature (K)</i>				
320	315	320	315	320
<i>Complete melting time (t) (min)</i>				
44	52	34	46	47
<i>Maximum heat flux (W/m². K)</i>				
22.337	16.94	91.9	72.2	47.1
<i>Empirical equation for an un-melt solid fraction (320 K)</i>				
$Sf = 0.8(1 - 0.4St^{3.6}Fo^{0.58})$		$Sf = 0.85(1 - 0.45St^{3.6}Fo^{0.58})$		$Sf = 0.85(1 - 0.5St^{3.6}Fo^{0.58})$

the contact area between solid PCM and cavity wall decreasing continuously. On the other hand, the contact area between un-melt solid and wall is decreasing very slowly in spherical cavities. This very slow change in the contact area is continued till the cavity is half-filled by un-melt or solid PCM. In both the cavities, the solid phase is sinking to the bottom of the cavity and takes shape of the bottom surface of the cavity. The change of height of solid PCM is lower compared to the bottom surface area of the cavity in a spherical cavity than the rectangular cavity. Therefore, a higher contact area between the hot wall and solid PCM makes the melting process much faster in a spherical cavity. Initially, the melt fraction in the rectangular cavity is higher than in the spherical cavity because the rectangular cavity contains less solid PCM and more air than the spherical cavity. But the change in melt fraction is much higher in the spherical cavity and after some time the melt fraction curve of the spherical cavity crosses the curve for the rectangular cavity. In the case of 315 K wall temperature after 21 min, the melt fraction is higher in a spherical cavity, and for 320 K temperature, the time is 18 min. The time required for completing melting

decreases by 10 min for a 5 K increase in cavity wall temperature, but this time may not be constant for every 5 K increase in temperature. The reason is that the difference between melting curves shows an increasing trend with increasing cavity wall temperature. The maximum volume-average heat flux at a wall for the same wall temperature is much lower in a rectangular cavity than in a spherical cavity.

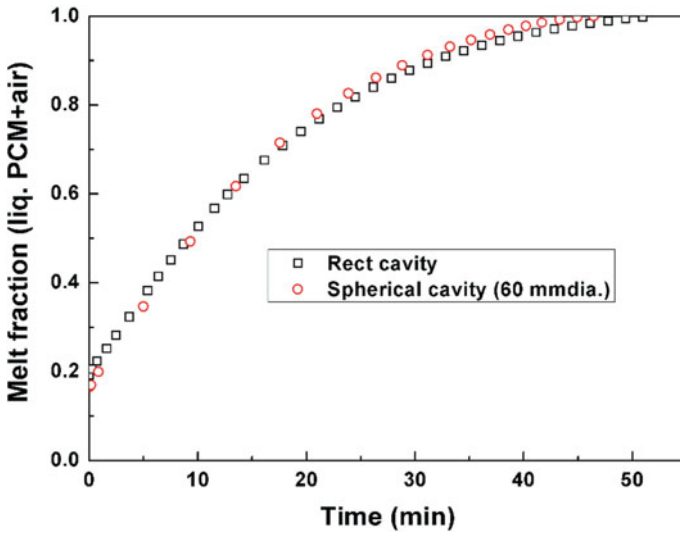


Fig. 4 Melt fraction in different shape cavities (wall temperature 315 K)

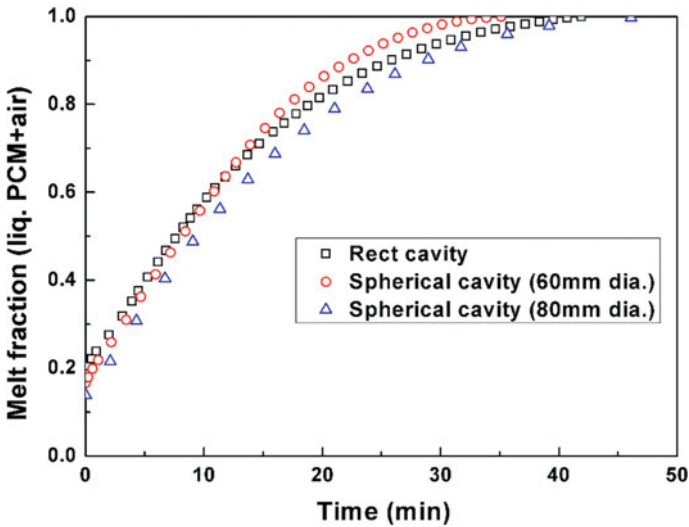


Fig. 5 Melt fraction in different shape cavities (wall temperature 320 K)

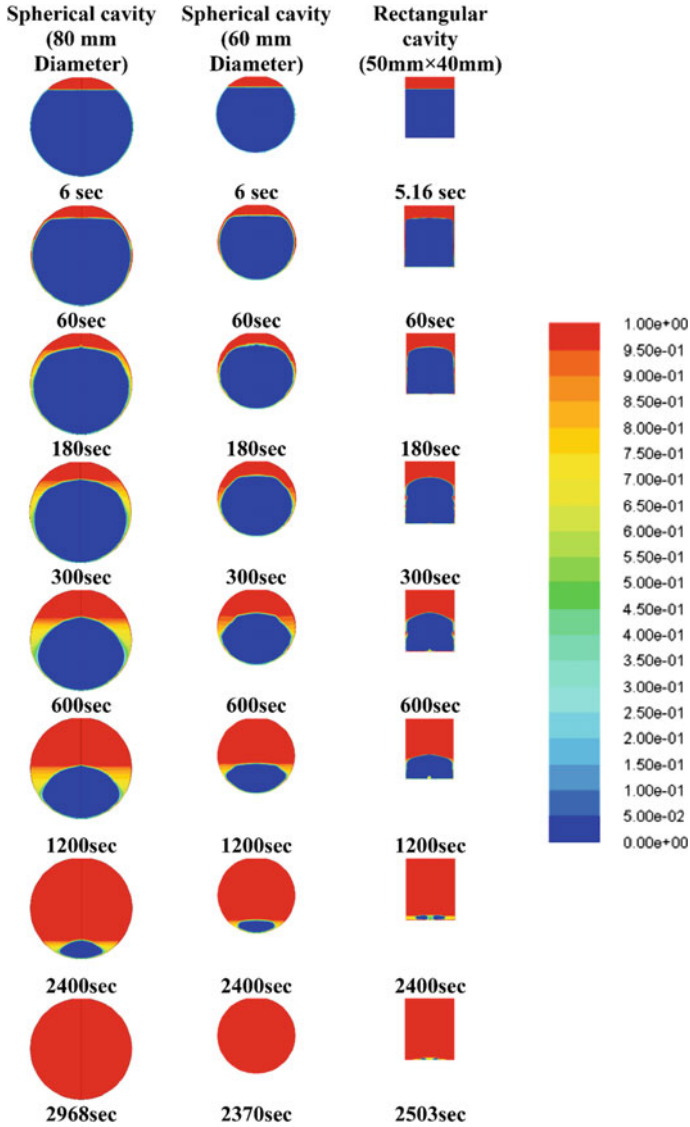


Fig. 6 Contour of melt fraction in different shape cavities (wall temperature 320 K)

The empirical relations were obtained to study the effect of cavity wall temperature or Stefan number and to compare the effect of cavity shape on melting. The expressions of Stefan number and Fourier number are as follows:

$$St = \frac{C_{pl}(T_w - T_m)}{L} \quad \left| \quad \right. \quad (9)$$

$$Fo = \frac{\alpha_D t}{s^2}$$

The empirical correlations relate solid fraction as a function of Stefan number and Fourier number. The empirical relation or the coefficients are modified for Stefan number 0.18 for wall temperature 320 K and shown in Table 3.

The correlations reveal that the solid fraction present in the cavity is varied with a fraction of PCM filled in the cavity, Stefan number, and Fourier number. Another important observation is that though the thermal and initial conditions are the same in the considered three cavities, the effect of surface area and shape of the cavity is different. The coefficient which measures the effect of area and shape is 0.4 for rectangular cavities and 0.45 and 0.5 for 60 mm and 80 mm diameter spherical cavities. The other parametric study shows that melting time (t) is directly proportional to the volume of PCM content (V) and inversely proportional to Stefan number (St) and area of the cavity (A). The relation may be written as follows:

$$t \propto \frac{V}{St^a \cdot A^b} \quad (10)$$

The volume (V) and area (A) of different shape cavities are given in Table 3. The time of melting is also given in Table 3 for different thermal boundary conditions or for different Stefan numbers. The constants a and b can be evaluated by substituting the values of t , V , A , and St in Eq. (10). The value of constants a and b is found same for 60 mm and 80 mm cavities. Their values are $a = 1.05$ and $b = 0.82$. Similarly, for the rectangular cavity, by substituting the value of t for different St and the same V and A , the constants a and b are calculated. The calculated values for the rectangular cavity are $a = 0.5$ and $b = 0.58$. Therefore,

For spherical cavity

$$t \propto \frac{V}{St^{1.05} \cdot A^{0.82}} \quad (11)$$

For rectangular cavity

$$t \propto \frac{V}{St^{0.5} \cdot A^{0.58}} \quad (12)$$

The above equations conclude that the increase in Stefan number or cavity wall temperature is more effective to minimize the melting time in a spherical cavity. Similarly, the increased area decreases the melting time much more in the spherical cavity than in the rectangular cavity.

4 Conclusion

The simulations of melting in a spherical cavity with different cavity materials control the melting time and shape of un-melt solid PCM in the cavity [22]. It has been observed that the melting time is the lowest for the highest thermal diffusivity cavity material. The melting is also lowest for the highest Stefan number. This study shows melting time is dependent on Stefan number and PCM content but also depends on the area and shape of the cavity. In the case of phase change like melting, the melting time is a nonlinear function of an area and Stefan number. The correlations among solid fraction, Stefan number, and Fourier number show that the shape and size of the cavity play an important role to predict the progress of the phase change process. On the other hand, the empirical relation for melting time shows that the melting time is inversely proportional to the area of the cavity. But the dependency is not limited to the numerical value of area; it depends on the shape of the cavity. In the case of 80 mm and 60 mm diameters, the degree of the area is the same but the degree of the area is different for the rectangular cavity. Therefore, apart from the thermal condition, melting time depends on the shape, size, or volume of the cavity and the amount of PCM in the cavity. The major conclusion from this study is that a single empirical equation is not sufficient to calculate melt fraction and melting time. These types of empirical relations will be very helpful to select an appropriate size and shape cavity with desired latent heat thermal storage capacity under available thermal boundary conditions. The proposed empirical equations can be verified with different PCMs to select the appropriate PCM for a particular application. Therefore, the selection of PCM, size, and shape of energy storage devices will be easier for designing LHTES equipment.

References

1. Mahfuz MH, Anisur MR, Kibria MA, Saidur R, Metselaar IHSC (2014) Performance investigation of thermal energy storage system with phase change material (PCM) for solar water heating application. *Int Commun Heat Mass Transf* 57:132–139
2. Xu B, Li P, Chan C (2015) Application of phase change materials for thermal energy storage in concentrated solar thermal power plants: A review to recent developments. *Appl Energy* 160:286–307
3. Kant K, Shukla A, Sharma A (2016) Performance evaluation of fatty acids as phase change material for thermal energy storage. *J. Energy Storage* 6:153–162
4. Ghosh D, Ghose J, Kumari P, Paul S, Datta P (2022) Strategies for phase change material application in latent heat thermal energy storage enhancement: Status and prospect. *J Energy Storage*
5. Ghosh D, Guha C, Ghose J (2019) Numerical investigation of paraffin wax solidification in spherical and rectangular cavity. *Heat Mass Transf Stoffuebertragung* 55:3547–3559
6. Assis E, Ziskind G, Letan R (2009) Numerical and experimental study of solidification in a spherical shell. *J Heat Transfer* 131:1–5
7. Assis E, Katsman L, Ziskind G, Letan R (2007) Numerical and experimental study of melting in a spherical shell. *Int J Heat Mass Transf* 50:1790–1804

8. Ghosh D, Guha C (2020) Numerical simulation of paraffin wax melting in a rectangular cavity using CFD. *Indian Chem Eng* 62:314–328
9. Ghosh D, Kumar P, Sharma S, Guha C, Ghose J (2021) Numerical investigation on latent heat thermal energy storage in a phase change material using a heat exchanger. *Heat Transf* 50:4289–4308
10. Tian LL, Liu X, Chen S, Shen ZG (2020) Effect of fin material on PCM melting in a rectangular enclosure. *Appl Therm Eng* 167
11. Nimrodi Y, Kozak Y, Portnikov D, Ziskind G (2020) Melting in a vertical pipe due to asymmetric heating. *Renew Energy* 152:179–188
12. Younsi Z, Naji H (2017) A numerical investigation of melting phase change process via the enthalpy-porosity approach: application to hydrated salts. *Int Commun Heat Mass Transf* 86:12–24
13. Fadl M, Eames PC (2019) Numerical investigation of the influence of mushy zone parameter Amush on heat transfer characteristics in vertically and horizontally oriented thermal energy storage systems. *Appl Therm Eng* 151:90–99
14. Kumar M, Krishna DJ (2017) Influence of Mushy zone constant on thermohydraulics of a PCM. *Energy Procedia* 109:314–321
15. Gao Z, Yao Y, Wu H (2019) A visualization study on the unconstrained melting of paraffin in spherical container. *Appl Therm Eng* 155:428–436
16. Bhatt S, Kumar M (2017) Effect of size and shape on melting and superheating of free standing and embedded nanoparticles. *J Phys Chem Solids* 106:112–117
17. Rozenfeld A, Kozak Y, Rozenfeld T, Ziskind G (2017) Experimental demonstration, modeling and analysis of a novel latent-heat thermal energy storage unit with a helical fin. *Int J Heat Mass Transf* 110:692–709
18. Kozak Y, Rozenfeld T, Ziskind G (2014) Close-contact melting in vertical annular enclosures with a non-isothermal base: theoretical modeling and application to thermal storage. *Int J Heat Mass Transf* 72:114–127
19. Ismail KAR, Lino FAM (2011) Fins and turbulence promoters for heat transfer enhancement in latent heat storage systems. *Exp Therm Fluid Sci* 35:1010–1018
20. Ogoh W, Groulx D (2012) Effects of the number and distribution of fins on the storage characteristics of a cylindrical latent heat energy storage system: a numerical study. *Heat Mass Transf Stoffuebertragung* 48:1825–1833
21. Murray RE, Groulx D (2014) Experimental study of the phase change and energy characteristics inside a cylindrical latent heat energy storage system: part I consecutive charging and discharging. *Renew Energy* 62:571–581
22. Ghosh D, Guha C (2019) Numerical and experimental investigation of paraffin wax melting in spherical cavity. *Heat Mass Transf Stoffuebertragung* 55:1427–1437
23. Versteeg HK, Malalasekera W (2007) An introduction to computational fluid dynamics the finite volume method LK. <https://www.tue.on.worldcat.org/oclc/901519689> (New york: Longman Scientific & Technical, 2007)

The Study of Wind Speed and Various Leak Size Repercussion on Toxic Chlorine Leakage from Tonner Using 3D Computational Fluid Dynamics (CFD) Analysis Technique



Govind K. Patil, Jitendra B. Naik, Nikita K. Patil, Prakash Dandawate, and Sagar R. Pardeshi

1 Introduction

Chemical Industrial disasters and emergencies involving highly toxic, flammable & explosive chemicals are not uncommon worldwide. One of the world's worst chemical industrial disasters has struck India "The Bhopal gas tragedy". On 3rd December 1984, approximately 41 tons of deadly Methyl isocyanide was released in the Bhopal city from the Union Carbide India Limited (UCIL), which caused the death of more than 2500 people and long-term injuries for over 300,000 [1]. Recently, the toxic gas Styrene released from the LG Polymer on 7th May 2020 (12 deaths, over 1000 injuries) reminded UCIL disaster of Bhopal that occurred 37 years back. Industrial accidents, despite happening in India on an unchanging basis, remain forsaken within the civil society at large.

The authors of the current article have collected the reported industrial accident, published in Indian newspapers for the years 2020 and 2021, specifically aiming at chemical, petrochemical, pharmaceutical, steel, and power plants. The data was then collated and analyzed. A shocking figure of 70+ accidents (170 fatalities and 1332 injuries) for 2020 and 120+ (169 fatalities and 299 injuries) accidents were noted for 2021 (January–October). Because these figures are based on recorded instances, the true figure could be much more. From the collected industrial accident data, it is

G. K. Patil (✉) · J. B. Naik · N. K. Patil · S. R. Pardeshi
University Institute of Chemical Technology, KBC-North Maharashtra University,
Jalgaon 425001, India
e-mail: govind656@gmail.com

P. Dandawate
Gexcon India Pvt. Ltd, Pune 411045, India

S. R. Pardeshi
Department of Pharmaceutics, St. John Institute of Pharmacy and Research, Palghar 401404, India

found that more than 25 accidents of toxic gas leakage happened between 2020 and 2021 but luckily there was no accident related to chlorine. The incidence of chlorine leakage and dissemination caused by physical, external disturbance, environmental circumstances, and other variables related to accidents is low, but the release repercussions are frequently severe, especially when rapid leakage is detected; it may be preceded by the influence of an external source on storage utility. As a result, hazardous chlorine dispersion is a popular research topic in gas storage safety.

Chlorine (Cl_2) is widely used, almost in all the chemical industrial processes as well as in society for various water purification processes [2]. Chlorine is greenish-yellow in color, has a density heavier than air, and is listed as a highly toxic chemical with National Fire Protection Association (NFPA) diamond ranking 4 (Highly Dangerous to health) in the (NFPA)-704 standards. According to the National Institute for Occupational Safety and Health (NIOSH), the TLV for 0.5 ppm or 1.5 mg/m^3 of air is 0.5 ppm, for the IDLH is 10 ppm, and the lethal concentration is 1000 ppm [3, 4].

In the recent years, several toxic chlorine leakage accidents are reported in India as well as in other countries in which several people got affected with a serious respiratory injuries. In China's Chongqing city on 16th April 2004 accidental chlorine release occurred in which 9 people were killed and more than 150,00 were evacuated[5]. In India on 31st May 2008 chlorine gas leak occurred at Jamshedpur in which around 150+ persons were hospitalized. On the 14th of July 2010, over 120 people have been exposed to the deadly chlorine gas inside the Mumbai Port's freight distribution center [6]. So, learning from previous accidents is always helpful to avoid future accidents.

For more than a century, Computational Fluid Dynamics (CFD) approaches for Hazardous Inventories' safety studies have been widely used in the chemical and manufacturing sectors, as well as in the oil and gas industry, for outcome analysis and risk evaluations. It is possible to quantify and avert future losses of assets, humans, and the environment using CFD anticipated outcomes and risk levels of prospective disaster situations [7]. Physical trials on dangerous (combustible) chemical fluid dispersion are not a cost-effective or reliable method of investigation, whereas mathematical modeling based on CFD is an alternate solution for predicting the ambiguous behavior of gas in any location following an accidental inventory release. CFD simulation can provide extensive consequences assessment of disaster scenarios, as well as the capacity to analyze numerous variables that directly and indirectly affect sensitive receptors. As a result, a CFD impact assessment simulation and assessment for gas dispersion release is required, which is beneficial for safety applications such as risk mitigation and emergency response planning [8].

Only a few safety-related researchers have looked into the effects of various parameters on heavy gas dispersion. Hui et al., (2017) used a CFD code to predict chlorine dispersion in open ground and explored the impact of motion on chlorine diffusion and leakage [7]. Liu et al. (2018) used a simulation study based on CFD to analyze the influence of complex construction impediments on natural gas leakage flow paths [9]. Wang et al. (2020) used a dynamic approach with a CFD code to analyze the danger of harmful gas dispersion in chemical facilities, looking at the

effects of environmental stabilities, origin locations, breeze directions, and escape modes [3]. Xin et al. (2020) analyzed the impacts of liquid chlorine dispersion and the risk of contamination following a release. They used CFD calculations to measure the impacts of multiple leak sizes in their research, and depending on the CFD results, they conducted a risk evaluation study [10]. Moreover, the impact of obstructions, leak site, and discharge location on chlorine leakage was investigated using a 3D CFD modeling method by Wang et al. [11].

The presented literature review clearly shows that recently different scientists' research examined the effect of wind speed and impediments on heavy gas leakage that has deteriorated over time, and very few researchers worked on the influence of various leak and wind stability classes on chlorine which is occasional. Therefore, in this paper computational fluid dynamic (CFD) simulations were performed to assess the effect of wind speed, wind speed stability class, and 2 types of leakage size (Small and Full-bore ruptured) on a chlorine leak scenario from 900 kg chlorine tonner was assumed based on an accidental leak in the open storage place, open storage with obstacles, and close storage shade in the chemical process industry. The present study results can be helping a theoretical and simulation basis for the industries for the development of chlorine storage in open or in close spaces.

2 Computational Methodology and Strategy

The research article of Efthimiou et al. 2017 and Sharma et al. 2020 has mentioned that consequence analysis modeling techniques fall into 3 categories, namely: (a) Gaussian model, (b) Integral model, and (c) Computational fluid dynamics (CFD) [12, 13] However, for the study of chlorine dispersion, the Gaussian model is the most fundamental since it takes into account that the terrain is flat and the climatic circumstances (wind direction and speed) are consistent; thus, the Gaussian model has the least adaptability [10]. Integral models are also called the lumped-element models (LEM) [14], usually one-dimensional equations which account for the calculation of the conservation of mass, momentum, and energy [15]. The LEM calculation does not require huge computational efforts and time [16]. Also, LEM is relatively easy to operate and suitable for the open space without obstacles to dispersion calculation but in terms of obstacles in the fluid path, it is not reliable. However, CFD always represents advantageous and advanced solutions in terms of numerical calculations for hazardous fluid atmospheric dispersion, terrain, unknown environment quantity turbulence, with and without obstacles, and proper atmospheric condition effect. Since Gaussian and Integral models are totally (1D) one-dimensional, CFD models provide a completely (3D) three-dimensional modeling of the included geometry, allowing for the calculation of the impact of the environment's objects on gaseous plume dispersion. In an open space environment with no barriers, both integral and CFD models are predicted to produce equivalent results [14]. The ALOHA, FDS, DNV Phast, DNV Safeti, and other codes are rooted in Gaussian and Integral models; moreover, such repercussion analysis models, and computation

codes are only dependable for dispersion in open space without barriers and cannot precisely imitate the real fluctuation caused by uncertain parameters of environmental geometric bodies in real-world scenarios [15].

Furthermore, in compressed condition liquid chlorine is held at low temperature and high pressure in toners and as a gas at normal room temperature and pressure; if a chlorine leak occurs accidentally, chlorine poisonous vapor would form and combines with air, resulting in a strong gas plume. Because chlorine leakage is a complicated process, using a basic consequence analysis modeling numerical code to mimic it is not advised [17]. With more than 40 years of research, constant validation, worldwide authority accreditation, and appropriate simulation characteristics, the GEXCON FLACS CFD tool is specifically developed for gas dispersion and explosion modeling. Hansen et al. (2010) used observational evidence and the Model Evaluation Protocol (MEP) to execute, replicate, and evaluate a set of 33. These results reveal that GEXCON's FLACS CFD algorithm is the most precise and ideal CFD system for simulating gas dispersion.

2.1 3D CFD Numerical Code and Machine

In the current study GEXCON's 3D CFD FLACS V. 21.1- Dispersion and Ventilation numerical code is used for the consequence analysis study and all simulations are performed on the high-speed computing system.

2.2 FLACS CFD Computational Methods

FLACS CFD code is working in 3 steps: Preprocessing (Geometry and Simulation), Processing (Numerical Iterations), and Postprocessing (Result visualization) [18] (Fig. 1).

2.2.1 Preprocessing-Geometrical Modeling

In the present study, 3 various geometries have been constructed for the analysis of chlorine dispersion in open, closed, and with/without obstacles systems. The overall

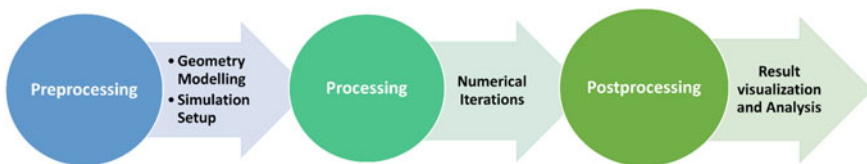


Fig. 1 FLACS CFD computational methods

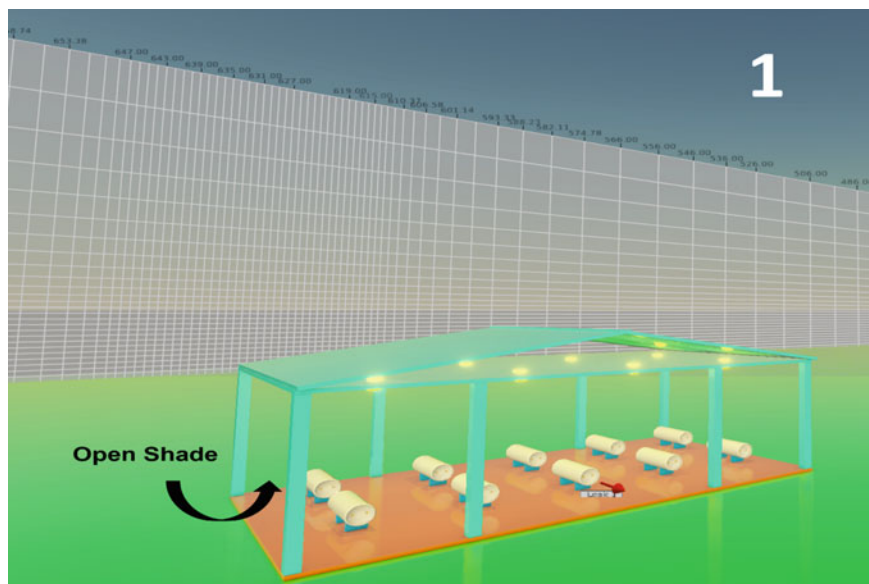


Fig. 2 Open shade system and grid used for Cl_2 dispersion study

geometrical domain dimension is 930×950 m and ground thickness is considered as 0.1 m, the dimension of chlorine shade and obstacles is $25 \times 15 \times 8$ m (Length \times Width \times Height). Figure 2 shows a model of chlorine storage in open shade without any obstacles, Fig. 3 Chlorine storage in open shade with obstacles, and Fig. 4 Chlorine storage in the closed shade with one side open. All 3 geometries consist of 10 numbers of chlorine tonner. All Chlorine tonner dimensions were considered the same as the real ones ($L \times D = 2.06 \times 0.778$).

2.2.2 Preprocessing- Simulation Setup (Initial and Boundary Conditions)

For the present study the following parameter has been considered: gravity, atmospheric pressure and temperature, leak size 5 mm and 10 mm, wind speed 2 and 5 m/s, stability class F&D, discharge coefficient 0.62, and ground roughness 0.03 m (open flat terrain, grass, few obstacles). The release rate (0.0395 kg/s and 0.1363 kg/s) of chlorine for both leak sizes (5 & 10 mm) has been calculated based on TNO yellow book- Paragraph 2.5.4 [19]. As cited in FLACS boundaries guidelines, the lower boundaries in X-, Y-, and Z-direction are denoted by X-LO, Y-LO and Z-LO, respectively, and the upper boundaries likewise by X-HI, Y-HI, Z-HI. In the dispersion simulation wind boundary condition is modeled as external wind filed, therefore, wind is considered as inflow boundaries in which velocity and turbulence profile (turbulent length scale, atmospheric stability classes) are specified and

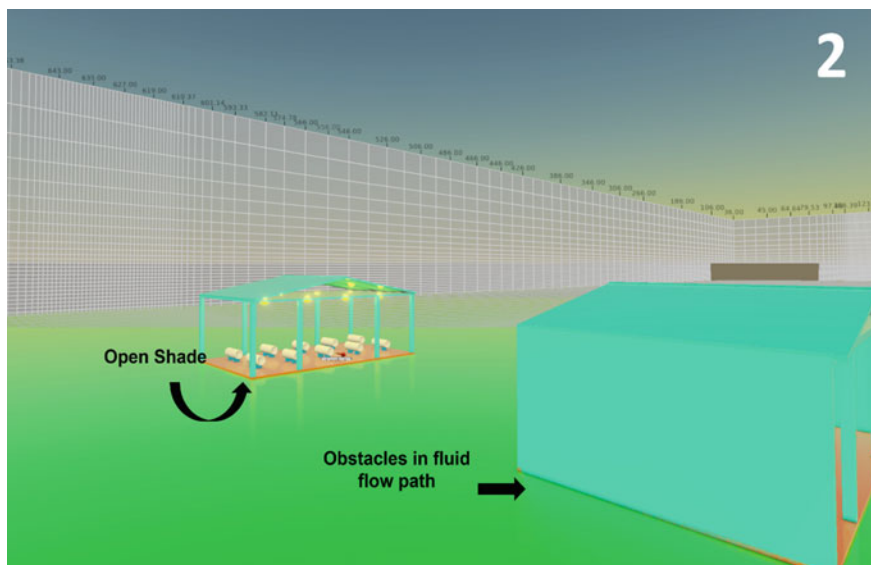


Fig. 3 Open shade with obstacle system and grid used for Cl_2 dispersion study

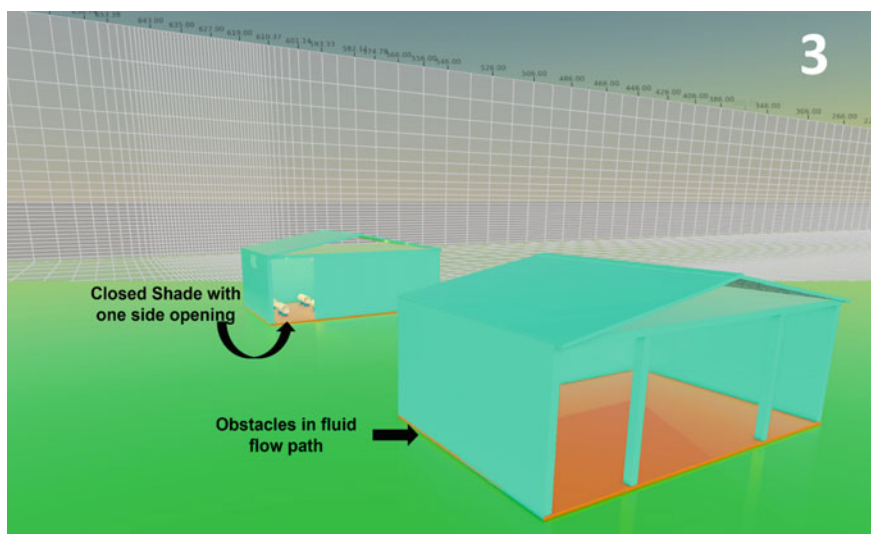


Fig. 4 Close shade with obstacle system and grid used for Cl_2 dispersion study

NOZZLE boundaries are used for sub sonic outflow at the exit boundary [18]. The WIND (inflow and parallel boundaries) and NOZZLE (exit boundary) are boundary conditions, whereas the outlet boundary is more robust and steadier than EULER for dispersion and ventilation [18]. In geometry, the wind is blowing at 180° (S-N). This blowing wind direction is parallel to the default X coordinate, therefore, XLO, YLO, XHI are WIND boundaries, inflow is parallel to ZHI: parallel boundaries and YHI, ZLO: NOZZLE boundaries. The relative turbulence intensity (RTI) was 0.1, the turbulence length scale (TLS) was 10% of RTI, and the wind stabilization time is considered 10 s. These all-boundary conditions and values are considered as per FLACS standard guidelines.

2.2.3 CFD Computational Domain

The Courant-Friedrich-Levy number (CFL) is used in FLACS CFD to link the time step of simulation to regulate volume (CV) size/dimensions via signal propagation velocity in terms of sound and fluid flow velocity for CFLC/CFLV, respectively. CFLC = 10 and CFLV = 1 were employed in the current chlorine dispersion investigation, as suggested by FLACS for dispersion and ventilation studies [18]. In FLACS, less than one million computation grids are often recommended [18]. Since chlorine is a heavy gas, it typically travels a large distance [20]. The fundamental grid size chosen was 1 m in order to take both computation accuracy and calculation speed into consideration [20–22]. Grid stretching (10 m uniform) was done for the area of the far field in the X, Y, and Z directions as well as the direction upwind of the main wind direction. Grid refining was done for the area that was downwind from the release source. In the x, y, and z dimensions, the total grid domains for modeling are 930 m, 950 m, and 60 m, respectively.

2.2.4 Governing Equations

In the present study, Favre-averaged transport equations for momentum, mass, enthalpy (h), turbulent K.E (k), the rate of dissipation of turbulent K.E (ε), fuel mass-fraction (Y_F), the fraction of mixture (ξ) are solved and the standard k- ε model for turbulence is used [18]. The k- ε model is based on Reynolds-averaged Navier-Stokes (RANS) in which k solves the transport equation for turbulent kinetic energy and ε for dissipation of turbulent kinetic energy.

2.2.5 Validation Approach

The ideal method for identifying the variety of scenarios for which a model system delivers accurate estimates for pertinent physical phenomena is validation against analytical solutions, experiments, and real incidents. Quality assurance also requires

systematic validation, which involves regularly observing the consequences of modifications to operating systems, compilers, and source code. Gexcon has, therefore, put in place an automated system for FLACS-CFD software validation. Currently, there are about 60 validation series and 2,700 FLACS-CFD simulations available in the FLACS automated framework (including a range of sensitivity simulations). The cases range from small-scale basic verification cases to large-scale dispersion and explosion cases [18]. The CFD tool FLACS employed in the current study has received considerable validation as a useful tool for creating the CFD code for a variety of gas dispersion instances and has been approved for risk management studies and risks related to dispersion by numerous researchers around the world [23–29]. Also, physical trials on the dispersion of hazardous (combustible, toxic) chemical fluids are also not a viable, economical, or reliable form of inquiry. Therefore, such validation is not repeated in this study.

3 Results and Discussion

3.1 *Effect of Wind Speed and Leak Size with Open/Open with Obstacles/Close with Obstacles System on Cl₂ Dispersion*

Figures 5, 6 and 7a–d, show the effect of wind speed and leak size on Cl₂ dispersion path length and shape of the plume at IDLH concentration level 10–1000 ppm. As the wind conditions changes, a drastic change in the length, height, and shape of the cloud is observed.

From the above open and open with obstacles system counter plots in Figs. 5 and 6, it is observed that the obstacles are strongly affected by dispersed plume length and width. In the open system (Fig. 5) the Cl₂ plume is dispersed parallel to the wind direction and covers the maximum vertical distance towards the downwind direction. While in the case of an open system with obstacles (Fig. 6) the Cl₂ plume stuck on obstacles and covered the maximum distance horizontally but the vertical distance towards downward wind direction is almost half of the open system distance. Also, it was observed that the obstacle in the path of fluid flow is responsible for the formation of eddies which directly affects the horizontal as well as vertical distance of the plume. In comparison to the other two systems, the distance traveled by the scattered Cl₂ plume in the downward wind direction is 1/4th in the case of a closed system (Fig. 7) with one side opening (Figs. 5 and 6). The detailed analysis of all systems is given in Table 1. The above analysis clearly shows that chlorine storage in an open space increases the probability of the formation of a toxic atmosphere in the nearby area. While chlorine storage in a closed system reduces the probability.

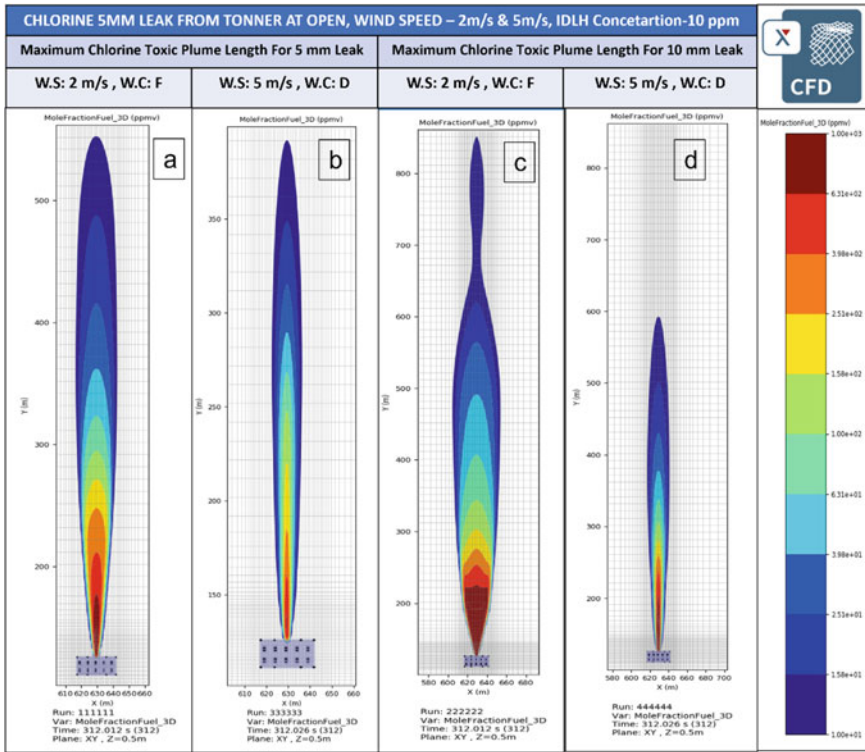


Fig. 5 a–d 2D counter XY plot for Cl₂ dispersion in the open system

3.2 Effect of Wind Speed and Leak Size on Cl₂ Dispersed Plume Height

From Figs. 8, 9 and 10a–d it can be seen that the effect of wind speed and leak size on Cl₂ plume height at an IDLH concentration level of 10–1000 ppm. In the open system (Fig. 8), it is observed that the height of the Cl₂ toxic plume in the Z+ direction is less than that in the open system with obstacles (Fig. 9). The increment of height in the Z+ direction in an open system with obstacles is due to the agglomeration of the plume at the obstacles wall surface. While in the case of a closed system (Fig. 10) it is observed that all the Cl₂ toxic gas gets filled inside the room and recirculated up to a certain time, after which it went outside through a closed system one side opening and covers less distance in Z + direction as compared to both systems (refer Table 1).

From Table 1 it can be seen that the larger the leak size and smaller the wind speed, the more will be the length of the plume as well as the height and vice versa. The 3D CFD pictorials (Figs. 11, 12 and 13) provide a realistic 3D isosurface view of the chlorine plume moment in the simulation domain. The height and width of the obstacles in the fluid flow path play an important role in terms of dispersion vertically

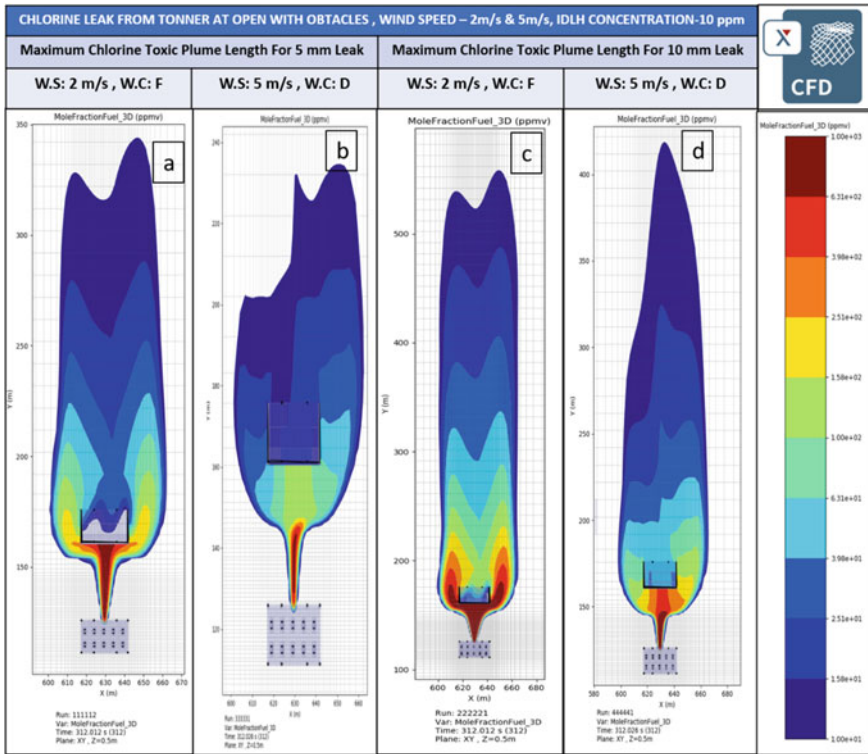


Fig. 6 a–d 2D counter XY plot of Cl₂ dispersion in open with obstacle system

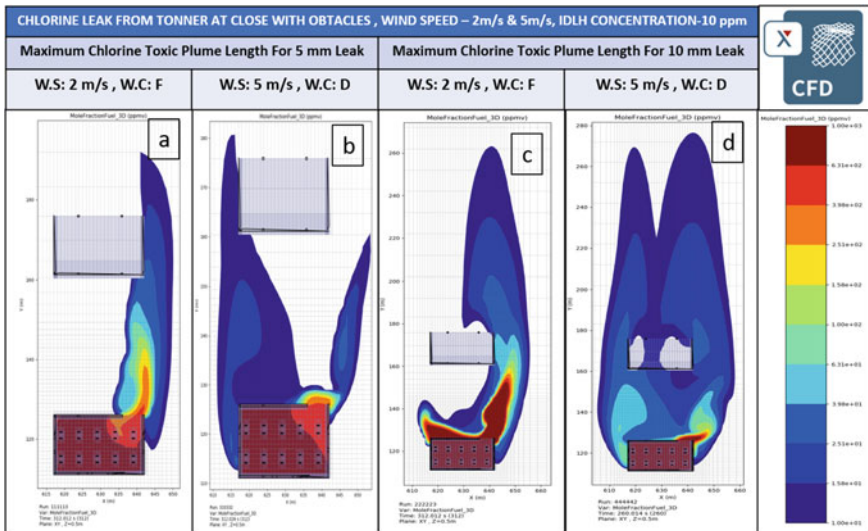


Fig. 7 a–d 2D counter XY plot of Cl₂ dispersion in close with obstacles

Table 1 Dispersed Cl₂ plume length/vertical distance and height analysis

System	Wind	Leak (mm)	Height (m)	Length/vertical (m)
Open	2F	5	11.5	428.43
	5D		7.5	264.96
	2F	10	20	727.03
	5D		14.25	468.53
Obstacles	2F	5	12.85	220.5106
	5D		11.95	112.0197
	2F	10	15.5	434.3465
	5D		13.5	293.9232
Closed	2F	5	9.4	68.89879
	5D		8	58.14415
	2F	10	14.6	139.391
	5D		10.2	152.4291

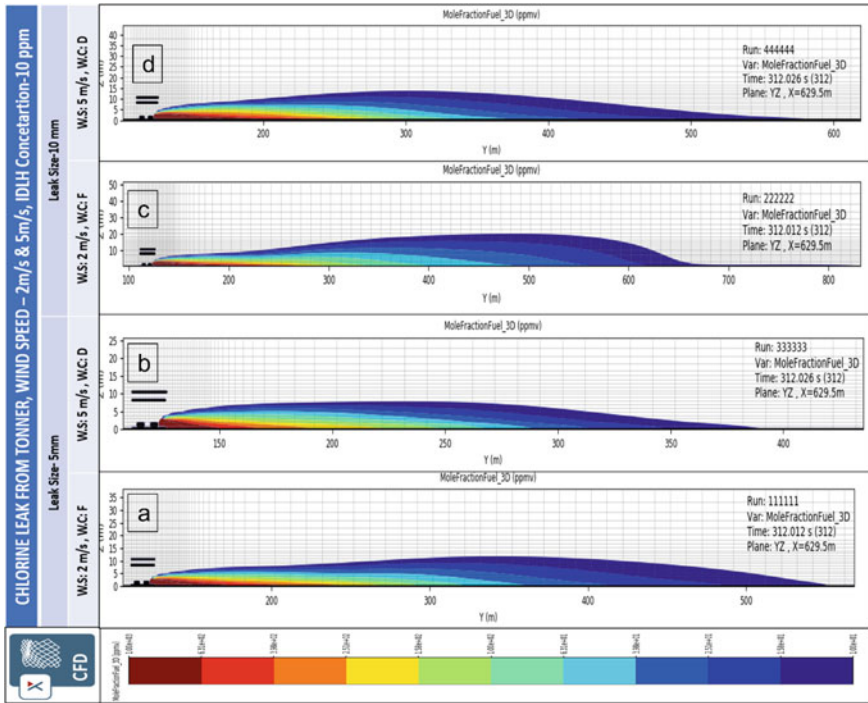


Fig. 8 a–d 2D counter YZ plot of Cl₂ dispersion in an open system

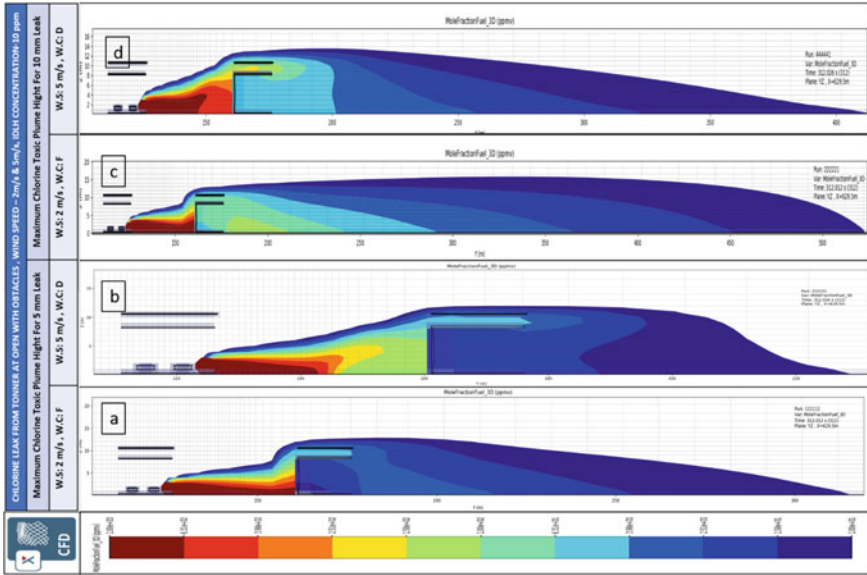


Fig 9 a–d 2D counter YZ plot of Cl₂ dispersion in open with obstacle system

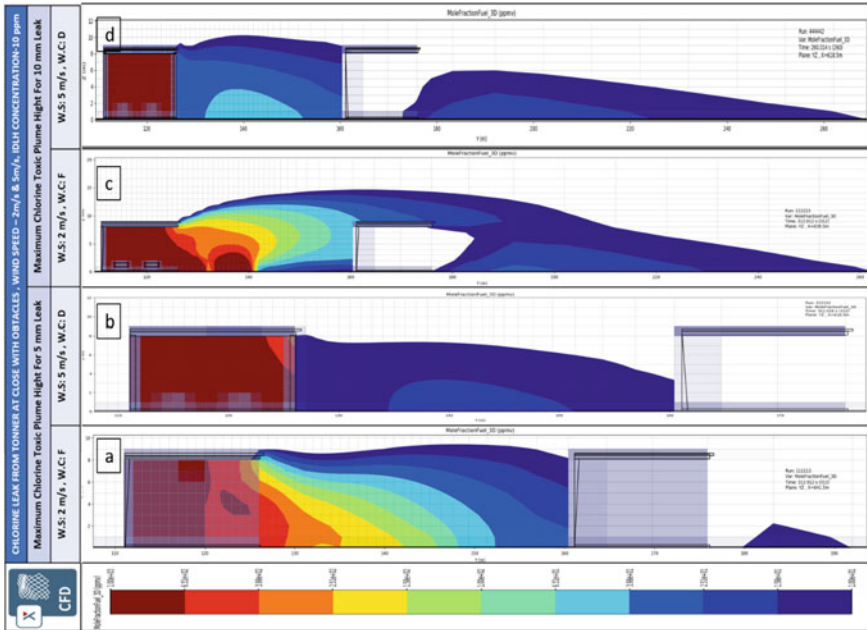


Fig. 10 a–d 2D counter YZ plot of Cl₂ dispersion in close with obstacles

as well as horizontally. So, from the open system with obstacles, it is found that the Cl_2 plume traveled over the obstacles due to the less height of the obstacles and eddies generated at the wall surface.

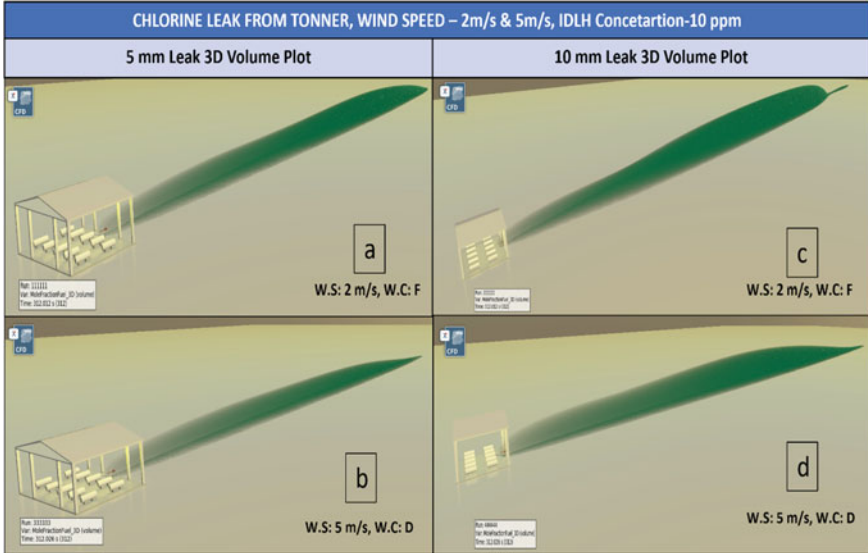


Fig. 11 a–d Open system 3D isosurface (10 ppm) plot of Cl_2 dispersion

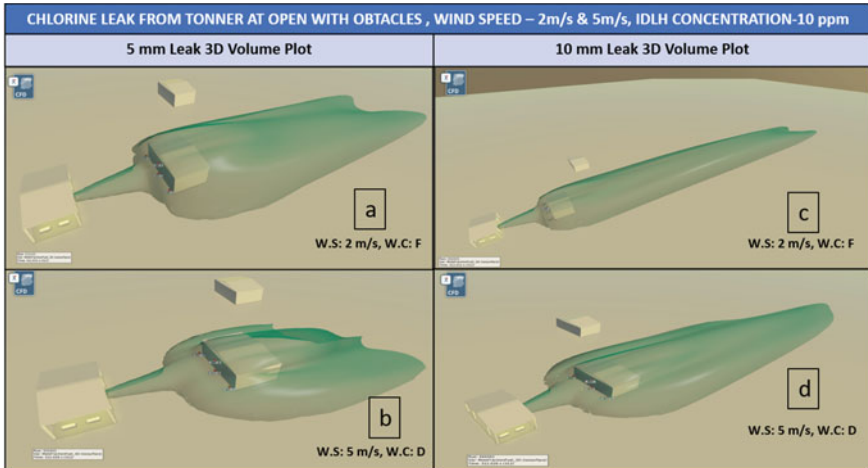


Fig. 12 a–d Open system with obstacles 3D isosurface (10 ppm) plot of Cl_2 dispersion

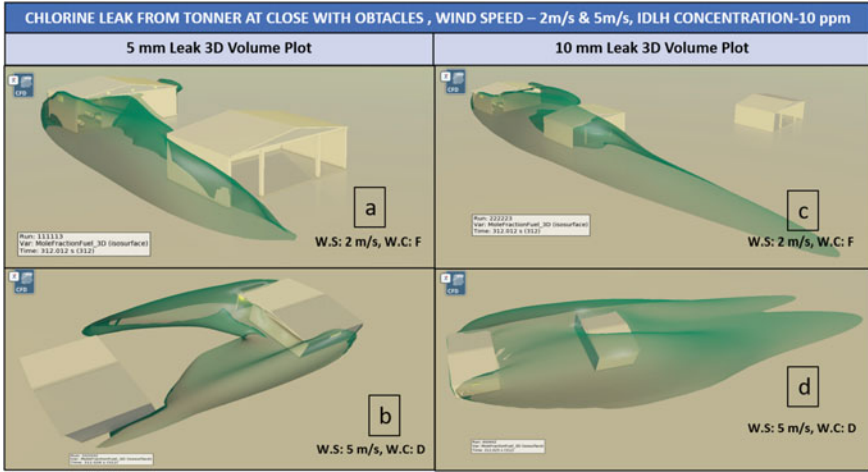


Fig. 13 a–d Closed system with obstacles 3D isosurface (10 ppm) plot of Cl₂ dispersion

3.3 Monitored IDLH Concentration at Obstacles Wall Surfaces and Inside a Closed System

In the current study, a total of four monitoring points were set up near the obstacles wall surface in the open system and inside the close system (Fig. 14). The IDLH concertation of chlorine (10 ppm) obtained at the wall surface in the time range of 19–33 s for the open system and 35–81 s inside the closed system. The detailed analysis of individual monitor points is mentioned in Table 2.

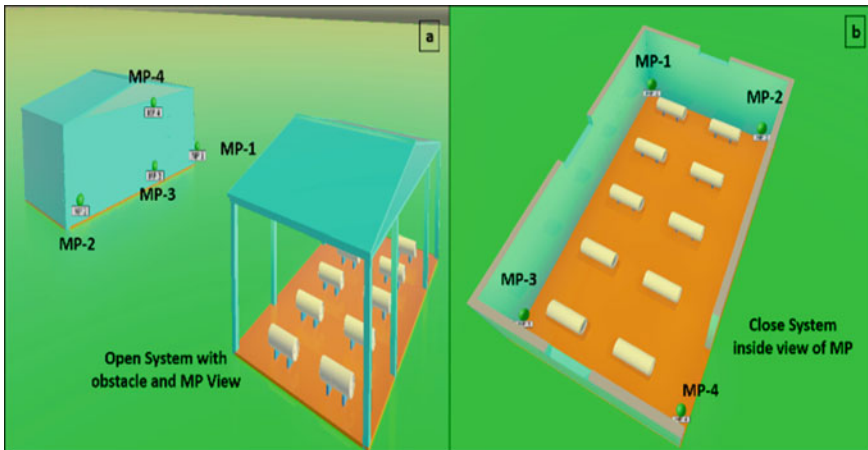


Fig. 14 a, b Monitor points positioned at the wall surface and inside the closed system

Table 2 Obtained dispersed Cl2 IDLH concentration at obstacles wall surface and inside closed room at individual monitor points (MP)

<i>Chlorine leak from tonner at open with obstacles, idlh concentration-10 ppm</i>															
Wind speed: 2 m/s, Wind class: F						Wind speed: 5 m/s, Wind class: D									
Leak size: 5 mm			Leak size: 10 mm			Leak size: 5 mm			Leak size: 10 mm						
MP1	MP2	MP3	MP4	MP1	MP2	MP3	MP4	MP1	MP2	MP3	MP4				
<i>10 ppm Concentration detection time (s) at individual monitor point (MP)</i>															
24.8	31.3	32.4	26.9	30.7	31.8	24.4	25.9	25.4	26.7	21.1	21.2	23.2	20.5	19.8	23.5
<i>Chlorine leak from tonner at close with obstacles, Idlh concentration-10 ppm</i>															
Wind speed: 2 m/s, Wind class: F						Wind speed: 5 m/s, Wind class: D									
Leak size: 5 mm			Leak size: 10 mm			Leak size: 5 mm			Leak size: 10 mm						
MP1	MP2	MP3	MP4	MP1	MP2	MP3	MP4	MP1	MP2	MP3	MP4	MP1	MP2	MP3	MP4
52.24	85.06	64.8	80.7	37.8	61.9	44.8	79.4	42.7	38.3	53.0	40.2	36.2	41.1	48.8	37.4

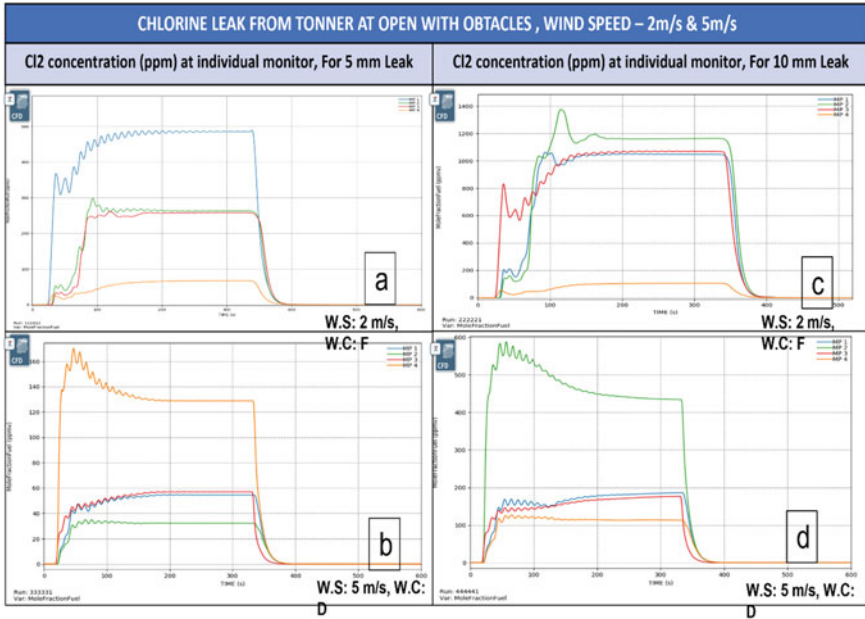


Fig. 15 a–d Cl₂ concentration at individual monitor points in the open system

The chlorine concentration at individual monitoring points is shown in Figs. 15 and 16. From the monitor points and 2D counter plots analysis it's observed that change in Cl₂ concentration and dispersion path distance with respective time towards the downwind direction have the same path. In the open system, the Cl₂ concentration in the range of 0–1300 ppm was observed at the obstacle's wall surface, while in the closed room the concentration in the range of 0–7000 ppm was monitored by MP. The highest range of chlorine concentration with low dispersion distance towards the downwind direction inside the chlorine system for a long time is found compared with the open and open system with obstacles.

4 Conclusion

The current study presents a dynamic approach using the FLACS CFD tool for the analysis of the consequences of the accidental Cl₂ toxic gas leakage by using gas dispersion modelling, considering that the toxic dense gas would keep closer to the ground level and bring great harm to the environment, humans, and assets. The FLACS CFD code's capacity to reasonably and accurately repeat the results was demonstrated through validation against comparable experiments. The present simulation was simulated with and without any obstacles in an open and closed system for Cl₂ to investigate the exposure risk in the surrounding and storage shade.

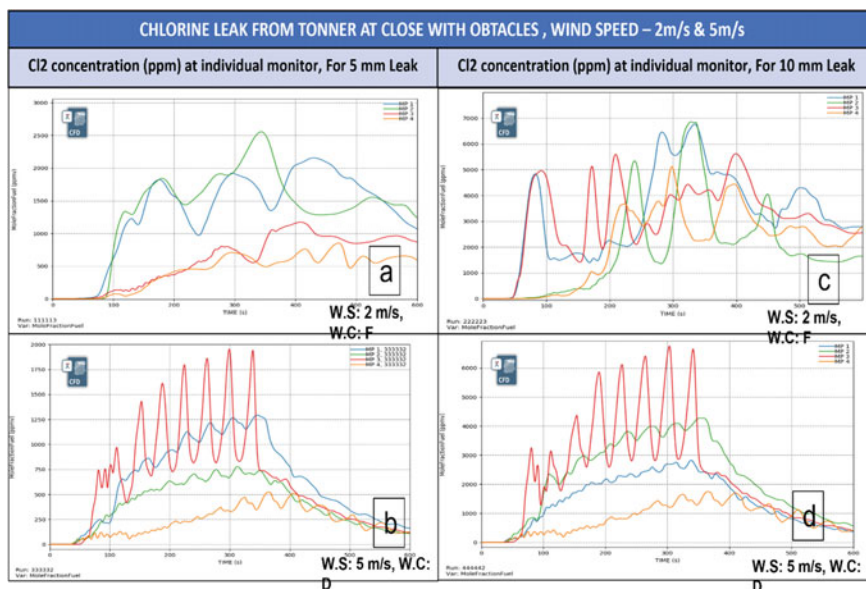


Fig. 16 a–d Cl₂ concentration at individual monitor points in close system

The propagation path of the plume is 600 s long, while the time taken for the leak to halt is 312 s long (considering 10 s of wind stabilization time by following FLACS best practice guidelines). With the different systems discussed earlier, the influence of diverse leak sizes and varied wind speed with wind stability class on chlorine dispersion was seen. The length, height, and structure of the plume alter dramatically when the wind conditions change, according to the results of the study. As mentioned in the result and discussion section, the obstacles in the fluid flow path play an important role in terms of a vertical and horizontal dispersion path.

The analyses of storage at various systems demonstrate that chlorine storage in open increases the possibility of the formation of a toxic atmosphere in the surrounding area which can harm the environment, humans, and assets as compared to the storage in a closed system. So, it is recommended to store chlorine inside the close room which is possible with a real time gas monitoring system, ventilation to safe location or room ventilation system connecting to appropriate scrubber system to neutralized effect of toxic gas.

Nowadays, the high application of hazardous chemicals in industrial processes and the day-by-day increment in frightening numbers of industrial accidents create fear amongst the society, making these industries unpopular and unsafe. As researchers, chemical industries need to create a centre of excellence (CoE) in process safety at the national level to address, train, and share development in hazardous chemicals by conducting education, training, and mitigation programs.

Acknowledgements We are thankful to Mr. Rajendra Narkhede (Country Manager) Gexcon India and the Gexcon Norway Team for providing the FLACS CFD code for this study.

References

1. Gupta JP (2002) The Bhopal gas tragedy: could it have happened in a developed country? *J Loss Prev Process Ind* 15(1):1–4
2. Masoumi G, Maniey M, Aghababaeian H, Ostadtaghizadeh A, Araghi Ahvazi L (2020) Lessons learned from a chlorine gas leakage in Dezful City, Iran, *Disaster Med. Public Health Prep* 1–7
3. CDC—Immediately dangerous to life or health concentrations (IDLH)_ Chlorine—NIOSH publications and products. NIOSH Publications & Products (2014). <https://www.cdc.gov/niosh/idlh/7782505.html>. Accessed 27 June 2022
4. Right to know hazardous substance fact sheet (2015). <http://www.nj.gov/health/workplacehealthandsafety/right-to>
5. Wang J, Yu X, Zong R (2020) A dynamic approach for evaluating the consequences of toxic gas dispersion in the chemical plants using CFD and evacuation modelling. *J Loss Prev Process Ind* 65:104156
6. Shinde SR (2020) A systematic review on advancements in drinking water disinfection technologies: a sustainable development perspective. *J Environ Treat Tech* 9(2):349–360
7. Hansen OR, Middha P (2008) CFD-based risk assessment for hydrogen applications. *Process Saf Prog* 27(1):29–34
8. Li X, Chen G, Zhang R, Zhu H, Xu C (2019) Simulation and assessment of gas dispersion above sea from a subsea release: a CFD-based approach. *Int J Nav Archit Ocean Eng* 11(1):353–363
9. Liu A, Huang J, Li Z, Chen J, Huang X, Chen K, bin Xu W (2018) Numerical simulation and experiment on the law of urban natural gas leakage and diffusion for different building layouts. *J Nat Gas Sci Eng* 54:1–10
10. Xin B, Yu J, Dang W, Wan L (2021) Dynamic characteristics of chlorine dispersion process and quantitative risk assessment of pollution hazard. *Environ Sci Pollut Res* 28(34):46161–46175
11. Wang W, Mou D, Sun B, Zhu C, Mi H (2021) Characteristics of leakage and diffusion for a chlorine storage tank based on simulation. *ACS Chem. Health Saf* 28(6):436–443
12. Sharma RK, Gopalaswami N, Gurjar BR, Agrawal R (2020) Assessment of failure and consequences analysis of an accident: a case study. *Eng Fail Anal* 109:104192
13. Efthimiou GC, Andronopoulos S, Tavares R, Bartzis JG (2017) CFD-RANS prediction of the dispersion of a hazardous airborne material released during a real accident in an industrial environment. *J Loss Prev Process Ind* 46:23–36
14. Derudi M, Bovolenta D, Busini V, Rota R (2014) Heavy gas dispersion in presence of large obstacles: selection of modeling tools. *Ind Eng Chem Res* 53(22):9303–9310
15. Rowley JR (2014) A new integral dispersion model based on one-dimensional turbulence theory. In: Hazards 24 conference proceeding, IChemE, Edinburgh International Conference Centre, Edinburgh, UK, pp 1–8
16. Sanchez EY, Colman Lerner JE, Porta A, Jacovkis PM (2013) Accidental release of chlorine in Chicago: coupling of an exposure model with a computational fluid dynamics model. *Atmos Environ* 64:47–55
17. Bauer TJ (2013) Comparison of chlorine and ammonia concentration field trial data with calculated results from a Gaussian atmospheric transport and dispersion model. *J Hazard Mater* 254–255(1):325–335
18. FLACS-CFD v21.1 user's manual (2021)
19. van den Bosch Ir CJH et al (2005) Methods for the calculation of physical effects due to releases of hazardous materials (liquids and gases)—Yellow book CPR 14E, 3rd edn

20. Xin B, Yu J, Dang W, Wan L (Sep. 2021) Dynamic characteristics of chlorine dispersion process and quantitative risk assessment of pollution hazard. *Environ Sci Pollut Res* 28(34):46161–46175. <https://doi.org/10.1007/s11356-020-11864-z>
21. Beji T, Merci B (Dec. 2018) Development of a numerical model for liquid pool evaporation. *Fire Saf J* 102:48–58. <https://doi.org/10.1016/j.firesaf.2018.11.002>
22. Brambilla S, Manca D (Jan. 2009) Accidents involving liquids: a step ahead in modeling pool spreading, evaporation and burning. *J Hazard Mater* 161(2–3):1265–1280. <https://doi.org/10.1016/j.jhazmat.2008.04.109>
23. Bernatfk A, Fabiano B, Hansen OR, Hansen ES (2022) Chemical engineering transactions CFD-modelling of large-scale LH2 release experiments. <https://doi.org/10.3303/CET2290104>
24. Hansen OR, Gavelli F, Ichard M, Davis SG (Nov. 2010) Validation of FLACS against experimental data sets from the model evaluation database for LNG vapor dispersion. *J Loss Prev Process Ind* 23(6):857–877. <https://doi.org/10.1016/j.jlp.2010.08.005>
25. Dadashzadeh M, Khan F, Hawboldt K, Amyotte P (2013) An integrated approach for fire and explosion consequence modelling. *Fire Saf J* 61:324–337. <https://doi.org/10.1016/j.firesaf.2013.09.015>
26. Baalisampang T, Abbassi R, Garaniya V, Khan F, Dadashzadeh M (Aug. 2019) Modelling an integrated impact of fire, explosion and combustion products during transitional events caused by an accidental release of LNG. *Process Saf Environ Prot* 128:259–272. <https://doi.org/10.1016/j.psep.2019.06.005>
27. Kim JH, Lee MK (Feb. 2021) A comparison on detected concentrations of lpg leakage distribution through actual gas release, cfd (Flacs) and calculation of hazardous areas. *Appl Chem Eng* 32(1):102–109. <https://doi.org/10.14478/ace.2020.1085>
28. Mishra S, Mishra KB (May 2021) Numerical study of large-scale LNG vapour cloud explosion in an unconfined space. *Process Saf Environ Prot* 149:967–976. <https://doi.org/10.1016/j.psep.2021.03.034>
29. Roald Hansen O, Melheim JA, Storvik IE (2007) CFD-modeling of LNG dispersion experiments

Design of a Centralized PI Controller for Three-Tank Hybrid System Based on Optimization Methods



N. Rajasekhar, V. S. V. Bhanukiran, T. K. Radhakrishnan,
and N. Samsudeen

Abbreviations

MIMO	Multi-Input and Multi-Output
TTH	Three-Tank Hybrid
PRBS	Pseudo-Random Binary Signal
FPM	First Principles Model
NRGA	Non-Square Relative Gain Array
MRFO	Manta Ray Foraging Optimization
PSO	Particle Swarm Optimization
SSGM	Steady-state Gain Matrix
ISE	Integral Squared Error
ITAE	Integral Time Absolute Error

1 Introduction

Multiple-Input and Multiple-Output (MIMO) system defines the processes with more than single input and more than single output and needs multiple control loops. Most of the processes generally encountered in chemical engineering practice are MIMO non-linear processes. The loop interactions make the MIMO system more complicated. Non-linear processes are those in which the input and the output are not proportionally related. The MIMO systems can be controlled using decentralized and

N. Rajasekhar · V. S. V. Bhanukiran · T. K. Radhakrishnan (✉) · N. Samsudeen
Department of Chemical Engineering, National Institute of Technology, Tiruchirappalli 620015,
Tamil Nadu, India
e-mail: radha@nitt.edu

© The Author(s), under exclusive license to Springer Nature Singapore Pte Ltd. 2023
E. Chinthapudi et al. (eds.), *Sustainable Chemical, Mineral and Material Processing*,
Lecture Notes in Mechanical Engineering,
https://doi.org/10.1007/978-981-19-7264-5_5

centralized controllers. A MIMO process is divided into multiple single-input single-output (SISO) processes in a decentralized control system, and a controller is created for each loop by providing for loop interactions. Due to its many benefits, including operational flexibility, failure tolerance, and simplified design and tuning processes, decentralized control has so far continued to be the most popular control system in multivariable control. A comprehensive multivariable controller with a non-diagonal controller matrix makes up the centralized control architecture. The need for centralized control has been extensively discussed in previous works [1–5]. The centralized controller simultaneously uses all the process inputs, output measurements, and interactions to calculate the values of all manipulated variables. The decentralized controllers perform poorly for systems with strong interactions. Therefore, a more sophisticated control scheme, such as the centralized control structure, is used when good performance is required for the strongly interacting systems. The centralized controller can be easily designed with the knowledge of the steady-state matrix.

In this study, a method of designing a centralized PI controller for a MIMO non-linear system is presented. A three-tank hybrid (TTH) process is considered to represent the MIMO non-linear process [6, 7]. The TTH system is a benchmark for process characteristics such as variable dynamics, interactions, and non-linearity and has both continuous and discrete dynamics [8–10]. Discrete dynamics due to the top-level interactions and continuous dynamics are present in the system inherently. A first principles model (FPM) is used to derive the governing equations of the system, and using those equations, the transfer function of the system is obtained. The transfer function matrix evolved is non-square because the number of the inputs (two input flow rates) and the number of the outputs (height of liquid in three tanks) are not the same. The non-square relative gain array (NRGA) [11] of the system is used to analyze the interactions present in the model. The Davison method [12] is used to design the proportional-integral (PI) controller, for the non-square three-tank system. The Davison method uses pseudo inverse (Moore-Penrose inverse) for designing the controller. Since the Davison method does not fine tune the controller, for optimal performance, an optimization technique, viz., Manta Ray Foraging Optimization (MRFO) [13] technique is implemented to tune the controller parameters φ and Ψ . This optimization gives the best values of φ and Ψ and improves the process response. The designed controller is compared with the parameters calculated using another optimization technique, viz., Particle Swarm Optimization (PSO) [14]. The closed loop simulation results verify the performance of the controllers.

The innovation and novelty aspects of the present study are as follows: A centralized PI controller is proposed using steady-state gain matrix (SSGM) for the TTH system. The PI controller parameters (φ and Ψ) of the Davison method are tuned using the MRFO and PSO optimization methods. The designed centralized PI controller performance is evaluated for both the servo and regulatory responses of the TTH system.

The paper is organized as follows, Sect. 2 presents the modeling of the TTH system, and Sect. 3 explains the design of a centralized PI controller. Section 4 explains about MRFO and PSO optimization algorithms and their pseudo codes.

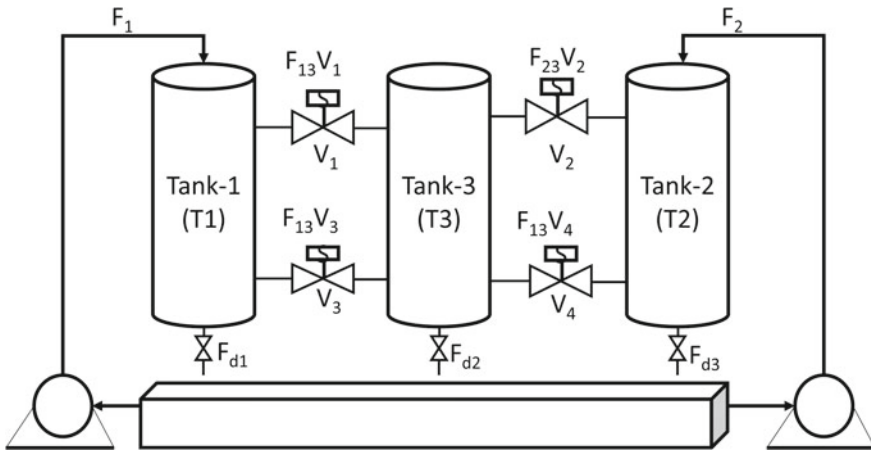


Fig. 1 Schematic of three-tank hybrid system

In Sect. 5, closed loop performance of the two optimization methods is compared. Finally, in Sect. 6, conclusions are given.

2 Modeling of Three-Tank Hybrid Process

2.1 Three-Tank Hybrid System

The pictorial representation of this TTH experimental system is shown in Fig. 1. It comprises of three cylindrical tanks T_1 , T_2 , and T_3 . On/Off solenoid valves are used to connect these tanks. V_1 , V_2 are single directional valves that connect T_1 to T_3 and T_2 to T_3 , respectively, and V_3 , V_4 are bidirectional valves. Through ball valves, there is a constant outflow from all of these tanks as F_{d1} , F_{d2} , F_{d3} . The level in the first tank is influenced by the inflow F_1 and interaction flows F_{13h} and F_{13l} . The level in the second tank is influenced by the inflow F_2 and interaction flows F_{23h} and F_{23l} , and the level in the third tank is influenced by all interaction flows F_{13h} , F_{13l} , F_{23h} , and F_{23l} , where the subscripts ‘h’ and ‘l’ represent top-level interaction and bottom-level interaction, respectively, which can be seen from the real-time experimental setup as shown in Fig. 2, and the system parameters are summarized in Table 1.

2.2 Modeling

First principles modeling is used for the above system to derive the governing equations.



Fig. 2 Experimental setup of TTH system

Table 1 TTH system parameters

Parameter	Value (m)
Tank heights	1.00
Tank inner diameter	0.15
Overflow height of the tanks	0.95
Interconnecting pipe diameter	0.02
Top interaction height tank-1 (l_{v1})	0.38
Top interaction height tank-2 (l_{v2})	0.425
Cross section area of each tank (a)	0.01767 m^2

$$\frac{dL_1}{dt} = \frac{F_1 - F_{13l}v_3 - F_{13h}v_1 - F_{d1}}{A} \quad (1)$$

$$\frac{dL_2}{dt} = \frac{F_2 - F_{23l}v_4 - F_{23h}v_2 - F_{d2}}{A} \quad (2)$$

$$\frac{dL_3}{dt} = \frac{F_{13l}v_3 + F_{13h}v_1 + F_{23l}v_4 + F_{23h}v_2 - F_{d3}}{A} \quad (3)$$

$$F_{13l} = d_{13l} \text{Sign}(L_1 - L_3) \sqrt{2g|(L_1 - L_3)|} \quad (4)$$

$$F_{23l} = d_{23l} \text{Sign}(L_2 - L_3) \sqrt{2g|(L_2 - L_3)|} \quad (5)$$

$$F_{13h} = d_{13h} (\max(L_1, L_{v1}) - \max(L_3, L_{v1})) \sqrt{2g|\max(L_1, L_{v1}) - \max(L_3, L_{v1})|} \quad (6)$$

$$F_{23h} = d_{23h}(\max(L_2, L_{v_2}) - \max(L_3, L_{v_2}))\sqrt{2g|\max(L_2, L_{v_2}) - \max(L_3, L_{v_2})|} \tag{7}$$

$$F_{d1} = d_{d1}\sqrt{2gL_1}; F_{d2} = d_{d2}\sqrt{2gL_2}; F_{d3} = d_{d3}\sqrt{2gL_3} \tag{8}$$

All the discharge coefficients are computed experimentally using the first principles model after allowing the system to reach the steady state and these estimated discharge coefficients are tabulated in Table 2.

Experimental data and simulated data of each tank are superimposed on one another as shown in Fig. 3. Initially, experimental data and simulated data are deviating due to inertial errors; after some duration, both the data are very close to each other, which shows modeling is satisfactory.

Table 2 Estimated values of discharge coefficients

Discharge coefficients	Value (m ²)
d_{13L}	0.00006
d_{13h}	0.00005
d_{23L}	0.0000072
d_{23h}	0.000035
d_{d1}	0.0000855
d_{d2}	0.000103
d_{d3}	0.00001839

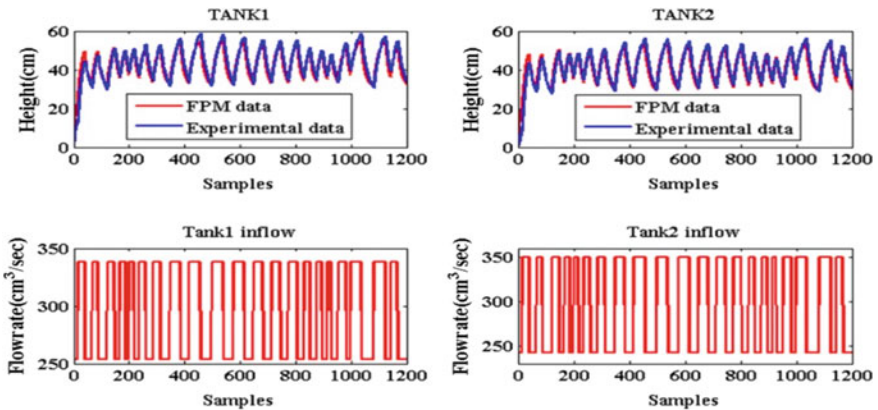


Fig. 3 Experimental data versus simulation data

2.3 Transfer Function Matrix of the System

For a given particular flow rate of $F_1 = 120 \times 10^{-6} \text{m}^3/\text{s}$, $F_2 = 125.7 \times 10^{-6} \text{m}^3/\text{s}$, the steady-state heights of liquid in tanks are $L_1 = 0.07415 \text{ m}$, $L_2 = 0.070257 \text{ m}$, $L_3 = 0.070253 \text{ m}$. The nominal process parameters are used to derive the linearized state-space model.

$$A = \begin{bmatrix} -0.1574 & 0 & 0.118 \\ 0 & -4.561 & 4.5125 \\ 0.118 & 4.5125 & -4.6387 \end{bmatrix} \quad (9)$$

$$B = \begin{bmatrix} 0.0057 & 0 \\ 0 & 0.0057 \\ 0 & 0 \end{bmatrix} \quad (10)$$

$$C = \begin{bmatrix} 1 & 0 & 0 \\ 0 & 1 & 0 \\ 0 & 0 & 1 \end{bmatrix} \text{ and } D = 0 \quad (11)$$

Using this state-space model, the transfer function matrix (G_p) is derived. The obtained G_p is a 3×2 matrix as shown in Fig. 4 where

$$G_p(s) = \begin{bmatrix} \frac{0.005659s^2+0.05206s+0.004496}{s^3+9.357s^2+2.228s+0.06147} & \frac{0.003013}{s^3+9.357s^2+2.228s+0.06147} \\ \frac{0.003013}{s^3+9.357s^2+2.228s+0.06147} & \frac{0.005659s^2+0.027146s+0.004}{s^3+9.357s^2+2.228s+0.06147} \\ \frac{0.0066678s+0.003046}{s^3+9.357s^2+2.228s+0.06147} & \frac{0.02554s+0.004018}{s^3+9.357s^2+2.228s+0.06147} \end{bmatrix} \quad (12)$$

3 Design of Centralized Controller

The non-square condition present in the input and output pairing is due to lesser number of manipulated variables (MV) than the controlled variables (CV). This

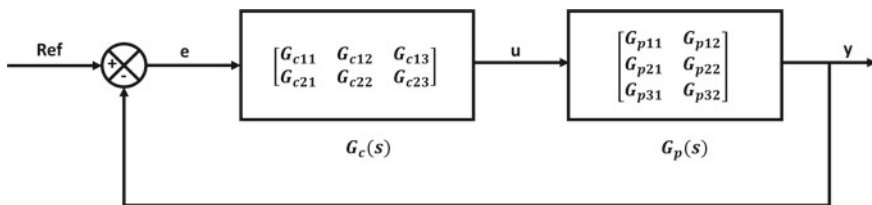


Fig. 4 Closed loop centralized control structure

leads to more interaction in the control loops, thereby increasing the tortuosity of the process; hence, centralized controllers are used. However, the control variables h_1 and h_2 are of interest in this literature.

3.1 Multivariable PI Controller

The Davison method [12], along with the optimization method, viz., MRFO and PSO, is used to design the PI controller. The Davison method uses the pseudo inverse of the steady-state gain matrix of the non-square system. The controller matrix (G_C) is in the following form.

$$\left. \begin{aligned} G_{Cij}(s) &= K_{Cij} + \frac{K_{Iij}}{s} \\ K_C &= \varphi A^\dagger \\ K_I &= \Psi A^\dagger \end{aligned} \right\} \quad (13)$$

where φ and Ψ are controller tuning parameters, and A^\dagger is the pseudo inverse of the steady-state gain matrix. φ and Ψ vary between 0 and 1. The steady-state gain matrix (SSGM) represented as 'K' is obtained ($G_p(s=0)$).

$$K = \begin{bmatrix} 0.0731 & 0.049 \\ 0.049 & 0.0659 \\ 0.0496 & 0.0654 \end{bmatrix} \quad (14)$$

The pseudo inverse [3] (A^\dagger) of K is found out by using the Moore–Penrose method.

$$A^\dagger = (K'K)^{-1}.K' \quad (15)$$

$$A^\dagger = \begin{bmatrix} 27.5084 & -10.7668 & -9.7727 \\ -20.6533 & 15.806 & 14.8502 \end{bmatrix} \quad (16)$$

Hence, G_c becomes

$$G_C(s) = A^\dagger_{ij}\varphi + \frac{A^\dagger_{ij}\Psi}{s} \quad (17)$$

where

$$G_c(S) = \begin{bmatrix} 27.5084\varphi + \frac{27.5084\Psi}{s} & -10.7668\varphi - \frac{10.7668\Psi}{s} & -9.7727\varphi - \frac{9.7727\Psi}{s} \\ -20.6533\varphi - \frac{20.6533\Psi}{s} & 15.806\varphi + \frac{15.806\Psi}{s} & 14.8502\varphi + \frac{14.8502\Psi}{s} \end{bmatrix}$$

The controller tuning parameters φ and Ψ are tuned using the MRFO optimization method, as shown in Sect. 4.

4 Optimization Methods

4.1 Manta Ray Foraging Optimization (MRFO)

The MRFO [13] is developed to accomplish a global optimization. The MRFO is a nature-based optimization technique that uses the foraging strategies of Manta rays. There are three different types of Manta ray foraging techniques, they are cyclone foraging, chain foraging, and somersault foraging, respectively, and the flowchart is shown in Fig. 5. The models of these foraging behaviors are developed mathematically. In this study, the Davison PI controller parameters φ and Ψ are optimized using the MRFO technique.

4.1.1 Chain Foraging

By lining up one after another, Manta rays form a foraging chain. With the exception of the Manta ray that is in the foremost position, every other in the chain moves toward the Manta ray in front of it, in addition to the direction of the food. That is, each individual in each iteration is updated by the best solution identified thus far and the solution in front of it.

$$y_i(t+1) = \begin{cases} y_i(t) + r(y_{best} - y_i(t)) + A(y_{best} - y_i(t)) & \text{for } i = 1 \\ y_i(t) + r((y_{i-1}(t) - y_i(t))) + A(y_{best} - y_i(t)) & \text{for } i = 2, \dots, N \end{cases}$$

$$A = 2r\{|\log(r)|\}^{0.5} \quad (18)$$

where $y_i(t)$ represent the location of the i th Manta ray, $r \in [0, 1]$, 'A' is the coefficient of the weight, and $y_{best}(t)$ is the position where the concentration of food is very high.

4.1.2 Cyclone Foraging

A single Manta ray does not always follow the one in front of it and also moves in a spiral path toward the food.

$$y_i(t+1) = \begin{cases} y_{rand} + r(y_{rand} - y_i(t)) + \beta(y_{rand} - y_i(t)) & \text{for } i = 1 \\ y_{rand} + r((y_{i-1}(t) - y_i(t))) + \beta(y_{rand} - y_i(t)) & \text{for } i = 2, \dots, N \end{cases} \quad (19)$$

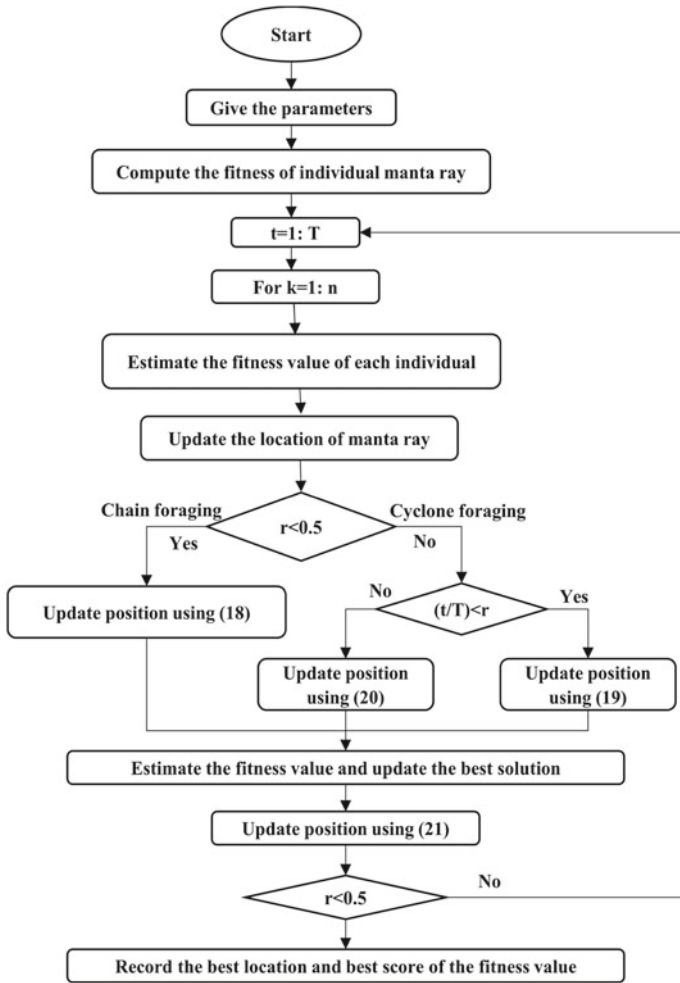


Fig. 5 Flowchart of MRFO

$$y_i(t + 1) = \begin{cases} y_{best} + r(y_{best} - y_i(t)) + B(y_{best} - y_i(t)) & \text{for } i = 1 \\ y_{best} + r((y_{i-1}(t) - y_i(t))) + B(y_{best} - y_i(t)) & \text{for } i = 2, \dots, N \end{cases} \quad (20)$$

$$B = 2e^{-r1(T-t+1/T)} \cdot \sin(2\pi r1).$$

where ‘B’ coefficient of the weight, $r \in [0, 1]$, and T is the maximum iterations.

4.1.3 Somersault Foraging

This behavior is thought to be influenced by the location of the food. Every team member swims around the axis, somersaulting into a new location.

$$y_i(t + 1) = y_i(t) + S_f(r \cdot y_{best} - r \cdot y_i(t)) \quad (21)$$

where $S_f \rightarrow$ Somersault factor and used $S_f \rightarrow 2$

$$r \in [0, 1]$$

4.1.4 Pseudo Code of Manta Ray Foraging Optimization

Initialize the Manta Ray Size (N) and the maximum number of iterations (T) and each manta ray $y_i(t) = y_i + r \cdot (y_u - y_l)$ for $i = 1, 2, \dots, N$ and $t = 1$. Evaluate the fitness value of each Manta ray $f_i = f(y_i)$ and obtain the optimal solution found so far y_{best} , where y_u and y_l are the upper and lower boundaries of problem space, respectively, and r is a random number.

while (end criterion is not reached)

do

for $i = 1:N$

do

if ($r < 0.5$)

then

if $t/T < r$

then

$$y_r = y_l + r(y_u - y_l)$$

$$y_i(t + 1) = \begin{cases} y_r + r(y_r - y_i(t)) + B(y_r - y_i(t)) & \text{for } i = 1 \\ y_r + r((y_{i-1}(t) - y_i(t))) + B(y_r - y_i(t)) & \text{for } i = 2, \dots, N \end{cases} \quad (22)$$

else

$$y_i(t+1) = \begin{cases} y_{best} + r(y_{best} - y_i(t)) + B(y_{best} - y_i(t)) \\ \text{for } i = 1 \\ y_{best} + r((y_{i-1}(t) - y_i(t))) + B(y_{best} - y_i(t)) \\ \text{for } i = 2, \dots, N \end{cases} \quad (23)$$

else if

else

$$y_i(t+1) = \begin{cases} y_i(t) + r(y_{best} - y_i(t)) + A(y_{best} - y_i(t)) \\ \text{for } i = 1 \\ y_i(t) + r((y_{i-1}(t) - y_i(t))) + A(y_{best} - y_i(t)) \\ \text{for } i = 2, \dots, N \end{cases} \quad (24)$$

end if

Evaluate the fitness of each Manta ray $f(y_i(t+1))$.

if $f(y_i(t+1)) < f(y_{best})$

then $y_{best} = y_i(t+1)$

for $I = 1: N$ *do*

$$y_i(t+1) = y_i(t) + S_f(r \cdot y_{best} - r \cdot y_i(t)) \quad (25)$$

where, $i = 1, 2, 3, \dots, N$

evaluate the fitness of each Manta ray $f(y_i(t+1))$.

if $(f(y_i(t+1)) < f(y_{best}))$

then $y_{best} = y_i(t+1)$

end for

end while

Return(the optimum solution found y_{best}).

4.2 Particle Swarm Optimization

Particle Swarm Optimization (PSO) algorithm is a computational intelligence technique that is acclaimed for its flexibility of using it in solving a high-dimensional problem space. It is widely used to increase the performance of non-linear functions. The flowchart for PSO is shown in Fig. 6.

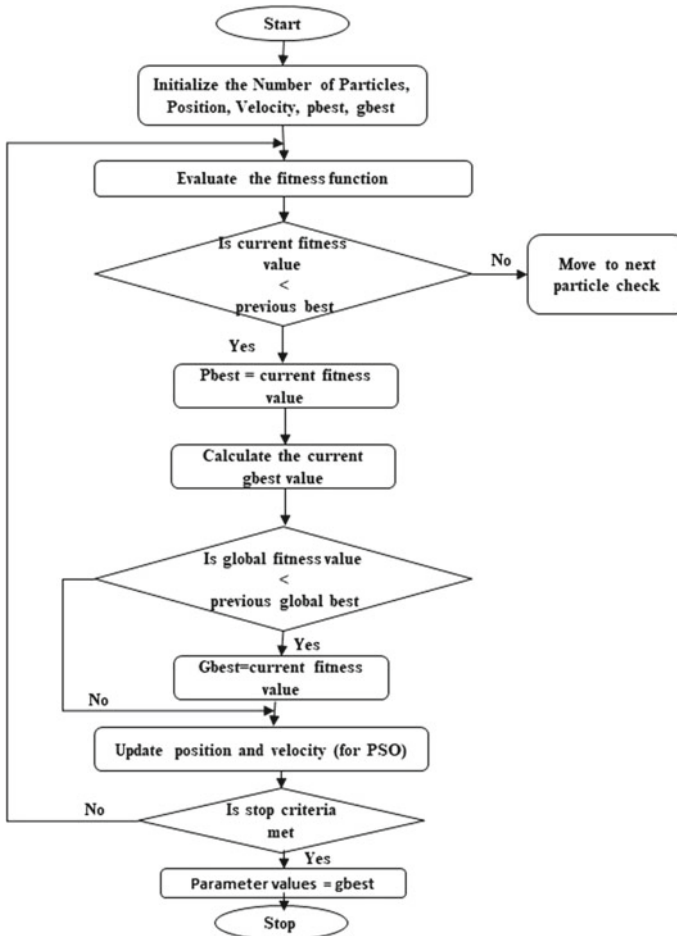


Fig. 6 Flowchart of PSO

4.2.1 Pseudo Code of Particle Swarm Optimization

for each particle (i)
for each dimension (d)
 set position randomly within permissible bound
 set velocity randomly within permissible bound
end

end

Iteration T = 1

do

for particle 1: N

evaluate fitness value

if

fitness value is better than pbest

assign pbest to the current value

end

end

Assign the gbest to the particle with the best fitness value.

for particle 1:N

for each dimension

find the particle velocity

$$V_i(t + 1) = \omega V_i(t) + c_1 r_1(t)(p_i(t) - y_i(t)) + c_2 r_2(t)(g_i(t) - y_i(t)) \quad (26)$$

Update the each particle position.

$$y_i(t + 1) = y_i(t) + V_i(t + 1) \quad (27)$$

end

end

T = T + 1

While (maximum iterations reached or minimum error criteria are not attained)

5 Results and Discussion

The MRFO and PSO techniques are used to optimize the parameters φ and Ψ . Evaluation criteria such as Mean Absolute Error (MAE) and Integral Time Absolute Error (ITAE) are used in the literature to define the cost function. In this case, the ITAE as mentioned in Eq. (28) is used as a cost function in the MRFO and PSO to find the optimized parameters, i.e. φ and Ψ , to improve its performance. The closed

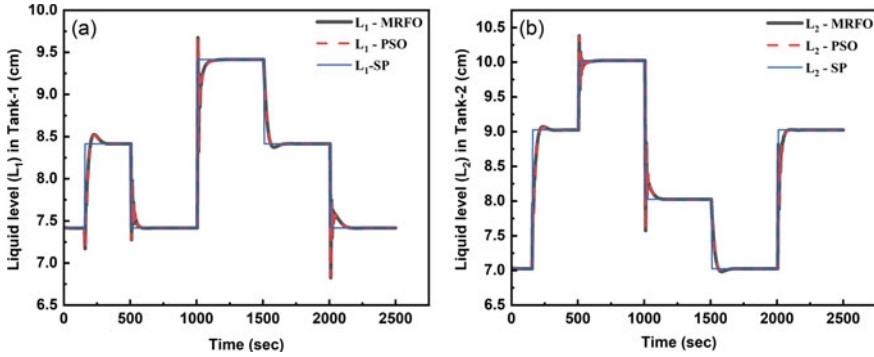


Fig. 7 Controller response comparison of two methods for multiple step input changes in L_1 and L_2 in TTH System

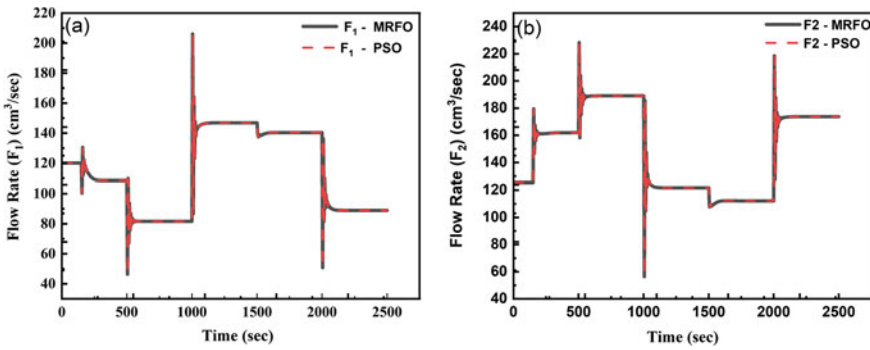


Fig. 8 Variations of Flow rates F_1 and F_2 with respect to non-uniform changes in L_1 and L_2

loop performance using the optimized parameters in G_C is shown in Figs. 7, 8, 9, 10, 11 and 12, and the tuned PI parameters from MRFO and PSO are shown in Table 3.

$$ITAE = \int_0^{\infty} t|e(t)|dt \tag{28}$$

The performance of the controllers is designed based on MRFO and PSO, when multiple non-uniform step changes are given in both the setpoints of L_1 (7.415–8.415–7.415–9.415–8.415–7.415 cm) and L_2 (7.0217–9.0217–10.0217–8.0217–7.0217–9.0217 cm), as shown in Fig. 7. It can be seen from Fig. 7 that the MRFO-based controller gives lesser overshoot and settles faster compared to a PSO-based controller. The MRFO-based controller also gives a lesser ISE value compared to a PSO-based controller ISE value as tabulated in Table 4. The variations in the manipulated variables F_1 and F_2 are also shown in Fig. 8, for the non-uniform step changes in L_1 and L_2 .

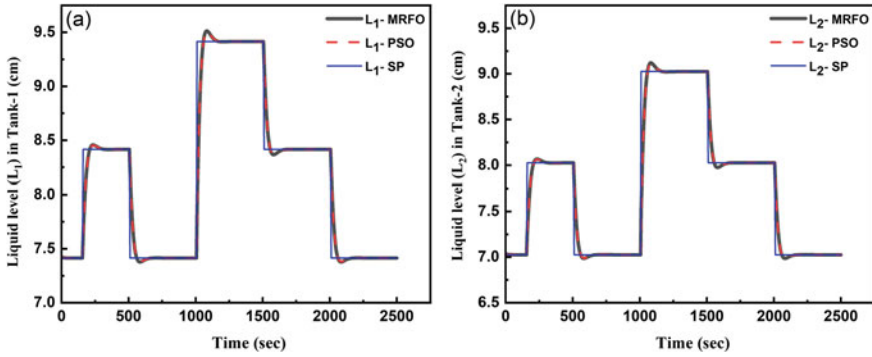


Fig. 9 Controller response comparison of two methods for uniform step input changes in L_1 and L_2 in TTH system

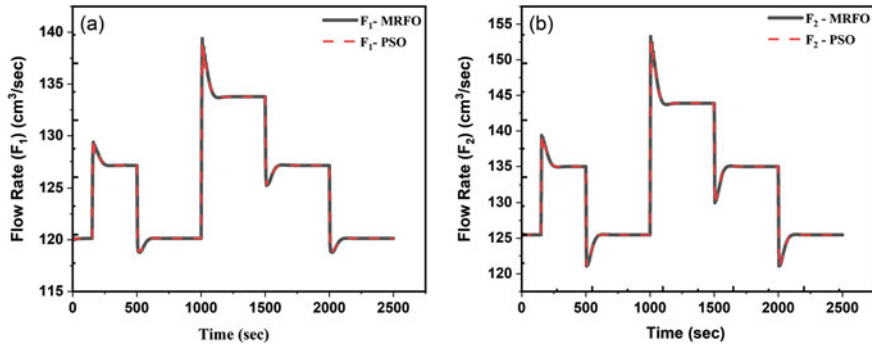


Fig. 10 Variations of flow rates F_1 and F_2 with respect to uniform changes in L_1 and L_2

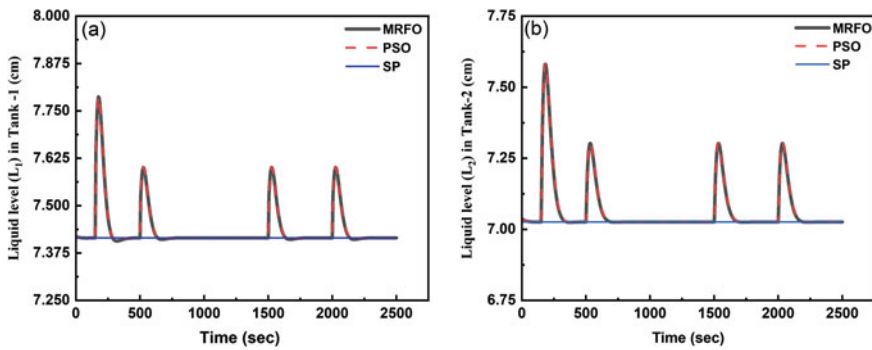


Fig. 11 Controller response comparison of two methods for disturbance changes in L_1 and L_2 in TTH system

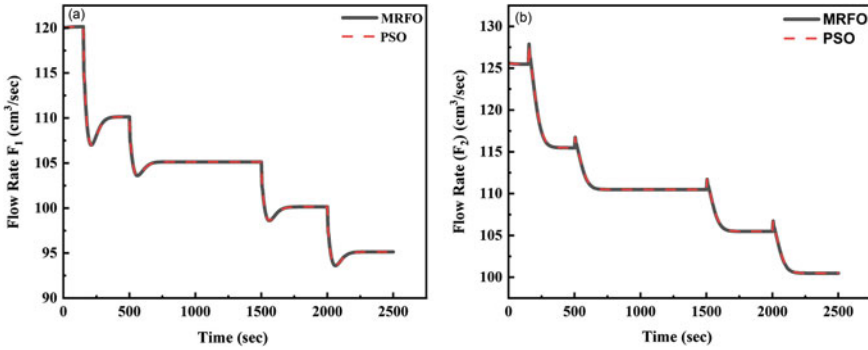


Fig. 12 Variations of flow rates F_1 and F_2 with respect to load changes in L_1 and L_2

Table 3 Controller tuning parameters

Optimization method	φ	Ψ
MRFO	1.0	0.0538
PSO	1.0	0.0525

Table 4 Comparison of ISE values

Optimization method	Servo		Regulatory ISE
	ISE (non-uniform changes)	ISE (uniform changes)	
MRFO	421	556	12.3669
PSO	568	568.75	12.6689

Figure 9 illustrates the performance of controllers designed using MRFO and PSO when multiple uniform step changes are made to the setpoints of L_1 (7.415–8.415–7.415– 9.415–8.415–7.415 cm) and L_2 (7.0217–8.0217–7.0217–9.0217–8.0217–7.0217 cm). In comparison to a PSO-based controller, the MRFO-based controller exhibits less overshoot and settles more quickly. Table 4 compares the ISE values of the two types of controllers. Figure 10 also shows the variations in the manipulable variables F_1 and F_2 for the uniform step changes in L_1 and L_2 .

The regulatory response for the two methods, the manipulated variables F_1 and F_2 change in different time intervals (100–500–1500–2000s), and the designed MRFO-based controller rejects the disturbance, and settles faster as compared to PSO-based controller. The regulatory controller response in L_1 and L_2 is shown in Fig. 11, and Fig. 12 shows the variations in manipulated variables F_1 and F_2 for the disturbance changes in L_1 and L_2 . Table 4 compares the values the ISE values of both the methods.

6 Conclusion

In this study, the TTH model is developed from the FPM and is linearized around the nominal steady-state values to obtain the transfer function model. A centralized PI controller has been developed for a TTH system based on the pseudo inverse of the steady-state gain matrix of a non-square process with two inputs and three outputs. The centralized controller based on the Davison method along with controller parameters φ and Ψ are tuned using optimization algorithms, viz., MRFO and PSO for a TTH system are designed. In comparison to a PSO-based controller, the MRFO-based controller exhibits less overshoot, settles more quickly, and gives a better response based on ISE values for both servo and regulatory disturbances. This type of centralized PI controller can be fused with smart controllers designed using deep learning to get better controller performance.

References

1. Garrido J, Vázquez F, Morilla F (2012) Centralized multivariable control by simplified decoupling. *J Process Control* 22(6):1044–1062. <https://doi.org/10.1016/j.jprocont.2012.04.008>
2. Majaaz VS, Thirunavukkarasu BI, Shanmuga Priya S (2015) Centralized controller tuning for MIMO process with time delay. In: 2015 International Conference on Renewable Energy Resources Applications ICRERA 2015, vol 5, pp 659–664. <https://doi.org/10.1109/ICRERA.2015.7418494>
3. Dhanya Ram V, Chidambaram M (2015) Simple method of designing centralized PI controllers for multivariable systems based on SSGM. *ISA Trans* 56:252–260. <https://doi.org/10.1016/j.isatra.2014.11.019>
4. Boeira E, Bordignon V, Eckhard D, Campestrini L (2018) Comparing MIMO process control methods on a pilot plant. *J Control Autom Electr Syst* 29(4):411–425. <https://doi.org/10.1007/s40313-018-0387-6>
5. Vijay Kumar V, Rao VSR, Chidambaram M (2012) Centralized PI controllers for interacting multivariable processes by synthesis method. *ISA Trans* 51(3):400–409. <https://doi.org/10.1016/j.isatra.2012.02.001>
6. Hariprasad K, Bhartiya S, Gudi RD (2012) A gap metric based multiple model approach for nonlinear switched systems. *J Process Control* 22(9):1743–1754. <https://doi.org/10.1016/j.jprocont.2012.07.005>
7. Kroll A, Schulte H (2014) Benchmark problems for nonlinear system identification and control using soft computing methods: need and overview. *Appl Soft Comput J* 25:496–513. <https://doi.org/10.1016/j.asoc.2014.08.034>
8. Branicky MS, Borkar VS, Mitter SK (1998) A unified framework for hybrid control: Model and optimal control theory. *IEEE Trans Automat Contr* 43(1):31–45. <https://doi.org/10.1109/9.654885>
9. Stursberg O (2004) A graph search algorithm. *Control* 1412–1417
10. Decarlo RA, Branicky MS, Pettersson S, Lennartson B (2000) Perspectives and results on the stability and stabilizability of hybrid systems. *Proc IEEE* 88(7):1069–1082. <https://doi.org/10.1109/5.871309>
11. Chang JW, Yu CC (1990) The relative gain for non-square multivariable systems. *Chem Eng Sci* 45(5):1309–1323. [https://doi.org/10.1016/0009-2509\(90\)87123-A](https://doi.org/10.1016/0009-2509(90)87123-A)
12. Davison EJ (2014) multivariable tuning regulators: the feedforward and robust control of a general servomechanism problem, *IEEE Trans Automat Control* 75(8):pp 457–461

13. Zhao W, Zhang Z, Wang L (2020) Manta ray foraging optimization: an effective bio-inspired optimizer for engineering applications. *Eng Appl Artif Intell* 87:103300. <https://doi.org/10.1016/j.engappai.2019.103300>
14. Clerc M (2010) Particle swarm optimization. *Part Swarm Optim* 1942–1948 <https://doi.org/10.1002/9780470612163>

Novel Systems for Utilization of Cold Energy of Liquefied Natural Gas at Regasification Terminal



Niteen R. Yeole

Abbreviations

W	Work
com	Compression
NG	Natural gas
pum	Pump

1 Introduction

The environmental pollution problems are responsible for climate change. The rising levels of CO₂ during the last decade are alarming. Carbon capture and storage are going to become important in the near future [1]. The power sector has contributed significantly to the release of harmful gases into the atmosphere [2]. The major challenge for a power sector is how to control the release of noxious compounds into the environment [3]. Natural gas (NG) is an environmentally friendly fuel. In India, part of it comes from liquefied natural gas (LNG). So the demand for LNG is increasing day by day [4, 5]. LNG is received at the LNG regasification terminal, transferred to the storage tanks, regasified to NG, and then sent to the end users. The operations at the LNG terminal are energy intensive [6]. Therefore, recovery of energy from hot/cold process streams may be necessary. The traditional methods of regasification use seawater as a source of heat. The cold energy of LNG is transferred to seawater, which goes back into the sea. Thus, cold energy is wasted without any energy recovery

N. R. Yeole (✉)

Chemical Engineering Department, School of Engineering, University of Petroleum and Energy Studies, Dehradun 248007, Uttarakhand, India

e-mail: nryeole@ddn.upes.ac.in

[7]. Hence, the search for alternative methods to recover LNG cold energy becomes very important from the energy utilization viewpoint. Various methods proposed are CO₂ capture, agro-food industry, air separation, floating storage regasification, etc. These are novel in nature. They possess the potential to improve process efficiency and exergy. In addition, they demonstrate required flexibility in case of varying demands of natural gas [5, 8–11]. The cold energy of LNG can also be utilized in liquid air energy storage through integration [12–14]. Present paper reviews such novel techniques along with analysis of variance (ANOVA) of data presented in one of the research articles using Microsoft Excel®.

2 Literature Review

Gao et al. [15] proposed two methods for the utilization of cold energy of LNG in the removal of hydrocarbons such as ethane, propane, and butane from LNG. One carried out at low pressure (1.5 MPa) was found to be more effective. The performance of each process was judged based on various parameters such as purity of methane in the natural gas stream, the calorific value of natural gas produced, production rates, power consumption, etc. Overall, the low-pressure process was found to be better than the high-pressure (4.5 MPa) one. The advantage of high-pressure process was its simplicity and compactness [15].

Mehrpooya et al. [16] proposed and analyzed the introduction of cold energy associated with LNG in an air separation process as shown in Fig. 1. The integration with air separation provides many benefits. Exchange of heat occurs in a very short time. Therefore, the start-up time reduces and the process becomes simple. In addition, exergy consumption decreases, production efficiency increases, and operating and construction cost decreases.

The LNG cold energy recovery helped reduce the required power for refrigeration from 2.9×10^6 kW to 2.69×10^4 kW for one column configuration. The extra electrical power required in a conventional process is saved due to the cold energy associated with LNG. The simulation results of Aspen HYSIS indicated lower energy consumption in comparison with the conventional process. The purity of products, liquid nitrogen, and oxygen was high [16]. Cao et al. [17] introduced a novel technique in the freeze desalination (FD) process with the objective of minimizing energy consumption. The process simulation was carried out using HYSYS software. The consumption of power in the LNG/FD process was quite negligible. Thus, the newer insight of utilizing cold energy associated with LNG in the area of FD was successful [17]. Zhao et al. [18] proposed a method for utilizing LNG cold energy for capturing carbon dioxide from exhaust gas, originating from the magnesite processing industry. The most important parameters investigated were LNG regasification pressure and CO₂ capture pressure. The authors studied the effect of these parameters on the

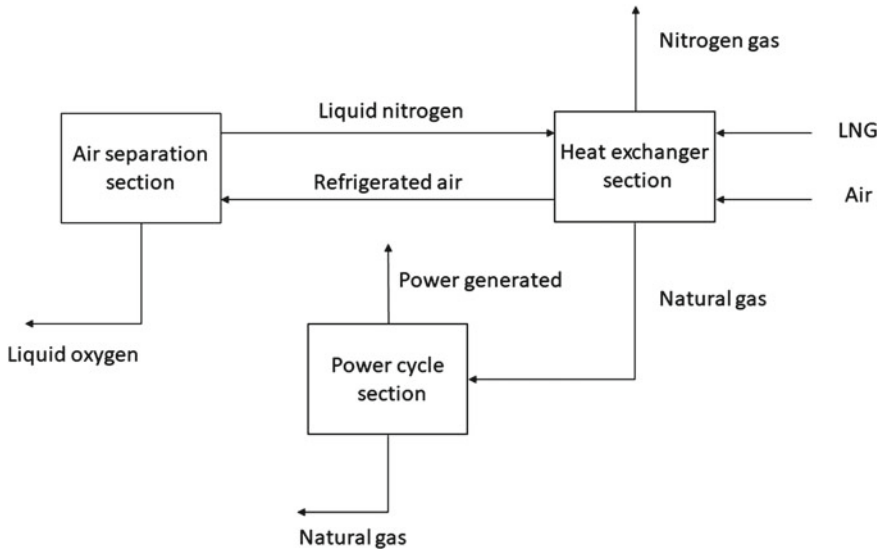


Fig. 1 Simplified block diagram of LNG cold energy utilization for cryogenic air separation [16]

performance of the system. A CO₂ utilization sub-system was proposed. Key parameters obtained were 1.0 MPa and 0.15 MPa as LNG regasification pressure and CO₂ capture pressure respectively [18]. Zhang et al. [19] suggested a new hybrid system. A combination of Liquid air energy storage (LAES) and organic Rankine cycle (ORC) was used. The benefits of the proposed system were stability and ease of implementation. Liu et al. [20] proposed a novel system for the capture of CO₂. The authors developed mathematical models and evaluated the performance of the system through the methods of energy and exergy. The key parameters chosen for the study were fuel utilization factor, turbine compression ratio, air-fuel ratio, and concentration of oxygen in the cathode feed.

Naveiro et al. [21] proposed a new system using steam as a heating medium in the regasification of LNG. It was found to be less harmful to the marine environment than seawater as a conventional heating medium. The system under study was the Floating Storage Regasification Unit (FSRU). However, it consumed fuel excessively. An integration of ORC with CO₂ capture gave rise to a novel system consisting of a closed loop, for FSRU. Monoethanolamine (MEA) solution was used as a solvent for capturing CO₂. Generated power met the requirement of the FSRU. Fuel consumption was found to be reduced in comparison with present closed-loop systems. Yin et al. [22] proposed a novel process to conserve energy on board, through the extraction of cold energy from LNG Boil-off Gas and regasified LNG. Pan et al. [23] presented a novel cascade integrated system for utilizing LNG cold energy for separating light hydrocarbons.

2.1 Case Study (Standalone Power Plant)

Yu et al. [3] investigated integration of LNG regasification with flue gas liquefaction in a stand-alone power plant as well as in a cogeneration system. In a stand-alone power plant, 100% of regasified LNG (RLNG) is used as fuel for combustion in an Allam cycle (AC), while in a cogeneration system, most of the RLNG is sent to the pipeline network for the end user and only a small portion is utilized as fuel for combustion in an AC.

Here a case study on a stand-alone power plant has been presented. A superstructure consisting of various possible flow diagrams was created and then optimized using the simulation tool, Aspen HYSIS V9. Two approaches for energy integration were studied. The first approach is the direct integration of Regasification of LNG with liquefaction of flue gas. The second approach is an indirect integration of Regasification of LNG with liquefaction of flue gas. The first approach involved an open rack vaporizer (ORV) with seawater as a heat source. The second approach involved an organic Rankine cycle (ORC) with some refrigerant as a heat source. The first approach was found to be fruitful for the stand-alone power plant, while the second approach was found to be fruitful for the cogeneration system. The power plants consisted of an AC with carbon capture and zero emission. The cost of electricity generation in an AC is lowest in comparison with other cycles [24]. Instead of air, oxygen is used in an AC for the combustion of fuel. CO_2 and H_2O are produced as flue gas. Cooling removes H_2O . Then CO_2 is liquefied and stored. Thus, carbon capture becomes easy as nitrogen is absent in the flue gas mixture [25]. For the transportation and storage of captured flue gas (CFG), there is a need to bring it to the desired pressure. This is possible in two ways. The first way is to use a compressor, while the second way is to liquefy and pump. In general, energy consumption in pumping a liquid is lower than that consumed in compressing a gas. In addition, the capital cost of a pump is lower than that of a compressor [26, 27]. The system based on the superstructure can be made more effective in a number of ways: (1) In order to reduce compression work, the LNG should be pumped to a greater pressure (2) Cold energy released should be used for flue gas liquefaction. An ORC can be used to integrate regasification and liquefaction. However, the regasification pressure depends on the amount of cold energy produced. The flue gas can't be entirely liquefied by the quantity of LNG cold energy released at 305 bar. The LNG regasification pressure needs to be lower than 305 bar in order to recover the maximum cold energy of LNG and then liquefy the flue gas completely. As a result, there is a trade-off between the compression of flue gas and LNG [3]. Present authors have proposed seven processes (A-G) with the objective of identifying the most efficient one. The process details along with flow diagrams given below.

Process A

It is a reference process without any integration. The process flow diagram is shown in Fig. 2. LNG is brought to high pressure of 305 bar through pumping. It flows through an open rack vaporizer (ORV) where it undergoes gasification to NG. Energy of

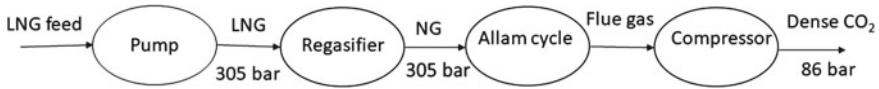


Fig. 2 Process A flow diagram (base case) [3]

seawater is used to vaporize LNG. NG is subjected to combustion in an Allam cycle. Flue gas is obtained. It is compressed to 86 bar. Here, the cold energy transferred to seawater is wasted due to the lack of integration with any other process.

Process B

It is the modification of Process A. The process flow diagram is shown in Fig. 3. LNG is pumped to a pressure below 305 bar. Then it is passed through an ORV where it undergoes complete regasification. Seawater is the heat source. Here, the cold energy of LNG is transferred to seawater. Regasified LNG, i.e., NG at a pressure < 305 bar is compressed to 305 bar and sent to an AC where the flue gas is produced because of combustion. A part of flue gas is recycled back to the combustor, while most of it acts as captured flue gas (CFG). Cold energy transferred to seawater is used to liquefy the CFG to the liquid phase, which is mainly liquid CO₂. Finally, it is pumped to 86 bar and stored. This process brings in an NG compressor and replaces a flue gas compressor with liquefied flue gas pump.

Process C

It is the modification of Process B. LNG feed pressure is increased to 305 bar. Therefore, a two-phase mixture of CO₂ is formed after the liquefaction of CFG. Figure 4 depicts the process flow diagram. A separator is used to separate gaseous CO₂. Liquefied CO₂ is pumped to 86 bar. A compressor is used to compress gaseous CO₂ to 86 bar. It is further mixed with liquefied CO₂ maintained at 86 bar.

Process D

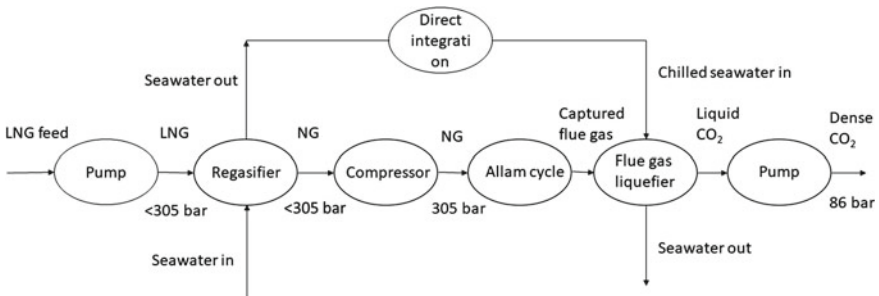


Fig. 3 Process B flow diagram [3]

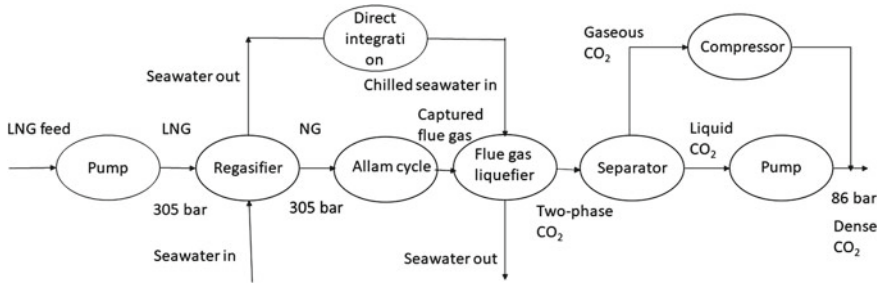


Fig. 4 Process C flow diagram [3]

Except for LNG feed pressure and the introduction of a compressor after regasifier, Process D is the same as Process C. Here, the LNG feed pressure is less than 305 bar. So a compressor is required to compress NG coming out from the regasifier to 305 bar.

Process E

It is the modification of Process B. An ORV is replaced by an organic Rankine cycle (ORC). Rest of the process is the same as Process B.

Process F

It is the slight modification of Process E as shown in Fig. 5. LNG feed pressure is increased to 305 bar. So NG at 305 bar is obtained after regasification. This eliminates the need for an NG compressor. It saves the capital cost of the NG compressor. However, CFG is partially liquefied. It gives a two-phase mixture of CO₂, needing a separator followed by a CO₂ compressor.

Process G

An adjustment to Process F lowers the LNG supply pressure to below 305 bar. It needs an NG compressor to take it to 305 bar. So it is added to Process F. Rest of the process is the same as Process F.

Both stand-alone power plant and cogeneration unit were found suitable for energy integration [3].

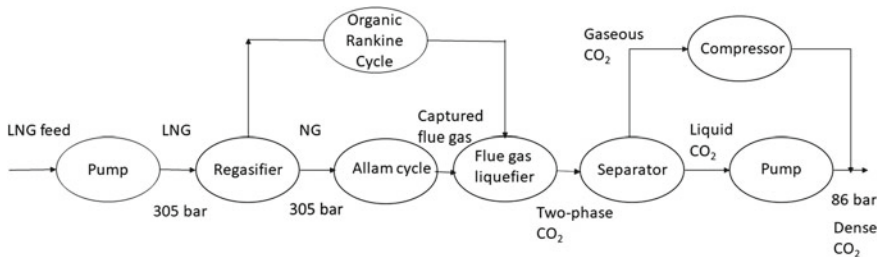


Fig. 5 Process F flow diagram [3]

Table 1 Summary of LNG cold energy utilization

Year	Author(s)	Application	References
2011	Gao et al.	Natural gas liquids (NGL) recovery	[15]
2015	Mehrpooya et al.	Cryogenic air separation	[16]
2015	Cao et al.	Sea water desalination	[17]
2016	Zhao et al.	CO ₂ capture from magnesite processing industry	[18]
2018	Zhang et al.	Liquid air energy storage (LAES)	[19]
2019	He et al.	Floating storage regasification unit (FSRU)	[28]
2019	Liu et al.	Combined cooling, heating and power system (CCHP)	[20]
2021	Yu et al.	Power generation	[3]
2022	Naveiro et al.	Floating storage regasification unit (FSRU)	[21]
2022	Huang et al.	Power generation	[10]
2022	Humayu et al.	Air separation	[9]

Table 1 summarizes various techniques for the utilization of LNG cold energy.

3 Data Analysis Through Analysis of Variance (ANOVA)

The impact of process variables on the response variable can be studied through analysis of variance (ANOVA). For verification of the results of any process, ANOVA can be used [29]. The data reported by Yu et al. [3] has been analyzed by the present author using Microsoft Excel®. The data reported by Yu et al. as shown in Tables 2 and 3 has been analyzed using ANOVA: Two-Factor Without Replication and ANOVA: Single Factor, respectively. The present author has generated additional Exergy% data considering $\pm 1\%$ error for single factor ANOVA as shown in Table 3.

Table 2 Shaft work required for various processes proposed by Yu et al. [3]

Process	W_{com}^{NG} kW	W_{pum}^{LNG} kW	W_{com}^{cap} kW	W_{pum}^{cap} kW	W_{tur}^{ORC} kW	W_{pum}^{ORC} kW
A	0	1415	2370	0	0	0
B	2499	537.8	0	290.1	0	0
C&D	0	1415	496.8	223.9	0	0
E	3223	393	0	290.1	1009	66.39
F&G	0	1415	706.6	194.4	733.8	28.79

Table 3 Exergy efficiency% obtained for various processes proposed by Yu et al. [3] along with data generated for $\pm 1\%$ error

Process	Exergy efficiency% [3]	Exergy efficiency% (+1% error)	Exergy efficiency% (-1% error)
A	72.96	73.69	72.23
B	76.15	76.91	75.39
C&D	78.03	78.81	77.25
E	77.73	78.51	76.95
F&G	80.68	81.49	79.87

4 Results and Discussions

The results of ANOVA performed on the data presented in Tables 2 and 3 along with discussions have been given below in Tables 4, 5, 6 and 7.

Table 4 shows that the average shaft work required is lowest for processes C&D, while it is highest for process E.

Table 4 Summary of ANOVA (Two or multiple factors without replication) for the data shown in Table 2

Summary	Count	Sum	Average	Variance
A	6	3785.00	630.83	1,046,284.00
B	6	3326.90	554.48	954,735.40
C&D	6	2135.70	355.95	307,792.80
E	6	4981.49	830.25	1,502,590.00
F&G	6	3078.59	513.09	299,794.40
W_{com}^{NG} kW	5	5722.00	1144.40	2,521,118.00
W_{pum}^{LNG} kW	5	5175.80	1035.16	273,142.90
W_{com}^{cap} kW	5	3573.40	714.68	952,289.10
W_{pum}^{cap} kW	5	998.50	199.70	14,209.54
W_{tur}^{ORC} kW	5	1742.80	348.56	237,268.30
W_{pump}^{ORC} kW	5	95.18	19.04	856.16

Table 5 F and P-value for summary of ANOVA as shown in Table 4

Source of variation	SS	df	MS	F	P-value	F crit
Rows	722,917.5	4	180,729.4	0.24	0.91	2.87
Columns	5,283,365	5	1,056,673	1.39	0.27	2.71
Error	15,272,620	20	763,631			
Total	21,278,902	29				

Table 6 Summary of ANOVA (single factor) for the data shown in Table 3

Groups	Count	Sum	Average	Variance
A	3	218.88	72.96	0.53
B	3	228.45	76.15	0.58
C&D	3	234.09	78.03	0.61
E	3	233.19	77.73	0.60
F&G	3	242.04	80.68	0.65

Table 7 F and P-value for summary of ANOVA as shown in Table 6

Source of variation	SS	df	MS	F	P-value	F crit
Between groups	96.3594	4	24.09	40.47	3.81E-06	3.48
Within groups	5.952376	10	0.59			
Total	102.3118	14				

Table 5 shows that the F value for rows (i.e., various processes) is less than F_{critical} value while P-value is greater than the alpha value of 0.05. Thus, it shows that there is no significant impact of the process on the required shaft work. However, looking at the data, this inference becomes unacceptable. Hence, ANOVA is performed for the same processes based on exergy% as shown in Table 3 and results presented in Tables 6 and 7.

Table 6 shows that processes C&D, E, and F&G show significant exergy%. Now looking at Table 7, the F value is greater than F_{critical} , while P-value is less than the alpha value of 0.05.

Thus, Table 7 indicates that at least one of the processes has a significant impact on the % exergy. The processes with significant positive impact are C&D, E, and F&G. Now comparing them with the results (average shaft work) given in Table 4, process C&D gives the optimum values of both shaft work required and average exergy%. Hence, process C&D must be chosen as the best process among all proposed processes for a stand-alone power plant. It matches the conclusion by Yu et al. [3]. Thus, the data analysis using Microsoft Excel is quite successful.

The results of ANOVA carried out by the present author have shown that the proposed processes C&D can be considered as the best process. Process C & D has a simple configuration. Their system performance is high. The main benefit is capital cost and system operation.

5 Novelty of the Study

The present paper highlights novel processes proposed by various researchers. Table 1 summarizes these processes. One of the novel processes is discussed below.

He et al. have demonstrated the novel concept of the Floating Storage Regasification Unit (FSRU) (Fig. 6) [28]. It is suitable for the area facing land issues. The available land /space is not sufficient to build an LNG regasification terminal. Hence, the marine area is utilized in constructing the terminal. The terminal is in a floating condition. It holds the LNG storage tanks. LNG ship is received at the terminal. Then LNG is transferred from the ship to the storage tanks. A warm coolant from a nearby floating data centre (FDC) is used to regasify LNG. As a result, NG is produced which is sent to the coastal area through the pipeline. Warm coolant loses its heat and becomes chilled. It is then used to cool the FDC, where the coolant liquid absorbs heat and becomes warm and recirculated through FSRU. Similarly, the air is circulated through FSRU to regasify LNG. As a result, the air becomes cold, which is sent to a nearby power generation unit. The use of cold air increases the efficiency of the power plant. Electricity generated is transferred to the coastal area through an electric line.

If the data center is located nearby FSRU, then ethylene glycol (EG) may be used as a coolant. Phase change materials (PCMs) may be a choice for data centers located far away [28].

Finally, the analysis of data by the present author, for optimum shaft work and exergy, using the ANOVA tool of Microsoft Excel, adds novelty to the study.

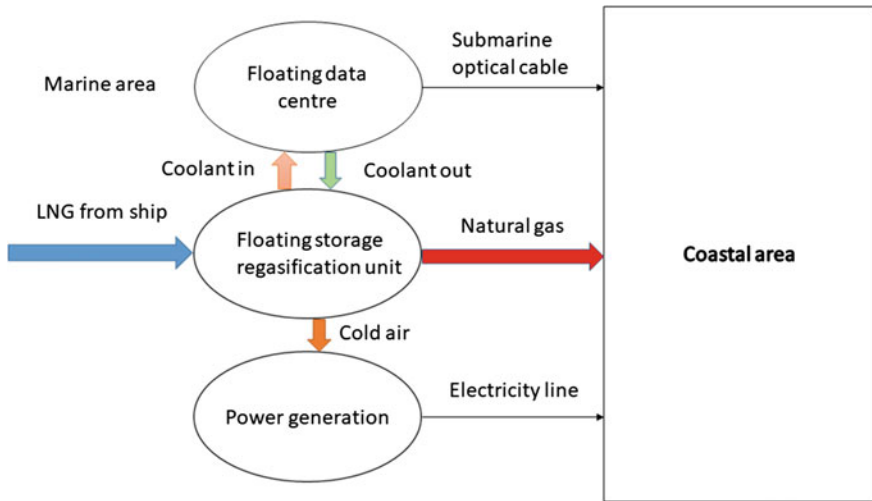


Fig. 6 Novel concept of LNG cold energy utilization at floating storage regasification unit (FSRU) [28]

6 Conclusion

LNG business is one of the fastest growing businesses. It is a source of clean energy. LNG is non-toxic It is odorless and non-corrosive. It is frequently used in a variety of industries. Major constituent of LNG is methane. It produces very little nitrogen oxide, nearly little sulfur oxide, and very little greenhouse gas emissions when combusted. The demand for gas is increasing day by day in India. There are plans to import additional LNG over the period of 10 years. This will create a huge amount of cold energy in the near future. Countries producing NG and countries importing NG are located far away from each other. Therefore, NG transport in the form of LNG is the only option. Moreover, it is feasible over a very long distance. This offers a chance to create eco-friendly technology that can use cold energy at the receiving end. In order to improve the energy efficiency of LNG regasification terminals and the financial advantages of the LNG supply chain, a significant amount of the cold energy that is stored in LNG should be recovered and used.

The conventional methods of using seawater for LNG regasification result in a huge loss of cold energy. Hence, the search for novel systems of LNG regasification with complete recovery of its cold energy is gaining the attention of researchers. Thus, the novel areas where cold energy of LNG can be utilized are cold storage, waste incineration, air separation, desalination, cryogenic CO₂ capture, and power generation. In addition, other areas such as natural gas processing and the boil-off process can also utilize the LNG cold energy.

The data analysis tool of Microsoft Excel has helped analyze literature data related to various processes. These processes provide various options for integrating LNG regasification with liquefaction of captured flue gas for a stand-alone power plant. ANOVA helped choose the optimum process based on shaft work and exergy. The conclusions from the results of ANOVA have been found to be matching with the article's conclusions.

Most of the novel processes have been studied through simulations. Hence, their implementation at the LNG regasification terminal will be a great challenge in the near future. Further studies will be required to overcome these challenges.

References

1. Selosse S, Ricci O (2017) Carbon capture and storage: lessons from a storage potential and localization analysis. *Appl Energy* 188:32–44 (2017). <https://doi.org/10.1016/j.apenergy.2016.11.117>
2. Akorede MF, Hizam H, Ab Kadir MZA, Aris I, Buba SD (2012) Mitigating the anthropogenic global warming in the electric power industry. *Renew Sustain Energy Rev* 16:2747–2761 (2012). <https://doi.org/10.1016/j.rser.2012.02.037>
3. Yu H, Gundersen T, Gençer E (2021) Optimal liquified natural gas (LNG) cold energy utilization in an Allam cycle power plant with carbon capture and storage. *Energy Convers Manage* 228:113725. <https://doi.org/10.1016/j.enconman.2020.113725>

4. Kumar S, Kwon HT, Choi KH, Lim W, Cho JH, Tak K, Moon I (2011) LNG: an eco-friendly cryogenic fuel for sustainable development. *Appl Energy* 88:4264–4273. <https://doi.org/10.1016/j.apenergy.2011.06.035>
5. Gómez MR, Garcia RF, Gómez JR, Carril JC (2014) Thermodynamic analysis of a Brayton cycle and Rankine cycle arranged in series exploiting the cold exergy of LNG (liquefied natural gas). *Energy* 66:927–937. <https://doi.org/10.1016/j.energy.2013.12.036>
6. Khan MS, Wood DA, Qyum MA, Ansari KB, Ali W, Wazwaz A, Dutta A (2022) Graphical approach for estimating and minimizing boil-off gas and compression energy consumption in LNG regasification terminals. *J Nat Gas Sci Eng* 101:104539 (2022). <https://doi.org/10.1016/j.jngse.2022.104539>
7. Xue F, Chen Y, Ju Y (2016) A review of cryogenic power generation cycles with liquefied natural gas cold energy utilization. *Front Energy* 10:363–374. <https://doi.org/10.1007/s11708-016-0397-7>
8. Tuinier MJ, Hamers HP, Van Sint Annaland M (2011) Techno-economic evaluation of cryogenic CO₂ capture—a comparison with absorption and membrane technology. *Int J Greenh Gas Control* 5:1559–1565. <https://doi.org/10.1016/j.ijggc.2011.08.013>
9. Hamayun MH, Ramzan N, Hussain M, Faheem M (2022) Conventional and advanced exergy analyses of an integrated LNG regasification-air separation process. *Ind Eng Chem Res* 61:2843–2853. <https://doi.org/10.1021/acs.iecr.1c03730>
10. Huang ZF, Wan YD, Soh KY, Islam MR, Chua KJ (2022) Off-design and flexibility analyses of combined cooling and power based liquefied natural gas (LNG) cold energy utilization system under fluctuating regasification rates. *Appl Energy* 310:118529 (2022). <https://doi.org/10.1016/j.apenergy.2022.118529>
11. Domingues A, Matos HA, Pereira PM (2022) Novel integrated system of LNG regasification/electricity generation based on a cascaded two-stage Rankine cycle, with ternary mixtures as working fluids and seawater as hot utility. *Energy* 238:121972. <https://doi.org/10.1016/j.energy.2021.121972>
12. Ding Y, Li Y, Tong L, Wang L (2022) 10—Liquid air energy storage. <https://doi.org/10.1016/B978-0-12-824510-1.00014-3>
13. Peng X, She X, Nie B, Li C, Li Y, Ding Y (2019) ScienceDirect liquid air energy storage with LNG cold recovery for air liquefaction improvement air energy storage with LNG cold recovery for air liquefaction improvement Li heat assessing the feasibility of using the temperature for a long. *Energy Proc.* 158:4759–4764. <https://doi.org/10.1016/j.egypro.2019.01.724>
14. She X, Zhang T, Cong L, Peng X, Li C, Luo Y (2019) Flexible integration of liquid air energy storage with liquefied natural gas regasification for power generation enhancement. *Appl Energy* 251:113355 (2019). <https://doi.org/10.1016/j.apenergy.2019.113355>
15. Gao T, Lin W, Gu A (2011) Improved processes of light hydrocarbon separation from LNG with its cryogenic energy utilized. *Energy Convers Manage* 52:2401–2404. <https://doi.org/10.1016/j.enconman.2010.12.040>
16. Mehrpooya M, Sharifzadeh MMM, Rosen MA (2015) Optimum design and exergy analysis of a novel cryogenic air separation process with LNG (liquefied natural gas) cold energy utilization. *Energy* 90:2047–2069. <https://doi.org/10.1016/j.energy.2015.07.101>
17. Cao W, Beggs C, Mujtaba IM (2015) Theoretical approach of freeze seawater desalination on flake ice maker utilizing LNG cold energy. *DES* 355:22–32. <https://doi.org/10.1016/j.desal.2014.09.034>
18. Zhao L, Dong H, Tang J, Cai J (2016) Cold energy utilization of liquefied natural gas for capturing carbon dioxide in the flue gas from the magnesite processing industry. *Energy* 105:45–56. <https://doi.org/10.1016/j.energy.2015.08.110>
19. Zhang T, Chen L, Zhang X, Mei S, Xue X (2018) Thermodynamic analysis of a novel hybrid liquid air energy storage system based on the utilization of LNG cold energy. *Energy* 155:641–650. <https://doi.org/10.1016/j.energy.2018.05.041>
20. Liu Y, Han J, You H (2019) ScienceDirect Performance analysis of a CCHP system based on SOFC/GT/CO₂ cycle and ORC with LNG cold energy utilization. *Int J Hydrogen Energy* 44:29700–29710. <https://doi.org/10.1016/j.ijhydene.2019.02.201>

21. Naveiro M, Romero Gómez M, Arias-Fernández I, Baaliña Insua Á (2022) Thermodynamic and environmental analyses of a novel closed loop regasification system integrating ORC and CO₂ capture in floating storage regasification units. *Energy Convers Manage* 257:115410. <https://doi.org/10.1016/j.enconman.2022.115410>
22. Yin L, Qi M, Ju Y, Moon I (2022) Advanced design and analysis of BOG treatment process in LNG fueled ship combined with cold energy utilization from LNG gasification. *Int J Refrig* 135:231–242. <https://doi.org/10.1016/j.ijrefrig.2021.12.004>
23. Pan J, Li M, Li R, Tang L, Bai J (2022) Design and analysis of LNG cold energy cascade utilization system integrating light hydrocarbon separation, organic Rankine cycle and direct cooling. *Appl Therm Eng* 213:118672. <https://doi.org/10.1016/j.applthermaleng.2022.118672>
24. Sanz W, Jericha H, Moser MFK, Heitmeir F (2004) Thermodynamic and economic investigation of an improved graz cycle power plant for CO₂ capture. *J Eng Gas Turb Power Trans ASME* 127:765–772
25. Allam R, Martin S, Forrest B, Fetvedt J, Lu X, Freed D, Brown GW, Sasaki T, Itoh M, Manning J (2017) Demonstration of the Allam cycle: an update on the development status of a high efficiency supercritical carbon dioxide power process employing full carbon capture. *Energy Proc* 114:5948–5966. <https://doi.org/10.1016/j.egypro.2017.03.1731>
26. Romeo LM, Lara Y, González A (2011) Reducing energy penalties in carbon capture with organic Rankine cycles. *Appl Therm Eng* 31:2928–2935. <https://doi.org/10.1016/j.applthermaleng.2011.05.022>
27. Baldwin P, Williams J (2009) Capturing CO₂: gas compression vs liquefaction. *Power* 153:68–71
28. He T, Rong Z, Zheng J, Ju Y, Linga P (2019) LNG cold energy utilization: prospects and challenges. *Energy* 170:557–568. <https://doi.org/10.1016/j.energy.2018.12.170>
29. Yeole NR, Parthasarthy V (2022) Design of experiments (DOE) for adsorptive desulfurization (ADS) of liquid fuels—a review. *Mater Today Proc* 57:1613–1618. <https://doi.org/10.1016/j.matpr.2021.12.230>

Ionic Mass Transfer in Electrolyte–Kerosene Flow Systems



K. Ashok Kumar, G. V. S. Sarma, and K. V. Ramesh

Notation

A	Area of reacting surface, m ²
C _o	Concentration of reacting ion, kmol/m ³
D _c	Circular conduit diameter, m
d _p	Particle diameter, m
F	Faraday constant, C/g·eq
i _L	Limiting current, A
k _L	Mass transfer coefficient, m/s
n	Number of electrons participated in the reaction
U _c	Continuous phase velocity, m/s
U _d	Dispersed phase velocity, m/s
U _g	Superficial gas velocity, m/s
X	Axial variation, m

Greek Symbols

ρ _c	Density of electrolyte, kg/m ³
μ _c	Viscosity of electrolyte, Pa·s

K. A. Kumar · G. V. S. Sarma (✉) · K. V. Ramesh
Department of Chemical Engineering, Andhra University, Visakhapatnam 530003, Andhra Pradesh, India
e-mail: gvssarma@gmail.com

© The Author(s), under exclusive license to Springer Nature Singapore Pte Ltd. 2023
E. Chinthapudi et al. (eds.), *Sustainable Chemical, Mineral and Material Processing*,
Lecture Notes in Mechanical Engineering,
https://doi.org/10.1007/978-981-19-7264-5_7

Dimensionless Groups

$$\text{Re}_p \quad \text{Particle Reynolds number} = \frac{\rho_c d_p U_c}{\mu_c}$$

$$\text{Re}_c \quad \text{Reynolds number} = \frac{\rho_c D_c U_c}{\mu_c}$$

$$\text{St} \quad \text{Stanton number} = \frac{k_L}{U_c}$$

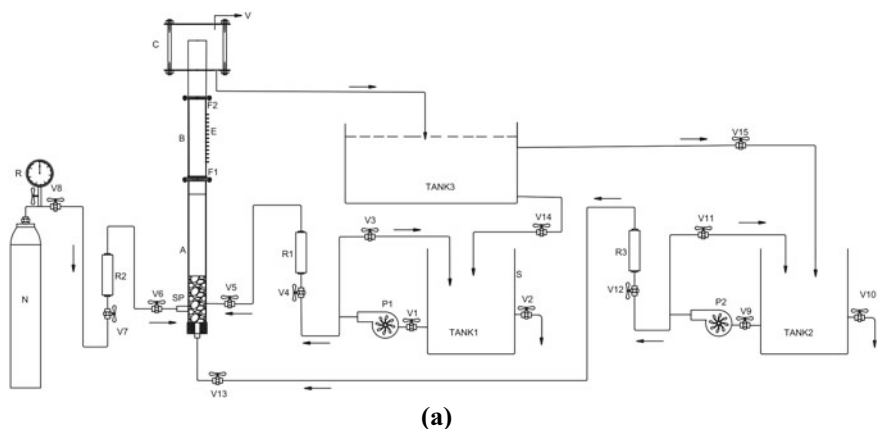
1 Introduction

An emphasis on the importance of the liquid–liquid flow phenomenon in process industries is the subject of technical interest in recent years. The phenomenon is very much concerned with unit operations like extraction, oil–water transport, liquid–liquid reactions, and separation processes. On many occasions, the transfer of heat or mass takes place from wall to liquid or vice versa. Such situations are widely prevalent in unit operations and processes like extraction, leaching, condensation, sublimation, dissolution, electrowinning, electrodeposition, electrorefining, metal extraction from ores, etc. By examining the relevant literature, it is observed that a vast majority of the reported studies focused mainly on the identification of flow patterns and their transition [1–5], and a few studies aimed at phase inversion [6] and drag reduction [7]. To the best knowledge of the authors, studies conducted on ionic mass transfer due to admitting another inert and immiscible liquid phase into the homogeneous flow of electrolyte were found to be scarce [8, 9]. The present study deals with electrochemical mass transfer between a liquid and wall under diffusion control, and also the effects of pertinent parameters on mass transfer coefficient have been evaluated. In the continuous phase, an electrolyte belonging to the ferri-ferro redox system is employed. Kerosene is employed as a dispersed phase. A limiting current technique is used for obtaining mass transfer coefficient. Details of the limiting current technique are presented by Harvind Kumar et al. [10]. The mass transfer coefficients were computed from the measured limiting current data using the equation derived by Lin et al. [11] and given as

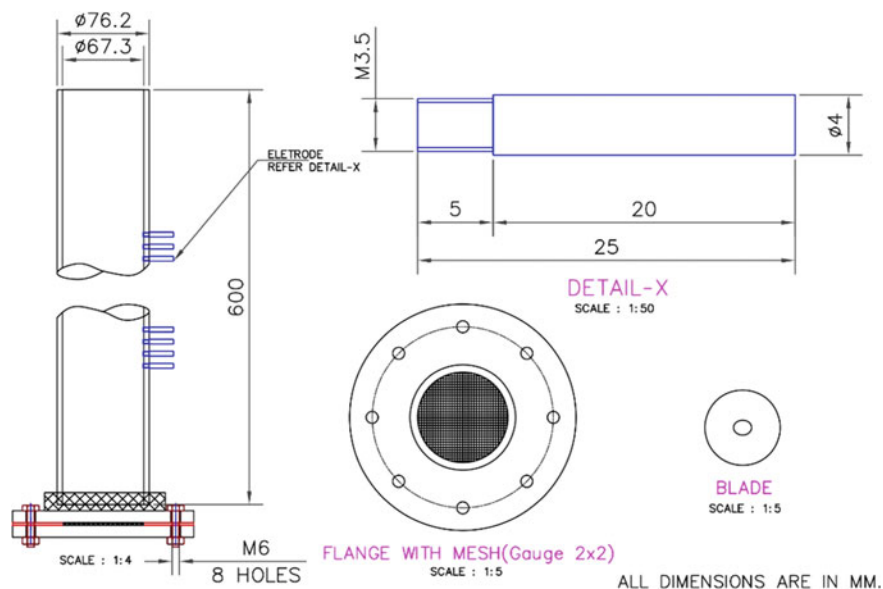
$$k_L = \frac{i_L}{nAFC_o} \quad (1)$$

2 Experimental

The aim of the present investigation is to obtain the mass transfer coefficient at the inner wall of the outer cylinder of the electrochemical reactor. The schematic of the experimental setup used in the present investigation is shown in Fig. 1a.



(a)



(b)

Fig. 1 a Schematic of the experimental setup. A—calming section; B—test section; C—exit section; E—electrodes; F1, F2—Flanges; N—nitrogen gas cylinder; P1, P2—pumps; R—gas regulator; R1 to R3—rotameters; V—vent; V1 to V15—valves. b Mechanical details of test section

In this unit, pumps are used for circulating kerosene and electrolyte. Rotameters are employed for the measurement of flow rates of kerosene, electrolyte, and nitrogen gas. Valves are used for regulating and controlling flow rates. Nitrogen was used as an inert gas. Glass balls were used as inert fluidizing solids. Arrangement of electrodes as shown in Fig. 1b has been done with extreme care so that one end of the electrode is in line with the inner surface of the test section. The other end is connected to

the external electric circuit that facilitated the measurement of limiting current. The diameter of each electrode is 3.5 mm. Electrodes, 32 in number, were arranged in line in the test section and the center-to-center distance between two neighboring electrodes is maintained as 1 cm. A stainless steel wire mesh, placed at the bottom of the test section, served as a fluid distributor and also acted as a supporter to the fluidizing solids, further facilitating the uniform distribution of gas, electrolyte, and kerosene.

3 Results and Discussion

In order to know the longitudinal variation of limiting current in the liquid–liquid flow system, initially limiting currents were measured at each of the 32 electrodes. The plot of these data for a fixed kerosene velocity of 0.02811 m/s is shown in Fig. 2. The plot revealed that there is no longitudinal variation in the limiting current values along the test section. Therefore, all the 32 electrodes were combined and shorted, and limiting current data at this combined electrode were obtained for all subsequent runs.

Similar studies were conducted with the gas–liquid–liquid flow, liquid–liquid–solid fluidized bed, and gas–liquid–liquid–solid fluidized bed flow systems. For all these cases, there is no significant variation of limiting current in the longitudinal direction. Hence, for all these cases also, all 32 electrodes were shorted and limiting current of the combined electrode is measured. In the following discussion, some abbreviations were used that denote the flow systems. These abbreviations are presented here as

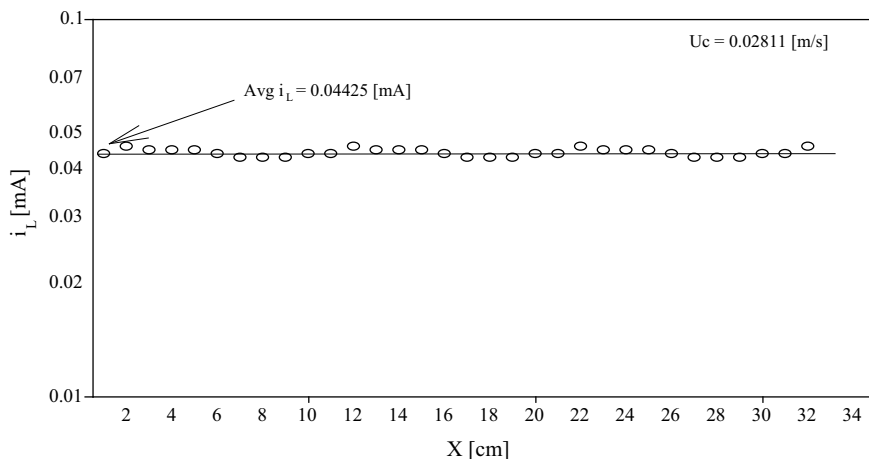


Fig. 2 Graph showing axial variation of limiting current in liquid–liquid flow

- LL: Liquid–Liquid flow system
- LLS: Liquid–Liquid–Solid fluidized bed
- LLG: Liquid–Liquid–Gas flow system
- LLGS: Liquid–Liquid–Gas–Solid fluidized bed

3.1 Effect of Velocity of Continuous Phase

The variation in mass transfer coefficient data obtained for the case of a constant velocity of the dispersed phase, i.e., kerosene, which is maintained at 0.00937 m/s, was drawn and plotted against varying continuous phase velocities, i.e., electrolyte. Plots of these data were obtained for four flow systems and shown in Fig. 3. The plot corresponding to the liquid–liquid flow system reveals that the mass transfer coefficient increased slightly with an increase in continuous phase velocity. The reason can be attributed to the increased turbulence due to the increase in the velocity of the electrolyte. The addition of gas flow to this system makes it into a liquid–liquid–gas (LLG) flow system. By fixing the gas velocity at a constant value of 0.014 m/s, the resulting plot obtained between the mass transfer coefficient and continuous phase velocity at the same dispersed phase velocity is also shown in the same figure. It can be noticed from this plot that the mass transfer coefficient very slightly increased with an increase in continuous phase velocity. The reason for this slight increase can be explained in the following way. Due to the addition of gas flow to the already existing liquid–liquid flow, the turbulence got nearly higher, and the increase in continuous phase velocity could add only very little to the total turbulence existing in the system. Therefore, only a slight increase in the mass transfer coefficient is noticed. The data corresponding to the liquid–liquid–solid fluidized bed system are also plotted in the same figure. This plot reveals that there is no variation in the mass transfer coefficient with continuous phase velocity. The reason can be attributed to the severe churning action resulted due to particulate fluidization, and variation in continuous phase velocity could not add any additional turbulence to the total turbulence of the system. This is due to the formation of an emulsion by the immiscible mixture of electrolyte and kerosene which in turn appears as a thick film on the electrode surface. Hence, there is no variation in mass transfer coefficient with electrolyte velocity. In order to know the behavior in the liquid–liquid–gas–solid system, gas flow is added to the LLS system and the resulting plot is also shown in the graph. Here also, it can be observed that the mass transfer coefficient remained constant with variation in electrolyte velocity. From the comparison of the mass transfer coefficient data obtained in all these flow systems, one can observe that all the points in this graph are bounded between 4.37×10^{-6} and 5.07×10^{-6} m/s with a mean value of 4.72×10^{-6} m/s. The points got distributed with a mean value of $\pm 8.0\%$.

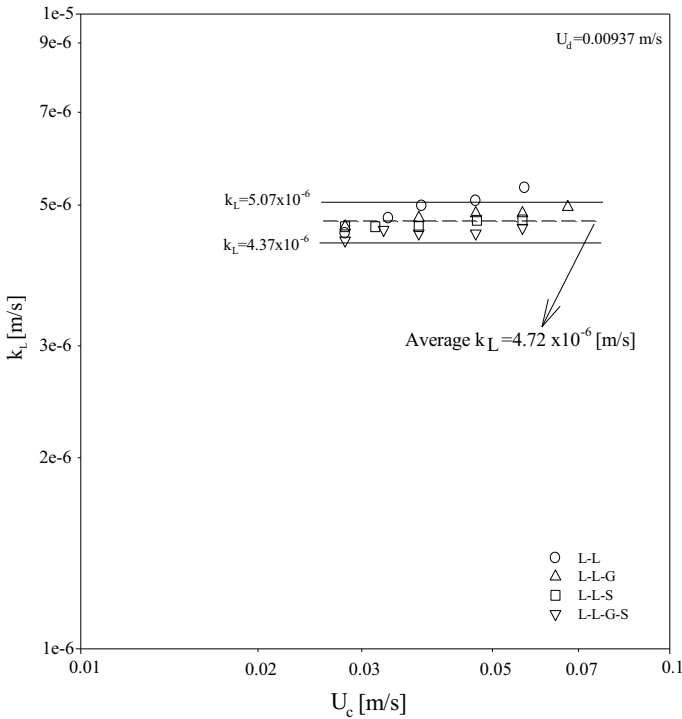


Fig. 3 Effect of continuous phase velocity

3.2 Effect of Velocity of Dispersed Phase

A similar graph was drawn for mass transfer coefficient against dispersed phase velocity and shown in Fig. 4. A close examination of the plots of these figures also reveals similar trends with entire data distributed between 4.62×10^{-6} and 5.28×10^{-6} m/s with a mean value of 4.95×10^{-6} m/s with a mean deviation of $\pm 7.1\%$. One can reason that the variation in dispersed phase velocity could not contribute significantly to total turbulence and hence there is not much noticeable variation of mass transfer coefficient with dispersed phase velocity.

3.3 Effect of Velocity of Gas

From Fig. 5, it can be noticed that the data for both the systems LLG and LLGS are nearly the same, and the addition of fluidizing solids to the LLG system has not yielded any augmentation.

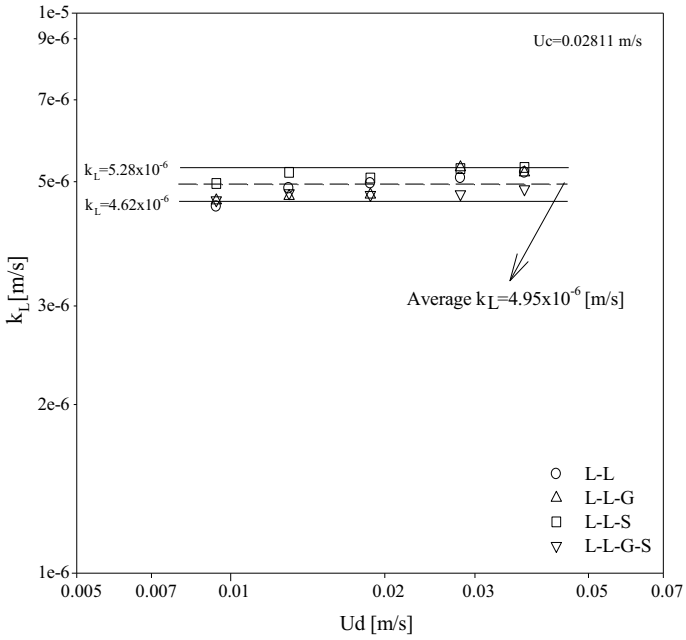


Fig. 4 Effect of dispersed phase velocity

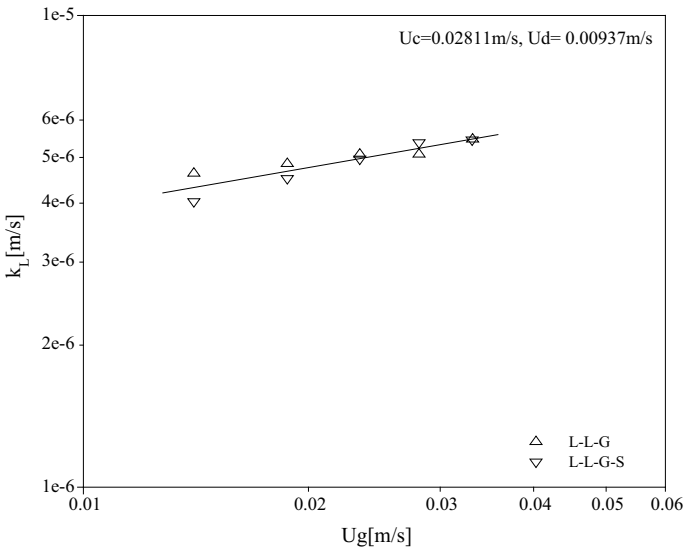


Fig. 5 Effect of gas velocity

Table 1 Correlations obtained for the present data

Flow systems	Correlations	% deviation		Eq. No.
		Avg.	Std.	
LL	$St = 0.0795Re_C^{-0.79} \left(\frac{U_d}{U_c}\right)^{0.085}$	2.68	3.56	(2)
LLG	$St = 0.0348Re_C^{-0.66} \left(\frac{U_d}{U_c}\right)^{0.092} \left(\frac{U_g}{U_c}\right)^{0.18}$	2.04	2.52	(3)
LLS	$St = 0.0158Re_p^{-1.008} \left(\frac{U_d}{U_c}\right)^{0.019}$	4.12	4.85	(4)
LLGS	$St = 0.0115Re_p^{-0.94} \left(\frac{U_d}{U_c}\right)^{-0.013} \left(\frac{U_g}{U_c}\right)^{0.055}$	4.52	5.47	(5)

3.4 Correlations

Correlations were obtained for the present data on mass transfer coefficient for all these flow systems expressed as Stanton number as a function of Reynolds number and velocity ratios. Using least squares regression analysis, the correlation equations obtained are shown in the following Table 1.

The calculated and experimental Stanton number values according to these recommended equations are plotted and shown in Fig. 6.

From Sects. 3.1 and 3.2, it can be understood that the spread of the mass transfer coefficient data is limited and stood within $\pm 8.0\%$. Further, it can be seen from the plots of various graphs from these sections that the studied variables viz., the velocities of the continuous phase, dispersed phase, and gas had only a very small effect on the mass transfer coefficient. Therefore, the data were analyzed using a dot diagram and are presented in Fig. 7.

It can be read from Fig. 7 that the mean value of mass transfer coefficient was around 4.81×10^{-6} m/s for the three flow systems viz., liquid–liquid–gas, liquid–liquid–solid, and liquid–liquid–gas–solid, whereas for the liquid–liquid system the mean value was found to be 4.921×10^{-6} m/s. In order to know the frequency of occurrence of the data, a histogram has been drawn and shown in Fig. 8. The histogram also supports these values.

In the order known to the symmetry of the distribution of mass transfer coefficient data, a box plot was drawn and is presented in Fig. 9. Examination of the box plot also shows that the data were spread over a small range from the mean value which can be taken as 4.83×10^{-6} m/s.

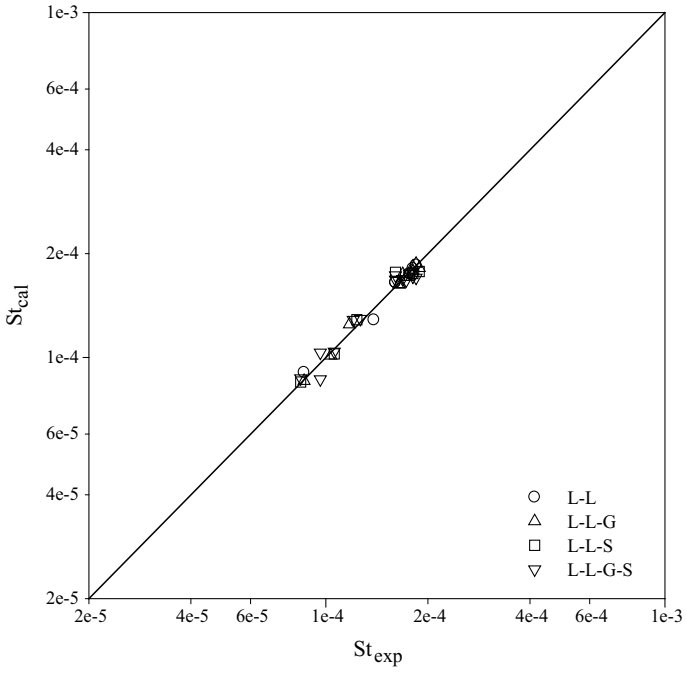


Fig. 6 Comparison of experimental and calculated Stanton number values

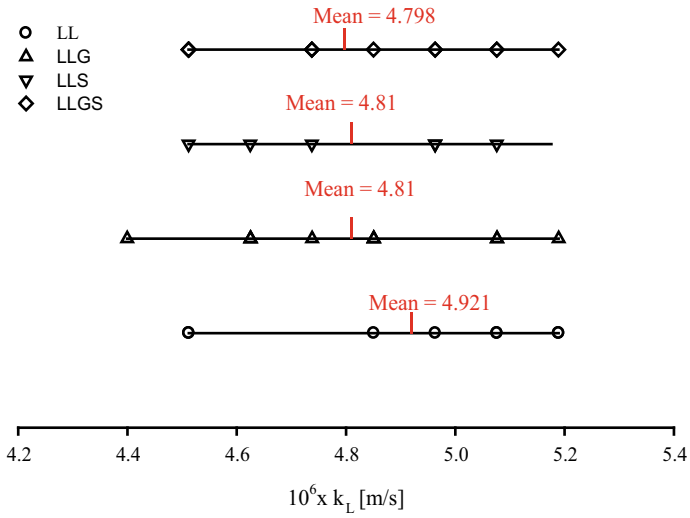


Fig. 7 Dot diagram for the mass transfer coefficient data

Fig. 8 Histogram for entire mass transfer coefficient data (for all systems: LL, LLG, LLS, and LLGS)

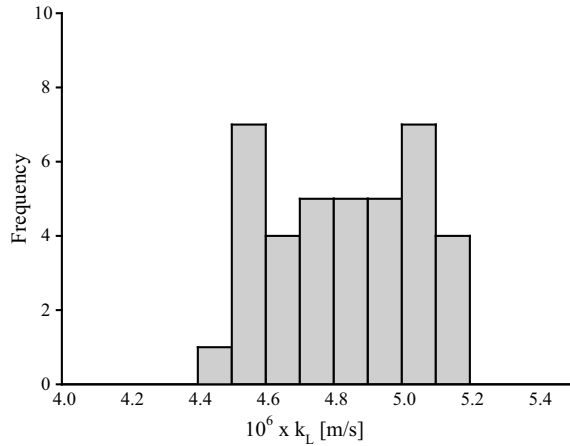
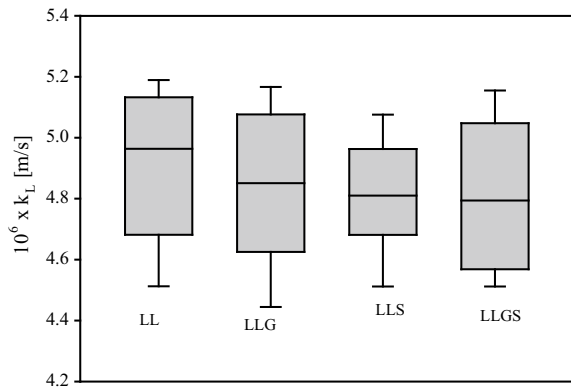


Fig. 9 Box plot for entire mass transfer coefficient data (for all systems: LL, LLG, LLS, and LLGS)



4 Conclusions

The present study revealed some interesting observations regarding mass transfer coefficient behavior in liquid–liquid flow systems. The conclusions drawn from the present study have been presented here as follows:

- The mass transfer coefficient obtained in the present case with different flow systems exhibited a narrow spread from the mean value, and the deviation was within $\pm 8.0\%$.
- The changes in dynamic variables such as continuous phase velocity, dispersed phase velocity, and gas phase velocity could not affect the mass transfer coefficient significantly.
- The addition of different phases such as gas, fluidizing solids, or both had not yielded any noticeable enhancement to the mass transfer coefficient.

- In the case of liquid–liquid and gas–liquid–liquid flow systems, correlation equations are obtained between the Stanton number and Reynolds number based on continuous phase velocity.
- For systems involving fluidizing particles, the correlations consisted of Stanton number and particle Reynolds number.

References

1. Chinaud M, Park KH, Angeli P (2017) Flow pattern transition in liquid-liquid flows with a transverse cylinder. *Int J Multiph Flow* 90:1–12
2. Park KH, Chinaud M, Angeli P (2016) Transition from stratified to non-stratified oil–water flows using a bluff body. *Exp Therm Fluid Sci* 76:175–184
3. Jana AK, Das G, Das PK (2006) Flow regime identification of two-phase liquid–liquid upflow through vertical pipe. *Chem Eng Sci* 61:1500–1515
4. Morgan RG, Markides CN, Hale CP, Hewitt GF (2012) Horizontal liquid–liquid flow characteristics at low superficial velocities using laser-induced fluorescence. *Int J Multiph Flow* 43:101–117
5. Sunder Raj T, Chakrabarti DP, Das G (2005) Liquid-liquid stratified flow through horizontal conduits. *Chem Eng Technol* 28(8):899–907
6. Ioannou K, Nydal OJ, Angeli P (2005) Phase inversion in dispersed liquid–liquid flows. *Exp Therm Fluid Sci* 29:331–339
7. Angeli P, Hewitt GF (1998) Pressure gradient in horizontal liquid-liquid flows. *Int J Multiph Flow* 24:1183–1203
8. Ashok Kumar K (2021) Liquid-wall mass transfer in non-conventional flow systems. PhD thesis, Andhra University, Visakhapatnam, India
9. Ramesh KV, Sarma GVS, Ashok Kumar K (2020) Wall-liquid mass transfer in liquid-liquid flow systems. Paper presented in AIChE spring meeting, Houston, TX, USA, Aug
10. Harvind Kumar R, Ramesh KV, Sarma GVS, Raju GMJ (2011) Mass transfer at the confining wall of helically coiled circular tubes in the absence and presence of packed solids. *Int Commun Heat Mass Transf* 38:319–323
11. Lin CS, Denton EB, Gaskill HS, Putan CL (1951) Diffusion controlled electrode reactions. *Ind Eng Chem* 43:2136–2413

Application of Epoxidized Vegetable Oil for Improving Rheological Properties of Crude Oil



Biswadeep Pal, Sampa Guin, and Tarun Kumar Naiya

1 Introduction

In the colder region, the petroleum industry is experiencing wax deposition problems in reservoirs, wellbores, surface facilities, and transportation in pipelines [1]. The petroleum industry spent billions of dollars for mitigating the wax deposition and associated problems in terms of the cost of heating and chemicals required for prevention and control, use of scrappers for preventing chock in pipelines, and stopping of production [2]. Several kinds of research have been carried, out and there are different remedial methods available for controlling wax deposition in pipelines. Crude oils are a mixture of complex hydrocarbon compounds which consist of more than 20 carbon numbers attached with different non-metals like sulfur, nitrogen, etc. There are different wax deposition mitigation techniques (mechanical, thermal, electrical, and chemical methods) commonly applied for flow assurance problems. Among them, chemical additives more specifically bio-additives are now widely accepted to solve this problem due to low production and operating costs [3].

Crude oil is a naturally occurring fossil fuel containing a mixture of hydrocarbons, namely paraffin, resins, aromatics, asphaltenes, etc. [4]. This long-chain paraffin gets dissolved in crude oil at a higher temperature. Below wax appearance temperature (WAT), wax particles are interlocking together and form large wax crystals which are separated from crude oil due to the action of gravity and precipitated at the bottom of the pipeline [5]. The pour point of the crude oil depends on the constituents of the crude oil like paraffin, asphaltene, and resin. The melting point of the paraffin wax is dependent on the molar mass of the paraffin; the higher the molar mass, the higher is the melting point [6, 7]. The melting point of the paraffin wax is also dependent on the

B. Pal · S. Guin · T. K. Naiya (✉)

Department of Petroleum Engineering, Indian Institute of Technology (Indian School of Mines),
Dhanbad 826004, Jharkhand, India

e-mail: tarunnaiya@iitism.ac.in

structure of the paraffin wax, linear wax melt at a higher temperature in comparison to that of branched with the same number of carbon atoms [8, 9].

As a result, the pour point of crude oil increases, and rheological properties such as viscosity, yield stress, and viscoelastic properties are greatly changed [10]. Recent studies concentrate on the synthesis of bio-based additives in which the structure and morphology of wax particles are changed with the interaction of these PPDs.

The use of pour point depressants, wax inhibitors, drag reducers, additives, and viscosity reducers all are considered in the use of the chemical method [11–13]. Other methods include microbial methods by use of different microbes and hot oil methods to reduce the viscosity [14, 15]. Different aliphatic solvents like kerosene or diesel with toluene or xylene are the efficient chemical solvents used for depression of pour point. The chemical methods is the most cost-effective and required very less quantity of sample. However, most commercial flow improvers are polymeric and toxic. So that, industries are more rely on naturally derived chemical additives which are bio-degradable and non-toxic in nature [12, 16]. Naturally derived bio-additives offer good efficiency as well as cutting operating cost significantly. Bio-additives are made from naturally derived resources to handle wax deposition problems. Recently, Fadairo et al. used sunflower-based biodiesel for improving rheological properties of Nigerian waxy crude oil [1]. Akinyemi et al. (2016) used plant seed oil as a flow improver of Nigerian waxy crude oil. Jatropha oil, Coconut oil, Canola oil, and Sunflower oil are already coming into play in the flow assurance of crude oil [11]. Besides, different plant-derived surfactant comes into play due to their saponin property like soapnut, *madhuka logiferra*, etc.

In this work, vegetable oil-based epoxidized additive was prepared by esterification, and its effectiveness was studied with two different types of crude oils. Additionally, vegetable oil-based bio-additives were characterized by Fourier transform electron spectroscopy (FTIR), and the performance has been measured with the help of pour point measurement. The structural properties of crude oil have been observed with the help of microscopic studies. Further, a rheological study was investigated to check the efficiency of bio-additives after the addition of crude oil.

2 Material and Methods

2.1 Materials

The crude oil was procured from ONGC Ahmadabad Asset, Gujrat, India. n-heptane, n-pentane, n-haxane, and toluene were purchased from Ramkin Chemical, India. Acetonitrile (AR grade), chloroform (AR grade), and methanol (LR grade) were procured from Merck Life Science Pvt Ltd., India. For the epoxidation process, Formic Acid, Sodium Chloride, Sodium Bicarbonate, Hydrogen Peroxide, and Soybean oil were procured from Loba Scientific, Mumbai, India.

2.2 Methods

2.2.1 Characterization of Crude Oil

All the characterization of crude oil was performed with the help of ASTM and other standard procedures. The pour point of crude oil is the temperature at which fluid ceases to flow. Pour point of crude oil is measured using the ASTM D5853 method in the cloud and pour point apparatus manufactured by Citadel Engineers Pvt. Ltd. In this method, a sample was heated and poured into a test jar where temperature was monitored at every 3 °C-temperature drop [17–19]. When the flow stops tilting the test jar horizontally, that temperature was noted as the pour point and it was 41 °C.

Wax content of the crude oil was measured by the BP237 method where 2 g of crude oil sample was dissolved in 40 mL of n-pentane solvent. The mixture was stirred using a magnetic stirrer for half an hour. 120 mL of acetone was further added to this mixture to make the acetone and n-pentane ratio 3:1. The mixture was kept in a deep freezer at –20 °C for 24 h. The mixture was filtered with Whatman 934 filter paper using a Buckner funnel. The separated solid part keeps washing with n-hexane to get rid of asphaltenes. The filter paper was dried and weighed with the waxy residue [20–22]. The Wax content of crude oil was found at 11.37%.

Specific gravity was calculated with the help of a hydrometer. The specific gravity of crude oil was found 0.919. API gravity was determined using the ASTM D287 method. It was calculated at 60 °F with the help of Eq. 1 and it was 22.32. This result identifies that the crude oil was heavy in nature.

$$API = \frac{141.5}{SG} - 131.5 \quad (1)$$

where SG represents the specific gravity of crude oil.

SARA analysis was done with the help of the solvent dilution method. The saturates, aromatics, resin, and asphaltene content were measured in weight percentage which is given in Table 1. 1 g of crude oil was mixed with 40 mL of n-heptane and mixed well for half an hour. Then the mixture was kept overnight. The mixture was then filtered through a Buckner funnel with the help of Whatman filter paper 934. The asphaltene was extracted using hot toluene using the Soxhlet apparatus. The filtered sample was further split into lighter fractions in the chromatography column to obtain saturated aromatic and polar resin. Trichloro-methane is used to recover resins, n-hexane is used for saturates, and hot toluene is used to extract aromatic resin [23].

The water content of the crude oil was measured by the Dean-Stark apparatus which is followed by the ASTM D95 method [24–26]. In this procedure, 50 mL of crude oil and 50 mL of toluene were mixed with a magnetic stirrer for 30 min to make a homogeneous solution. The solution was placed into a round bottom flask and heated at 110 °C. The emulsified water was carried with toluene and condensed into the receiver. The final emulsified water was obtained at about 6%.

Table 1 Crude oil characterization

	Parameter	Unit	Method	Value
	Specific gravity	NA	ASTM 287-12b	0.919
	°API gravity	°API	ASTM 287-12b	22.32
	Wax content	% (W/W)	BP237	11.37
	Water content	% (V/V)	ASTM D95	6%
	Pour point	°C	ASTM 5853	41
	Saturates	% (W/W)	SARA	36
	Asphaltene	% (W/W)	SARA	12
	Aromatics	% (W/W)	SARA	22
	Resin	% (W/W)	SARA	29

2.2.2 Epoxidation of Soybean Oil

The bio-additive was synthesized with the help of soyabean oil and formic acid. 1 mol of soyabean oil and 1 mol of formic acid were taken into a round bottom flux. The flux was kept at 60 °C at 500 rpm speed. 30% hydrogen peroxide solution was prepared and added drop-wise into the reactor. The bleached soyabean oil was kept for 5 h for continuous mixing. After completion of the reaction, the mixture was neutralized with sodium bicarbonate solution followed by ethyl acetate to remove moisture from it and placed in a separating funnel for separating the upper part of soyabean oil. Lastly, the product was run with a rotary evaporator (Maker Buchi, Switzerland) to remove the ethyl acetate to make a purified product [27]. The reaction scheme is shown in Fig. 1.

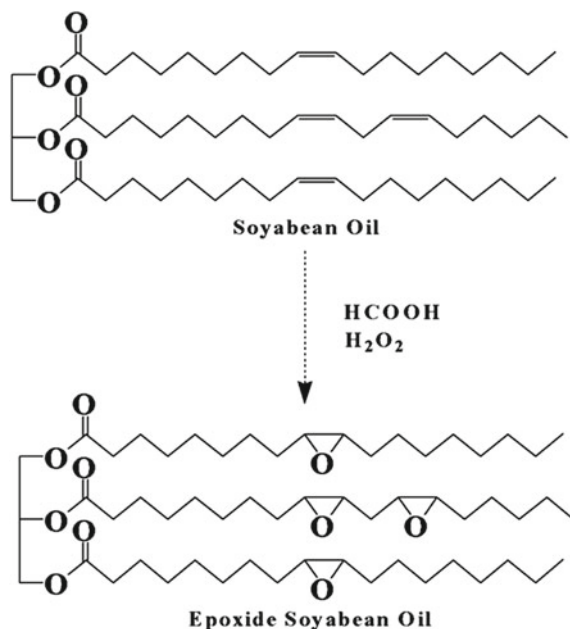
2.2.3 Sample Preparation

Pre-processing of crude oil is an essential step before going into the further application. Crude oil is treated with a 2000 ppm commercial demulsifier in a glass beaker and placed in a hot water bath for 6–8 h at 70 °C. After treatment, decant the upper part of the crude oil for the experiment. The treated crude oil was mixed with 400, 800, and 1200 ppm ESO in a glass beaker using a magnetic stirrer at 1200 rpm for 30 min for making a proper homogeneous mixture. The final sample was further studied for pour point and viscosity analysis [28].

2.2.4 FTIR Measurement

FTIR was used to measure the functional group of crude oil. The FTIR spectra were conducted with the help of PerkinElmer spectrophotometers, USA. The sample was

Fig. 1 Reaction mechanism of ESO procedure



placed between liquid KBr windows and into the apparatus for taking a scan. The observed FTIR peak was analysed by Spectrum 10 Software, version 10.

2.2.5 Measurement of Pour Point of Crude Oil with the Help of Epoxidized Soybean Oil

The pour point was measured using cloud and pour point apparatus made by Citadel Engineers by the ASTM-5853 method. In this method, crude oil was heated up to 60 °C then with reduced temperatures of 3 °C intervals. When the flow of crude oil in a glass tube stopped, that point is called the pour point.

2.2.6 Measurement of Rheological Studies of Crude Oil with the Help of Epoxidized Soybean Oil

Measured rheological properties of crude oil were measured with the help of the rheometer model no-MCR102 manufactured by Anton Paar Austria. The Crude oil rheological property was measured from 0 to 500 cm⁻¹ shear rate and 30 to 50 °C temperature range. Viscosity was studied using cup and bob cylinder geometry in which a crude oil sample was placed in the cylinder. The flat-faced bob spindle was placed inside the cup and viscosity was measured at varying speeds. The viscosity data was generated by drag created by crude oil with a cup wall surface.

2.2.7 Microscopic Studies

Microscopic studies were done with the help of the Olympus EX-51 microscope. The measurement was done with the help of a room temperature of 40 °C.

3 Result and Discussion

3.1 FTIR Characterization

From Fig. 2, the FTIR studies of bio-additive confirmed the presence of symmetric and asymmetric methyl and methylene bonds present at 2981 and 2915 cm^{-1} , respectively. The peak near 3400 cm^{-1} represents the conjugate hydroxyl group present in ester. The peak at 1454 cm^{-1} was observed due to the presence of an aliphatic group (C–H) bond. Stretching vibration of the carbonyl group of esters was present on the absorption band of 1746 cm^{-1} , and the peaks at 1251, 1172, and 1112 cm^{-1} were attributed due to carboxylic acid present in soyabean oil. The presence of a doublet group coming near 828 cm^{-1} spectra confirmed the completion of a successful epoxidation reaction. The 722 cm^{-1} peak was observed due to the presence of an alkane (–CH₃) bond [29].

Fig. 2 FTIR spectra of ESO bio-additive spectra

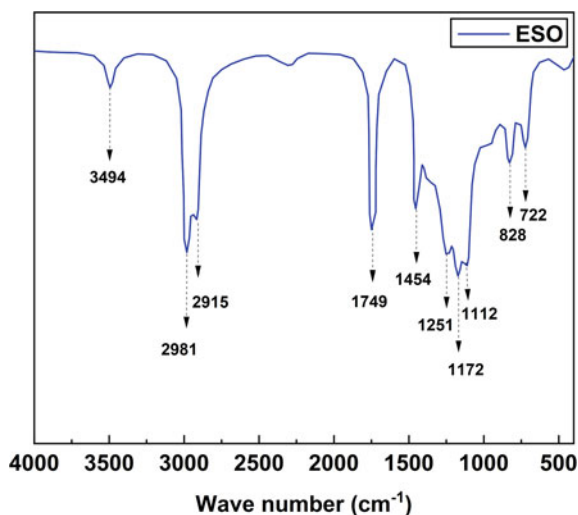


Table 2 Pour point measurement of crude oil with bio-additives

Sample	Temperature (°C)
Crude oil	41 ± 1
Crude oil + 400 ppm	38 ± 1
Crude oil + 800 ppm	35 ± 1
Crude oil + 1200 ppm	32 ± 2
Crude oil + 1600 ppm	35 ± 1

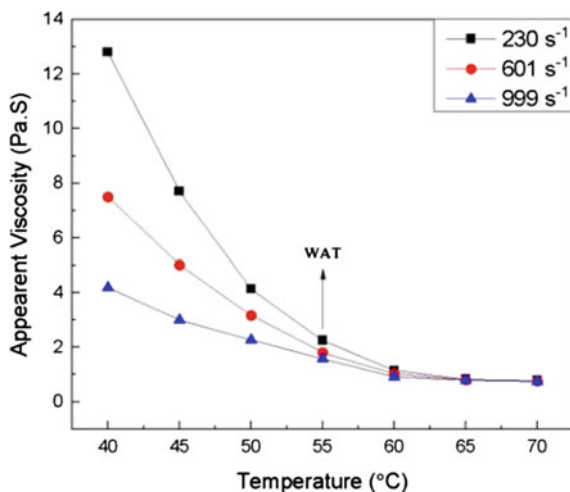
3.2 Measurement of Pour Point of Crude Oil with the Help of Epoxidized Soybean Oil

According to the ASTM D5853 standard method, the cold flow properties of the tested crude oil samples and pure crude oils were investigated. To get the correct result, a sample was tested three times and an average value was taken according to the standard test method. The effect of bio-additive on the pour point depressions of crude oil samples are shown in Table 2, and the pour point of the untreated crude oil is 41 °C. The pour point of the crude oil was reduced by 9 °C after addition of 1200 ppm epoxidized soybean oil. The pour point was reduced due to the interaction of long-chain wax with a long fatty acid of epoxidized soybean oil, and the reduction of the pour point occurs by co-crystallization of wax particles so that viscosity of the crude oil was also reduced. After 1200 ppm dosage, the pour point of crude oil was increased due to bulkiness of the polymer and less soluble. As a result, it made ineffective with increasing concentration [30]. During cooling of crude oil from 70 °C to 40 °C, wax crystals starts to appear at wax appearance temperature (WAT) which is here found 55 °C. With further reduction in temperature, wax molecules start to agglomerate with each other and trap the crude oil which turns crude oil from Newtonian to non-Newtonian flow behavior (Fig. 3). The bio-additive reduced the pour point of both crude oil in various degrees. The effectiveness increased with the increase in the concentration of the additive in the crude oil firstly, and when the concentration of bio-additive is 1600 ppm, the effectiveness is not changed or decreased with the increase of bio-additive concentration. Because when the concentration of PPDs is small, it is difficult to co-crystallize between PPD molecules and paraffin wax of crude oil; while when the concentration of PPDs is too high, the excessive PPD molecules form smaller grains by themselves, which inhibit the co-crystallization between PPD molecules and paraffin wax. So, 1200 ppm dose is the optimum amount [31].

3.3 Measurement of Rheological Studies of Crude Oil with the Help of Epoxidized Soybean Oil

The effectiveness of Epoxidized soybean oil in flow assurance studies was investigated with rheological experiment (Fig. 4). At the low shear rate, the variation of

Fig. 3 WAT calculation by viscometry mode



viscosity was very large due to the non-Newtonian fluid behavior of crude oil but with increase in the shear rate the difference of viscosity comes closer which shows Newtonian flow conversion and as a result the flow properties were increased. At 30 °C, crude oil shows 42.30 Pa·s which is decreased by 36.38% after the addition of 1200 ppm bio-additive. With the increasing dosage level up to 1200 ppm, the viscosity reduction of undoped crude oil was decreased by 65% at 50 °C. Crude oil shows non-Newtonian characteristics above wax appearance temperature (WAT) and when it crosses WAT, the crude oil behaves like Newtonian flow. It is also suggested that at a high shear rate, the crude oil shows Newtonian behavior which can be depicted after 300 s⁻¹ shear rate due to high torque generated from bob and cylinder wall. The synthesized PPD was very effective which can clearly show from rheology as well as pour point which were justified by the result [32].

3.4 Microscopic Studies

Figure 5 is clearly shows that untreated crude oil has a greater number of wax crystals compared to bio-additive treated crude oil. This phenomenon is observed due to bio-additive restrictions on the wax agglomeration. The bio-additive provides active sites which are attached to the wax crystals and increase the flowability of crude oil [33].

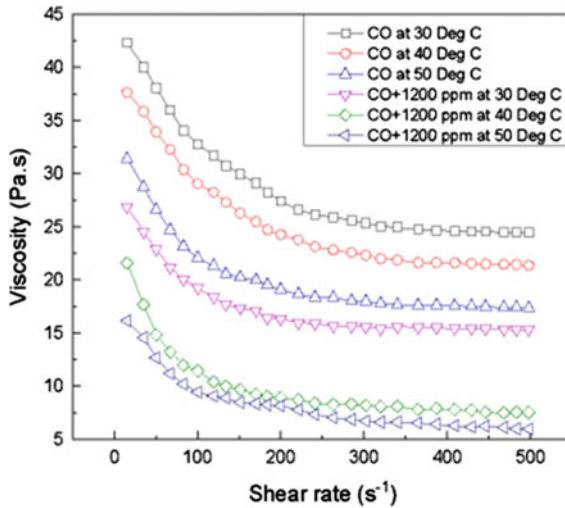


Fig. 4 Viscosity reduction of crude oil with ESO bio-additives

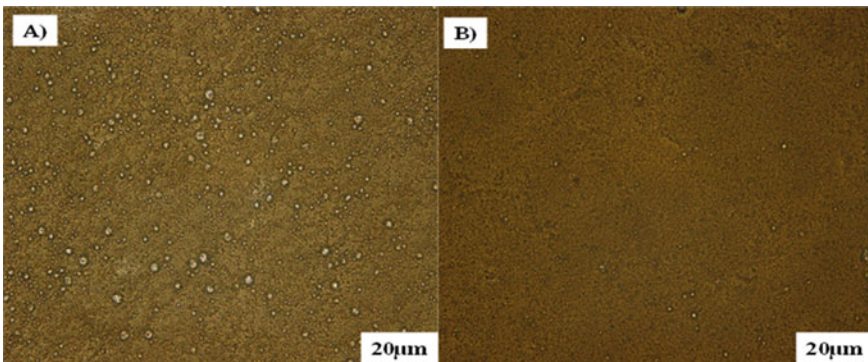


Fig. 5 Microscopic studies of CO and with addition of 1200 ppm bio-additive

4 Conclusion

The pour point and viscosity of crude oil were reduced after the addition of epoxidized soybean oil. The 1200 ppm is the optimum dosage level of additive in the crude oil of which maximum pour point reduction was observed. The viscosity was reduced by 65% and a reduction of pour point at 9 °C was observed. Therefore, epoxidized soybean oil has immense potential for flow assurance problems. Soybean oil is easily available which could reduce the production cost as well. Due to the environment-friendliness, it is not toxic and vegetable oil can be modified so that reduction of pour point and viscosity will reduce more.

References

1. Fadaïro A, Ogunkunle T, Asuquo V, Oladepo A, Lawal B (2018) Dataset on the effect of sunflower-based biodiesel on the rheology of Nigeria waxy crude oil. *Elsevier Data Brief J* 20:948–953
2. Mahto V, Singh H (2013) Effect of temperature and pour point depressant on the rheology of Indian waxy crude. *Int J Gen Eng Technol (IJGET)* 2(4):25–30
3. Borthakur A, Chanda D, Dutta Choudhury SR, Rao KV, Subrahmanyam B (1996) Alkyl fumarate–vinyl acetate copolymer as flow improver for high waxy Indian crude oils. *Energy Fuel* 10:844–848
4. Farrington JW (1980) An overview of the biogeochemistry of fossil fuel hydrocarbons in the marine environment
5. Gupta A, Anirbid S (2015) Need of flow assurance for crude oil pipelines: a review. *Int J Multidiscip Sci Eng* 6(2):1–7
6. Thomas JE, Eduardo J (2001) Fundamentos de engenharia de petróleo. Interciência
7. Oliveira LMSL, Nunes RCP, Melo IC, Ribeiro YLL, Reis LG, Dias JCM, Guimarães RCL, Lucas EF (2016) Evaluation of the correlation between wax type and structure/behavior of the pour point depressant. *Fuel Process Technol* 149:268–274
8. Mózes G (ed) (1983) Paraffin products. Elsevier
9. Vieira LC, Buchuid MB, Lucas EF (2013) Evaluation of pressure on the crystallization of waxes using microcalorimetry. *J Therm Anal Calorim* 111(1):583–588
10. Visintin RF, Lockhart TP, Lapasin R, D'Antona P (2008) Structure of waxy crude oil emulsion gels. *J Nonnewton Fluid Mech* 149(1–3):34–39
11. Bello OO, Ademodi BT, Akinyemi PO (2005) Xylene-based inhibitor solves crude oil wax problems in Niger-Delta pipeline. *Oil Gas J* 103:10–56
12. Popoola CB, Ayo JA, Adedeji OE, Akinleye O (2015) Triethanolamine (TEA) as flow improver for heavy crude oils. *IOSR J Appl Chem* 8(3):34–38
13. Soriano NU Jr, Migo VP, Sato K, Matsumura M Jr (2005) Crystallization behavior of neat biodiesel and biodiesel treated with ozonized vegetable oil. *Eur J Lipid Sci Technol* 107(9):689–696
14. Soni HP, Bhamambe DP (2006) Synthesis and evaluation of polymeric additives as flow improvers for Indian crude oil
15. Straub T, Autry S, King G (1989) An investigation into practical removal of downhole paraffin by thermal methods and chemical solvents. In: SPE production operations symposium, Society of Petroleum Engineers, Oklahoma City, OK, March 13–14
16. Etoumi A (2007) Microbial treatment of waxy crude oils for mitigation of wax precipitation. *J Pet Sci Eng* 55(1–2):111–121
17. Li H, Chen C, Huang Q, Ding Y, Zhuang Y, Xie Y, Zhang J et al (2020) Effect of pour point depressants on the impedance spectroscopy of waxy crude oil. *Energy Fuels* 35(1):433–443
18. Nadzeri MI (2014) Applicability study of rotational method based from ASTM D5985 for crude oil pour point measurement
19. Lee HS, Singh P, Thomason WH, Fogler HS (2008) Waxy oil gel breaking mechanisms: adhesive versus cohesive failure. *Energy Fuels* 22(1):480–487
20. Gudala M, Banerjee S, Kumar R, Rama Mohan Rao T, Mandal A, Kumar Naiya T (2018) Experimental investigation on hydrodynamics of two-phase crude oil flow in horizontal pipe with novel surfactant. *J Fluids Eng* 140(6)
21. Vakili S, Mohammadi S, Derazi AM, Alemi FM, Hayatzadeh N, Ghanbarpour O, Rashidi F (2021) Effect of metal oxide nanoparticles on wax formation, morphology, and rheological behavior in crude oil: an experimental study. *J Mol Liq* 343:117566
22. Hejazi H, Bayati B, Mansouri M (2021) The effect of inhibitor on wax precipitation in Iranian oil fields using differential scanning calorimetry and microscopy methods. *Iran J Oil Gas Sci Technol* 10(3):01–19
23. Fan T, Wang J, Buckley JS (2002) Evaluating crude oils by SARA analysis. In: SPE/DOE improved oil recovery symposium. OnePetro

24. El Nagggar AY, Saad EA, Kandil AT, Elmoher HO (2010) Petroleum cuts as solvent extractor for oil recovery from petroleum sludge. *J Pet Technol Altern Fuels* 1(1):10–19
25. Sugeng DA, Abrori M, Syafrinaldy A, Kadir HA, Saputro FR, Kusdi BH, Yahya WJ et al (2021) Determining water content of non-surfactant emulsion fuel using bomb-calorimeter. In: *IOP conference series: materials science and engineering*, vol 1096, no 1. IOP Publishing, p 012044
26. Nadkarni RA, Nadkarni RA (2007) *Guide to ASTM test methods for the analysis of petroleum products and lubricants*, vol 44. ASTM International, West Conshohocken
27. Saremi K, Tabarsa T, Shakeri A, Babanalbandi A (2012) Epoxidation of soybean oil. *Ann Biol Res* 3(9):4254–4258
28. Banerjee S, Kumar R, Akhtar A, Bairagi R, Mandal A, Naiya TK (2017) Effect of pour point depressant on wax deposition and drag reduction in horizontal pipelines. *Pet Sci Technol* 35(6):561–569
29. Vlček T, Petrović ZS (2006) Optimization of the chemoenzymatic epoxidation of soybean oil. *J Am Oil Chem Soc* 83(3):247–252
30. Sharma S, Mahto V, Sharma VP (2014) Effect of flow improvers on rheological and microscopic properties of Indian waxy crude oil. *Ind Eng Chem Res* 53(12): 4525–4533
31. Pal B, Naiya T (2022) Application of novel fruit extract for flow assurance of Indian field waxy crude oil. *SPE J* 1–18
32. Naiya TK, Banerjee S, Kumar R, Mandal A (2015) Heavy crude oil rheology improvement using naturally extracted surfactant. In: *SPE Oil & Gas India conference and exhibition. OnePetro*
33. Banerjee S, Kumar R, Mandal A, Naiya TK (2015) Effect of natural and synthetic surfactant on the rheology of light crude oil. *Pet Sci Technol* 33(15–16):1516–1525

Quaternary Recycling Studies for Desalination Membrane Management



M. Srija, S. Bhandari, and T. L. Prasad

1 Introduction

Potable water by desalination can be produced either by a thermal process or membrane processes. Membrane technology, and in particular “pressure-driven” membrane systems, using reverse osmosis (RO) are long established as a large-scale industrial membrane process for desalination [1, 2]. Membrane-based desalination plants constitute a 50% share of commercial desalination plants across the world [2, 3]. More than 840,000 end-of-life membranes are disposed of annually in the world, which is equivalent to more than 14,000 tons per year. Various components of spent RO modules, at the End of Life (EoL), need to be managed without sending to landfills [4]. The polymers used in these RO modules are not amenable to bio-degradation easily. Many technologies are being explored to address the issue of managing spent polymers. Plasma gasification technology offers an efficient, economic, and environmentally friendly way to treat various types of wastes including municipal, medical, and even radioactive wastes [5].

Advanced oxidation processes for aqueous organic waste handling are known and are being practiced in industries. Zhanga et al. [6] studied the depolymerization of thermosetting epoxy resin with hetero poly acid catalyst at temperatures between 270 and 350 °C in a water medium. Kanga et al. [7] studied the hypochlorite degradation of aromatic polyamide RO membrane to get some understanding of the prevention of membrane depreciation and develop membranes with improved chlorine resistance.

M. Srija · T. L. Prasad (✉)

Homi Bhabha National Institute, Bhabha Atomic Research Centre, Mumbai 400085, India

e-mail: tlp@barc.gov.in

S. Bhandari

Beam Technology Group, Bhabha Atomic Research Centre, Mumbai 400085, India

T. L. Prasad

Chemical Engineering Group, Bhabha Atomic Research Centre, Mumbai 400085, India

Prasad et al. [8] studied low-temperature AOP-based processes for the management of spent desalination membranes. Anyaegnunam [9] outlines the usage of thermal plasma processes for hazardous waste such as hospital waste and thermal batteries and presented measured emissions along with toxicity leaching aspects. Ismail and Ani [10] reviewed the studies on plasma treatment of solid waste for the production of syngas by using various plasma such as thermal; microwave, and radiofrequency to evolve the future direction for MSW management in Malaysia.

Quaternary recycling refers to the recovery of polymeric membrane energy content. Incineration aiming at the recovery of energy is currently the most effective way to reduce the volume of organic materials. Although polymers are actually high-yielding energy sources, this method has been widely accused as ecologically unacceptable owing to the health risk from airborne toxic substances, e.g. dioxins (in the case of chlorine-containing polymers). To achieve improved and efficient combustion, exploratory studies were carried out using air plasma. The comparative studies of conventional resistance heating and thermal plasma are briefly discussed in this paper. The observed mass reduction factors and gasification efficiencies are discussed. This paper highlights the feasibility studies of the treatment of spent RO module components using air plasma gasification technology developed by BARC. The conceptual process flow scheme to address the requirements of 6.3 MLD desalination plant NDDP Kalpakkam is discussed. Air plasma gasification was tried as a new technology for the new stream of waste consisting of desalination membranes, and stability of plasma was observed with efficient conversion.

2 Material and Methods

2.1 Materials

The domestic filter candles of 8" size and made of polypropylene shown in Fig. 1 are procured from M/s. Dattaguru Enterprises, Mumbai, and are used for the studies. The filter candles are uncoated. The used filter candles are coated with a poly sulfone layer.

The various RO module components taken from commercial RO module of KOCH make are shown in Fig. 2 and mainly consist of Thin Film Composite membranes.

2.2 Methods

The standard laboratory programmable furnace system is used for resistance heat-based quaternary recycling studies under an ambient atmosphere. The silica crucibles of 100 g capacity were used for loading the samples.

Fig. 1 Typical uncoated domestic filter candles

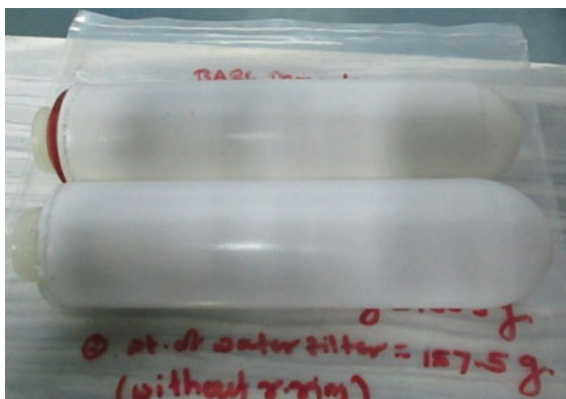
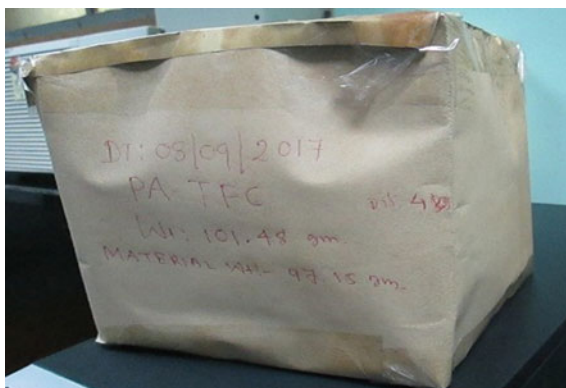


Fig. 2 SWRO membranes



The Radio Frequency (RF)-based air plasma of 100 kW capacity system shown in Fig. 3 is used for thermal plasma-based quaternary studies. The thermal air plasma system is of 100 kW capacity. The flue gas compositions are measured along flue gas lines at various locations using portable Testo make gas monitors.

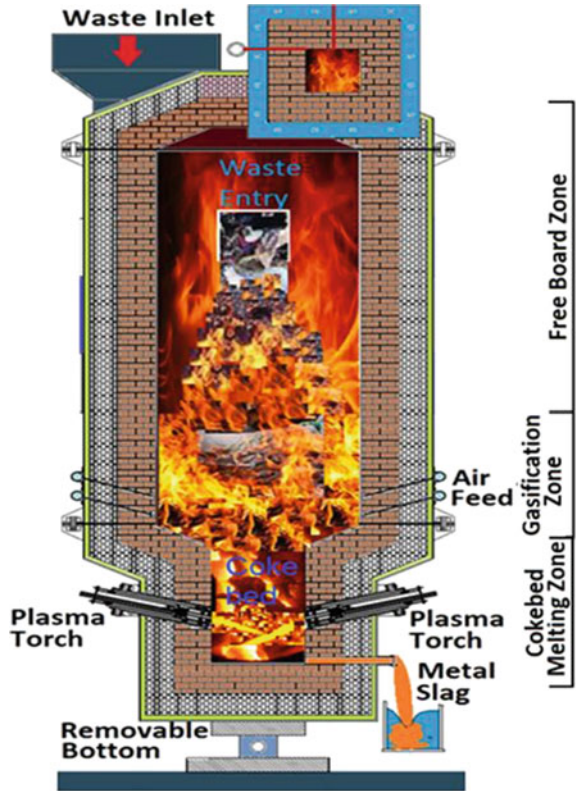
3 Results and Discussion

3.1 *Lab-Scale Studies Using Conventional Resistance Heating*

3.1.1 BARC Domestic Water Filters

Thermal depolymerization process studies were carried out for BARC domestic water filters in the temperature range up to 1000 °C. The Mass Reduction Factors (MRF) are

Fig. 3 Typical process zones inside the RF plasma primary chamber



evaluated during lab-scale studies for different desalination polymers, and observed values are shown in Fig. 4. The ambient atmosphere conditions were maintained. Thermal depolymerization was carried out to establish quaternary recycling aspects for desalination membranes. The morphology of the residue collected is shown in Fig. 5.

Fig. 4 Mass reduction factors for domestic water purifiers

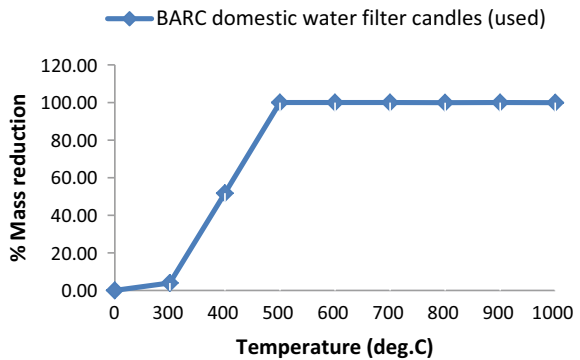


Fig. 5 Morphology of residue after treatment with resistance heating



3.1.2 Desalination Membranes

Thermal depolymerization process studies were also carried out for different polymers used in desalination membranes in the temperature range up to 1000 °C. The mass reduction factors are evaluated during lab-scale studies for different desalination polymers. The ambient atmosphere conditions were maintained. The threshold values observed for achieving reasonable mass reductions are shown in Fig. 6.

Fig. 6 Mass reduction factors for RO components

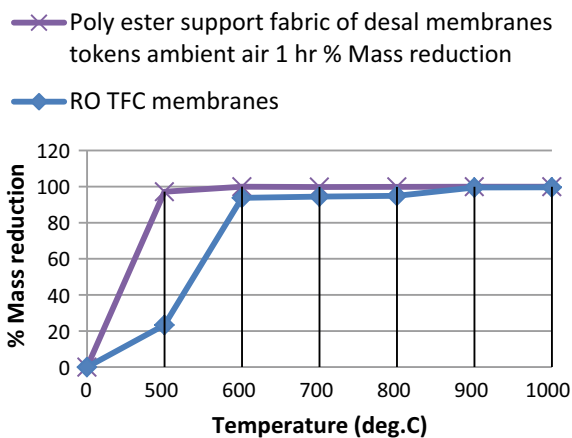


Table 1 Air plasma studies for domestic water purifiers

Operation	BARC domestic water filters (used)	Uncoated filter candles (UCF) Sample-1	Uncoated filter candles (UCF) Sample-2
Voltage (V)	159	147	144
Current (A)	200	201	107
Power (kW)	31.8	29.54	15.40
Plasma gas flow (lpm)	30	20	20
Additional airflow (lpm)	200	10	6
Duration (min)	20	65	30
Initial mass (g)	800.48	3686.67	1835.96
Final residue mass (g)	6.41	11.01	0
Mass reduction factor	99.20	99.70	100

3.2 Pilot Scale Studies Using Thermal Plasma Treatment (TPT) Systems

3.2.1 BARC Domestic Water Filters

In this study, air plasma is used at different plasma power and plasma gas flow rates as shown in Table 1 for domestic filters. The most frequently used plasma gas is air, for economic reasons and for providing oxygen for reactions with carbonaceous materials. The morphology of residue and composition observed are also shown in Table 2. Based on carbon compositional analysis, a gasification efficiency of up to 89% is observed.

Thermal plasmas can be obtained by arc discharges (DC or AC plasma) or by Radio Frequency (RF)-Microwave (MW) plasma. RF or MW plasmas don't have electrode erosion but have low energy efficiency, about 40–70% (60–90% for arc torches). The nature of RF air plasma observed during operation is shown in Fig. 7. The morphology of the residue collected for domestic filters is shown in Fig. 8.

3.2.2 Desalination Membranes

In this study, air plasma is used at different plasma power and plasma gas flow rates as shown in Table 3 for desalination membranes. The morphology of residue and composition observed are also shown. Based on carbon compositional analysis, gasification efficiency of up to 89% is observed. The morphology of the residue sample collected at the end of the operation is shown in Fig. 9.

Table 2 Elemental composition of virgin samples and residue

Element	BARC domestic water filters (used)	Plasma residue BARC domestic water filters (RES2)	UCF	Plasma residue of UCF (RES3 of sample-1)	Plasma residue of UCF (RES4 of sample-2)
Aluminium	0.13%	0.81%	2.50%	5.6%	NA
Iron	4.70%	2.10%	1.80%	8.1%	NA
Copper	48.00%	0.80%	1.90%	2.9%	NA
Silver (detection limit < 25 ppm)	ND	ND	ND	ND	NA
Hafnium (detection limit < 25 ppm)	ND	ND	ND	171 ppm	NA
Silica	0.14%	4.01%	8.15%	7.22%	NA
Carbon	8.00%	4.00%	52.00%	4.76%	2.98%
Hydrogen	13.60%	1.70%	NA	NA	NA
Nitrogen	3400 ppm	33 ppm	10 ppm	290 ppm	1.30%
Oxygen	4.50%	39.80%	2.40%	20.70%	35.10%
Sulphur	800 ppm	2 ppm	1.00%	0.44%	0.14%

*ND: not detected; NA: not analyzed

Fig. 7 Stability of air plasma during the operation



3.3 Conceptual Plant Design for Meeting NDDP Requirement

Nuclear Desalination Demonstration Plant (NDDP) at Kalpakkam uses hybrid desalination with 1.8 MLD capacity of Sea Water Reverse Osmosis (SWRO) and 4.5 MLD capacity of Multi Stage Flash (MSF) desalination coupled with 2×220 MWe capacity Nuclear Atomic Power plants [11]. SWRO plant shown in Fig. 10 uses

Fig. 8 Morphology of filter residue after air plasma treatment



around 160 elements and is discarded every 3 years of operation. The typical technical specifications of the 1.8 MLD SWRO plant are as given in Table 4 and uses 156 elements configured into 26 modules. Presently, it is being stored at the plant site and awaiting suitable process technology. Approximately 2000 kg per year needs to be taken care. Conceptual RF power-based TPT of capacity 50 kg per shift operation on a campaign basis is being planned for meeting the requirements of NDDP.

A conceptual gasifier with the given informative sketch shown in Fig. 11 is being planned and the operation is being considered to address the basic gaps of air-based TPT technology listed in the article above, providing a systematic and extensive data source further. Steam supply to plasma reactor can be optional for increased syngas production.

4 Conclusion

This is an entirely new waste stream from the desalination industry being addressed. Our studies have established the technical feasibility of TPT for desalination membranes with MRF of more than 90%. The compatibility of desalination membrane substrates with various plasma systems and under-beam handling aspects is established. Compared to conventional methods, TPT offers the advantage of decomposing toxic compounds into harmless chemical elements. The gasification efficiency of around 89% was achieved. Wastes with high concentration of organic materials having high heating values, and recovery of this heating value in the form of synthesis gas (syn-gas) using a plasma process is an attractive alternative to complete combustion and steam generation. However, there is a need for an extensive experimental study in which the systematic influence of reactor characteristics, plasma environment, and process characteristics and operation characteristics are going to be determined.

Table 3 Air plasma studies for reverse osmosis (RO) membranes

<i>Operating conditions</i>		
Voltage (V)	160	
Current (A)	199	
Power (kW)	31.84	
Plasma gas flow (lpm)	30	
Additional airflow (lpm)	50	
Duration (min)	15	
Average temperature (K)	3000	
<i>For reverse osmosis thin film composite (RO TFC) membranes</i>		
Initial mass (g)	97.00	
Final residue mass (g)	10.31	
Mass reduction factor	89.38	
<i>Elemental composition</i>		
<i>Element</i>	<i>RO TFC</i>	<i>Plasma residue of RO TFC (RES1)</i>
Aluminium	NA	0.64%
Iron	NA	1.20%
Copper	NA	0.61%
Silver (detection limit < 25 ppm)	ND	ND
Hafnium (detection limit < 25 ppm)	ND	ND
Silica	NA	1.80%
Carbon	64%	7.00%
Hydrogen	6%	NA
Nitrogen	<0.05 ppm	NA
Oxygen	NA	NA
Sulphur	2 ppm	3 ppm

*ND: not detected; NA: not analyzed

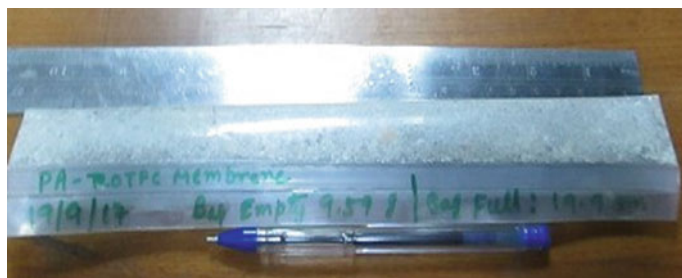


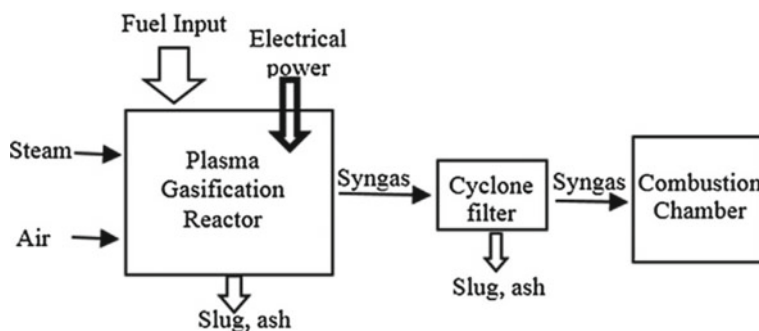
Fig. 9 Morphology of RO residue after air plasma treatment

Fig. 10 SWRO section of hybrid NDDP desalination plant



Table 4 Typical SWRO specifications of NDDP plant

(i)	Product out	75 m ³ /h
(ii)	Product quality	500 ppm
(iii)	Feed seawater flow	215 m ³ /h
(iv)	Feed seawater TDS	35,000 ppm
(v)	Membrane element (a) Type (b) Model (c) Elemental capacity	TFC spiral wound 8040 HSYSWC/TFC 2822 SS 22 m ³ /day/element
(vi)	Product recovery	35%
(vii)	Design pressure	55 kg/cm ²
(viii)	Solute rejection	99.60% at standard seawater test condition (32,800 ppm NaCl, pH = 7.5, 25 °C)
(ix)	No. of elements required	156
(x)	No. of elements per module	6
(xi)	Total no. of modules	26

**Fig. 11** Schematic gasifier diagram

Acknowledgements The authors wish to thank the Director Chemical Engg Group and Beam Technology Group for giving encouragement to the programme. Thanks are also due to HBNI for the acceptance of the proposal through DGFS-PhD-2018 scholar. The authors wish to express thanks to Head L&PTD & DD and Head Analytical Chemistry Division for sample analysis.

References

1. Drioli E, Giorno L (2010) Comprehensive membrane science and engineering, 1st edn. Elsevier Publishers
2. Semiat R (2000) Desalination: present and future. Water Int 25(1):54–56
3. IDA desalination year book 2016–2017, pp 1–11

4. Prasad TL, Goswami D, Tewari PK (2013) Status review on spent desalination membranes management. In: Founder's day special issue of BARC newsletter, October, pp 291–294
5. Sanlisoy A, Carpinlioglu MO (2017) A review on plasma gasification for solid waste disposal. *Int J Hydrog Energy* 42:1361–1365
6. Zhanga J, Dengb W, Zuc J, Dingd H, Caie P (2011) Catalytic hydrothermal depolymerisation technology and kinetics of DGEBA/EDA epoxy resin. *Adv Mater Res* 201–203:2814–2819
7. Kanga G-D, Gaoc C-J, Chend W-D, Jie X-M, Caoa Y-M, Yuan Q (2007) Study on hypochlorite degradation of aromatic polyamide reverse osmosis membrane. *J Membr Sci* 300:165–171
8. Prasad TL, Avilasha S, Sandhya VL, Bindal RC (2019) Low temperature AOP studies for spent reverse osmosis module components. *Sep Sci Technol* 54(9):1533–1541. <https://doi.org/10.1080/01496395.2019.1584223>
9. Anyaegunnam FNC (2014) Thermal plasma process for hazardous waste treatment. *Int J Eng Res Technol* 3(3):1769–1773. ISSN 2278-0181
10. Ismail N, Ani FN (2015) A review on plasma treatment for the processing of solid waste. *J Teknol* 72(5):41–49. eISSN 2180-3722
11. Nuclear India, vol 30, no 1–2, July_August 2003. Department of Atomic Energy, Govt of India

Mineral Processing

Kaolin: An Alternate Resource of Alumina



Sonidarshani Routray, Barsha Dash, Abdul R. Sheik, C. K. Sarangi, and Kali Sanjay

1 Introduction

Global metallurgical alumina demand is fulfilled mostly by bauxite. However, some non-metallurgical alumina demand is somehow fulfilled by other small and local resources like waste aluminium dross and flyash. Bauxite is a major resource of alumina in places where it is found in sufficient amounts to be exploited. But in some parts of the globe Bauxite is found in lower economic value as [1], whereas alternative non-bauxitic resources like Clay, Mica, Alunite, etc. are plenty and extensive in many parts of the globe. Clays are abundantly available which mostly consist of aluminosilicates. In the clay category, Kaolin is the main and most preferred source of alumina. In this context, alumina production from Kaolin can also be an alternative process for alumina production to meet the need for non-metallurgical activated alumina for different applications like fillers, adsorption, catalysis, and so on. Normally, Kaolin is used as pigment or filler material in plastic, polymer, ceramic, etc. Kaolin is a century-old skin care and cosmetic component. Kaolin has a chemical composition of $\text{Al}_2\text{Si}_2\text{O}_5(\text{OH})_4$ which is having a lamellar crystal structure of aluminium silicate layers bonded with a hydrogen bond. The alumina content of a typical Kaolin is 15–25% varying from place to place. Kaolin is highly silicious having around 50% silica. That is the reason it follows a different route of roasting and chloride leaching to extract alumina. Leaching with acids like HCl [2] and H_2SO_4 [3, 4] is conducted with Kaolin or metakaolin to extract alumina. Some researchers have used Microwave [5] and Ultrasound [6] exposure to Kaolin followed by leaching. A combination of pyro and hydrometallurgical operation is mostly preferred for alumina extraction from Kaolin [7]. Apart from acid, Kaolin is also leached with all acids to extract alumina [8]. In some cases, it is treated

S. Routray · B. Dash (✉) · A. R. Sheik · C. K. Sarangi · K. Sanjay
CSIR-Institute of Minerals and Material Technology, Bhubaneswar 751013, India
e-mail: barshadash@immt.res.in

© The Author(s), under exclusive license to Springer Nature Singapore Pte Ltd. 2023
E. Chinthapudi et al. (eds.), *Sustainable Chemical, Mineral and Material Processing*,
Lecture Notes in Mechanical Engineering,
https://doi.org/10.1007/978-981-19-7264-5_10

135

with thiourea to reduce the iron content from raw kaolin [9]. The process liquor is used to synthesize alumina-based value-added products like alumina powder [6], nano-sized α -alumina [10], and porous alumina [11]. Alumina is also extracted from Kaolin by lime sintering followed by sodium carbonate treatment [7, 12]. Nano-sized α -alumina is also reported from kaolin via the hydrochloric acid leaching route [10]. Aluminium may be extracted from kaolin as aluminium chloride by the salting out process [13]. Sometimes, combined processes are also adopted to extract alumina like NaCl roasting followed by sulphuric acid leaching and HCl leaching too [14].

There are so many critical applications of non-metallurgical grade alumina. That alumina may be easily produced from clays like kaolin which will reduce the load on bauxite resources and in addition, it will support growth of alumina industries. Value-added products of non-metallurgical applications like aluminium sulphate salt [15], nano alumina [16], and activated alumina [14, 17] are produced from kaolin acid leachate.

In this study, attempts have been made to extract alumina from kaolin by roast-leach-precipitation method to extract alumina from thermally treated kaolin and then produce alumina from the solution after due removal of iron and calcination of the precursor. Normally, hydrochloric acid leaching is reported in the available literature, but in this study sulphuric acid leaching is also reported which is both economically and ecologically viable.

2 Material and Methods

2.1 Materials

Kaolin is a clay mineral of the 1:1 category. It has a layered structure of octahedral sheets of AlO_6 stacked on SiO_4 layers. The Kaolin used in this study is synthetic Kaolin procured from a local vendor in Odisha. It was yellowish in colour. The composition of the Kaolin is 19.77% Al, 0.728% Fe, and 48.998% SiO_2 . The X-Ray Diffraction (XRD) patterns (Fig. 1) of Kaolin mostly match with the mineral Kaolinite 1A and Quartz. The rest of the silica parts are amorphous silica as only quartz would be detected in XRD.

2.2 Methods

Extraction of alumina from Kaolin has a combination of both Pyro and Hydrometallurgical processes. The methods followed are roasting and leaching followed by purification and precipitation as discussed in separate sections described below. The precipitated aluminium hydroxide is further calcined to produce activated alumina which is the highly demanded material in the market.

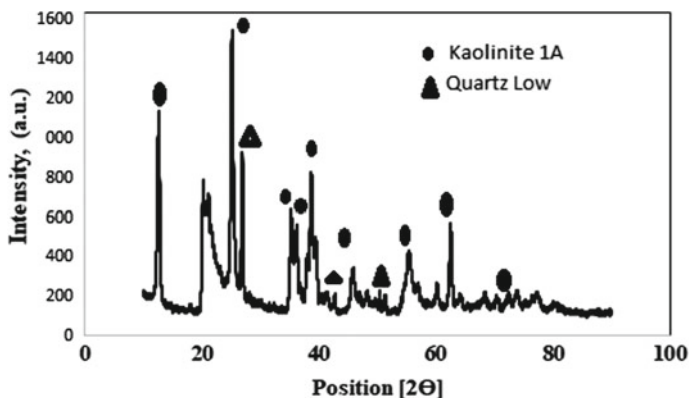


Fig. 1 XRD of kaolin

2.2.1 Roasting and Leaching

Kaolin was roasted at 850 °C for 2 h in a muffle furnace. The sample was placed in an alumina crucible and kept inside the chamber, and the temperature was maintained at 850 °C in the five-stage program. The roasted Kaolin was leached in HCl and H₂SO₄ to liberate alumina. The leaching was carried out with a 250 mL water-jacketed flask where the acid of fixed concentration with a particular temperature was circulated. The acid was allowed to get heated and after the stipulated temperature was achieved, Kaolin and thermally treated kaolin were added in different sets of experiments. Parameters like temperature, and acid concentrations were varied in different sets of experiments. The mixing was carried out by an externally placed magnetic stirrer just below the flask. After the stipulated time period, the solution was removed, filtered, and allowed for analysis and determination of the concentration of different elements through Atomic Absorption Spectrophotometry (AAS) and Inductively Coupled Plasma-Optical Emission Spectrophotometry (ICP-OES).

2.2.2 Purification and Precipitation

The acid leach liquor was allowed to increase the pH up to 7.0 where all the iron and aluminium ions got precipitated. Further increase in the pH up to 12.0 dissolved the precipitated aluminium hydroxide leaving behind the precipitates of iron. Thus, Fe and Al are separated and filtered. The filtrate was allowed to re-precipitate with sulphuric acid to get aluminium hydroxide which after calcination produces activated alumina.

Table 1 Treatment of kaolin with different acids

Leaching reagent and conditions	Al (%)	Fe (ppm)
3 M H ₂ SO ₄ , 10% PD, at temperature 90 °C, 3 h	4.27	50
6 M HCl, 10% PD, at temperature 90 °C, 3 h	2.66	20
1 M H ₂ SO ₄ , 10% PD, at temperature 120 °C, 2 h	2.76	200

2.2.3 Calcination

The as-obtained aluminium hydroxide is calcined at 800 °C for 2 h to get activated alumina where the physically bonded as well as chemically bonded water is removed resulting in a change in new bond formation thereby producing voids and increased surface area.

3 Results and Discussion

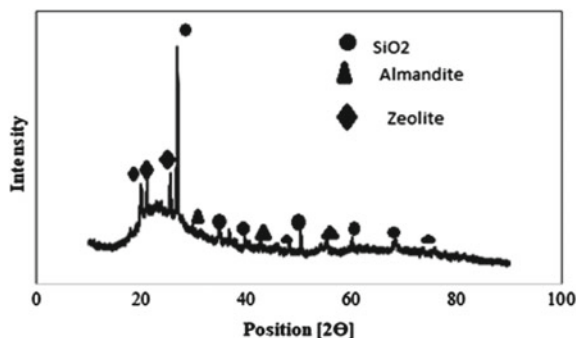
Kaolin is treated with acid in two ways. One is acid leaching of original Kaolin without thermal treatment and the second one is thermal treatment of Kaolin at 850 °C for 2 h to destabilize the internal structure of Kaolin to make it reactive.

3.1 Treatment of Kaolin in Different Acids

The Kaolin (Al₂Si₂O₅(OH)₄) used for the study was subjected to treatment with acid without any pre-treatment like thermal treatment. It was treated with 3 M sulphuric acid (H₂SO₄) and 6 M hydrochloric acid (HCl) with 10% pulp density (PD) and 90 °C for 3 h and found that the extraction of aluminium was very poor. It was even subjected to hydrothermal treatment at 120 °C for 2 h with 1 M H₂SO₄, but there was no significant improvement in the leaching efficiency as mentioned in Table 1. The reason behind the acid resistance of kaolin is that it has a strong natural layered structure of tetrahedral SiO₄ linked with octahedral AlO₆ which are normally nonreactive in nature because of its high stability.

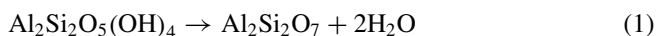
3.2 Thermal Treatment of Kaolin

In this study, Kaolin was roasted at 850 °C for 2 h to destabilize its structural strength so that it will react with the acid and liberate aluminium. The surface hydroxyl group combines together to form a water molecule which is subsequently removed from the system. The phases obtained after rigorous heat treatment are Silica, Almandite, and

Fig. 2 XRD of roasted kaolin**Table 2** XRF data of kaolin before and after thermal treatment

Sample	Al ₂ O ₃ , %	Fe ₂ O ₃ , %	SiO ₂ , %
Kaolin	37.351	1.405	48.998
Heat-treated kaolin	42.387	1.324	53.207

Zeolite as obtained from the XRD pattern presented in Fig. 2. The alumina content of the heat-treated Kaolin is increased as compared to the original Kaolin.



The overall composition of the Kaolin before and after heat treatment is reported here in Table 2. The alumina and silica content was found to be increased after thermal treatment as there is removal of physically and chemically bonded water molecules, removal of organics, and other volatile impurities. After heat treatment, it may respond to the acid attack as zeolite is a porous material so that it allows acids to percolate and liberate the minerals.

The SEM images of kaolin and thermally treated Kaolin are presented in Fig. 3a, b. Flaky morphology was observed in the original Kaolin (Fig. 3a) sample as it is known that kaolin is layered structures. In the case of thermally treated Kaolin (Fig. 3b), the morphology is flaky but there is observed some kind of change in surface structure. As is already known from XRD patterns, the Kaolinite phase is converted to Zeolite and Almandite.

3.3 Leaching of Thermally Treated Kaolin

As reported in the literature, roasted Kaolins are treated with HCl. But in this case, the thermally treated Kaolin was treated with both HCl and H₂SO₄ at 90 °C for 2 h to have a comparison of both acid leaching and to find out the best suggested one. It was observed that untreated Kaolin was highly resistant to acid attack. After thermal

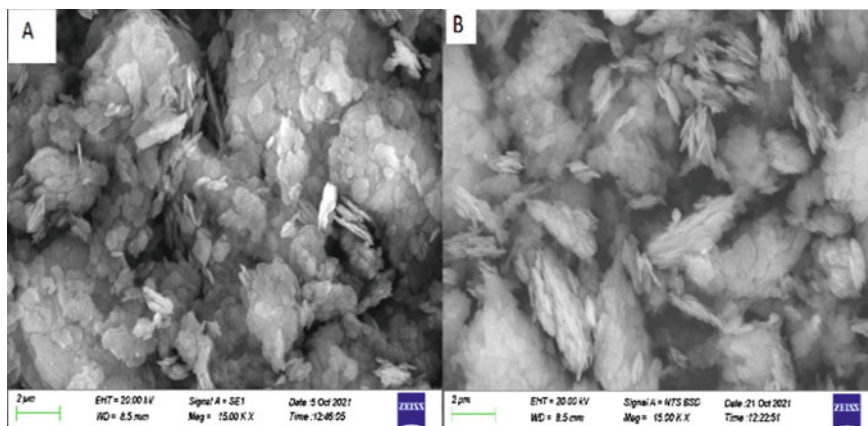


Fig. 3 a SEM images of kaolin and b thermally treated kaolin

treatment, the metals were liberated into the solution after the acid attacks the roasted matrix which apparently weakened the lamellar structure thermally.

3.3.1 HCl Leaching

Thermally treated Kaolin was treated with HCl in the aforementioned condition of 10% pulp density, i.e., the solid to a ratio (w/v), 90 °C and 2 h. The concentration of the acid was varied to get the optimum concentration of leaching. The composition of the leach liquor reveals the presence of mainly Al and Fe. The amount of acid was varied to optimize the condition and is presented in Fig. 4. It was observed that the extraction efficiency of Al was 34.07% in 1 M HCl which was increased to 86.59% in 2.5 M HCl. Further increase in HCl concentration up to 6 M results in an increasing efficiency of 88.41%.

Fig. 4 Variation of HCl concentration for the leaching of thermally treated kaolin. Condition: 10% PD, 90 °C, 2 h

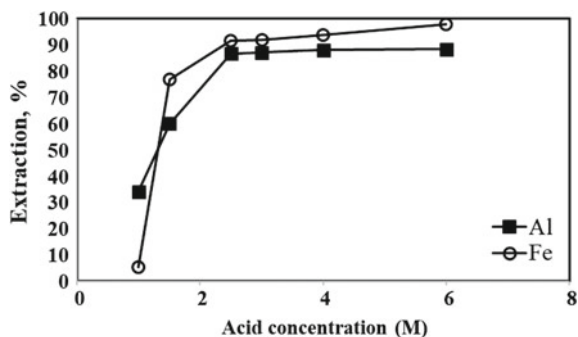


Table 3 H₂SO₄ leaching efficiency of thermally treated kaolin (condition: 10% PD, 90 °C, and 2 h)

Acid variation	Al, %	Fe, %
1 M	33.99	10.90
2 M	63.53	81.04
3 M	85.43	98.90

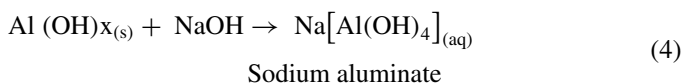
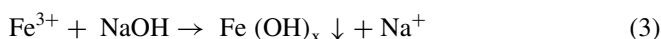
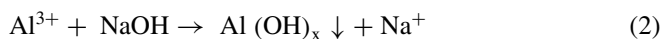
3.3.2 H₂SO₄ Leaching

Looking into the cost of HCl as well as the production of chlorine gas during the process makes the process not only costly but harmful to the biosphere also. So, the leaching with sulphuric acid was also tried with roasted Kaolin. The heat-treated Kaolin was treated with sulphuric acid at 90 °C and 2 h in 10% pulp density (w/v). The major elements that came into the solution were Al and Fe. The leaching results are presented in Table 3. The leaching efficiencies of sulphuric acid are in agreement with HCl leaching as with 1 M H₂SO₄ the leaching efficiency was 33.995 which was increased to 53.53% with 2 M H₂SO₄ and 85.43% with 3 M H₂SO₄. The leaching efficiency of iron was also increased from 10.90 to 98.90% which needs separation downstream.

It is well observed that after calcination, the acid successfully attacks the matrix thereby dissolving alumina from the surface. In this way, alumina and silica are separated where the silica portion is reported to the residue and alumina to the leach liquor. The extraction of alumina before calcination was hardly 2–4% but it increased sharply to 88.41% in the HCl system and 85.43% in the sulphuric acid system. The good part is that sulphuric acid leaching can replace HCl leaching as it has a similar leaching efficiency. The process in fact is economical as well as ecologically safe to operate.

3.4 Precipitation and Recovery of Alumina

In order to separate aluminium and iron present in the solution and to get high pure alumina, the solution is allowed to get precipitated. For this, the leach liquor was treated with 10 M sodium hydroxide (NaOH) to increase the pH of the solution up to pH 7.0 where both Al and Fe were precipitated as their corresponding hydroxides as per Eqs. (2) and (3):



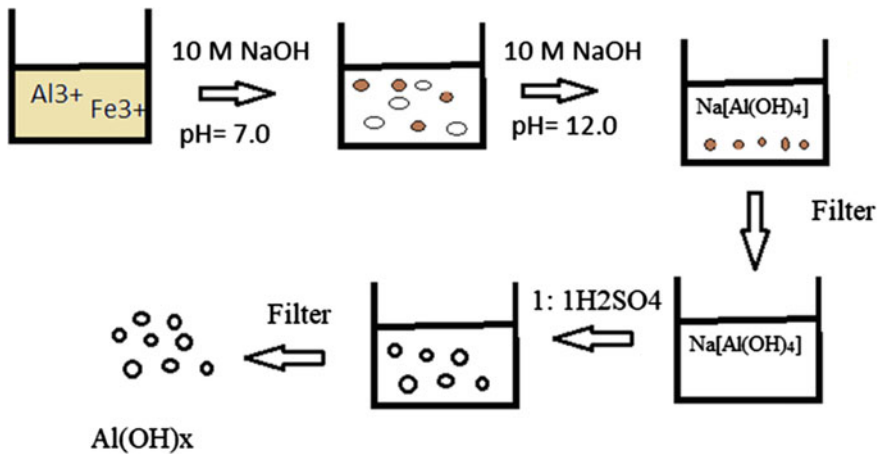
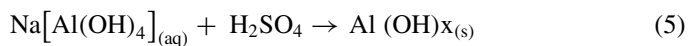


Fig. 5 Schematic diagram of precipitation



The precipitated aluminium hydroxide is re-dissolved in the form of sodium aluminate with the addition of excess alkali up to pH 12.0, whereas $\text{Fe}(\text{OH})_x$ doesn't dissolve. In this stage, it is filtered where aluminium and iron are separated. The alkaline leach liquor now contains only aluminium as sodium aluminate. The pH of the sodium aluminate was decreased by adding 1:1 sulphuric acid again, and again a white precipitate of aluminium hydroxide was obtained. That was collected, and washed. It was calcined at 800 °C to get alumina. A schematic diagram is provided in Fig. 5 to better understand the precipitation process.

It is also observed that if pH is increased up to pH 3.0 to 3.8 where iron is precipitated as iron hydroxide but the standard pH of precipitation of aluminium is at pH 4.2. But due to the local precipitation effect and others, the clear separation of iron and aluminium precipitation is not there. So, if the precipitation was stopped at pH 4 and precipitated aluminium is also reported in the residue of iron, the aluminium which is precipitated is less in amount. So, precipitation, re-dissolution, and re-precipitation route is a better option for the clear separation of aluminium and iron.

The aluminium hydroxide thus precipitated was subjected to calcination at 800 °C, and it was found that the structure matrix has a combination of alumina (Al_2O_3) and aluminium hydroxide ($\text{Al}(\text{OH})_3$). The XRD of the 800 °C calcined alumina is presented in Fig. 6. It is observed that there is the presence of alumina as well as aluminium hydroxide. Calcination at higher temperatures will convert the $\text{Al}(\text{OH})_3$ phases completely to the activated alumina phase.

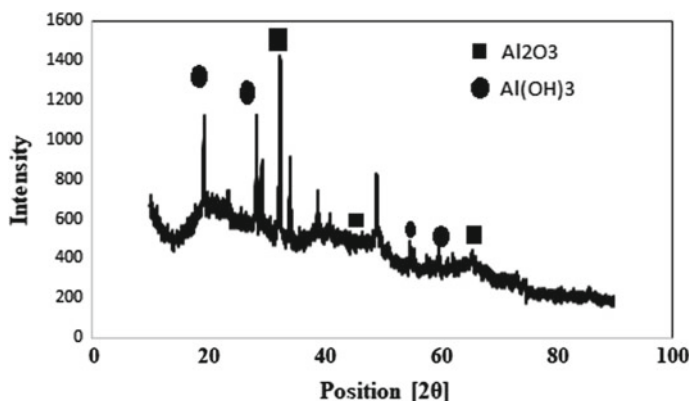


Fig. 6 XRD of calcined $\text{Al}(\text{OH})_3$ at $800\text{ }^\circ\text{C}$

4 Conclusion

The feasibility of extraction of alumina from kaolin is studied here. Kaolin in its original form is resistant to acid attacks. After thermal treatment at $850\text{ }^\circ\text{C}$ for 2 h, metal liberation of $>85\%$ was observed through acid leaching with both HCl and H_2SO_4 . The pH acid leach liquor was increased up to 7.0 where aluminium and iron are precipitated as hydroxides. To separate them, the pH was again raised up to 12.0 where aluminium hydroxide is re-dissolved as sodium aluminate and iron was left in its solid form of ferric hydroxide. The aluminium-bearing liquor was treated with H_2SO_4 to re-precipitate aluminium hydroxide which after calcination at $800\text{ }^\circ\text{C}$ produces activated alumina. It was found that the extraction efficiencies of HCl leaching and sulphuric acid leaching are very much similar. So, it is also proposed that sulphuric acid leaching can replace HCl leaching for extraction of alumina from Kaolin which is economically and ecologically more viable. This process can be employed to extract alumina from Kaolin and similar clay materials to fulfil the demand for metallurgical and non-metallurgical grade alumina.

Acknowledgements The authors would like to thank the Director, CSIR-IMMT, for supporting this research work. The authors are also thankful to MoES for providing facilities which have supported the work a lot.

References

1. Tantawy MA, Alomari AA (2019) Extraction of alumina from Nawan kaolin by acid leaching. *Orient J Chem* 35:1013–1021
2. Ali AH, Al-Taie MH, Ayoob IF (2019) The extraction of alumina from kaolin. *Eng Technol J* 37:133–139

3. Numluk P, Chaisena A (2012) Sulfuric acid and ammonium sulfate leaching of alumina from Lampang clay. *E-J Chem* 9:1364–1372
4. Colina FG, Esplugas S, Costa J (2002) High-temperature reaction of kaolin with sulfuric acid. *Ind Eng Chem Res* 41(17):4168–4173
5. Park SS, Hwang EH, Chan BC, Park HC (2000) Synthesis of hydrated aluminum sulfate from kaolin by microwave extraction. *J Am Ceram Soc* 83:1341–1345
6. Park JH, Kim SW, Lee SH, Kim HS, Park SS, Park HC (2020) Synthesis of alumina powders from kaolin with and without ultrasounds. *Mesoporous Microporous Mater* 109795
7. ElDeeb AB, Brichkin VN, Kurtenkov RV, Bormotov IS (2019) Extraction of alumina from kaolin by a combination of pyro- and hydro-metallurgical processes. *Appl Clay Sci* 172:146–154
8. Hulbert SF, Huff DE (1970) Kinetics of alumina removal from a calcined kaolin with nitric, sulphuric and hydrochloric acids. *Clay Miner* 8:337–345
9. Lu M, Xia G, Cao W (2017) Iron removal from kaolin using thiourea dioxide: effect of ball grinding and mechanism analysis. *Appl Clay Sci* 143:354–361
10. Bhattacharyya S, Behera PS (2017) Synthesis and characterization of nano-sized α -alumina powder from kaolin by acid leaching process. *Appl Clay Sci* 146:286–290
11. Yadav AK, Bhattacharya S (2002) A new approach for the fabrication of porous alumina beads using acid leachate of kaolin. *J Mater Synth Process* 10:289–293
12. ElDeeb AB, Brichkin VN, Bertau M, Savinova YA, Kurtenkov RV (2020) Solid state and phase transformation mechanism of kaolin sintered with limestone for alumina extraction. *Appl Clay Sci* 196:105771
13. Pak VI, Kirov SS, Nalivaiko AU, Ozherelkov DY, Gromov AA (2019) Obtaining alumina from kaolin clay via aluminum chloride. *Materials* 12:3938
14. Ibrahim KM, Moumani MK, Mohammad SK (2018) Extraction of γ -alumina from low cost kaolin. *Resources* 7:63
15. China CR, Hilonga A, Maguta MM, Nyandoro SS, Kanth SV, Jayakumara GC, Njau KN (2019) Preparation of aluminium sulphate from kaolin and its performance in combination tanning. *SN Appl Sci* 1:920
16. Said S, Mikhail S, Riad M (2020) Recent processes for the production of alumina nano-particles. *Mater Sci Energy Technol* 3:344–363
17. Hosseini SA, Niaei A, Salari D (2011) Production of γ -alumina from kaolin. *Open J Phys Chem* 1:23–27

Effect of Rheology on Filtration of a Brecciated Limestone Ore Slurry



Md. Serajuddin, Amit Bhai Patel, Sulekha Mukhopadhyay,
and K. Anand Rao

1 Introduction

Fine particles are very commonly transported and used, in the form of slurry at different stages in mineral, chemical, and other industries. The rheology of slurry is the most important property that governs the motion of these fine particles. Rheology is a well-established discipline dealing with the flow and deformation of materials and finds applications in several engineering fields. Even though the fundamentals of rheology as science are well known, it is not as much used in mineral processing as compared to other engineering fields such as pharmaceutical and polymer industries [1]. Mineral slurries generally show non-Newtonian type rheological behavior characterized by a non-linear relationship between shear stress and shear rate with the complex flow or deformation patterns [2, 3]. The slurry rheology is closely related to its physicochemical properties. It is affected by several factors such as shear rate, shear time, solid concentration, slurry temperature, particle size and particle size distribution (PSD), particle shape, surface charge, pH, and suspending medium [4]. At higher solid concentrations, the yield stress may be developed in the slurry, and/or it becomes time-dependent because of the formation of network structures of agglomerates.

Md. Serajuddin (✉) · A. B. Patel · K. A. Rao
Mineral Processing Division, Bhabha Atomic Research Centre (BARC), AMD Complex,
Begumpet, Hyderabad 500016, Telangana, India
e-mail: md_serajuddin@yahoo.com

Md. Serajuddin · S. Mukhopadhyay
Department of Engineering Sciences, Homi Bhabha National Institute (HBNI), Anushaktinagar,
Mumbai 400094, Maharashtra, India

S. Mukhopadhyay
Chemical Engineering Division, Bhabha Atomic Research Centre (BARC), Mumbai 400085,
Maharashtra, India

A lot of operational difficulty in the measurement of slurry rheology is experienced while handling low viscous heterogeneous slurries due to fast settling of particles, non-ideal flow conditions, turbulence created, formation of Taylor vortices, etc. [5, 6]. It is well known that several processes such as mixing, unit operations based on mass transfer, and separation processes are affected by the flow behavior of the slurries. These includes grinding [4, 7, 8], flotation [5, 6], solid–liquid separation (filtration) [9, 10], leaching [3], pipeline transportation [11, 12], and mixing [13]. The rheological behavior of slurries indicates the level of inter-particle interaction or aggression in the slurry [5, 7]. It is therefore a useful variable to be controlled in industrial processes [8]. The understanding of slurry rheology is thus essential for maximizing their efficiencies.

A brecciated limestone uranium ore from Gogi (Karnataka, India) requires very fine grinding and alkaline leaching as the uranium values are finely disseminated in the carbonate host rock. The very fine grind size of this slurry and its high alkalinity makes solid–liquid separation an arduous task [14]. In addition, as the ore contains a mixture of minerals, its rheological behavior differs from that of pure minerals.

A few attempts, mostly for sludge used in wastewater treatment plants, were made in the past to correlate the rheological behavior of slurry/sludge with the filtration parameters, such as specific resistance to filtration (SRF), cake solid content, filtrate suspended solids, and capillary suction time (CST) [9, 10, 13, 15]. However, the research dealing with the rheological behavior of fine-grained mineral slurry with high alkalinity and correlating it with the filtration rate has not been reported in the literature. In the present work, the rheological behavior of the aforementioned ore slurry (9.5–10 in situ pH) was investigated. The effect of solid concentration, temperature, particle size and particle size distribution, shearing time, and dosages of surfactant on the slurry rheology was studied. In addition, the rheological behavior of the slurry was correlated with the filtration rate. The present study provides vital data for the design of a filter unit and optimization of its operating parameters.

2 Materials and Methods

2.1 Materials

The rheology and filtration experiments were conducted on an exploratory mine brecciated uranium ore sample received from Gogi, Karnataka, India. The density of the ore is 2680 kg/m^3 . A machine based on the X-ray diffraction technique, the GE-XRD-3003 TT machine (Germany), was used to identify the mineral phase present in the brecciated limestone ore (Table 1). Uraninite and schoepite were identified as the atomic minerals along with calcite and quartz as the major gangue minerals in the ore sample.

Table 1 Mineralogical composition of the brecciated limestone ore sample

Minerals	wt%
Calcite	62.1
Quartz and chert	12.9
Sulfides (chalcopyrite, marcasite, pyrite, and galena in traces)	6
Micaceous minerals (biotite, chlorite, and clay)	6
Feldspars	1.6
Barite	0.6
Oxides (hematite, goethite, and magnetite)	0.5
Ferromagnesian minerals (hornblende mainly; epidote in less quantity)	0.4
Zircon	0.1
Radioactive minerals	0.9
Others (by difference)	8.9
Total	100

Table 2 Partial chemical analysis of the brecciated limestone ore sample

Analyte	CaCO ₃	MgCO ₃	SiO ₂	Fe ^T	Mo	P ₂ O ₅	S	LOI	U ₃ O ₈
Percentage (w/w)	60.9	0.0001	19.8	3.4	0.003	0.0002	2.6	27.5	0.23

The Inductively Coupled Plasma-Optical Emission Spectrometer (ICP-OES), supplied by M/s Horiba Jobin Yvon (ULTIMA 2, France), was used for the chemical analysis of the sample. The ore contains 0.23% U₃O₈, 61% CaCO₃, and 2.6% total sulfur (Table 2). A surfactant, namely Guar gum, supplied by M/s H.B. Gum Industries of Gujarat, was tested for improvement in the rheological behavior of the slurry.

2.2 Methods

2.2.1 Particle Size Analysis

Four particle sizes of 92, 66, 57, and 53 μm (d_{90} , 90% passing size) were generated by several stages of crushing using jaw and roll crushers followed by ball mill grinding. The particle size and particle size distribution of solid samples were determined using a laser particle size analyzer, based on the diffraction technique (CILAS-1090, France).

2.2.2 Rheological Measurements

A Modular Compact Rheometer (MCR-52, Anton-Parr, Austria) was used to characterize the rheological behavior of the ore slurry. Measurement setup with concentric cylinder geometry (gap width = 1.639 mm) was used. The instrument is based on the Searle principle. A thermal jacket around the sample holder enables temperature control (−5 to 200 °C). The rheograms and flow curves were generated under the controlled shear rate (CSR, 100–1400 s^{−1}) test mode. This test mode was chosen as it simulates the processes that are dependent on fluid velocities such as mixing, pumping, and pipe flow processes. At the highest shear rate, the slurry was pre-sheared for a specified time period, and the measurement was taken in a step-down fashion. A known quantity of thoroughly mixed slurry (about 70 mL) was withdrawn for each test.

The rheological behavior of the slurry or suspension is generally modeled using the Power-law, Bingham plastic, Herschel–Bulkley, Casson, and Sisko models [4, 7, 9, 16–19]. The non-Newtonian fluid behavior of the slurry was modeled here using the Herschel–Bulkley (H.B. model) (Eq. 1) [16]

$$\tau = k\gamma^m + \tau_y \quad (1)$$

where τ indicates shear stress; τ_y is yield stress; k and m are model coefficients. This model allows us to study the rheograms or flow curves on the complete shear rates ($\dot{\gamma}$) range investigated.

The variation of temperature was modeled using the Arrhenius type model equation, whereas the particle size distribution (PSD) was modeled using the Rosin Rammler particle size distribution model.

2.2.3 Filtration Tests

The filtration studies were conducted with Whatman filter paper (541) at a fixed vacuum of 650 mm Hg using a standard laboratory vacuum filtration system which includes a Buchner funnel of diameter 12 cm.

3 Results and Discussion

During parametric variation studies, the fixed condition was taken as 50% solids (w/w), 53 μm particle size (d_{90}), and 30 °C temperature, unless mentioned otherwise, and solid concentration in w/w.

3.1 Effect of Solid Concentration

The rheograms of the ore slurry at different solid concentrations (10–75%) are shown in Fig. 1a, b. The nature of the curve is very different at higher solid concentrations (>60%), which is why it is shown separately in Fig. 1a, b. These two plots indicate that shear stress non-linearly increases with shear rate. These figures also indicate that shear stress increases with solid concentration, which is more obvious when the shear rate is high. The H.B. model coefficients (k , m , and τ_y) obtained at different solid concentrations are given in Table 3. The predicted shear stress obtained using the H.B. model coefficients are also shown in Fig. 1a, b along with the experimental data. The apparent viscosity was found to decrease at higher shear rates (Fig. 1c) for all solid concentrations.

The H.B. model gives an approximate value of the yield point and an indication of the dilatant or pseudo-plastic behavior of the suspension. This model was found to

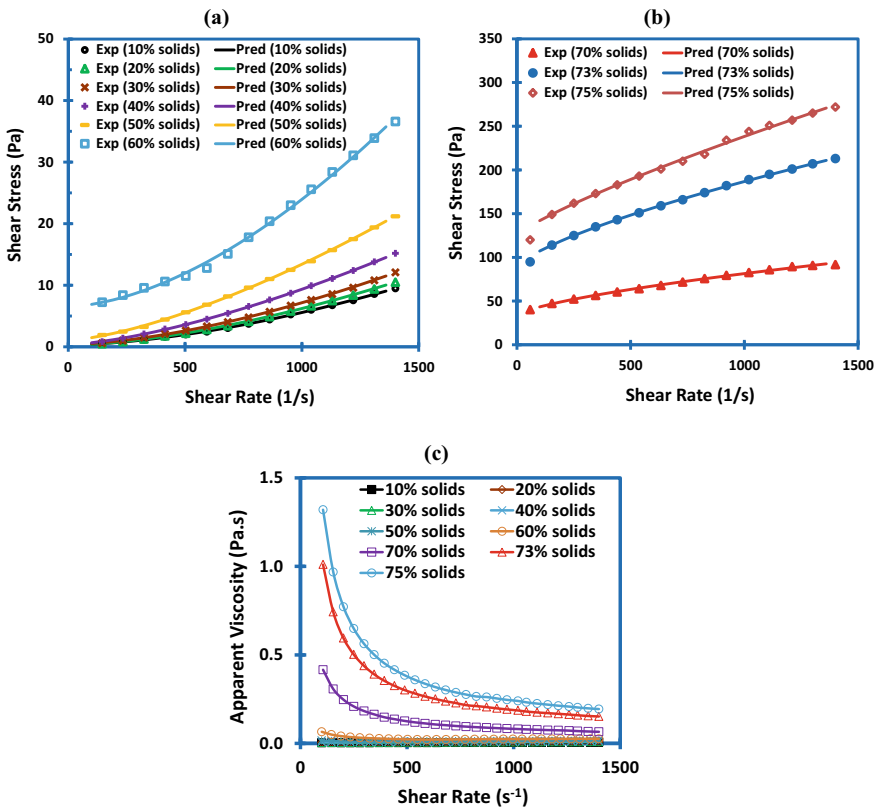


Fig. 1 Shear stress **a** 10–60% and **b** 70–75% solids; apparent viscosity **c** 10–75% solids, against shear rate for different solid concentrations. From 10 to 60% solids, slurry is shear thickening and beyond that, its behavior is shear thinning

Table 3 The H.B. model coefficients for the ore slurry at different solid concentrations

% Solids (w/w)	k	m	τ_y	R^2
10	0.00006	1.649	0.250	0.9997
20	0.00009	1.608	0.258	0.9998
30	0.00010	1.607	0.356	0.9997
40	0.00033	1.478	0.360	0.9999
50	0.00051	1.461	1.058	0.9997
60	0.00016	1.681	6.528	0.9977
70	0.44390	0.679	33.250	0.9967
73	0.71810	0.713	88.080	0.9997
75	0.39890	0.818	124.700	0.9970

provide the best description of the flow curves for the brecciated limestone ore slurry. A good agreement between the experimental and predicted shear stress (regression coefficients, $R^2 > 0.998$) is quite obvious in these figures.

Figure 1 and Table 3 also indicate that the flow is weakly dilatants (shear-thickening) at 10–60% solids as $m > 1$ and pseudo-plastic (shear-thinning) at 70–75% solids as $m < 1$. Researchers have also reported similar flow behavior trends for different slurries of pure minerals such as limestone, quartz, sphalerite, and galena [17, 19]. It is believed that some order–disorder transition, which takes place at a critical shear rate (γ_c) under the application of shear, is responsible for the shear-thickening [19].

The observed pseudo-plastic behavior at higher solid concentration (70–75%) may be due to the disruption of the slurry structure by the applied shear. As the shear rate is increased, randomly arranged particulate matter orients them to the direction of the flow. This orientation lowers the internal friction and resistance of the particles to flow, resulting in a decrease in slurry viscosity [12].

Table 3 and Fig. 2a indicate that the H.B. yield stress (τ_y) increases with solid concentration in the range studied. Furthermore, the increase of yield stress is very sharp with an increase in solid concentration (>60%). Other researchers also reported similar behavior [16]. In addition, the trend of the curve also indicates strong interactions among the particles in the slurry at higher solid concentration range (70–75%). This is due to small inter-particle distances occurring in the denser slurry that produces increased inter-particle attractive forces.

The relation between solid concentration and apparent viscosity at a given shear rate (Eq. 2) can be written as [17]

$$\mu = a(\gamma)e^{b(\gamma)\phi} \quad (2)$$

where μ stands for apparent viscosity; Φ is solid concentrations (v/v); $a(\gamma)$ and $b(\gamma)$ are coefficients related to a fixed shear rate. Figure 2b indicates that the viscosity of the ore slurry exponentially increases with solid concentration at randomly selected

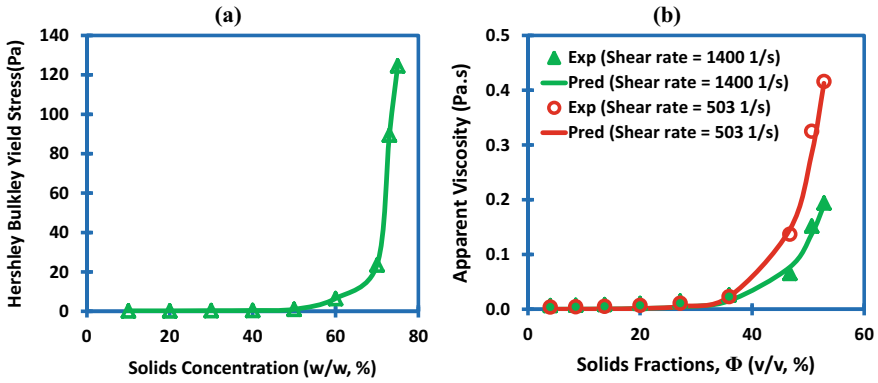


Fig. 2 a The H.B. yield stress; b apparent viscosity versus solid concentration

shear rates of 1400 and 503 s^{-1} . In addition, beyond 52.8% (v/v) or 75% (w/w) solid, the slurry viscosity increases rather sharply and tends to infinity at limiting solid concentration. The same trend is also observed (Fig. 3a) when the apparent viscosity (μ) changed to relative viscosity (μ_r), which is defined as the viscosity of the slurry in respect of the viscosity of the liquid medium (μ_0), i.e. $\mu_r = \mu/\mu_0$.

The shear rate-dependent coefficients obtained using Eq. 2 are given in Table 4, which indicates that as the shear rate increases, values of $a(\gamma)$ increase whereas the values of $b(\gamma)$ decrease. The predicted apparent viscosities using these coefficients are also shown in Fig. 2b. A perfect fit between the predicted and experimental values is quite obvious in this figure.

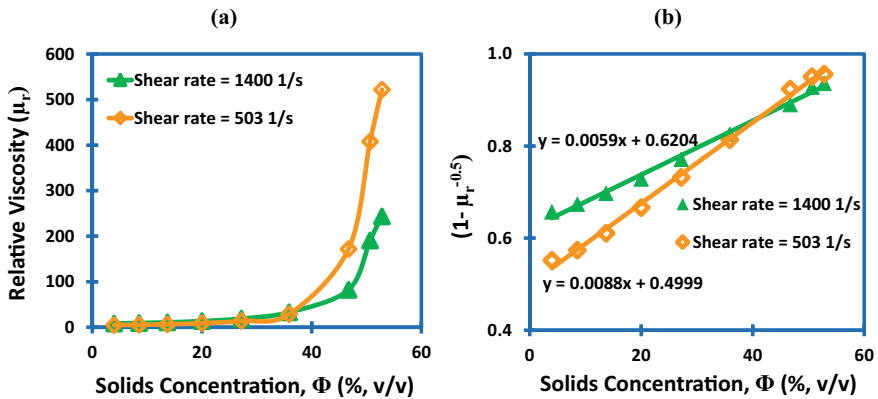


Fig. 3 a Relative viscosity; b $(1 - \mu_r^{-0.5})$ versus solid concentration

Table 4 Shear rate-related coefficient of model equation (Eq. 2) interlinking apparent viscosity and solid concentration by volume

Shear rate ($\dot{\gamma}$)	a ($\dot{\gamma}$)	b ($\dot{\gamma}$)
1400	0.0000749	0.1484
503	0.0000496	0.1709

3.1.1 Maximum Solid Loading

The maximum solid volume fraction (Φ_m) is defined as a value of solid volume fraction at which relative viscosity becomes infinite and the slurry no longer flows. This value can be determined by two methods: (a) using the experimental data from rheological measurements and (b) using a theoretical approach. By the experimental method, a plot of relative viscosity as a function of solid volume fractions (Fig. 3a) was used, and Φ_m was taken, as a value of Φ for which a sharp increase in the viscosity was observed, as 0.640 and 0.585 at a fixed shear rate of 1400 and 503 s^{-1} , respectively.

By theoretical approach, the Liu model can be used to calculate Φ_m directly. This model gives a relation (Eq. 3) between the volume fraction of solids (Φ) in the slurry and the relative viscosity (μ_r) [17, 19]

$$1 - \mu_r^{-\frac{1}{u}} = a\phi + b \quad (3)$$

where μ_r is a relative viscosity, u is an integer, and a and b are the constants. Here, u is a suspension-dependent parameter in the range of 2–4 ($u = 2$ at high shear rates) [19]. It is clear that when Φ closes Φ_m , the relative viscosity of the suspensions becomes infinite. Thus, $\Phi_m = [(1 - b)/a]$ or Φ_m can be determined by the extrapolation of the linear line of $1 - \mu_r^{-1/u}$ to 1.0. A plot of $(1 - \mu_r^{-1/2})$ versus Φ (Fig. 3b) gives Φ_m as 0.647 and 0.569 at a fixed shear rate of 1400 and 503 s^{-1} , respectively. It is interesting to note that the Φ_m determined experimentally from Fig. 3a and theoretically from Fig. 3b are in close agreement. In addition, the linear curve with good correlation shown in Fig. 3b indicates that the assumption made for the exponent u as 2 is indeed valid. Moreover, the maximum packing volume fraction, 0.647, obtained at a shear rate of 1400 s^{-1} , is very close to the theoretical random close packing for the spheres (0.64) [19, 20].

The variation of shear stress and apparent viscosity along with filtration rate as a function of solid concentration is shown in Fig. 4. It is seen from the figure that an increase in shear stress at higher solid concentration resulted in a decrease in filtrate rate from 905 $m^3/(h \cdot m^2)$ at 10% to 64 $m^3/(h \cdot m^2)$ at 73% solids (w/w). The decrease in the filtration rate is due to an increase in slurry viscosity at higher solid concentration.

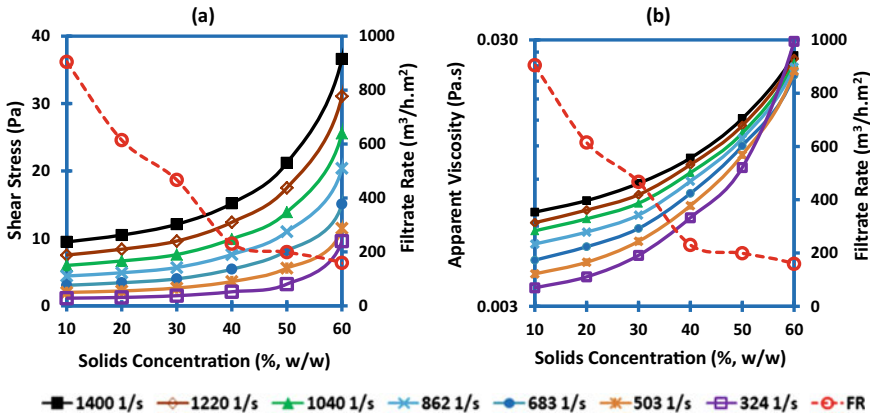


Fig. 4 a Shear stress; b apparent viscosity with filtration rate against solid concentration at fixed shear rates

3.2 Effect of Slurry Temperature

The rheograms (flow curves) of the ore slurry (Fig. 5) indicated that the flow behavior does not change when the temperature changes. However, both shear stress and apparent viscosity decreased with an increase in temperature. The viscosity of the slurry decreased from 0.0165 to 0.012 and 0.0118 to 0.00922 Pa·s at a shear rate of 1400 s⁻¹ and 234 s⁻¹ respectively at 50% solids. The corresponding reduction in apparent viscosity is 0.169 to 0.111 and 0.591 to 0.410 Pa·s with 73% solids. This trend is consistent with the results reported by other researchers [18].

Table 5 gives the H.B. model coefficients obtained at different temperatures. The predicted (using Table 5) and experimental shear stress are shown in Fig. 5a, b for 50% and 73% solids, respectively. In this case too, R² values > 0.998 were obtained between the experimental and predicted shear stress for all temperature ranges studied.

Viscosity dependent on temperature is well established. The relation between these two can be represented by the Arrhenius type equation as (Eq. 4 or 5) [18, 19]

$$\mu_r = Ae^{E/RT} \tag{4}$$

$$\ln\mu_r = \frac{E}{RT} + \ln A \tag{5}$$

where μ_r indicates relative viscosity at a particular shear rate; E is fluid flow activation energy (J/mol); T is temperature (Kelvin), R is universal gas constant (J/mol·K), and A is model parameter. A plot of $(\ln(\mu_r))$ versus $(1/T)$ was drawn and is shown in Fig. 6. The slope of this curve gives the fluid flow activation energy as 5.76 and 7.67 kJ/mol at 50% and 73% solids respectively at a shear rate of 1120 s⁻¹. The

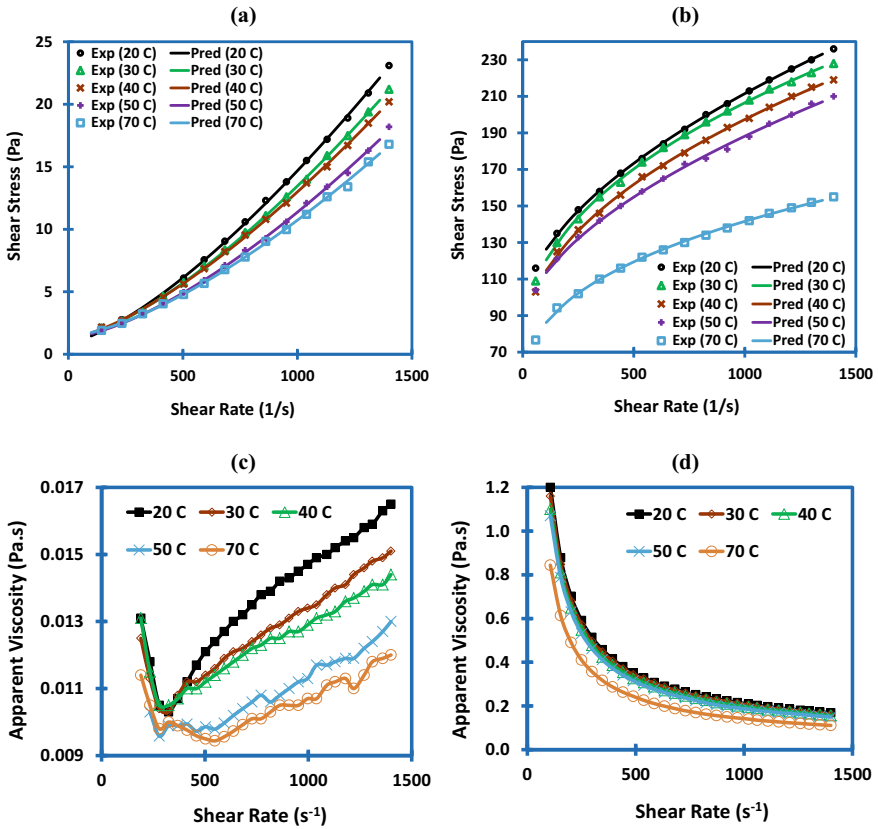
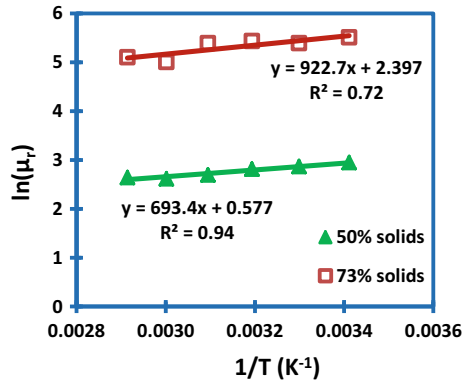


Fig. 5 Shear stress **a** 50% and **b** 73% solids; apparent viscosity **c** 50% and **d** 73% solids against shear rate for different slurry temperatures (in °C)

Table 5 The H.B. model coefficients for the ore slurry at different temperatures

% Solids (w/w)	Temperature (°C)	k	m	τ_y	R^2
50	20	0.00083	1.407	0.924	0.9993
	30	0.00055	1.449	1.206	0.9997
	40	0.00065	1.419	1.250	0.9996
	50	0.00036	1.484	1.300	0.9993
	70	0.00035	1.475	1.429	0.9990
73	20	2.60300	0.554	91.830	0.9998
	30	6.09300	0.449	71.030	0.9996
	40	4.41900	0.484	72.520	0.9994
	50	2.40700	0.547	82.610	0.9987
	70	7.78800	0.368	43.000	0.9990

Fig. 6 Effect of slurry temperature on relative viscosity at a fixed shear rate of 1120 s^{-1}



high activation energy at 73% solids indicates the strong sensitivity of viscosity to temperature. Thus, at a fixed shear rate, activation energy increases with solid concentration. In other words, the viscosity of the thicker slurry is more influenced by temperature.

The variation of shear stress and apparent viscosity along with filtration rate as a function of slurry temperature is shown in Fig. 7. The cohesive force between the molecules reduces when the slurry is subjected to heat, due to thermal motion. It then results in a decrease in shear stress as well as fluid viscosity [16]. Thus, a decrease in viscosity at higher temperatures resulted in an increase in filtrate rate from $199 \text{ m}^3/(\text{h}\cdot\text{m}^2)$ at $30 \text{ }^\circ\text{C}$ to $393 \text{ m}^3/(\text{h}\cdot\text{m}^2)$ at $70 \text{ }^\circ\text{C}$.

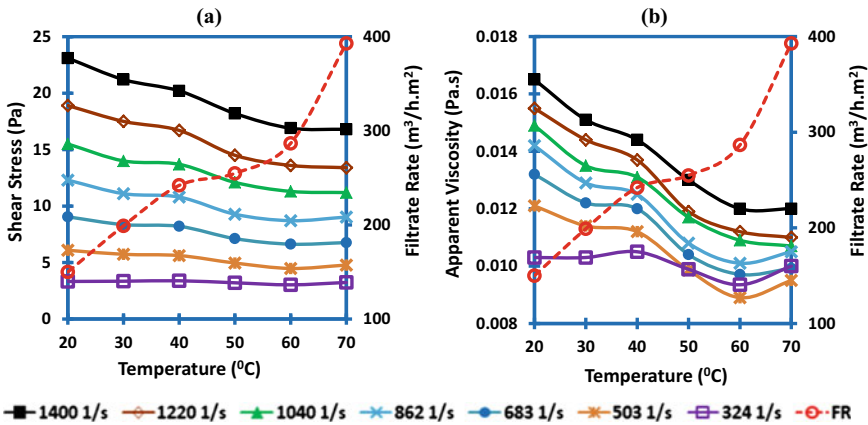


Fig. 7 a Shear stress; b apparent viscosity with filtration rate against slurry temperature at fixed shear rates

3.3 Effect of Particle Size and Particle Size Distribution

The rheological behavior of the ore slurry was investigated with four-particle sizes and particle size distributions (d_{90} of 92, 66, 57, 53 μm) along with two solid concentrations (50 and 73%). The particle size distribution of the ore was modeled using the well-known Rosin–Rammler particle size distribution model (Eq. 6) [17]

$$P = 1 - e^{-\left(\frac{d}{d_0}\right)^n} \tag{6}$$

where P stands for cumulative weight % passing size d ; d_0 is fineness or size modulus; and n is particle size distribution modulus.

Figure 8 shows a plot of cumulative wt% passing as a function of particle size. The Rosin–Rammler model coefficients obtained at different sizes are given in Table 6, whereas the H.B. model coefficients are given in Table 7. The flow curves at different particle sizes are shown in Fig. 9. The predicted and experimental shear stress as a function of shear rate for 50% solids is shown in Fig. 9a whereas for 73% solids in Fig. 9b. Coefficient of regression (R^2) values > 0.99 are given in Table 7, indicating a perfect correlation between the predicted and experimental shear stress for all particle sizes studied.

Fig. 8 A plot of cumulative wt% passing versus particle size

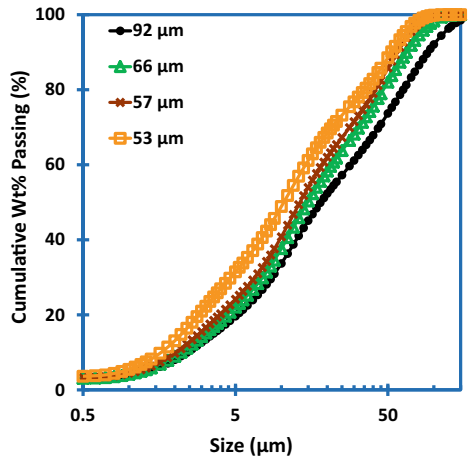


Table 6 The Rosin–Rammler model coefficients obtained at different sizes

Particle size, d_{90} (μm)	d_0	n	R^2
92	32.33	0.86	0.9972
66	24.73	0.92	0.9983
57	21.11	0.95	0.9979
53	17.27	0.96	0.9955

Table 7 The H.B. model coefficients for the ore slurry at different sizes

% Solids	d_{90} (μm)	k	m	τ_y	R^2
50	92	0.00025	1.555	0.502	0.9995
	66	0.00032	1.519	0.512	0.9992
	57	0.00052	1.449	0.574	0.9997
	53	0.00051	1.461	1.058	0.9997
73	92	0.29870	0.802	38.280	0.9980
	66	0.42790	0.759	45.800	0.9989
	57	0.40640	0.769	52.150	0.9982
	53	1.36700	0.633	78.780	0.9992

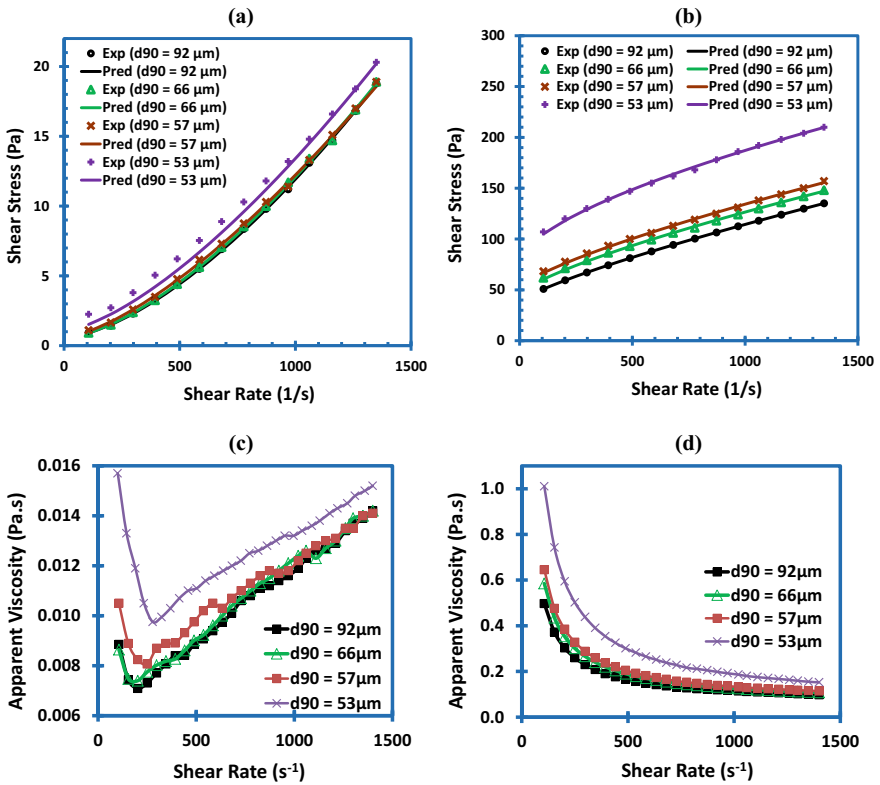


Fig. 9 Shear stress **a** 50% and **b** 73% solids; apparent viscosity **c** 50% and **d** 73% solids against shear rate for different sizes

The extrapolated H.B. yield stress exponentially increases with particle size distribution modulus (n), whereas it decreases with an increase in characteristic sizes (i.e. d_{90} and d_0). A similar conclusion is also drawn by other researchers for coal and other mineral slurries [18]. Shear stress and apparent viscosity with filtration rate as a function of particle size are shown in Fig. 10. Though the trends of the flow curves are similar, it was found that as the slurry becomes finer, it results in more viscous slurry both at 50 and 73% solids. The high apparent viscosity at finer sizes is due to an increase in the specific surface area of the particles (because of the presence of more fine-size particles), which resulted in a decrease in the inter-particle distance, and therefore, stronger inter-particle attractions.

As indicated earlier, slurry with finer particles ($d_{90} < 55 \mu\text{m}$) results in viscous slurry, which ultimately makes filtration very difficult. Thus, the filtrate rate was reduced from 400 to 199 $\text{m}^3/(\text{h}\cdot\text{m}^2)$ at 50% solids and 150 to 100 $\text{m}^3/(\text{h}\cdot\text{m}^2)$ at 73% solids when the particle size (d_{90}) changed from 92 to 53 μm .

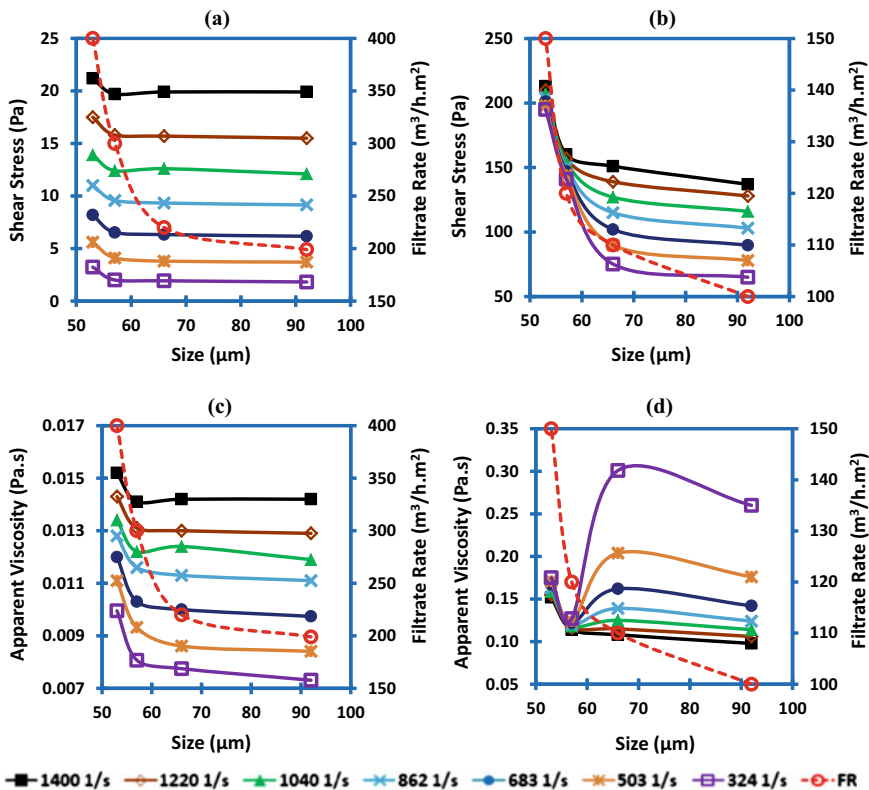


Fig. 10 Shear stress a 50% and b 73%; apparent viscosity c 50% and d 73% solids with filtration rate against particle sizes at fixed shear rates

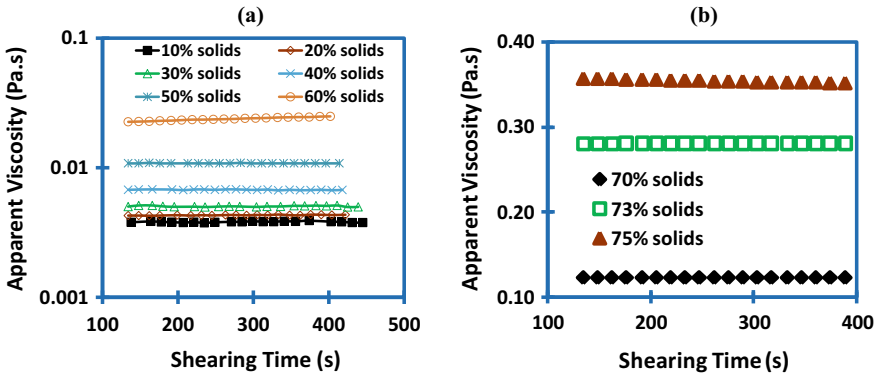


Fig. 11 Apparent viscosity a 10–60% and b 70–75% solids versus shearing time at a shear rate of 500 s⁻¹

3.4 Effect of Shearing Time

The dependence of time on the flow behavior was carried out for different solid concentrations for 8 min of shear. As indicated in Fig. 11a, up to a solid concentration of 60%, the viscosity of the slurry is nearly constant and is almost independent of the time of shear at 500 s⁻¹ (fixed shear rate). However, the ore slurry with >60% solids (70, 73, and 75%), which is shown in Fig. 11b indicated that the viscosity of the slurry decreased as the shear time increased. This indicates that shear time at a particular shear rate affects the flow behavior of the system. Furthermore, the viscosity of the slurry becomes saturated after a time period of about 176 s and 374 s respectively for 73% and 75% solid concentration. Thus, a thixotropic phenomenon occurs with highly pseudo-plastic material [3]. Agglomerated or flocculated suspensions are a typical example that shows shear-thinning behavior with definite yield stress associated with thixotropic characteristics. At rest, this type of system imparts rigidity to a system resembling a gel. As shear is applied, the structure begins to break and the material undergoes gel to sol kind of transformation [19].

3.5 Effect of Surfactant Dosages

The addition of dewatering aids changes the rheological behavior of the slurry and helps in its faster settling and filtration at an optimum dosage [10]. In uranium ore processing, Guar gum, which is a non-ionic natural surfactant, is frequently used as a dewatering aid. The variation of apparent viscosity along with filtration rate as a function of Guar gum dosages is shown in Fig. 12. The H.B. model coefficients, *m* and τ_y obtained at different dosages of Guar gum range from 1.408 to 1.610 and 0.827 to 2.067 Pa, respectively. It was found that even at a dosage of 500 g/t, the

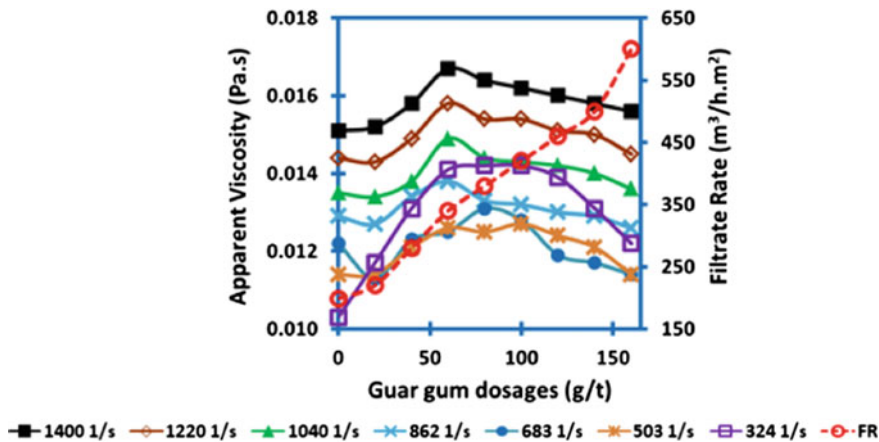


Fig. 12 Apparent viscosity and filtration rate against Guar gum dosages at fixed shear rates

shear stress (<23.4 Pa) or viscosity (<0.0167 Pa·s) has not increased appreciably. Furthermore, Guar gum might have reduced the surface tension of the liquid and helped in particle agglomeration [11, 15], thereby increasing the filtrate rate from 199 m³/(h·m²) (without surfactant) to 600 m³/(h·m²) at a dosage of 160 g/t.

4 Conclusions

The rheological behavior of a brecciated limestone ore slurry was investigated in the present study. The Herschel–Bulkley model was used to describe the rheological behavior of the slurry, and the model was found in good agreement with experimental data in the entire shear rate range. The rheological behavior changed from weakly dilatants to pseudo-plastic when solid concentration exceeds 60% (w/w). The shear stress, apparent viscosity, and yield stress increased exponentially with solid concentration in the range of 10–75% (w/w). This increase resulted in a decrease in filtration rate at higher solid concentration, because of small inter-particle distances and more inter-particle attractive forces occurring in denser slurry. A linear relationship was observed between relative viscosity and reciprocal temperature for the system investigated. A decrease in shear stress and viscosity resulted in an increase in filtration rate at elevated temperatures because of a reduction in cohesive force between the molecules due to a thermal motion. The slurry with more fines (<55 μm) increased the shear stress and made the slurry more viscous, which resulted in a decrease in filtration rate due to a decrease in inter-particle distance and stronger inter-particle attractions. At a fixed shear rate, an increase in shear time resulted in a decrease in the apparent viscosity of the slurry when solid concentration exceeds 70% (w/w). It was found that even at a high surfactant (Guar gum) dosage of 500 g/t, the shear stress or apparent viscosity has not increased appreciably, indicating that the Guar

gum can be used at a higher dosage. The Guar gum facilitates better wetting of the particles and reduces the resistance to flow, thereby increasing the rate of filtration. Furthermore, for the filtration process, it can be concluded that the changes in solid concentration, temperature, and particle size can be directly correlated with its rheological behavior. Having studied the effect of particle size on slurry rheology, the effect of particle shape could be part of future work. The measurement of zeta potential, specific resistance to filtration, moisture percent retained by the filter cake, cake washing efficiency, etc. can also be incorporated in future studies. The role of dewatering aids and the chemistry behind its adsorption on the mineral surface to form flocs and their impact on the slurry could be in the future scope of work.

Acknowledgements The authors are thankful to M/s Uranium Corporation of India Limited (UCIL) for providing the ore sample for the study. They also thank the Director, Materials Group, BARC, for their interest and encouragement in the present work.

References

1. Kudo Y, Yasuda M, Matsusaka S (2020) Effect of particle size distribution on flowability of granulated lactose. *Adv Powder Technol* 31:121–127
2. Wu D, Chen W, Glowinski D et al (2020) Modelling mineral slurries using coupled discrete element method and smoothed particle hydrodynamics. *Powder Technol* 364:553–561
3. MacCarthy J, Nosrati A, Skinner W et al (2015) Acid leaching and rheological behaviour of a siliceous goethitic nickel laterite ore: influence of particle size and temperature. *Miner Eng* 77:52–63
4. He M, Wang Y, Forssberg E (2004) Slurry rheology in wet ultrafine grinding of industrial minerals: a review. *Powder Technol* 147:94–112
5. Farrokhpay S (2012) The importance of rheology in mineral flotation: a review. *Miner Eng* 36–38:272–278
6. Wang L, Li C (2020) A brief review of pulp and froth rheology in mineral flotation. *J Chem* 2020:3894542
7. Faitli J, Bohacs K, Mucsi G (2017) Online rheological monitoring of stirred media milling. *Powder Technol* 308:20–29
8. Shi FN, Napier-Munn TJ (2002) Effects of slurry rheology on industrial grinding performance. *Int J Miner Process* 65:125–140
9. Koseoglu H, Yigit NO, Civelekoglu G et al (2012) Effects of chemical additives on filtration and rheological characteristics of MBR sludge. *Bioresour Technol* 117:48–54
10. Ormeci B (2007) Optimization of a full-scale dewatering operation based on the rheological characteristics of wastewater sludge. *Water Res* 41:1243–1252
11. Naik HK, Mishra MK, Karanam UMR et al (2009) Evaluation of the role of a cationic surfactant on the flow characteristics of fly ash slurry. *J Hazard Mater* 169:1134–1140
12. Usui HLH (2001) Rheology and pipeline transportation of dense fly ash-water slurry. *Korea-Aust Rheol J* 13:47–54
13. Das GK, Kelly N, Muir DM (2011) Rheological behavior of lateritic smectite ore slurries. *Miner Eng* 24:594–602
14. Sreenivas T, Rajan KC (2013) Studies on the separation of dissolved uranium from alkaline carbonate leach slurries by resin-in-pulp process. *Sep Purif Technol* 112:54–60
15. Jiang J, Zhou Y (2020) A specious correlation between sludge rheology and dewaterability. *Environ Sci Technol* 54:5928–5930

16. Baroutian S, Eshtiaghi N, Gapes DJ (2013) Rheology of a primary and secondary sewage slurry mixture: dependency on temperature and solids concentration. *Bioresour Technol* 140:227–233
17. He M, Wang Y, Forssberg E (2006) Parameter studies on the rheology of limestone slurries. *Int J Miner Process* 78:63–77
18. Yang HG, Li CZ, Gu HC et al (2001) Rheological behavior of titanium dioxide suspensions. *J Colloid Interface Sci* 236:96–103
19. Senapati PK, Panda D, Parida A (2009) Predicting viscosity of limestone–water slurry. *J Miner Mater Charact Eng* 8(3):203–221
20. Torquato S, Truskett TM, Debenedetti PG (2000) Is random close packing of spheres well defined? *Phys Rev Lett* 84(10):2064–2067

Integrated Approach for Extraction of Molybdenum and Silica from an Unexploited Nigerian Molybdenite Rich Ore



Adeyemi Christianah, Santosh Deb Barma, Mamata Mohapatra, Alafara A. Baba, and Suddhasatwa Basu

1 Introduction

The increased industrial demand for molybdenum metals has prompted study into its extraction from minerals and other secondary sources [1]. There are surplus mineral occurrences in Nigeria with the piqued interest of exploration and mining companies from around the world [2]. However, thorough investigation of their constituents as well as exploration and their economic viability, extensive research effort is required. The northern part of this country has deposits of molybdenum-based minerals, incorporated with other minor valuable metals. One of such typical minerals has been obtained from Kigom (9° 45' 50" N, 8° 37' 31" E), Jos, Plateau state, Nigeria. This particular kind of rock-based mineral is yet not exploited till date for any R&D ventures for feasible extraction of valuables. For these R&D efforts have been initiated through a sustainable hydrometallurgical approach to develop an integrated extraction of molybdenum and other associated metal from such ores. For these ores, many metallurgical processes, including dissolving molybdenum as a soluble chloride, sulfate, or nitrate and purifying the resulting liquor using various technologies such as solvent extraction, precipitation, electro-winning, or adsorption into activated matrices have been initiated [1] and the implementation of emerging technologies was heralded by the potential to reduce the risk of pollution of the ecosystem [3].

A. Christianah · S. D. Barma · M. Mohapatra (✉) · S. Basu
CSIR-Institute of Minerals and Materials Technology, Bhubaneswar 751013, India
e-mail: mamata@immt.res.in

A. Christianah · A. A. Baba
Department of Industrial Chemistry, University of Ilorin, P.M.B 1515, Ilorin 240003, Nigeria

A. Christianah
Department of Biochemical and Chemical Sciences, Federal Polytechnic, Offa, Kwara State, P.M.B 420, Offa, Nigeria

For example, Medvedev and Aleksandrov [4] worked on molybdenum extraction processing from the Bugdainskoe deposit by the nitric-acid method. The process initially occurred in the kinetic region before introducing H_2SO_4 which later prevents the formation of molybdic acid and hence accelerates the process, thereby leading to a high degree of Mo transfer into the solution. The optimum recovery of molybdenum with HNO_3 was not more than 94%, though with the addition of up to 100 g/L of sulfuric acid into the starting solution, the yield increases to 95.3%. Alvaro et al. [5] investigated the H_2O_2 - H_2SO_4 System, and the maximum molybdenum recovery of 81.3% was achieved. The derived activation energy (E_a) of 75.2 kJ/mol, first and zero order reactions, with a diffusion-controlled mechanism. Xie et al. [6] investigated direct leaching of molybdenum and lead from lean wulfenite raw ore containing 2.87% Mo and 9.39% Pb. The authors reported more than 99.7% of Mo and 64.6% of Pb under 75 °C, a ratio of 2:1, 100 rpm, and 80 g/L [NaOH] within 120 min. In this present study, an integrated method of treatment for the extraction of molybdenum and other associated metal values from Nigerian low-grade molybdenite by the hydrometallurgical process was established.

2 Material and Methods

2.1 Materials

The source material (hand-picked) is collected from Kigom village, Jos, Plateau state, Nigeria (9° 45' 50" N, 8° 37' 31" E). The chemicals used for the experiment were of analytical grade. Sulphuric acid and sodium hydroxides were obtained from Thermo Fisher Scientific India Pvt. Ltd (98.08% assay) and oxalic acid was from E-Merc, India.

2.2 Methods

2.2.1 Grinding and Sieving of the Source Material

As-received mineral was identified by a geologist; it was grinded, pulverized, and then sieved into three particle sizes: <50 μ , <63 μ , and <75 μ . The finest particle size (50 μ) was used for all the experiments unless otherwise stated.

2.2.2 Roasting

The treated sieved molybdenite of 50 μ particle size was roasted in a (Nabertherm 30–3000 °C) muffle furnace at a temperature between 400 and 600 °C for about 6 h

to further the dissolution experiments. During the roasting, a complete chemical and physical transformation occurred via the oxidation process.

2.2.3 Leaching Experiment

All leaching experiments were carried out in a closed 25 mL flask, with a required concentration of leachant at varying temperatures and durations. Constant stirring was provided during leaching at a defined speed which was controlled using a magnetic stirrer in a heating mantle (TARSONS DIGITAL SPINOT). The roasted sample was added to the reaction flask after the reaction temperature was reached. Evaporation of the reactants was prevented by covering the reaction flask throughout the experiment. Leaching time, concentration, and reaction temperature were varied while other parameters were kept constant. The effect of leaching time, leachant concentration, and reaction temperature on the extraction of molybdenum along with other minor minerals were investigated at 0–120 min, 0.5–3.0 mol/L and 30, 55, 65, 75, and 90 °C, respectively, using roasted samples, while pulp density, stirring speed were kept constant in the first stage leaching. At desired particle size (50 μ) of the concentrate i.e., 95% distributed was below 50 μ . The residual product of first stage leaching was subjected to alkali using sodium hydroxide as leachant at a specified condition. After the required reaction period, the solution was filtered using vacuum filter paper and washed with distilled water. The residue was dried in an oven overnight and weighed [7]. The amount of molybdenum metal dissolved was measured using Inductive Coupled Plasma-Optical Emission Spectroscopy (ICP-OES) after required dilutions (Fig. 1).

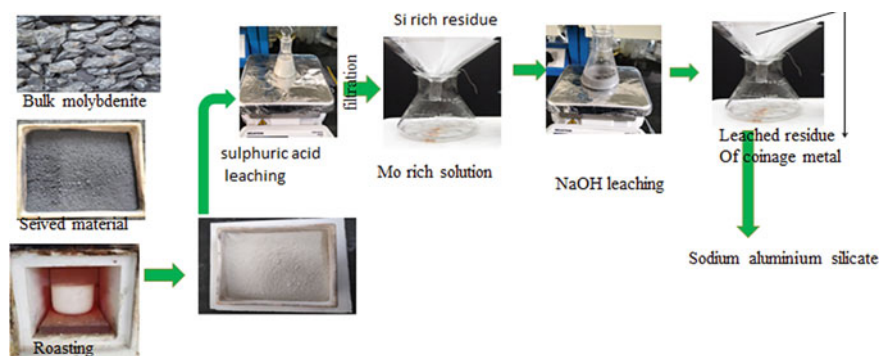


Fig. 1 A schematic leaching flow-sheet of a Nigerian molybdenite ore processing

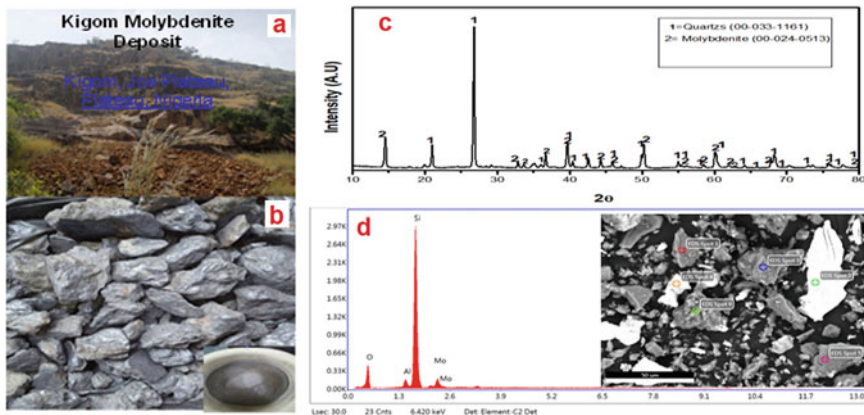


Fig. 2 **a** and **b** Surface topography of molybdenite source; **c** and **d** X-ray diffraction (XRD) and the EDS image of the sieved samples

3 Results and Discussion

3.1 Ore Powder Characterization

Characterization of the powdered ore ($50\ \mu$) was performed by XRD and SEM to study the phase and morphology of the samples. From Fig. 2c, the diffraction peak of quartz and Molybdenite could be observed evidently, which are the main phases of the mineral. SEM micrograph along with EDAX shows that the sample contained molybdenum and silica majorly. The microstructure shows that the particle surface of Molybdenite is relatively dense and compact. Figure 3 shows the morphological images and the XRD of the roasted and residual product of leaching.

3.2 Leaching Efficiency

The leaching effect on the extraction of molybdenum and other minor minerals was studied at varies acid concentrations (0.5–3.0 M), temperatures (27, 55, 65, 75, 90 °C), and times (5–120 min). Thus, the leaching of Mo metal from the roasted molybdenite mineral by sulphuric acid solution is proposed at desired particle size (below $50\ \mu$). Also, in the second stage leaching, the alkaline concentration, reaction temperature, and leaching time effect were also investigated in the extraction of silicon compound from the residue obtained in the first leaching reaction (residual product: see Fig. 3b). The percentage of Si extraction increases with the addition of sodium hydroxide solution. The amount of Si achieved was 50% at optimum leaching conditions i.e., reaction temperature = 90 °C, alkaline concentration = 5 M [NaOH], contact time = 120 min, stirring speed = 400 rpm, and pulp density = 10%.

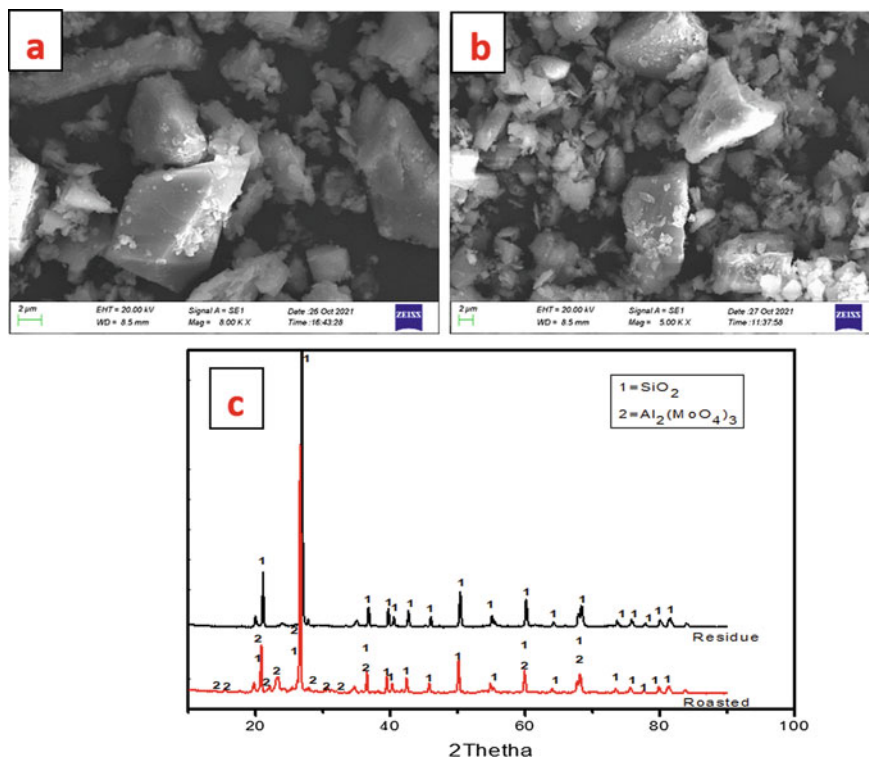
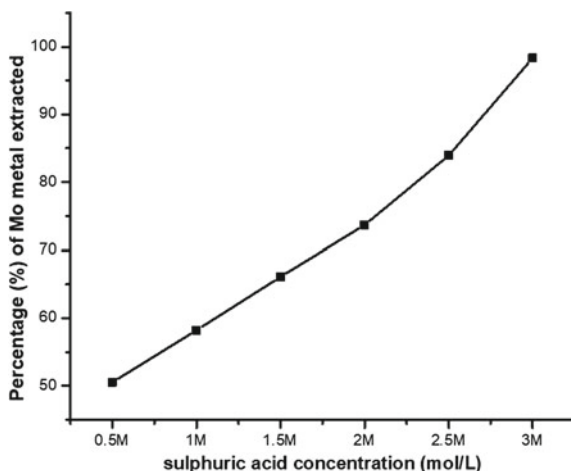


Fig. 3 SEM morphology for **a** roasted mineral **b** residual product of leaching and **c** X-ray diffractometer (XRD) pattern of residual product and roasted ore, respectively

3.2.1 Sulphuric Acid Concentration

As indicated in Fig. 4, the leaching rate of molybdenum along with other elements gradually increased with an increase in acid addition. The amounts of the ore reacted with different sulphuric acid concentrations at different leaching times are shown in Fig. 4. Condition: $[H_2SO_4]$ reaction temperature = 27–75 °C, contact time = 0–120 min, stirring speed = 400 rpm, pulp density = 10%, and particle size = 50 μ . The extraction percentage of molybdenum metal increases with an increase in sulphuric acid addition to 3.0 mol/L; a substantial amount of Mo dissolution of ~98% was achieved. This result could be attributed to the transformation of sulphide to tri-oxide form, thereby enhancing the leaching efficiency. From this study, 3.0 mol/L is sufficient for Mo dissolution as compared to reported data [8] where 94.8% Mo dissolutions were recorded.

Fig. 4 Leaching percentage of Mo metal ions from roasted molybdenite ore versus sulphuric acid concentration (leaching condition: reaction temperature = 75 °C, contact time = 120 min, stirring speed = 400 rpm and pulp density = 10%)



3.2.2 Reaction Temperature

The reaction temperature effect was investigated from 27 to 90 °C. As can be seen from the results plotted in Fig. 5, the extraction efficiency shows an increase from 41 to 98.3% with leaching temperature changing from 27 to 75 °C. During the course of this investigation the leaching parameters stated in Fig. 5 were kept constant. The endothermic character of the leaching technique, which favors a high rate of molybdenum dissolution, may justify the increasing trends in extraction efficiency for molybdenum metal dissolution at relatively high temperatures. The rate dissolution of Mo appears to increase with an increase in temperature below 90 °C, similar to the reported data [9]. Hence, 75 °C temperature is sufficient for molybdenum extraction in this study.

Fig. 5 Leaching percentage of Mo metal ions from roasted molybdenite ore versus leaching temperature (leaching condition: sulphuric acid concentration = 3.0 M, contact time = 120 min, stirring speed = 400 rpm and pulp density = 10%)

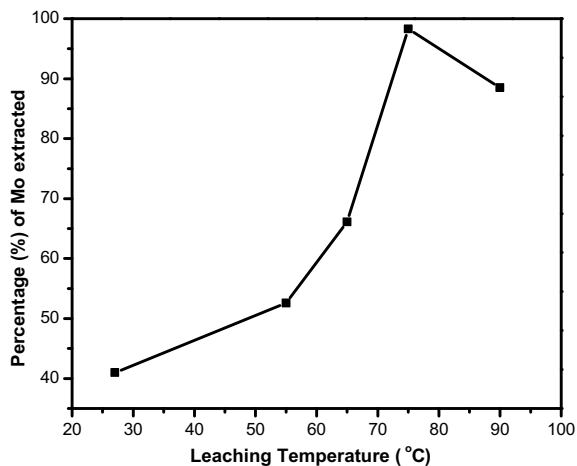
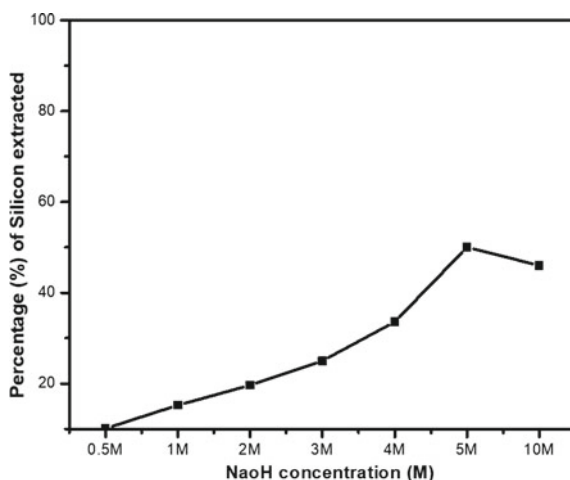


Fig. 6 Percentage of silicon extracted versus sodium hydroxide concentration (leaching condition: sodium hydroxide concentration = 0.5–10 M, reaction temperature = 90 °C, contact time = 120 min, pulp density = 10%)



3.2.3 Alkali Leaching

As indicated in Fig. 6, about 52% extraction of silicon metal was recorded in the second stage leaching of roasted molybdenite sample with sodium hydroxide (NaOH) solution under defined conditions. The extent of Si dissolution increases with the addition of sodium hydroxide solution from 15 to 50% dissolution was achieved between 0.5 and 5 M [NaOH] at varying reaction temperatures and leaching time of 120 min, while other parameters were kept constant. The leaching efficiency increases with increasing alkali solution till 5 mol/L. However with further addition of leachant concentration to 10 mol/L, the amount of Si dissolution drastically decreases below 50% at defined conditions. This could be a result of precipitation phenomena at higher alkaline concentrations [10].

3.3 Kinetic Studies

To investigate the reaction mechanism for roasted molybdenite mineral leaching by sulphuric acid solution, attempts were made by subjecting the complete obtained dissolution data in Figs. 6 and 7 to describe the specific mechanism for the metal dissolution reaction using the shrinking core kinetic model (SCM), which is widely practiced in solid state processes [11]. The solid-phase products, according to the SCM, result in the formation of ashes that surrounds the undissolved center [12]. There are three established reaction phases in which the overall process is based on heterogeneous leaching: these are surface chemical controlled, diffusion controlled, and mixed controlled. The fundamental SCM equation is given as:

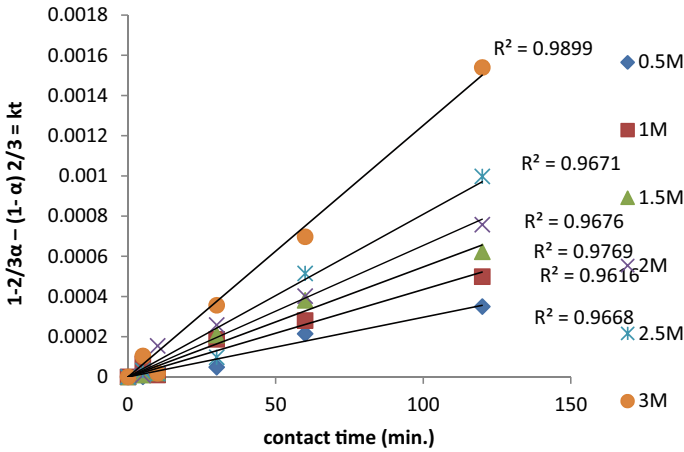


Fig. 7 Shrinking core kinetic model for molybdenum (conditions: same as in Fig. 4)

$$1 - (1 - x)^{\frac{1}{3}} = \frac{KC}{r_0\rho}t = K_C t$$

(Chemical reaction controlled) (1)

$$1 - \frac{2}{3}\alpha - (1 - \alpha)^{\frac{2}{3}} = \frac{2MDC}{B\rho r_0^2}t = K_d t$$

(Diffusion reaction controlled) (2)

$$1 - (1 - x)^{\frac{1}{3}} + \frac{y}{6}[1 - (1 - x)^{\frac{1}{3}} + 1 - 2(1 - x)^{\frac{2}{3}}] = K_m t$$

(Mixed reaction controlled) (3)

where α is the fraction of Mo metal extracted in the overall leaching data, t is the reaction time, K_c , K_d , and K_m are the diffusion rate constants, ρ is the density, M is the solid’s molecular mass, D is the diffusion coefficient, r_0 is the particle’s original radius, and C is the leachant concentration [8].

According to Eq. (2), a plot of $1 - \frac{2}{3}\alpha - (1 - \alpha)^{\frac{2}{3}}$ against contact time generates a perfect straight line with average correlation (R^2) values of 0.96 for various sulphuric acid concentrations as shown in Fig. 8. The obtained slopes obtained in Fig. 8 were used to derive the experimental rate constants K_d , which were then used to produce the graph of $\ln K_d$ versus $\ln [H_2SO_4]$, with a calculated slope of 1.2. Thus, the reaction order for H_2SO_4 leaching at a 3.0 M concentration suggests a first-order dissolution relationship, as illustrated in Fig. 9. In addition, the activation energy E_a associated with Mo metal dissolution in sulphuric acid is a critical factor to be considered in investigating the reaction mechanism. The Arrhenius graph, $\ln K_d$ versus $1/T$ (K),

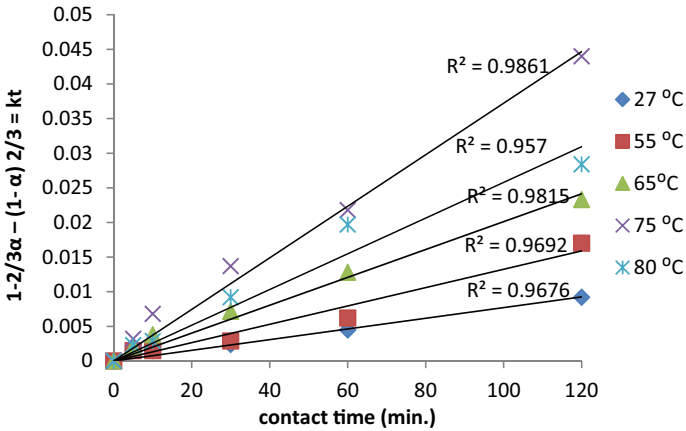
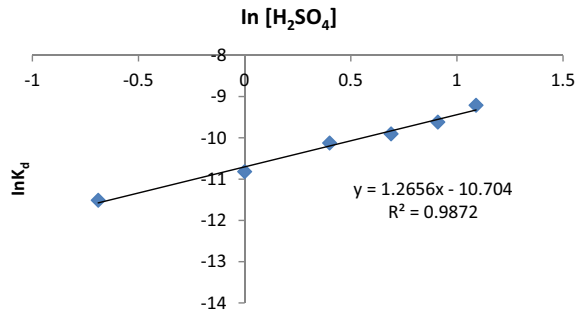


Fig. 8 Shrinking core kinetic model for molybdenum (conditions: same as in Fig. 5)

Fig. 9 Plot of $\ln K_d$ against $\ln [H_2SO_4]$ (conditions: same as Fig. 4)



was made using the diffusion rate constants (K_d) derived from Eq. (2) according to the following equation:

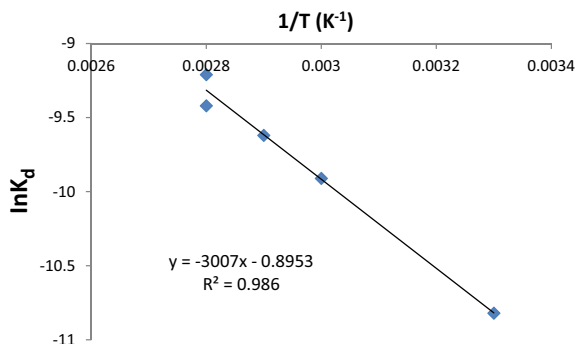
$$K_d = A_{exp} - \left(\frac{Ea}{RT} \right) \tag{4}$$

$$\ln K_d = \ln A - \left(\frac{Ea}{RT} \right) \tag{5}$$

Ea: activation energy (kJ/mol), R: gas constant, T: reaction temperature, K: reaction rate constant, A: pre-exponential factor.

Depending on the activation energy associated with the metal leaching process, the reaction is either controlled by diffusion in the product layer or a boundary fluid film or chemically controlled. If the activation energy is ≤ 40 kJ/mol, the leaching process is controlled by diffusion, but when the activation energy is ≥ 40 kJ/mol, the leaching

Fig. 10 Arrhenius relation $\ln K_d$ against $1/T$ (K^{-1}) (conditions: same as Fig. 5)



process is chemically controlled, according to Baba (2017) and Ksohnevishan (2012) [13, 14]. The calculated activation energy from the slope in Fig. 10 gave ($E_a = 25.0$ kJ/mol) with a perfectly fit shrinking-core diffusion control mechanism [4].

4 Conclusion

This study examined the dissolution kinetics and operational efficiencies behavior of molybdenum from a roasted molybdenite mineral from Kigom, Jos, and Plateau Nigeria. Sulphuric acid was chosen as the first leachant due to its ability to dissolve all important metals in the mineral, as well as its selectivity for molybdenum. It was also found that sodium hydroxide (NaOH) as the second leachant has proven to be highly selective for silicon dissolution. The extraction of molybdenum was found significant at the optimum conditions of sulphuric acid: 3.0 M, pulp density: 10%, reaction temperature: 75 °C, contact time: 120 min, and particle size: 50 μ in the first stage of leaching. The second stage of leaching confirms optimized conditions as NaOH concentration: 5 mol/L, reaction temperature: 90 °C, contact time: 120 min, and particle size: 50 μ as established by EDAX analysis of the leached residual products.

Acknowledgements The authors appreciate the CSIR-TWAS and IMMT Bhubaneswar for supporting this research.

References

1. Lasheen TA, El-Ahmady ME, Hassib HB, Helal AS (2015) Molybdenum metallurgy review: hydrometallurgical routes to recovery of molybdenum from ores and mineral raw materials. *Miner Process Extr Metall Rev* 36(3):145–173. <https://doi.org/10.1080/08827508.2013.86837>
2. Olade M (2020) Mineral deposits and exploration potential of Nigeria

3. Jha MK, Kumari A, Panda R, Kumar JR, Yoo K, Lee JY (2016) Review on hydrometallurgical recovery of rare earth metals. *Hydrometallurgy* 165:2–26
4. Medvedev AS, Aleksandrov PV (2009) Investigations on processing low-grade molybdenum concentrate by the nitric-acid method. *Russ J Nonferrous Metals* 50:353–358
5. Alvaro A, Alan A, Juan PI, Oscar J (2019) Mechanism and leaching kinetics of molybdenite concentrate in a hydrogen peroxide-acid system. *Physicochem Probl Miner Process* 55(1):140–152
6. Xie K, Wang H, Wang S (2019) Direct leaching of molybdenum and lead from lean wulfenite raw ore. *Trans Nonferrous Metals Soc China* 29:2638–2645
7. Baba AA, Adeyemi CO, Mohapatra M, Raji MA, Akanji FT, Alabi AGF (2022) Purification of a low grade molybdenite ore for industrial steel production. In: *Rare metal technology. The minerals, metals & materials series*. https://doi.org/10.1007/978-3-030-92662-5_13
8. Pradhan D, Pattanaik A, Krishna Samal DP, Sukla LB, Kim DJ (2020) Recovery of Mo, V and Ni from spent catalyst using leaching and solvent extraction. *Mater Today Proc* 30:322–325. <https://doi.org/10.1016/j.matpr.2020.01.614>
9. Kang JX, Li XK (2021) Thoughts on the development of molybdenum beneficiation technology. *IOP Conf Ser: Earth Environ Sci* 647(1). <https://doi.org/10.1088/1755-1315/647/1/012001>
10. Ayinla KI, Baba AA, Padhy SK, Adio O, Odeleye KA, Tripathy BC (2019) Synthesis and characterization of pure silica powder from a k-feldspar silicate ore for industrial value addition. *Commun Fac Sci Univ Ank Ser B* 61(1–2):69–87. ISSN 2687-4806
11. Baba AA, Raji MA, Abdulkareem AY, Ghosh MK, Bale RB, Adeyemi CO (2019) Dissolution kinetics potential of a biotite-rich kaolinite ore for industrial applications by oxalic acid solution. *Min Metall Explor* 36:1091–1099. <https://doi.org/10.1007/s42461-019-00108-5>
12. Wanta KC, Astuti W, Perdana I, Petrus HTBM (2020) Kinetic study in atmospheric pressure organic acid leaching: shrinking core model versus lump model. *Minerals* 10:1–10. <https://doi.org/10.3390/min10070613>
13. Khoshnevisan A, Yoozbashizadeh H, Mozammel M, Khatiboleslam S (2012) Kinetics of pressure oxidative leaching of molybdenite concentrate by nitric acid. *Hydrometallurgy* 111–112:52–57
14. Baba AA, Balogun AF, Olaoluwa DT, Bale RB, Adekola FA, Alabi AGF (2017) Leaching kinetics of a Nigerian complex covellite ore by the ammonia-ammonium sulfate solution. *Korean J Chem Eng* 34:1133–1140

A Comparative Study on Flotation of Coal Using Eco-Friendly Single Reagent and Conventional Dual-Reagent System



N. Vasumathi, M. Sai Kumar, D. S. V. Abhishek, T. V. Vijaya Kumar, and S. J. Gopalkrishna

1 Introduction

Coal, an organic sedimentary rock, is the backbone on which electricity generation and steel making rest. Coal contains mainly carbon, hydrogen, oxygen, nitrogen and sulphur as well as trace amounts of other elements, including the mineral matter that refers to the inorganic constituents of coal [1]. Mineral matter is the principal source of the elements that make up the ash content while the organic matter or the coal macerals contributes to carbon constituents. Most of the high ash coals are subjected to beneficiation for reducing the ash levels so as to make them suitable for various applications. Coking coal or metallurgical coal are coals when baked in absence of air, form a grey, hard, carbonaceous porous residue called 'coke'. These are mainly used for iron and steel manufacturing. Generally coking coals are a part of the bituminous group. While non-coking coals are mainly used for power generation. The mined coal is associated with inorganic impurities during its formation that forms the ash residue in coal which is undesirable for effective utilization of coal for many applications. The high-rank coal with high carbon and less ash content is depleting rapidly. As high-rank coal resources are running out due to the rise in energy demand and steel production, it is therefore imperative to use low-rank, oxidized coal to meet the increasing need for coal [2, 3]. Hence, the need for utilizing low-rank coals with low carbon and high ash is of utmost importance. As these low-rank coal can be effectively utilized after cleaning or washing in order to reduce the ash-forming mineral phases and thereby improving the carbon content of the coal for further suitable utilization.

N. Vasumathi (✉) · M. S. Kumar · D. S. V. Abhishek · T. V. V. Kumar
CSIR NML Madras Centre, Chennai, Tamil Nadu 600113, India
e-mail: vasumatisamy@gmail.com

N. Vasumathi · S. J. Gopalkrishna
VSKU PG Center, Nandihalli, Ballari, Karnataka 583119, India

A fine coal washery losses ten times as much high-quality coal as a coarse coal washery. Recovering good quality fines will improve the economics of coal washery [4]. Generally, coal washing involves crushing and screening of Run-of-Mine (ROM) coal into smaller fractions, separating the gangue and mineral matter by using physical separation methods such as dense media separation/heavy media separation (HMS) or physico-chemical process, called froth flotation. As flotation process is based on differences in the ability of air bubbles to selectively attach to specific mineral surfaces in a mineral–water slurry and float to the top based on their degree of hydrophobicity [5–7]. Froth flotation is one of the beneficiation methods in fine coal washing by exploiting the surface hydrophobicity difference between coal macerals that are naturally hydrophobic and its associated ash forming minerals impurities that are mostly hydrophilic in nature. This naturally hydrophobic surface property of coal surface provides a high response while processed by flotation as it is a surface-phenomenon-based separation technique. Hence, coal particles have a natural affinity toward air bubbles [8, 9] as they are naturally hydrophobic.

It is generally recognized that recovering coarse coal by flotation is challenging [10, 11]. One factor that should not be overlooked is detachment. To reduce the particle detachment, several techniques have been used and one such way is the addition of flotation reagents which enhances the natural hydrophobicity of the particles that are to be floated. Rahman et al. (2012) discovered that the collector dosage, the aeration rate, and the concentration of fine particles had an impact on how easily the coarse particles detached during the froth phase [12]. In order to enhance this separation process efficacy, certain chemicals called as flotation reagents namely collectors, frothers, etc. are added to transform the coal-water mixture suitable for flotation by enhancing the relative hydrophobicity of coal particles and to maintain froth characteristics [13]. The collectors such as diesel, kerosene, and frothers such as MIBC, and pine oil is the most commonly and widely used reagents in coal flotation to increase the selective hydrophobicity of coal [14, 15]. These non-polar oils are non-environment friendly. As flotation process is very complex and could be balanced only with the appropriate selection of a reagent. Better separation efficiency is obtained when the ability of the flotation reagents gets adsorbed selectively and swiftly onto the coal particle surfaces [16]. Researchers have examined particle size extensively and its significance in flotation in addition to the type and dosage of the reagent and its impact on flotation [17, 18]. Carboxylic, phenolic, and carbonyl groups are the most prevalent types of functional groups on the surface of oxidized coal [19]. Jia et. al. investigated the efficacy of newly developed reagents for flotation of low rank and/or oxidized coals, which are difficult to float using conventional reagents such as fuel oil or kerosene. Experiments were conducted using these Tetra- hydrofurfuryl esters series (THF) as collectors for coal flotation, and the performance of these reagents was compared with that of dodecane and nonylbenzene. Results showed that the nonionic surfactants (THF series) were more effective collectors for both oxidized and unoxidized coals and greatly enhanced the flotation performance when used as a promoter for oxidized coals. Non-ionic tetrahydrofurfuryl ester surfactants are more effective in the flotation of both oxidized and unoxidized coals than dodecane (an oily collector) [20]. The use of dodecane, ethyl

esters and dodecane-esters mixed collector on low-rank coal flotation and their interactions with coal particles were studied [21]. Apart from high collecting ability, the specific selectivity of high-efficiency ternary compound collectors such as oleic acid, methyl oleate, and diesel was investigated on low-rank coal [22]. The flotation efficiency of the new oxygenated polar compound collector along with blending frother was compared with conventional diesel (collector) and octanol (frother) on oxidized coals prepared using peroxide oxidation solution [23]. Also, the flotation reagent consumption rate is lower for higher-rank coals than low-rank coals because of their high natural hydrophobicity. It can be observed that most of the coal flotation process involves the usage of a dual reagent system (collector and frother) like hydrocarbon oils and chemically synthesized non-environment friendly collector and frothers. In this study, a single reagent, Collector AB, as an alternative to two reagent practices was developed from a natural percussor without using any harmful synthetic chemicals. This eco-friendly collector AB was used as coal collector-cum-frother and is safe to use in coal washeries as it was synthesized from natural product precursors unlike most commercial coal collectors. The performance of this developed collector AB in effectively separating the ash-forming minerals and collecting the coal particles in terms of its yield was studied. The results obtained were also compared with that of commonly used commercial reagents (collector & frother dual reagent system) to assess their flotation separation efficiency.

2 Material and Methods

2.1 Materials

A coking coal sample collected from one of the mines in Jharkhand was utilized in this flotation study. Commercially available synthetic flotation reagents widely used in coal washeries were used as collectors and frother. An eco-friendly 'Collector AB', synthesized from the natural product was used as coal collector-cum-frother (single reagent), and its flotation separation efficiency was compared with that of commercial dual reagents.

2.2 Methods

Flotation experiments on the coal sample were carried out using a laboratory D12 Denver flotation machine at natural pH (~7.0 pH) and at 12% solids by weight. The flotation experiments were carried out on two different sizes of flotation feed, 100% passing 0.5 and 0.25 mm. The flotation products were dried and subjected to ash analysis.

3 Results and Discussion

3.1 Characterization of Coal Sample

The organic matter or the coal maceral's composition was characterized as different maceral have varied degrees of hydrophobicity [24]. The petrological characterization of the coal sample taken in this study revealed the predominant presence of inertinite along with vitrinite (Fig. 1 and Table 1).

The Mean Reflectance of Vitrinite was found to be 1.1431. The coal maceral composition plays a major role in the surface hydrophobicity of the coal and thereby the selectivity of coal particles influencing the performance of the flotation process.

Fig. 1 Petrological image showing the presence of vitrinite and inertinite of the coal sample

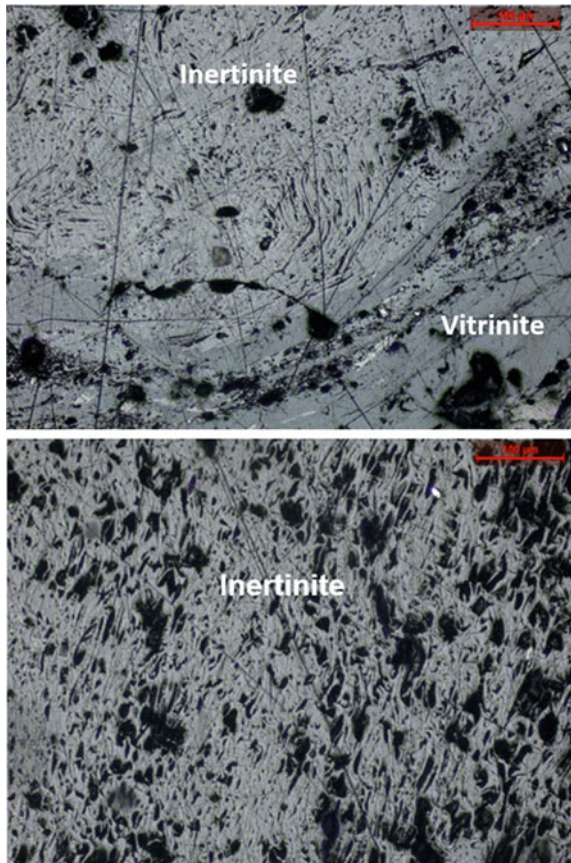


Table 1 Maceral composition of coal

Maceral	Volume, %
Vitrinite	24.84
Inertinite	42.08
Heat affected	13.02
Mineral matter	20.06

3.2 Size and Ash Distribution Analysis

The proximate analysis of coal taken for this study is given below. The proximate analysis reveals that the coking coal contains 25.75% ash content and 53.89% fixed carbon with 19.51% volatile matter (Table 2).

The coal sample was size reduced to two size different fractions namely 100% passing 0.5 mm and 100% passing 0.25 mm in order to study the flotation response at these two size fractions. The size distribution and size wise ash analysis were carried out on the coal sample is given in Figs 3 and 4. The sieve analysis indicates that 40.42% of the material is above 300 μm in size, and the rest of the material is distributed in lower-size fractions. Also, the + 300 μm size fraction has higher ash content. From the ash distribution, it can be observed that the coarser fraction contributes higher ash content and below 150 μm is observed to be lower. The + 300 μm size fraction has higher ash content and thus the relatively coarser fractions contribute to higher ash content in comparison to that of below 150 μm size fractions implying that better liberation may be of coal macerals and ash forming minerals on further size reduction (Figs. 2 and 3).

In the sieve analysis on further fine-sized fraction of -0.25 mm coal, it can be observed that ash content gradually decreases with the fineness of the size reduced material. The amount of ash in -75 μm fraction is marginally lower than the coarser size ranges. Relatively lower ash in the finer size ranges could be attributed to better liberation of coal macerals. This size fraction of 100% passing 0.25 mm was also prepared for improved liberation and subjected to flotation studies using a commercial dual-reagent system and synthesized single eco-friendly reagent, 'Collector AB'.

Table 2 Proximate analysis of coal

Parameter	Value, %
Moisture	0.85
Volatile matter	19.51
Ash	25.75
Fixed carbon	53.89

Fig. 2 Size-wise ash analysis of -0.5 mm coal fraction

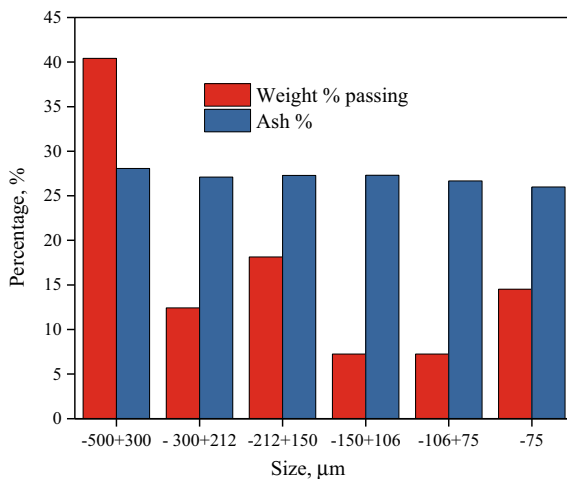
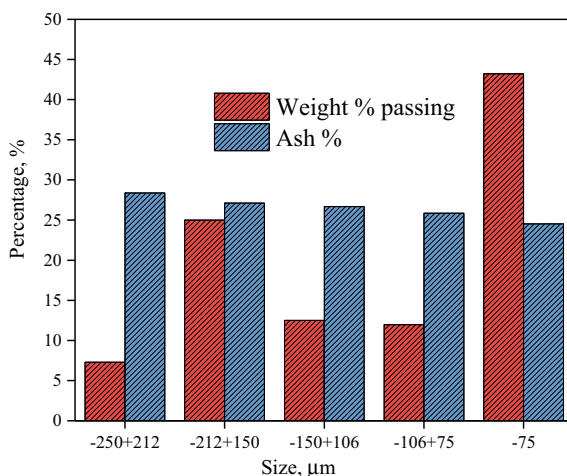


Fig. 3 Size-wise ash analysis of -0.25 mm coal fraction



3.3 FTIR Analysis of Flotation Reagents

The flotation reagents used in this study were characterized by Fourier Transform Infrared Spectroscopy (FTIR, Bruker Alpha II Spectrometer) to decipher the details of the functional group present (Figs. 4, 5 and 6).

The FTIR analysis of the feed coal sample was also studied. The FTIR data reveals that the weak intensity broad peaks in between 3600 to 3700 cm^{-1} indicate the presence of surface hydroxyl groups. The peak at 1600 cm^{-1} indicates the presence of the $\text{-C}=\text{C}$ -group. The peak at 1023 cm^{-1} shows the presence of sulphate in coking coal. The FTIR of Collector AB suggests that the peaks at 2923 cm^{-1} and 2853 cm^{-1} are the presence of -CH_3 and -CH_2 groups. The FTIR spectrum and peak values are

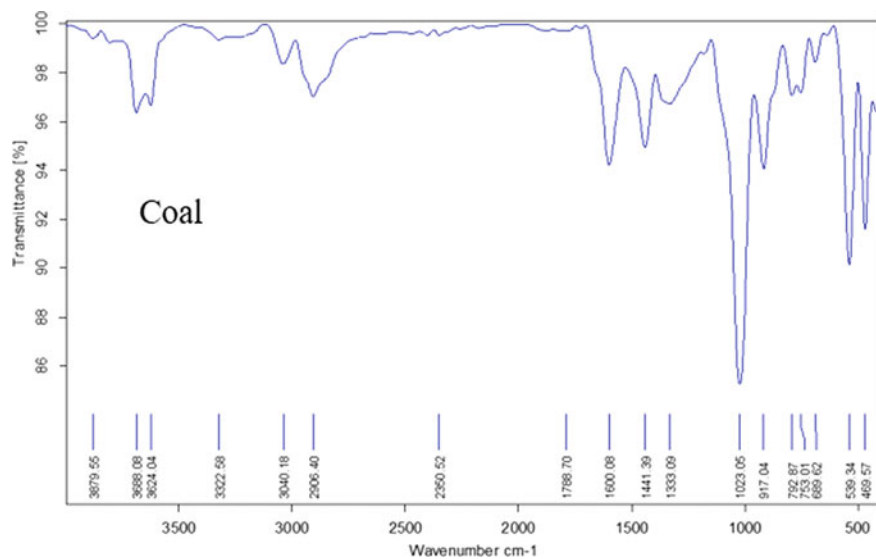


Fig. 4 FTIR analysis of coal

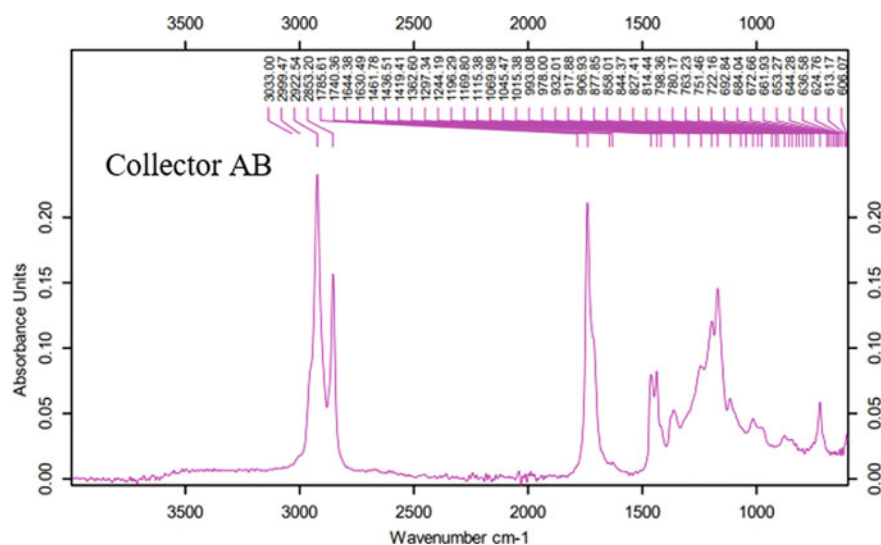


Fig. 5 FTIR analysis of Collector AB

well matched with natural product precursors [25]. The FTIR of commercial frother suggests that the peak in between 3000 to 3550 cm^{-1} of the hydroxyl group. The peaks at 2958 cm^{-1} , 2930 cm^{-1} , and 2873 cm^{-1} clearly indicate the presence of an alkyl chain in the frother.

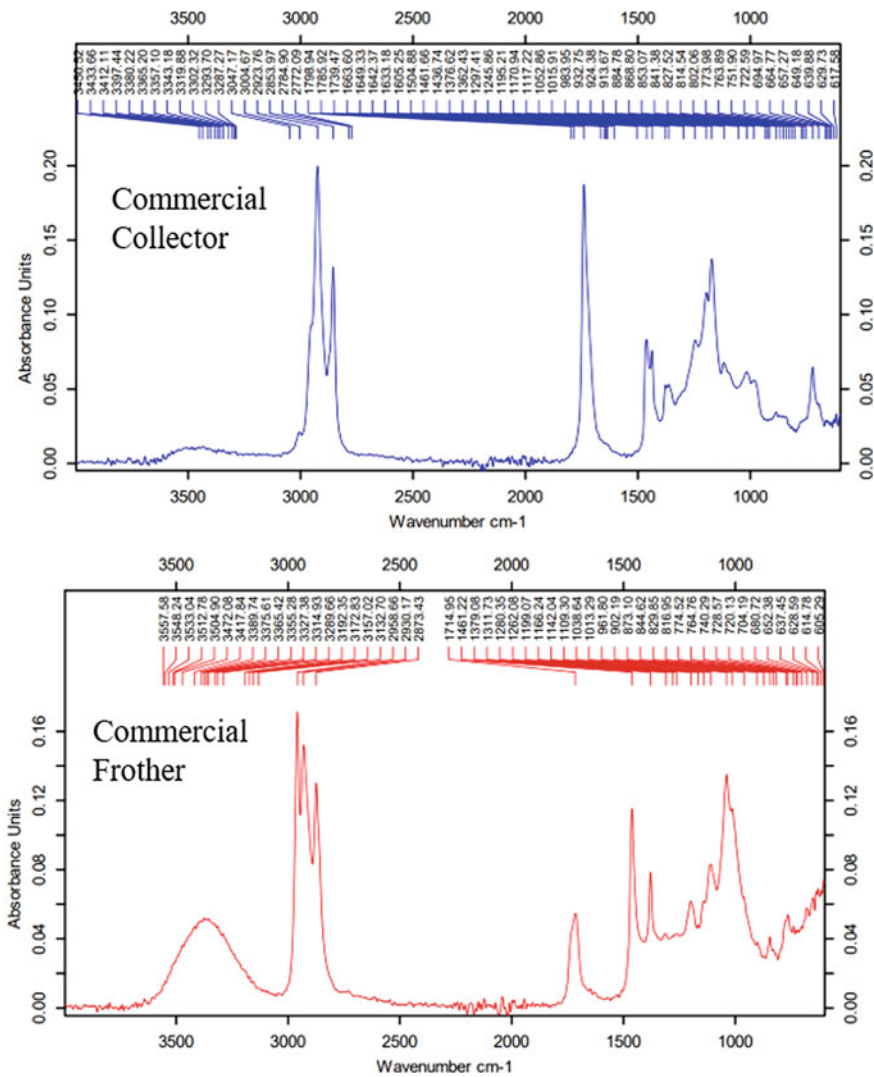
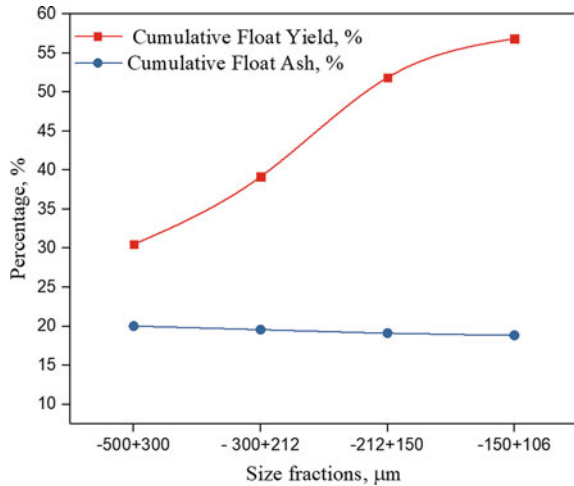


Fig. 6 FTIR analysis of commercial flotation reagents

3.4 HMS of Coarser Size Fraction of 100% –0.5 mm and 100% –0.25 mm

The heavy media separation (HMS) studies of coarser size fractions of two size ranges namely, 100% –0.5 mm and 100% –0.25 mm were carried out. The relatively coarser sieve fractions of 100% –0.5 mm viz., –500 + 300 μm, –300 + 212 μm, –212 + 150 μm, and –150 + 106 μm were subjected to the HMS test to elucidate

Fig. 7 Cumulative yield versus ash of float (-0.5 mm)



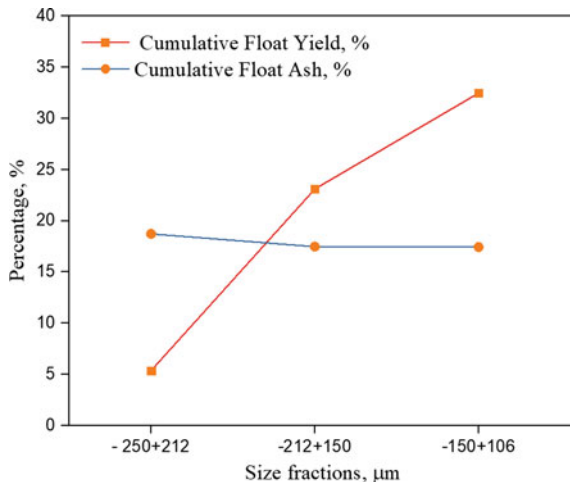
information on the liberation of coal macerals. It is observed that in 100% -0.5 mm fraction, the ash in successive floats was found to be decreasing which could be attributed to better liberation of coal macerals at finer sizes. Theoretically, 56.86% by weight (cumulative weight of floats) of the size fraction -500 + 106 μm could be obtained as concentrate/float at 18.83% ash as shown in Fig. 7.

The relatively coarser sieve fractions of 100% -0.25 mm viz., -250 + 212 μm , -212 + 150 μm , and -150 + 106 μm were subjected to the HMS test to study the information on the liberation of coal macerals. In case of 100% -0.25 mm size fraction, the ash in successive floats was found to be decreasing which could be attributed to better liberation of coal macerals at finer sizes than compared to -0.5 mm size fraction. Theoretically, 32.49% yield (cumulative weight of floats) of the size fraction -250 + 106 μm could be obtained as concentrate/float at 17.43% ash as shown in Fig. 8. This study indicates the possible separation that could be achieved in a washing process. Further these two size fractions were subjected to flotation studies using commercial flotation reagents and the eco-friendly collector AB to study the performance efficacy of the developed reagent.

3.5 Flotation Studies on -0.5 mm and -0.25 mm Size Fractions Using Commercial Collector and Frother and ‘Collector AB’

Flotation studies on -0.5 mm coal and -0.25 mm size fractions using commercial collector-frother and the developed single reagent Collector AB were performed. The dosage variation optimization studies were carried out extensively and the main outcome of the tests are highlighted here at comparable ranges of yield and ash

Fig. 8 Cumulative yield versus ash of float (-0.25 mm)

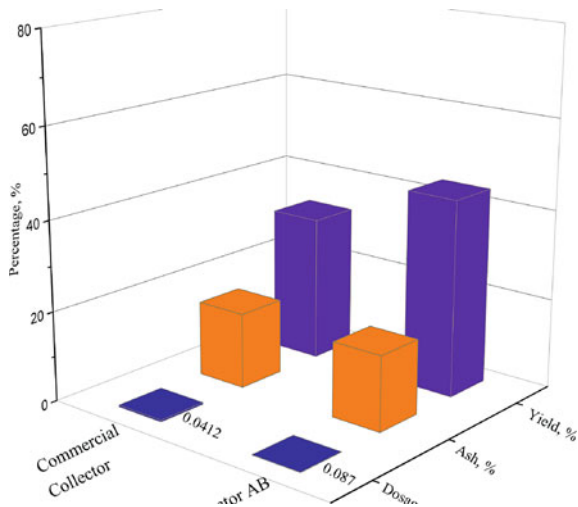


content of the concentrates. Table 3 shows the flotation test results on variation of yield at similar/equivalent ash values in the concentrate (Figs. 9 and 10).

The commercial collector at 0.0412 kg/t and commercial frother at 0.0055 kg/t indicate that a concentrate of 32.45% yield at 16.84% ash could be obtained in – 0.5 mm size fraction.

The newly developed single reagent, Collector AB at 0.087 kg/t resulted in a concentrate of 43.83% yield at 16.69% ash which was found to be superior to the commercial reagent dual system at (32.45% yield & 16.84% ash) equivalent ash levels in the concentrate at 0.0412 kg/t collector and 0.0055 kg/t frother dosages. These results indicate that the single reagent, ‘Collector AB’ has better flotation separation

Fig. 9 Flotation results of – 0.5 mm coal concentrate



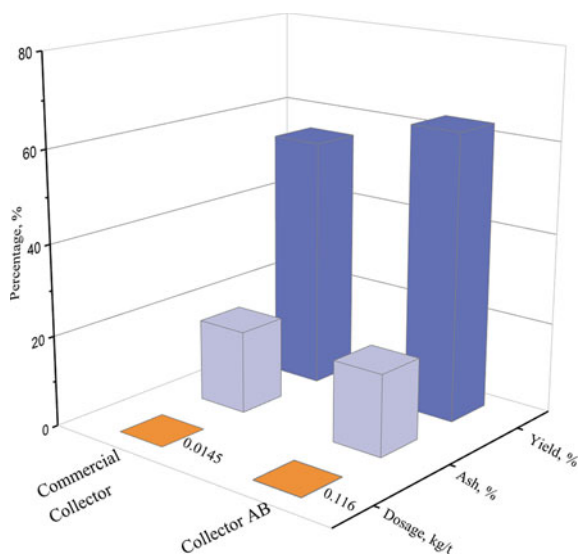


Fig. 10 Flotation results of -0.25 mm coal concentrate

Table 3 Flotation test results of coal

Flotation Reagent	Product	Yield, %	Ash, %	Ash distribution, %
-0.5 mm size coal				
Commercial collector & frother	Concentrate	32.45	16.84	20.61
	Tailings	67.55	31.16	79.39
Collector AB	Concentrate	43.83	16.69	27.28
	Tailings	56.17	34.71	72.72
-0.25 mm size coal				
Commercial collector & frother	Concentrate	55.40	18.23	38.41
	Tailings	44.60	36.33	61.59
Collector AB	Concentrate	63.18	17.92	44.45
	Tailings	36.82	38.45	55.55

efficiency in terms of better yield of concentrate at equivalent ash in the concentrate. This also indicated that the coal macerals are not liberated to the requisite levels for the facilitation of better flotation to improve the yield with lower ash levels. It appears that more coal particles are in an interlocked state as the ash rejection in the tailings/non-float remains low around 30–35%.

A concentrate of 55.40% yield at 18.23% ash could be obtained at a commercial collector dosage of 0.0145 kg/t and frother of 0.0055 kg/t. This is superior to the concentrate obtained on 100% -0.5 mm coal using the same commercial reagents.

Flotation studies were also conducted on 100% -0.25 mm coal. A concentrate of 55.40% yield at 18.23% ash could be obtained using commercial collector (0.0145 kg/t) and frother (0.0055 kg/t). A concentrate of 63.18% yield at 17.92% ash could be obtained using the newly developed 'Collector AB' at 0.116 kg/t dosage. At equivalent ash levels (around 18% ash) in the concentrate, there is an improvement in yield when 100% -0.5 mm coal was reduced to 100% -0.25 mm size.

4 Conclusion

The flotation studies on coal using a commercial dual-reagent system of collector & frother and newly synthesized natural product based 'Collector AB' at two different size fractions indicate that the 'Collector AB' has better flotation performance efficiency with a higher yield of the concentrate. An improvement in yield was observed when 100% -0.5 mm coal was reduced further to 100% -0.25 mm size which could be attributed to better liberation at a relatively finer grind. The Collector AB, a novel single reagent, synthesized from a natural product is eco-friendly in nature and proved to be a good alternative to commercially available flotation reagents and other hydrocarbon oils presently being used for coal flotation. Hence, the developed single reagent for coal flotation paves the way to a sustainable and environmentally friendly solution to the coal washeries in treating coal fines and low-rank coals.

References

1. Speight J (2015) Handbook of petroleum product analysis, 2nd edn
2. Patra AS, Patra P, Chowdhury S, Mukherjee AK, Pal S (2020) Cationically functionalized amylopectin as an efficient flocculant for treatment of coal suspension. *Colloids Surf A* 586:124229. <https://doi.org/10.1016/j.colsurfa.2019.124229>
3. Sharma DK, Dhawan H (2018) Separative refining of coals through solvolytic extraction under milder conditions: a review. *Ind Eng Chem Res* 57:8361–8380. <https://doi.org/10.1021/acs.iecr.8b00345>
4. Yeriswamy P, Patil DP, Barnwal JP, Govindrajan B, Rao TC (2000) Evolution of different flotation techniques treating Indian coal fines. *Indian Min Eng J* 39(9):40–43
5. Sripriya R, Rao PVT, Choudhury RB (2003) Optimisation of operating variables of fine coal flotation using a combination of modified flotation parameters and statistical techniques. *Int J Miner Process* 68:109–127
6. Chehreh S, Chelgani S, Rudolph M, Kratzsch R, Sandmann D, Gutzmer J (2016) A review of graphite beneficiation techniques. *Miner Process Extr Metall Rev* 37(1):58–68
7. Yuan XM, Palsson BI, Forsberg KSE (1996) Statistical interpretation of flotation kinetics for a complex sulphide ore. *Minerals engineering*, pp 429–442
8. Esterle JS, O'Brien G, Kojovic T (1994) Influence of coal texture and rank on breakage energy and resulting size distributions in Australian Coals. In: Proceedings of the 6th Australian coal science conference, newcastle, Australia, Australian institute of energy, pp 175–181
9. Smith KL, Smoot DL (1990) Characteristics of commonly-used U.S. coals. *Prog Energy Combust Sci* 16:1–53

10. Liang L, Li Z, Peng Y, Tan J, Xie G (2015) Influence of coal particles on froth stability and flotation performance. *Miner Eng* 81:96–102. <https://doi.org/10.1016/j.mineng.2015.07.004>
11. Xia W, Xie G, Liang C, Yang J (2014) Flotation behavior of different size fractions of fresh and oxidized coals. *Powder Technol* 267:80–85. <https://doi.org/10.1016/j.powtec.2014.07.017>
12. Rahman RM, Ata S, Jameson GJ (2012) The effect of flotation variables on the recovery of different particle size fractions in the froth and the pulp. *Int J Miner Process* 106:70–77. <https://doi.org/10.1016/j.minpro.2012.03.001>
13. Chander S, Nagaraj DR (2007) Flotation: flotation reagents. Academic Press, Encyclopedia of separation science, pp 1–14
14. Aplan FF, Coal Flotation; Flotation AM (1976) In: Fuerstenau MC (ed) Gaudin memorial volume (SME, Littleton, CO, vol 2, pp 1235–1264, 1976)
15. Brown DJ (1962) In: Fuerstenau DW (ed.) Coal flotation, froth flotation, 50th anniversary volume. AIME, New York, pp 518–538
16. Kadagala MR, Nikkam S, Tripathy SK (2021) A review on flotation of coal using mixed reagent systems, Vol 173
17. Wang Y, Xing Y, Gui X, Cao Y, Xu X (2016) The characterization of flotation selectivity of different size coal fractions. *Int J Coal Prep Util*. <https://doi.org/10.1080/19392699.2016.1256875>
18. Zhang L, Hower JC, Liu W, Men D (2017) Maceral liberation and distribution of bituminous coal for predicting maceral-separation performance. *Int J Coal Prep Util* 37(5):237–251. <https://doi.org/10.1080/19392699.2016.1160898>
19. Chang Z, Chen X, Peng Y (2019) The interaction between diesel and surfactant Triton X-100 and their adsorption on coal surfaces with different degrees of oxidation. *Powder Technol* 342:840–847. <https://doi.org/10.1016/j.powtec.2018.10.047>
20. Jia R, Harris GH, Fuerstenau D (2002) Chemical reagents for enhanced coal flotation. *Coal Preparation* 22(3):123–149
21. Liao Y, Yang Z, An M, Ma L, Yang A, Cao Y, Chen L, Ren H (2022) Alkanes-esters mixed collector enhanced low rank coal flotation: Interfacial interaction between oil drop and coal particle, *Fuel*, vol 321
22. Bao X, Xing Y, Liu Q, Liu J, Dai S, Gui X, Li J, Yang Z (2022) Investigation on mechanism of the oleic acid/methyl oleate/diesel ternary compound collector in low-rank coal flotation, *Fuel*, vol 320
23. Xing Y, Gui X, Cao Y, Wang Y, Xu M, Wang D, Li C (2017) Effect of compound collector and blending frother on froth stability and flotation performance of oxidized coal powder technology, vol 305, pp 166–173
24. Maria EH, Mastalerz MD (2015) Coal maceral chemistry and its implications for selectivity in coal floatability. *Int J Coal Prep Util* 35(2):99–111
25. Rohman A, Che Man YB (2011) The optimization of FTIR spectroscopy combined with partial least square for analysis of animal fats in quaternary mixtures. *Spectroscopy* 25:169–176

Beneficiation Aspects to Improve the Quality of Bauxite Mining Waste PLK Rock



Satyasish Rout, Santosh Deb Barma, Rahul Kumar Soni,
Prasanta Kumar Baskey, C. Eswaraiah, and Danda Srinivas Rao

1 Introduction

India is rich in Bauxite ore minerals, and their occurrences have been witnessed in various parts of Indian regions of Eastern Ghats (Eastern coast), Central India and Western Ghats (Western Coast). Around 90% of the most commonly used Bauxite are the Lateritic Bauxite (aluminosilicate) which is commonly found in the Eastern region/Andhra Pradesh [1]. Bauxite is a naturally occurring heterogeneous substance that is predominantly formed of aluminium hydroxide minerals in association with a number of impurities like silica, iron oxide, titanium, sulphur, and phosphorous in varying amounts [2].

It is noteworthy to mention that Indian Bauxite is known to have good percentage of reactive silica. It is considered uneconomic to treat reactive silica with more than 5% by Bayer's process because of high soda consumption during the process. For instance, one tonne of silica dissolving from bauxite at the time of digestion requires 1.2 tonnes of soda. Soda is used to process high silica bauxites, and it accounts for up to 20% of alumina production expenses. High levels of reactive silica in the ore wreak havoc on the process's settling, crystallisation, filtration, and calcination. To reduce the reactive silica from bauxite ore, substantial amount of silica mineral bearing rocks has to be rejected during mining. These rejected rocks are technically known as PLK rocks which is a nothing but a waste occurred during mining.

The National Mineral Policy (NMP) 2019, concerning mineral resources, focuses significantly on sustainable utilisation of low-grade mineral resources and associated wastes into Wealth. For the production of 1 tonne of alumina, 8–10 tonnes of mining

S. Rout (✉) · S. D. Barma · R. K. Soni · P. K. Baskey · C. Eswaraiah · D. S. Rao
CSIR-Institute of Minerals & Materials Technology, Bhubaneswar, Odisha 751 013, India
e-mail: satyasishsanu@gmail.com

S. Rout · R. K. Soni · D. S. Rao · D. S. Rao
Academy of Scientific and Innovative Research, Uttar Pradesh, Ghaziabad 201 002, India

© The Author(s), under exclusive license to Springer Nature Singapore Pte Ltd. 2023
E. Chinthapudi et al. (eds.), *Sustainable Chemical, Mineral and Material Processing*,
Lecture Notes in Mechanical Engineering,
https://doi.org/10.1007/978-981-19-7264-5_14

Bauxite wastes are generated. It is important to note that most of the Bauxite mining wastes generated are PLK rock containing 40–55% Al_2O_3 , 0.3–30% Fe_2O_3 , 0.97–3% TiO_2 , 20–30% SiO_2 and 20–30% LOI. In spite of having the metallurgical grade of Al_2O_3 it cannot be used as an important material in the metallurgical industry because of its high reactive silica content. Therefore, after suitable Beneficiation techniques, PLK material can be used as a substitute potential source for the refractory, ceramic, fillers, and adhesives for industrial applications.

In one of the studies, Schneider et al. investigated the refractory grade bauxites and their burning under various conditions. They obtained two samples, CR1 and CR2, and compared them. CR1 contains Fe_2O_3 at a rate of 1.47% and TiO_2 at a rate of 3.48%, whereas CR2 contains Fe_2O_3 at a rate of 1.75% and TiO_2 at a rate of 3.36%. CR1 exhibits microstructures such as corundum, mullite, tillite, and glass after the fire in air and gases [3]. Also et al. reported that Indian bauxite ores can be utilised in refractory industries [4]. The procedure of removing iron from bauxite containing 2.7% Fe_2O_3 was disclosed by Sadler and Venkataraman. A product was produced from Alabama bauxite containing 1.5% Fe_2O_3 using calcinations followed by magnetic separation [5]. Nivedita et al. researched the removal of iron from 5.6% Fe_2O_3 bauxite by a leaching study to make the product suitable for the refractory industry [6]. After flotation, Besra et al. investigated on calcareous bauxite for refractory usage. They proposed a two-stage process of calcination followed by magnetic separation and flotation to remove both iron and calcium. It was possible to make a product with around 2.7% iron and 1.5% calcium that might be used as a refractory [7]. The magnetic separator was used by Rao et al. to decrease the iron minerals so that they could be employed in refractory applications [8]. Banerjee et al. employed a gaseous reduction technique followed by magnetic separation to lower the iron concentration in Jamnagar bauxite ore, which can be used as a refractory material further [9]. The beneficiation of bauxite was studied by few researchers where they explained about the different grades of bauxite found in India. $\text{Al}_2\text{O}_3\%$ > 56–58%, $\text{SiO}_2\%$ —5%, and $\text{Fe}_2\text{O}_3\%$ —3% are all present in refractory grade bauxite [10]. The acceptable Indian bauxite range for $\text{Fe}_2\text{O}_3\%$ and $\text{TiO}_2\%$ for refractory purposes is 2–4% and 2–4%, respectively, according to the Central Pollution Control Board, India. They also mentioned that the unfavourable composition present in bauxite is $\text{Fe}_2\text{O}_3\%$ and $\text{TiO}_2\%$ [11].

With the above literature, it can be understood that Bauxite mining waste such as PLK could act as one of the potential resources of alumina if extracted in a feasible way. Herein, in this paper, we investigated on the PLK waste to improve of alumina content by wet (hydrocyclone followed by wet magnetic separation) and dry (air classifier followed by dry magnetic separation) beneficiation techniques.

2 Materials and Methods

The total sample of 1440 kg was received from UTKAL Alumina International Limited, Rayagada at CSIR-IMMT, Bhubaneswar to carry out various R & D work

Fig. 1 Bauxite mining waste (PLK rock)



related to the utilisation of Bauxite wastes for refractory applications. Initially, 1440 kg of the sample was crushed by a Jaw crusher followed by a roll crusher below 1000 μm . Test sieves (BIS standard) were used for the classification of materials. Representative sub-samples were prepared for characterisation, grindability studies, and beneficiation studies.

2.1 *Characterisation*

Three different coloured samples (shown in Fig. 1) were selected for physical and chemical characterisation. Dry and wet methods were adopted for size classification by standard sieves (BIS). Mineralogical phases and composition were studied by X-ray diffraction methods and X-ray fluorescence, respectively. X-ray diffraction analysis of the sample was carried out by PANalytical X-Pert X-ray powder diffractometer with Mo- KI radiation varying the angle between 10 and 80 degree at a scanning rate of 0.02 degree/s. X-ray Fluorescence analysis of the sample was carried out by Philips (now PANalytical) PW2440 with Rh anode tube (operated at 4 KW).

2.2 *Grindability Studies*

Comminution is an important energy-intensive process for the size reduction of ore. Bond's grindability test is a widely accepted test for the energy consumption of ore from coarser size to finer size. Stage crushing was used to make representative samples which can be passed through a 6 mesh sieve. The mill was loaded with a 700 cc sample weight. These experiments have been carried out in a typical ball mill with a dimension of 300 mm x 300 mm. Steel balls weighing 20.125 kg were employed as grinding media. The number of balls used and respective sizes are mentioned in Table 1.

Table 1 Number of balls with respect to size

No. of Balls	Size, mm
43	36.83
67	29.72
10	25.4
71	19.05
94	15.94

The ball mill was charged with the material weight of a 700 cc volume sample with the balls and ground at 100 revolutions at first. The weight of the undersized sample was noted, and fresh unsegregated feed was added to the oversize to bring it back to its original weight. The number of revolutions needed to produce a sieve undersize equal to 1/3.5 of the total charge in the mill was determined using the previous period's findings. The grinding time cycles were repeated until the net grams of sieve undersize produced per mill revolution were balanced. The undersized product and circulating load were next screened, and the final three net grams per revolution (Gbp) were calculated. Bond Work Index, W_i can be calculated by (Eq. 1)

$$W_i = 44.5/(P_1)^{0.23} \times (Gbp)^{0.82} [10/(P_{80})^{1/2} - 10/(F_{80})^{1/2}] \quad (1)$$

where,

F_{80} is the size in microns at which 80 percent of the new feed to ball mill passes

P_{80} is the size in micron at which 80 percent of the last cycle sieve undersize product passes

P_1 is the opening in microns of the sieve size tested

2.3 Beneficiation Studies

Physical beneficiation techniques such as hydrocyclone and air classification were adopted to improve the quality of PLK rock as discussed below.

2.3.1 Study on Hydrocyclone

Experiments were carried out using Mozley Hydrocyclone unit with varying spigot diameter vortex finders at different pressures. The experiments were performed at different conditions as provide in Table 2. Total number of 22 experiments were designed which is shown in Table 3. Then, the Hydrocyclone products obtained were subjected to Wet High Intensity Magnetic Separator (WHIMS) having 14,000 gauss to decrease iron bearing material from the products.

Table 2 Operating conditions of Hydrocyclone

Parameters	Variables
Cyclone size, mm	50
Spigot diameter, mm	2.2, 3.2, 4.5, 6.4
Vortex finder, mm	8.1, 11.1, 14.3
Pressure, psi	0.75, 1.25, 1.75, 2.25

Table 3 Design for Hydrocyclone studies

Run No	Spigot diameter, mm	Vortex finder, mm	Pulp density, %	Pressure, psi
1	6.4	11.2	10	3
2	2.2	11.2	10	3
3	2.2	14.3	10	2
4	4.3	11.2	5	1
5	4.3	11.2	15	3
6	2.2	11.2	15	2
7	2.2	11.2	10	1
8	6.4	11.2	15	2
9	2.2	11.2	5	2
10	6.4	11.2	10	1
11	4.3	11.2	15	1
12	4.3	14.3	15	2
13	4.3	14.3	10	3
14	4.3	14.3	5	2
15	4.3	14.3	10	1
16	6.4	14.3	10	2
17	4.3	8.1	5	2
18	4.3	8.1	10	3
19	6.4	8.1	10	2
20	2.2	8.1	10	2
21	4.3	8.1	10	1
22	4.3	8.1	15	2

2.3.2 Air Classification

Experiments were conducted at varying rpms (800, 1000, 1200 rpm) and vibrating feed rates (2, 2.5, 3, 3.5 kg/h). Material was fed into the vibratory feeder at different rpms, and the product (coarse & fines) were collected at the outer sections. A cloth entrapment was done at the coarse and fines product section in order to prevent the loss of ultrafine materials. The ultrafine materials or ultrafines collected were subjected

to Dry High Intensity Magnetic Separator (DHIMS) to separate the fractions of magnetic and non-magnetic materials.

3 Results and Discussions

3.1 Characterisation

Three handpicked samples collected from the bulk sample (shown in Fig. 1) were ground and mixed in a homogenous way for physical and the chemical characterization. Results of characterizations are provided in Tables 4 and 5. From Table 5, it can be observed that Al_2O_3 is predominantly high (~39.63%) as compared to other mineral oxides present in it. As determined, the contents of Fe_2O_3 , SiO_2 and TiO_2 were 17.47, 16.8 and 5.32%, respectively, indicating its low-grade nature.

XRD pattern in the Fig. 2 shows the presence of hematite, kaolinite, quartz, gibbsite, ilmenite phase, etc. Kaolinite shows its intense peak at 12.41, 24.90 (2 theta), gibbsite shows its peak at 18.35, 20.41, 37.71 (2 theta), quartz shows its peak at 12.41, 26.72 (2 theta) and hematite shows its peak at 33.19, 35.71 (2theta), etc.

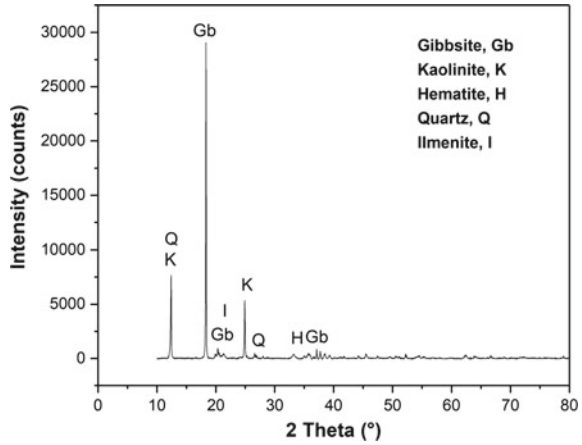
Table 4 Physical properties of the PLK rock sample

Sl. No	Properties	Results
1	Nature of sample	Yellow, grey, red, pinkish, brownish
2	Angle of repose, θ	35
3	Bulk density, g/cm^3	1.2
4	Specific gravity	3.3
5	True density, g/cm^3	2.7
6	Porosity, %	50.8

Table 5 Chemical properties of the PLK rock sample

Sl. No	Chemical name	Composition, %
1	Al_2O_3	39.63
2	SiO_2	16.8
3	Fe_2O_3	17.47
4	TiO_2	5.32
5	LOI	20.22

Fig. 2 XRD of representative PLK rock sample



3.2 Grindability Study

The grindability factor and the Bond’s work index of the following materials were calculated by product 80% passing and the feed. The following is the work index value of rock obtained from Bond grindability test results for typical PLK rock:

Weight of PLK rock sample in 700 cc = 1037.3 gm

B, % of the feed in the undersize = 38.93%

C, weight of the product = $1037.3 * 0.286 = 296.7$ gm

As the three grindability factor results are in equilibrium at 2.42 to 2.57 gm/rev with F_{80} at 910 micron and P_{80} at 72 microns. The Bond work index is calculated using Eq. 1. Table 6 represents the results of grinding. The work index of PLK rock is found to be 8.6 kWh/ton.

Table 6 Calculation of Grindability factor

Revolution	Product, C	Feed, B	C–B	Grindability factor
100	618.30	403.82	214.48	2.15
96	331.90	240.70	91.20	2.30
73	320.20	129.21	190.99	2.35
73	316.10	124.65	191.45	2.42
72	296.50	123.06	173.44	2.54
71	296.40	11.43	180.97	2.57

Table 7 Chemical analysis of different fractions of PLK rock feed sample

Particle size, μm	Wt., %	Fe_2O_3 , %	Al_2O_3 , %	SiO_2 , %	TiO_2 , %	LOI, %
+20,000	1.4	18.1	39.45	16.2	5.3	20.8
+15,000	5.0	18.4	39.44	15.9	5.3	20.8
+10,000	9.1	17.4	39.74	16.3	5.7	20.4
+5000	15.8	17.5	39.88	16.3	5.1	20.4
+3000	2.5	17.2	39.74	16.2	5.8	20.8
+2000	6.8	17.3	39.66	15.1	5.2	21.5
+1000	6.7	17.4	39.64	15.8	5.2	21.8
+710	1.3	17.4	39.64	16.4	4.8	21.5
+500	3.9	17.4	39.62	16.2	5.4	20.9
+355	2.3	17.4	39.68	16.7	5.3	20.1
+250	4.9	17.4	39.62	16.6	5.44	20.6
+180	0.7	17.4	39.64	16.7	5.4	20.2
+150	2.3	17.4	39.61	16.8	5.23	20.3
+125	0.7	17.4	39.62	16.9	5.41	20.4
+106	0.3	17.4	39.67	16.8	5.4	20.1
+90	1	17.4	39.62	16.5	5.4	20.4
+75	0.7	17.4	39.61	16.9	5.3	20.1
-75	34.6	17.4	39.66	16.8	5.3	20.3

3.3 Beneficiation Studies

3.3.1 Size Classification

In order to understand the chemical distribution matrices in each fraction of feed sample, size fractional analysis was performed. The size fractions were considered from 20 mm to 75 μm . Table 7 indicates that, Al_2O_3 contains ~ 39–40%, whereas SiO_2 , Fe_2O_3 and TiO_2 contains ~ 15.1–16.8%, ~ 17.2–18.4%, ~ 4.5–6% with LOI varying ~ 20–22% respectively.

3.3.2 Hydrocyclone Study

Hydrocyclone study was conducted on -1 mm particle size at different spigot diameter and vortex finder with varying pressure as discussed below in the Table 8 in reference with the design of Table 3. It can be seen from Table 8 that Al_2O_3 , SiO_2 and Fe_2O_3 were found to be varying in the range of ~40–45%, ~14–15% and ~14–16.5%, respectively, for under flow (UF) product. Conversely, Al_2O_3 , SiO_2 and Fe_2O_3 were found to be varying in the range of ~35–38%, ~16.2–16.7% and ~18.03–20.8%, respectively, for over flow (OF) product. These underflow and overflow products were

subjected to Wet High Intensity Magnetic Separator (WHIMS) at 15,400 gauss to remove the ferruginous minerals from the hydrocyclone product sample. Table 9 represents the magnetic separation data of WHIMS.

3.3.3 Air Classification Studies

This study was conducted to compare the hydrocyclone study with air classification. Total 12 number of experiments were conducted varying the speed of cage wheel in rpm (800, 1000, 1200) and feeder rate in kg/hr (2, 2.5, 3, 3.5) which is shown in Table 10. From the above design for each experiment at different times, the amount of coarse and fines obtained in kg/hr was noted. From the Table 10 it is observed that with increase in speed, the fines wt.% is increasing gradually. Table 11 shows the analysis of the air classification products which involves Al_2O_3 , SiO_2 and Fe_2O_3 varies in the range of ~41–42.5%, ~15.2–15.7% and ~14.2–14.5%, respectively, for coarse product. Conversely, Al_2O_3 , SiO_2 and Fe_2O_3 varies in the range of ~35.6–37.2%, ~16.1–16.7% and ~20–21.5%, respectively, for fines product. The products obtained from the coarse and fines were subjected to permroll at 0.14 T to remove the ferruginous minerals (Table 12).

4 Conclusion

The investigations carried out on PLK waste rock bauxite contain 39.63% Al_2O_3 , 16.80% SiO_2 , 17.47% Fe, and 5.32% TiO_2 . The sample was characterised to understand the association between alumina, iron and silica-bearing minerals. Mineralogical studies indicated that the sample consists of hematite, kaolinite, quartz, gibbsite, ilmenite as the major mineral phases. XRD study revealed that 2 theta value of Hematite varies in the range of 33.19, 35.71; Quartz shows its 2-theta peak at 12.41, 26.72; Gibbsite shows its 2-theta peak at 18.35, 20.41, 37.71; Kaolinite shows its 2-theta peak at 12.41, 24.90°. Grindability study shows that the Bond work Index value for PLK is 8.6 kWh/t. Beneficiation studies using hydrocyclone were compared to air classification. Hydrocyclone study shows that Al_2O_3 , SiO_2 and Fe_2O_3 were found to be varying in the range of ~40–45%, ~14–15% and ~14–16.5%, respectively, for under flow (UF) product; On the other hand, air classification study showed that Al_2O_3 , SiO_2 and Fe_2O_3 varies in the range of ~41–42.5%, ~15.2–15.7% and ~14.2–14.5%, respectively, for coarse product. Therefore, from the above study, we can conclude that Hydrocyclone followed by WHIMS could be preferred as one of the best ways to improve the quality of PLK over Air classification technique.

Table 8 Results of hydrocyclone studies

Run No	Products	Wt., %	Al ₂ O ₃ , %	SiO ₂ , %	Fe ₂ O ₃ , %	TiO ₂ , %	LOI, %
1	UF	48.2	44.5	14.3	14.3	5.64	21
	OF	51.8	35.23	17.3	20.8	4.8	21.64
2	UF	48.6	42.6	15.58	15.3	5.23	21.2
	OF	51.4	36.61	16.2	20.2	5.1	21.4
3	UF	47.2	42.1	15.4	15.8	5.44	20.8
	OF	52.8	37.1	16.2	19.8	5.01	21.4
4	UF	48.3	40.3	15.23	16.2	5.56	21.8
	OF	51.7	37.94	16.3	19.2	4.87	21.5
5	UF	49.1	40.8	15.43	16.4	5.54	21.2
	OF	50.9	37.8	16.4	19.1	5.1	21.4
6	UF	48.9	41.2	15.2	16.8	5.89	20.8
	OF	51.1	37.81	16.4	18.03	5.2	21.6
7	UF	49	41.4	14.8	15.9	5.84	21.4
	OF	51	37.82	16.7	18.34	5.5	20.99
8	UF	48.1	41.3	15.17	15.2	5.95	21.44
	OF	51.9	37.23	16.23	19.23	5.6	20.23
9	UF	47.3	41.4	15.2	15.6	5.96	21.44
	OF	52.7	37.23	16.11	19.4	5.2	21.2
10	UF	48.1	41.3	15.3	15.4	5.45	22.1
	OF	51.9	37.23	16.2	19.44	5.3	21.3
11	UF	49	41.2	15.2	15.4	5.23	22.1
	OF	51	37.44	16.3	19.53	5.4	21.2
12	UF	49.1	41.8	15.4	15.2	5.12	21.8
	OF	50.9	37.99	16.2	19.23	5.2	21.23
13	UF	49.8	41.2	15.6	16.2	5.47	21.23
	OF	50.2	37.44	16.2	19.1	5.1	21.44
14	UF	48.9	41.3	15.7	15.7	5.2	21.2
	OF	51.1	37.6	16.2	19.2	5.2	21.6
15	UF	49.2	40.6	15.6	16.5	5.88	21.1
	OF	50.8	38.23	16.3	18.2	5.43	21.8
16	UF	48.1	44.23	15.6	15.1	5.23	19.23
	OF	51.9	35.94	16.3	19.8	5.3	22.34
17	UF	49.2	41.23	15.1	15.7	5.44	22.5
	OF	50.8	37.2	16.5	19.8	5.3	20.28
18	UF	49.7	42.2	14.2	15.9	5.66	21.4
	OF	50.3	37.4	16.4	19.6	5.4	20.44

(continued)

Table 8 (continued)

Run No	Products	Wt., %	Al ₂ O ₃ , %	SiO ₂ , %	Fe ₂ O ₃ , %	TiO ₂ , %	LOI, %
19	UF	49.4	42.2	15.3	15.6	5.12	20.99
	OF	50.6	37.23	16.5	19.4	5.3	21.42
20	UF	49.2	41.9	15.7	15.4	5.21	20.96
	OF	50.8	37.44	16.2	19.2	5.3	21.2
21	UF	48	41.3	15.8	15.9	5.31	20.98
	OF	52	37.21	16.4	19.3	5.23	21.3

OF = Overflow Product Hydrocyclone; UF = Underflow Product of Hydrocyclone

Table 9 Results of hydrocyclone products subjected to WHIMS

Run No	Overflow		Underflow	
	Magnetic, %	N-Magnetic, %	Magnetic, %	N-Magnetic, %
1	1.4	98.6	14.7	85.3
2	1.5	98.5	16.5	83.5
3	3.9	96.1	15.0	85
4	2.9	97.1	15.9	84.1
5	1	99.0	16.8	83.2
6	2.6	97.4	16.6	83.4
7	3.3	96.7	15.8	84.2
8	3.5	96.5	12.4	87.6
9	1.5	98.5	12.9	87.1
10	3.6	96.4	12.7	87.3
11	2.3	97.7	14.0	86
12	5	95.0	12.2	87.8
13	5.1	94.9	13.6	86.4
14	4.6	95.4	15.4	84.6
15	2.4	97.6	14.1	85.9
16	2.3	97.7	14.0	86
17	2.2	97.8	12.5	87.5
18	2.2	97.8	13.7	86.3
19	2.3	97.7	12.5	87.5
20	1.5	98.5	12.9	87.1
21	2.6	97.4	12.4	87.6

Table 10 Air classification studies of PLK rock

Sl. No	Speed, rpm	Feeder rate, kg/hr	Coarse wt., %	Fines wt., %
1	800	2	59.2	40.8
2	800	2.5	51.8	48.2
3	800	3	52.6	47.4
4	800	3.5	58.8	41.2
5	1000	2	51.3	48.7
6	1000	2.5	53.8	46.2
7	1000	3	52.9	47.1
8	1000	3.5	53.2	46.8
9	1200	2	50.0	50.0
10	1200	2.5	51.9	48.1
11	1200	3	50.0	50.0
12	1200	3.5	49.7	50.3

Table 11 Analysis of Air classification studies

Sl. No	Sample	Wt., %	Al ₂ O ₃ , %	Fe ₂ O ₃ , %	SiO ₂ , %	TiO ₂ , %	LOI, %
1	Coarse	59.2	41.8	14.2	15.3	5.18	22.3
	Fines	40.8	37.2	21	16.1	5.2	19.1
2	Coarse	51.8	41.4	14.7	15.4	5.11	22.6
	Fines	48.2	37.6	20.5	16.4	5.25	19.5
3	Coarse	52.6	41.4	14.3	15.2	5.18	22.81
	Fines	47.4	37.4	20.5	16.5	5.23	20.5
4	Coarse	58.8	42.4	14.8	15.4	5.08	21.1
	Fines	41.2	36.4	20.8	16.1	5.2	21.3
5	Coarse	51.3	42.2	14.5	15.2	5.18	21.9
	Fines	48.7	36.5	20.6	16.5	5.23	20.33
6	Coarse	53.8	42.3	14.8	15.3	5.2	21.8
	Fines	46.2	35.6	20.2	16.3	5.2	21.9
7	Coarse	52.9	42.2	14.7	15.4	5.2	21.87
	Fines	47.1	36.8	20.4	16.3	5.23	20.23
8	Coarse	53.2	42.5	14.4	15.3	5.2	21.8
	Fines	46.8	36.3	20.3	16.7	5.3	21.0
9	Coarse	50	42.1	14.5	15.2	5.2	22.4
	Fines	50	36.5	20.2	16.7	5.1	20.6
10	Coarse	51.9	42.2	14.2	15.4	5.2	22.3
	Fines	48.1	36.6	21.4	16.2	5.3	19.8
11	Coarse	50	42.1	14.5	15.2	5.1	22.2
	Fines	50	36.4	20.1	16.4	5.2	21.2
12	Coarse	49.7	42.12	14.3	15.4	5.21	21.4
	Fines	50.3	36.5	20.1	16.4	5.12	21.7

Table 12 Air classification products subjected to DHIMS

Speed, rpm	Feeder rate, kg/hr	Coarse (%), Mag	Coarse (%), N-Mag	Fines (%), Mag	Fines (%), N-Mag
800	2	40.15	59.85	87.35	12.65
	2.5	40.85	59.15	87.45	12.55
	3	38.75	61.25	93.10	6.90
	3.5	37.00	63.00	87.30	12.70
1000	2	50.20	49.80	86.50	13.50
	2.5	41.50	58.50	85.65	14.35
	3	41.25	58.75	88.00	12.00
	3.5	47.60	52.40	84.50	15.50
1200	2	49.80	50.20	87.10	12.90
	2.5	48.75	51.25	90.25	9.75
	3	44.00	56.00	73.35	26.65
	3.5	52.30	47.70	79.90	20.10

Acknowledgements The authors would like to acknowledge the Director, CSIR-IMMT, Bhubaneswar for his permission to communicate this work. The funding from CSIR (project no. MLP-66) is highly acknowledged.

References

- Bhukte P, Daware GT, Masurkar S, Chaddha MJ (2021) Beneficiation of low-grade bauxite: a case study of lateritic bauxite of India. https://doi.org/10.1007/978-3-030-73796-2_6
- Bhukte P, Chaddha M, Najar M, Daware G, Masurkar S, Karn A, Agnihotri A (2020) Beneficiation aspects of low-grade unutilized materials (Partially Lateritised Khondalite and Laterite) associated with bauxite mine. In: TRAVAUX 49, proceedings of the 38th international ICSOBA conference, 16–18 November 2020
- Schneider H, Wang J, Majdic A (1987) Firing of refractory grade chinese bauxites under oxidizing and reducing atmosphere. In: DECA 5334/C5, cfi/BER. DKG 64, No. ½-87, 1987, 29–31
- , Bhima Rao R, Ansari MI Seminar on beneficiation of refractory raw materials. Indian Refractory Markers
- Sadler LY, Venkataraman C (1991) A process for enhanced removal of iron from bauxite ores. *Int J Miner Process* 31:233–246
- Patnaik N, Das B, Rao RB (1996) Removal of calcium and iron from bauxite for use in refractory industry. *Erzmetall* 49(9):555–558
- Besra L, Banerjee GN, Reddy BR, Rao RB (1996) Flotation studies of calcareous bauxite for refractory use. In: BAUXAL – 96, Bhubaneswar, Orissa, India, pp 467–477
- Rao RB, Besra L, Reddy BR, Banerjee GN (1997) The effect of pretreatment on magnetic separation of ferruginous minerals in bauxite. *Magn Electrical Sep* 8:115–123
- Banerjee GN, Reddy BR, Rao RB (2000) Deironation of bauxite by gaseous reduction and magnetic separation for refractory uses. *Trans. Indian Inst Met* 53(4–5):527–529
- Bhattacharya S, Mookherjee S (1987) Bauxite beneficiation in India. *CEW*, XXII 12:62–67
- Comprehensive industry document series, COINDS/68/2007 (2011) comprehensive industry document for refractory industry. Central pollution control board, ministry of environment and forests, 2007, www.cpcb.nic.in

Study on Flotation of Sillimanite Using Plant-Based Collector



N. Vasumathi, K. Chennakesavulu, I. Cassandra Austen, M. Sai Kumar, T. V. Vijaya Kumar, and Ajita Kumari

1 Introduction

In India, the heavy mineral beach sand carry minerals like ilmenite, garnet, rutile, monazite, sillimanite, and zircon. The west coast of Kerala, the east coast from Tamil Nadu to Odisha contains heavy mineral (ilmenite) rich beach sand deposits. These ilmenite samples of Indian origin has 50–60% of TiO_2 and is most suited for beneficiation by different processes. Also minerals such as monazite, sillimanite, and zircon are present in inland red Teri sands, apart from heavy mineral beach sands and has high potential for beneficiation. The conducting and magnetic minerals are separated first, leaving behind the non-conducting and non-magnetic sillimanite along with quartz in the processing of heavies in beach sand. The placer minerals of 348 Million tons (Mt) ilmenite, 107 Mt garnet, 21 Mt zircon, 18 Mt monazite, and 130 Mt Sillimanite are present in Indian resources. About 35% of world resources are contributed from India. The heavy mineral sands are basically sedimentary deposits of dense minerals which pile up with sand, silt, and in association with clay along the coastal line, leading to economic concentrations of these heavy minerals [1–5]. The conducting and magnetic minerals are separated first, leaving behind the non-conducting and non-magnetic sillimanite along with quartz in the processing of heavies in beach sand. Sillimanite, an important mineral for refractory application, is mainly recovered by flotation technique from its associated major gangue mineral, quartz by imparting selective surface hydrophobicity on sillimanite using a suitable collector. Sillimanite is a non-conducting and non-magnetic mineral and hence flotation technique was

N. Vasumathi (✉) · M. S. Kumar · T. V. V. Kumar · A. Kumari
CSIR – National Metallurgical Laboratory, Madras Center, Chennai 600 113, India
e-mail: vasumatisamy@gmail.com

K. Chennakesavulu · I. C. Austen
Department of Chemistry, Sathyabama Institute of Science and Technology, Jepiaar Nagar,
Chennai 600 119, Tamil Nadu, India

© The Author(s), under exclusive license to Springer Nature Singapore Pte Ltd. 2023
E. Chinthapudi et al. (eds.), *Sustainable Chemical, Mineral and Material Processing*,
Lecture Notes in Mechanical Engineering,
https://doi.org/10.1007/978-981-19-7264-5_15

203

adopted to separate it from other associated gangue minerals mainly quartz. Flotation is physico-chemical process and depends on surface hydrophobicity for separation of valuable minerals from its accompanying gangue minerals. Flotation process have been effectively used for fines and size of the sillimanite mineral present in the heavy mineral beach sand is most appropriate to be processed by flotation. In any separation process based on flotation, the flotation reagents added in order to modify/enhance the surface hydrophobic nature of the minerals intended to be separated and hence the appropriate selection of reagent plays a vital role in the efficiency of the flotation technique. Apart from the reagent selection, the dosage of the reagents added in the flotation circuits needs to be optimized for the required grade and recovery. Flotation studies on sillimanite by flotation column on Odisha sands were carried out using oleic acid as collector [6–14]. Recovery of sillimanite by flotation tree analysis method and conventional flotation technique from the non-magnetic product of red sediments were also studied. Also, some investigation on flotation of sillimanite at acidic pH were reported.

In this work, one such Indian beach placer sample has been attempted for beneficiation using flotation method. In preliminary flotation studies, pH and depressant dosage were varied to establish the optimized process criteria. Types of collectors used for flotation studies are oleic acid and plant-based collector SFA. Flotation of sillimanite sample was optimized by studying various process parameters. Sillimanite feed sample, collectors, and concentrate obtained from optimized set have been characterized using X-ray diffraction (XRD) and Fourier-transform infrared (FTIR) spectroscopy.

2 Material and Methods

2.1 Materials

In this study, a placer sample after the removal of heavies from western coast of southern India containing 55.4% sillimanite along with 33.9% quartz, 1.7% magnetics, 1.4% rutile, 2.4% zircon, and 5.6% kynite was subjected to froth flotation for enriching the sillimanite content. A representative head sample was drawn, and the remaining material was used for flotation studies. A laboratory synthesized plant-based reagent, Collector SFA, and oleic acid were used as collector. Methyl isobutyl carbinol (MIBC) was used as frother. Sodium silicate was used as depressant and soda ash as pH regulator. The sillimanite used in this study was the feed to sillimanite flotation circuit of an operating heavy mineral beach sand beneficiation plant.

2.2 Methods

Bench scale flotation experiments were carried out in a standard Denver laboratory flotation machine. Representative feed and concentrate samples were subjected to X-ray diffraction (XRD) to identify the mineral phases. Fourier transform infrared (FTIR) was used to detect various functional groups present using Bruker Alpha II Compact FTIR Spectrometer-ATR module.

3 Results and Discussion

3.1 Characterization Studies

Fourier transform infrared (FTIR) spectroscopy analysis is used to identify organic, inorganic, and polymeric materials. Mineral phases present in the sample were identified qualitatively using a BRUKER ALPHA-II Compact FTIR Spectrometer—ATR module over the range of $4000\text{--}400\text{ cm}^{-1}$ at room temperature with resolution of $\pm 4\text{ cm}^{-1}$. The FTIR analysis method uses infrared light to scan test samples and observe chemical properties.

The characterization of this natural source-based sillimanite collector is carried out and compared with that of the most commonly used oleic acid collector using FTIR to study the functional groups that enhances the selective sillimanite flotation. The peaks at 2700 to 3100 cm^{-1} and 1708 cm^{-1} confirm the presence of -COOH in the natural source-based collector (Fig. 1).

The adsorption of oleate and collector SFA on sillimanite surface were examined by FTIR spectroscopy. The FTIR spectrum of sillimanite does not show any peaks in 1400 to 4000 cm^{-1} region. The FTIR of oleic acid coated sillimanite displayed few bands at 1462 , 1372 , and 722 cm^{-1} indicating the oleic acid on sillimanite surface with calcium ions. The band at 1708 cm^{-1} clearly suggests the presence of carbonyl group on sillimanite surface. The peaks at 2922 and 2853 cm^{-1} corresponds to asymmetric and symmetrical stretching vibrations of -CH_2 and CH_3 group. The peak shifts in FTIR spectrum of oleic acid coated sillimanite indicates the chemisorption of oleate on sillimanite surface.

The FTIR of SFA reagent and SFA coated sillimanite samples showed that the SFA has chemical interaction with sillimanite hydroxyl group. The peaks at 1696 cm^{-1} confirm the presence of free -COOH in then SFA collector. In order to distinguish the physical or chemical interaction between SFA and sillimanite surface, the SFA adsorbed sillimanite sample was washed with water, the samples was dried at room temperature and analyzed for FTIR. The peak at 1690 cm^{-1} shifted to 1712 cm^{-1} clearly indicates the chemical interaction between collector SFA and sillimanite (Fig. 2).

The sillimanite feed to flotation and the concentrate obtained from the flotation of feed is analyzed for its mineralogy using x-ray diffraction (XRD) studies. XRD study

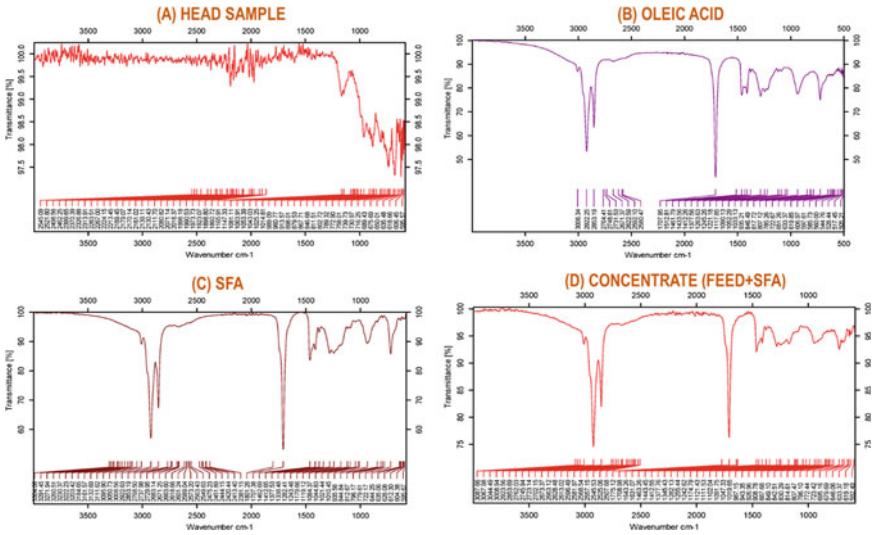


Fig. 1 FTIR images of placer head sample (a), oleic acid (b), plant-based collector SFA (c), and concentrate obtained at optimized experimental set with SFA as collector (d)

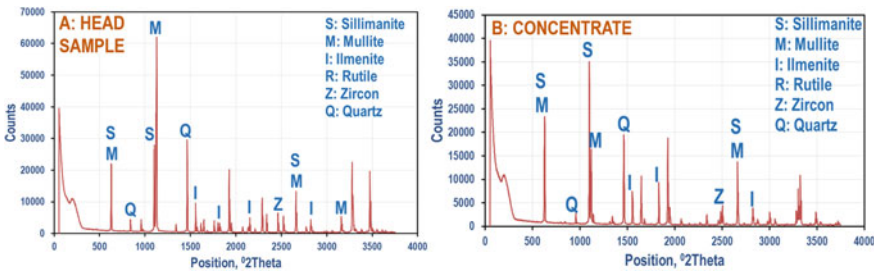


Fig. 2 XRD spectra of a sillimanite head sample (feed) and b flotation concentrate obtained with SFA as collector

of the representative sample was carried out using X-Ray Diffractometer AXRD Benchtop, Canada. The anode material used was copper, and the generator settings were maintained at 30 mA and 40 kV. The X-ray patterns were acquired in the 2θ range of 10° – 90° with a step size of 0.001° /s.

The XRD pattern indicates the presence of sillimanite, ilmenite, and rutile along with quartz as mineral phases. The ilmenite and rutile phases are present because of the contamination of wet circuit heavies product of the heavy mineral beach sands report to the sillimanite feed. The quartz mineral is the major phase and contributes as the major impurity mineral in the sillimanite flotation process. If the recovery process of ilmenite and rutile are effective, then these minerals would not report into the sillimanite circuit. It can be observed that from the x-ray diffractogram of sillimanite

concentrate, the sillimanite phase appears to be prominent than the quartz gangue mineral phase indicating the better separation efficiency of the flotation process.

3.2 Beneficiation Studies Using Froth Flotation

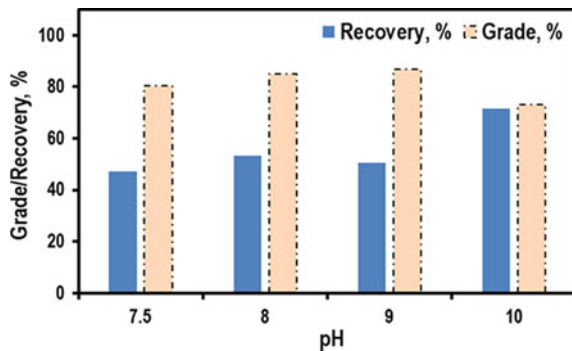
The flotation process optimization and the effect of variation of process parameters such as pH, depressant, and both the collectors were evaluated. Operational parameters maintained during flotation experiments are 33% solids by weight, 1250 rpm, 5 min conditioning time. Reagent dosages and pH have been varied in the successive series of experiments.

3.2.1 Effect of Variation in pH

Effect of variation in pH on sillimanite flotation was studied. Initial test was conducted at natural pH (~7), and then pH was varied to 8.0, 9.0, and 10.0 using soda ash while maintaining depressant dosage at 0.8 kg/t and collector (oleic acid) dosage at 0.65 kg/t.

As it can be seen from Fig. 3 that maximum recovery of 53.41% could be obtained at a concentrate grade of 85% sillimanite at pH 8.0. Hence it was considered as the optimum and maintained constant in the subsequent series of tests for optimizing the depressant dosage. The flotation of aluminosilicate minerals using alkyl guanidine as collector was done and results are effective at pH 4 to 12. The extensive study on adsorption of oleic acid on sillimanite also suggest that at pH 8.0, the adsorption density of oleate on sillimanite was maximum.

Fig. 3 Grade and recovery of sillimanite obtained at varying pH



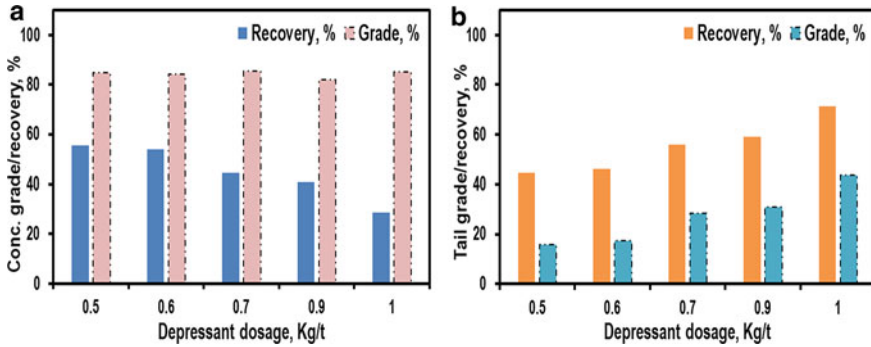


Fig. 4 Grade and recovery of sillimanite concentrate **a** and tailings **b** obtained at various dosage of depressant, sodium silicate

3.2.2 Effect of Variation in Depressant Dosage

Effect of variation in depressant dosage on sillimanite flotation was observed. Flotation tests were conducted at varying dosage of depressant (sodium silicate) while maintaining constant collector (oleic acid) dosage of 0.65 kg/t at pH 8.0.

It can be seen from Fig. 4 that increase in depressant dosage from 0.5 to 1.0 kg/t resulted in increasing tailings loss of sillimanite from 15.8 to 31.0%. A lower dosage of 0.5 kg/t was found to be optimum. At this depressant dosage, a concentrate of 84.9% sillimanite with 55.54% weight recovery could be obtained. On gradual increase in dosage of sodium silicate, the recovery of the sillimanite concentrates decreases gradually, indicating that the depressant is effective as a depressant to quartz as the grade is not diluted even at lower dosage of sodium silicate. In case of tailings, the recovery is increasing as more gangue are being depressed on increasing the dosages of depressant. It is also proven that from various investigations that sodium silicate proves to be a better depressant in depressing quartz mineral.

3.2.3 Effect of Variation in Collector Dosage

Effect of variation in collector dosage on sillimanite flotation was observed. Flotation tests were conducted at varying dosage of collector (SFA and oleic acid) while maintaining constant depressant (sodium silicate) dosage of 0.5 kg/t at pH 8.0.

By using the plant based collector SFA, the increase in dosage of this collector showed a gradual improvement in recovery thereby indicating the better and steady collective property of this novel reagent developed. Apart from collection property, Collector also has better selectivity which is evident from the increase in grade along with recovery with increase in reagent dosages. This can be achieved when the reagent specifically adsorbs on the surface of the targeted mineral, here its sillimanite, and imparts hydrophobicity to the mineral surface and thereby enhancing

the mineral's ability to float to the surface of the slurry. Because of the high selectivity nature of Collector SFA, the grade and recovery improvement is observed with increasing dosage of the collector. However, in case of collector oleic acid, the recovery decreases as the dosage is increased leading to the diluting the grade of the tailings due to loss of sillimanite in to the tailing. This is a clear indication of inferior collection property of the oleic acid as compared to that of the plant-based sillimanite collector SFA.

It can be observed from Fig. 5 that grade and recovery is higher in case of plant-based collector SFA than that of the conventional collector oleic acid. The study on flotation of kyanite and sillimanite with collector oleic acid also suggests that the sillimanite recovery is maximum at pH 8.0 and 1 mM oleate concentration. Concentrate weight recovery of 67.8% with 85.1% sillimanite was obtained using the plant-based collector SFA (1.5 kg/t dosage) while the concentrate weight recovery of 58.5% with 79.9% sillimanite was obtained using oleic acid from feed with 55.4% sillimanite (collector dosage: 0.55 kg/t). This shows that plant-based collector SFA has better collector properties in case of sillimanite flotation. The present study also confirms the plant-based SFA was selective towards sillimanite and hence maximum recovery could be observed at pH 8.0. The sillimanite collector SFA developed is also bio-degradable and environmental friendly and provides a safe and economically viable option for heavy mineral beach sand separation industries.

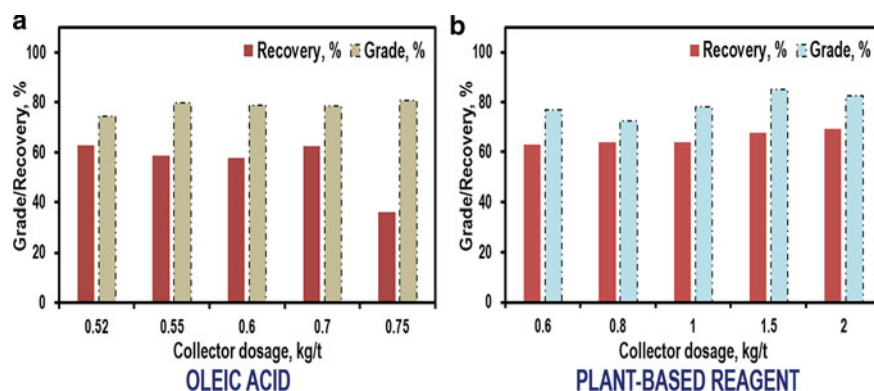


Fig. 5 Grade and recovery of sillimanite obtained at various collector dosage of **a** oleic acid and **b** plant-based reagent SFA

4 Conclusion

Flotation process for sillimanite was optimized by varying process parameters such as pH, depressant dosage and two types of collectors. It was observed that flotation performance of the natural plant source based-collector SFA has better selectivity resulting in improved recovery as compared to that of oleic acid as sillimanite collector. An improved weight recovery of 67.8% with 85.1% sillimanite was obtained using the newly developed natural source-based collector SFA while a weight recovery of 58.5% with 79.9% sillimanite from feed with 55.4% sillimanite was obtained using oleic acid. The improved sillimanite recovery by above 9% using this new plant source-based collector SFA than that of the conventional oleic acid would be more economical in industrial scale sillimanite recovery in beach sand processing industries.

References

1. Babu N, Vasumathi N, Rao RB (2009) Recovery of ilmenite and other heavy minerals from teri sands (red sands) of Tamil Nadu, India. *J. Miner. Mater. Charact. Eng.* 08. <https://doi.org/10.4236/jmmce.2009.82013>
2. Laxmi T, Rao RB (2015) Flotation tree analysis for recovery of sillimanite from red sediments. *Int J Min Sci Technol* 25:843–848. <https://doi.org/10.1016/J.IJMST.2015.07.021>
3. Van-Gosen B, Fey DL, Shah AK, Verplanck PL, Hoefen TM (2014) Deposit model for heavy-mineral sands in coastal environments, U.S. Geol. Surv. Investig. Rep. 2000–5070, pp 1–51. <https://pubs.usgs.gov/sir/2010/5070/>
4. Chen Z, Ren Z, Gao H, Lu J, Jin J, Min F (2017) The effects of calcium ions on the flotation of sillimanite using dodecyl ammonium chloride. *Minerals* 7:1–11. <https://doi.org/10.3390/min7020028>
5. Viswanathan D (2007) Processing of plant rejects-for sillimanite recovery. In: Proceedings of mineral processing technology, Mumbai, India, p 3
6. Prabhakar S, Bhaskar Raju G, Subba Rao S (2006) Beneficiation of sillimanite by column flotation—a pilot scale study, 2006, vol 81, 3, pp 159–165
7. Prusty S, Mohapatra BK, Singh SK, Bhima Rao R (2009) Recovery of sillimanite from beach sand of Chhatrapur, Orissa, India and its thermal treatment for refractory application. *Int J Mining Mineral Eng* 1(4)
8. Mihir DM, Rama Rao VV, Padmasree R (2016) Sodium benzoate and urea as promoters in sillimanite flotation, vol 7, No. 3
9. Bonda R, Patil MR, Gopalkrishna SJ, Murthy CH VGK, Sankar NJ, Chakravarthy DP, Rao NJ Beneficiation studies on beach sand minerals of Trimex Sands Private Limited, Srikakulam–Andhra Pradesh
10. Rao YYN, Rao GVU, Majumdar KK (1964) Recovery of economic minerals from Indian Beach sands, *Mining Magazine*, pp 401–408
11. Manjeera PB, Pulipati K, Rao J (2016) Ilmenite recovery from beach sands minerals industrial rejects using dry magnetic separator (RED). *Int J Eng Sci Comput Res* 6(6)
12. Feng G, Zhong H, Liu G-Y, Zhao S-G, Xia L-Y (2009) Flotation of aluminosilicate minerals using alkylguanidine collectors. *Trans Nonferrous Metals Soc China* 19(1): 228–234. ISSN 1003-6326

13. Vijaya Kumar TV, Prabhakar S, Bhaskar Raju G (2002) Adsorption of oleic acid at sillimanite/water interface. *J Colloid Interface Sci* 247(2):275–281
14. Junxun J, Huimin G, Zijie R, Zhijie C (2016) The flotation of kyanite and sillimanite with sodium oleate as the collector. *Minerals* 6:3

Flotation of Low-Grade Graphite Ore Using Collector Derived from Low-Density Polyethylene Waste



M. Sai Kumar, K. Rashid Sulthan, N. Vasumathi, Ajita Kumari, and T. V. Vijaya Kumar

1 Introduction

Polymorphs of carbon ranges from soft, blackish graphite to hard, transparent diamond. From the early fifteenth century itself graphite was widely used as it shows the properties of both metal and non-metal, has an extraordinarily low specific gravity, incredibly soft and cleaving with noticeably light pressure, exceptionally heat resistant and inert when in contact with other materials. That is why it is called as a “Mineral of Extremes” [1]. Crystalline forms of natural graphite have small flake size and as metamorphic grade increases it leads to microcrystalline forms. These flake graphites are graded based on the graphitic carbon content and flake size. Hexagonal crystal structure is the thermodynamically stable form of graphite which results in tremendous properties. The properties of graphite vary from place to place as the geography of the mined area play a crucial role in metamorphism.

Among various beneficiation techniques, froth flotation is more suitable for treating fines and naturally hydrophobic ores. Flotation is a surface phenomenon based on the surface hydrophobicity of the mineral surfaced to be separated [2–4]. Due to the natural hydrophobicity of graphite, this technique is adopted for beneficiation. The hydrophobic mineral particles which are attached to air bubbles floats on top as froth and is separated, while the remaining hydrophilic gangue particles that attach with water molecules stay in liquid [2–6]. Nanobubbles can be produced by ultrasonication, but this doesn’t have any effects on the floatation performance of graphite [7]. Ultrasonic-assisted flotation has effects on floatability which enhances the recovery flaky graphite from low-grade graphite ore [8]. The particle size has

M. Sai Kumar (✉) · N. Vasumathi · A. Kumari · T. V. Vijaya Kumar
CSIR - National Metallurgical Laboratory Madras Centre, Chennai 600113, Tamil Nadu, India
e-mail: saikumar.madhira@gmail.com

K. Rashid Sulthan
Department of Chemistry, Amrita School of Arts and Sciences, Kollam 690525, Kerala, India

crucial roles in the overall multi-stage grinding-regrinding-flotation steps [9]. Selective adsorption of particular reagents on the mineral surface depends on the particle size of the mineral present in the pulp [10]. Controlled grinding is very important to achieve ideal cost-effective separation [11]. Surface chemistry can be affected by flotation. The purity of single graphite particles, on the other hand, is rarely compromised. Flotation reagents, viz., collectors, frothers, etc., are added to transform the mineral–water mixture suitable for flotation by controlling the relative hydrophobicity of particles and maintain froth characteristics [12]. These chemicals have critical role and importance in the entire process as they involve complex interactions. Graphite has natural affinity towards air bubbles. The chemical reagents commonly used in graphite flotation increase the selective hydrophobicity and a variety of non-polar hydrocarbon-based oils such as kerosene, diesel, and fuel oil are generally used collectors in combination with frothers such as pine oil, Methyl Isobutyl Carbinol (MIBC) or higher alcohol [13–15]. A jump-in phenomena exist between non-polar collectors and the hydrophobic surface, indicating the existence of an attractive force. Polar collectors form hydrogen bonding with water results in a weaker adhesive force. Jump-in distance, jump-out distance, friction force, and adhesion force are greater and play crucial role in the interaction of collectors with graphite surface [16]. Diesel oil as collector and MIBC as frother was found to yield best results in graphite flotation comparing other hydrocarbon oils like dodecane, kerosene, pine oil, iso octonal in terms of total carbon content and total carbon recovery of the rougher concentrate of graphite [13, 17]. In graphite flotation, the selectivity index between collector and graphite increases as the average droplet size of collector emulsions (e.g., Kerosene) lowers [18]. Conventional reagents are not economic when used in industrial scale due to the continuous price escalation of fuel oils.

Synthetic plastic, the world's most used polymer, whose disposal poses the utmost threat to environment as it is not readily bio-degradable and uses non-renewable resources as key ingredient in manufacturing of plastics. Around 12.7 tonnes per year of plastic waste is produced around the world which pollutes the entire ecosystem.

The present work evaluates the flotation performance efficacy of the oil (collector PE) derived using LDPE, i.e., low-density polyethylene waste as collector in combination with MIBC as frother and compares with the conventional reagent combination of diesel and MIBC for flotation of low-grade graphite ore (run-of-mine) from Tamil Nadu.

2 Material and Methods

A low-grade graphite ore (run-of-mine, R.O.M) from Tamil Nadu, India, was utilized in this study for recovery of graphite by flotation. The R.O.M graphite ore was size reduced in stages in a laboratory jaw crusher and a representative sample was drawn by riffle sampling. The preliminary laboratory scale tests for optimization of process parameters such as mesh-of-grind (grinding time), collector and frother dosages to recover graphite with reduced ash content were conducted.

2.1 Flotation Methodology

The flotation experiments were carried out in Denver D-12 laboratory flotation machine, at natural pH of the slurry (about 7) and impeller speed of 1240 rpm. The graphite slurry was conditioned with the reagents for 3 min each and the froth (float) was collected till froth formation ceased. The collected froth and tailings were dewatered, dried, weighed, and subjected to ash analysis. During the cleaning stages, no reagents were added and the froth from roughing stage was collected and subjected to cleaner flotation.

2.2 Flotation Reagents

Commercially available diesel, MIBC (LR grade), collector PE (oil-derived LDPE waste) were used as reagents in graphite flotation.

3 Results and Discussion

3.1 Proximate Analysis of Graphite Ore

The proximate analysis of R.O.M graphite ore was carried out to determine the (1) moisture, (2) volatile matter, consisting of gases and vapors driven off during pyrolysis, (3) fixed carbon, the non-volatile fraction of graphite, and (4) ash, the inorganic residue left over after combustion. The results are shown in Table 1, and it can be observed that ore is containing high ash content of 84.71% and fixed carbon content of 9.07% representing that the ore is of very low grade.

Table 1 Proximate analysis of graphite ore

Analysis	Value, %
Moisture	0.09
Volatile matter	6.13
Ash	84.71
Fixed Carbon	9.07

3.2 Characterization of Graphite Ore for Mineralogy and Morphology

The graphite ore was characterized by X-Ray Diffraction (XRD) shown in Fig. 1 for the identification of mineral phases of graphite and associated inorganic gangue minerals using copper-K α radiation with 1.54 Å wavelength are done using D2-Phaser of Bruker. The XRD results indicate the presence of graphite, quartz, pyrite, muscovite, and kaolinite mineral phases. Graphite has a distinct peak at $2\theta = 26.69^\circ$ in the X-ray Diffraction pattern and a minor peak at $2\theta = 40.42^\circ$ indicates 100 and 110 planes, respectively, for the graphite phases. The high intensity peaks of Quartz and the presence of clay mineral (Kaolinite) and mica mineral (Muscovite) indicate the high ash content of the graphite ore sample.

Scanning electron microscopy (SEM) was carried out using JCM-6000Plus in order to visualize the morphology of graphite ore sample as well as the concentrate which is separated from the gangue through flotation. The results in Fig. 2 show the clear difference of the sample's surface morphology. The SEM images in Fig. 2a show micro-scale graphite with thick flake size and layers, as well as partial porosity spots in the sample. The presence of minor associated gangue minerals is indicated by the different shades of light in mineral surface. However, in Fig. 2b of the graphite sample, the graphite concentrate shows minimized gangues resulting in exfoliated morphology formed after the removal of impurities like quartz and silica in the separation process that intrinsically intercalate graphite. Figure 2c shows the non-float of graphite which is the separated impurities.

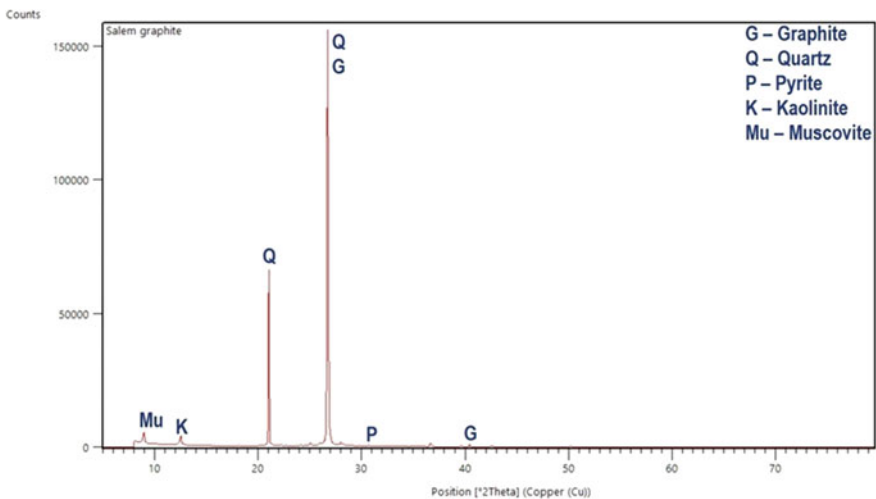
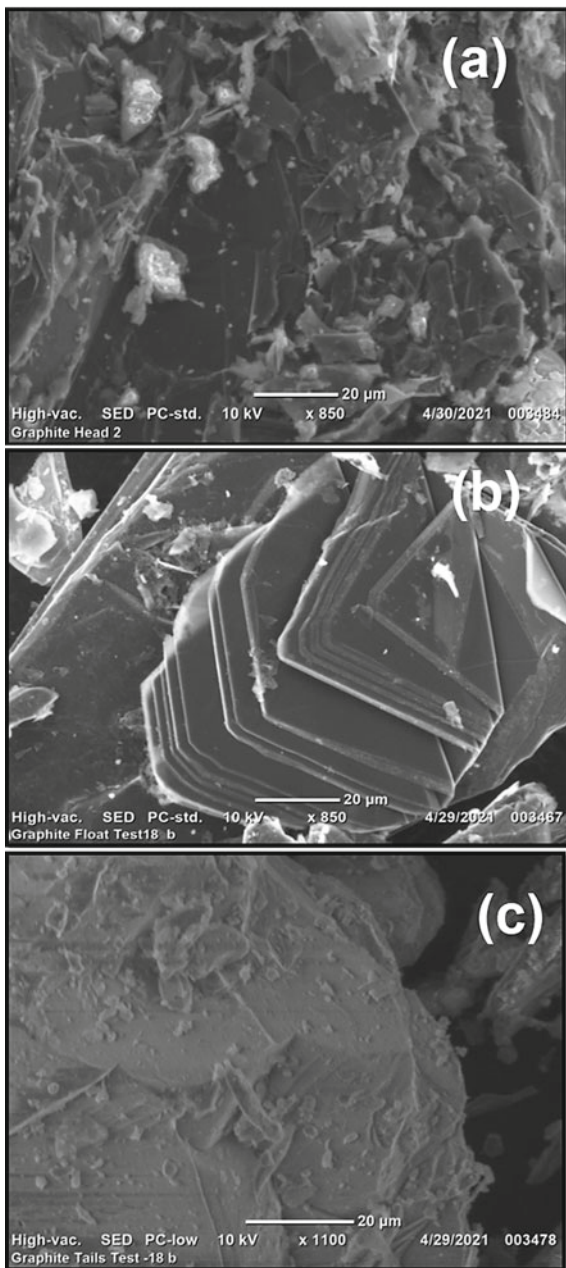


Fig. 1 X-ray diffractogram of graphite ore

Fig. 2 SEM images of **a** Graphite ore **b** concentrate **c** tailings



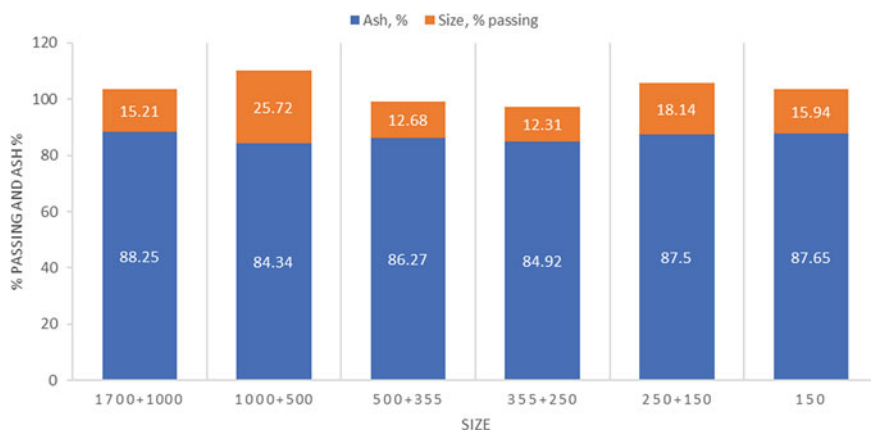


Fig. 3 Size distribution analysis of graphite ore

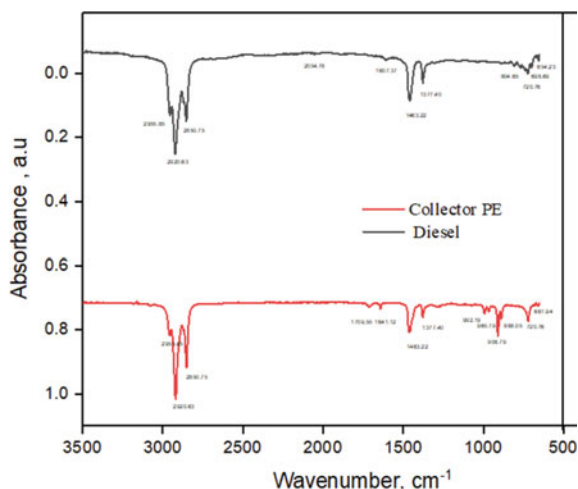
3.3 Size Distribution of Graphite Feed to Flotation

The particle size distribution of the -1.7 mm crushed graphite ore was carried out using a set of BSS screen/sieves with the top screen as $1700 \mu\text{m}$ and the bottom sieve as $150 \mu\text{m}$. The size distribution and the ash content in each size range are shown in Fig. 3. From the size analysis, 80% of the material (d_{80}) passes through $862.54 \mu\text{m}$. This material is taken as feed to flotation at coarse size fraction study. The size distribution indicated that $-1000 + 500 \mu\text{m}$ fraction is 25.72% by weight while rest of the fractions are found to be less than 20%. The size-wise ash analysis reveals that ash content of each size fraction is ranging from 84.34% to 88.25%. From the ash distribution, it is observed that the $-1000 + 500 \mu\text{m}$ size fraction contributes to higher ash % among other size fractions. This size-wise ash distribution shows that liberation of graphite values from its associated gangue/ash has not occurred to a considerable level and hence this 100% passing $1700 \mu\text{m}$ sized sample can be used directly as feed to flotation. So further grinding has to be adopted to attain better liberation thereby for better separation efficiency in flotation.

3.4 FTIR Analysis

The Fourier Transform Infrared Spectroscopy of the graphite ore sample was done using Bruker Alpha II Spectrometer. From the FTIR analysis of collector PE, two strong peaks at 2920 cm^{-1} and 2850 cm^{-1} are due to symmetric and asymmetric C-H stretching in CH_2 and CH_3 groups, typical of aliphatic carbons. The well-defined peaks at 1463 cm^{-1} and 1377 cm^{-1} are due to symmetric and asymmetric deformation vibrations experienced in C-H bond, i.e., C-H bending in C-H_2 and C-H_3 groups.

Fig. 4 FTIR Analysis of Collector PE and diesel



Peak at 908 cm^{-1} can be attributed to out-of-plane bending vibrations of C-H bonds. Another peak at 720 cm^{-1} can be attributed to C-H₂ rocking vibrations.

Diesel oil is a long alkane hydrocarbon chain which shows characteristic peaks at 2920 cm^{-1} and 2850 cm^{-1} due to symmetric and asymmetric C-H vibrations in CH₂ and CH₃ groups. Presence of alkyl group can be confirmed by bands at 1463.60 cm^{-1} and 1377 cm^{-1} corresponding to C-H bending vibrations. Peak at 720 cm^{-1} corresponds to the CH₂ rocking vibrations which are the characteristic feature of long-chain hydrocarbons. PE collector has similar peaks that of diesel oil resembling a mere long chain hydrocarbon (Fig. 4).

From the above observations, we can confirm that the collector PE is a long chain hydrocarbon which has similar backbone as that of the typical diesel oil. However, despite the fact that PE oil and diesel oil are synthesized from different sources, they still have some functional groups in common. The result obtained herein implies that both collectors are similar in terms of qualities and features. Hence, collector PE remains the best alternative for diesel oil in flotation.

3.5 Flotation Studies of Graphite Ore

3.5.1 Optimization of Grinding Time

Optimization of grinding time was carried out by grinding R.O.M graphite ore at different time intervals of 5, 10, 15, 20, and 25 min while maintaining a constant pulp density of 64.5% solids by weight. The ground product is then followed by flotation maintaining a constant collector (diesel) dosage of 0.56 kg/t and frother (MIBC) dosage of 0.07 kg/t. Results are depicted in Fig. 5.

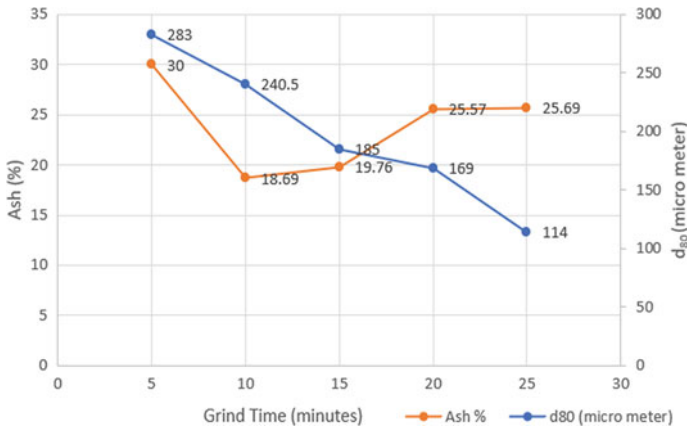


Fig. 5 Effect of grinding time and d_{80} size on ash content of concentrate

It is evident from the graph that the lowest ash value (18.69%) can be observed at 10 min grind time (d_{80} : 240.5 μm). The experiment results show that a float with 30% ash at 5 min of grinding time was obtained. This could be due to lack of liberation at relatively coarser size. The graphite used in this study was of low grade (with 84.71% ash content) and was found to be associated with the gangue minerals such as quartz. Also, the increase in ash % with increase in grinding time that was observed could be attributed to generation of more fines. Hence, grinding is one of the critical factors in liberation of values. Controlled grinding is very important to achieve ideal cost-effective separation [11]. Entrainment of gangue minerals depends closely on size of the particle [19]. The efficiency of flotation process depends mainly on the liberation and surface hydrophobicity of the values to be floated.

3.5.2 Optimization of Collector (Diesel) Dosage

The diesel collector dosage was optimized by carrying out flotation tests by varying collector dosages of 0.42, 0.56, 0.70, 0.85, 0.99 to 1.13 kg/t while maintaining a constant frother dosage (0.075 kg/t) and grind time of 10 min.

Figure 6 shows that at higher dose of collector (diesel) dilutes the grade of the concentrate with high ash content indicating the low selectivity of diesel at higher dosages. Lowest ash value (17.71%) with 15.23% recovery at 0.85 kg/t of collector was observed. This demonstrates that a collector dosage of 0.85 kg/t resulted in optimal selectivity of graphite particles in float and maximum rejection of gangue in non-float as rejects leading to an effective separation.

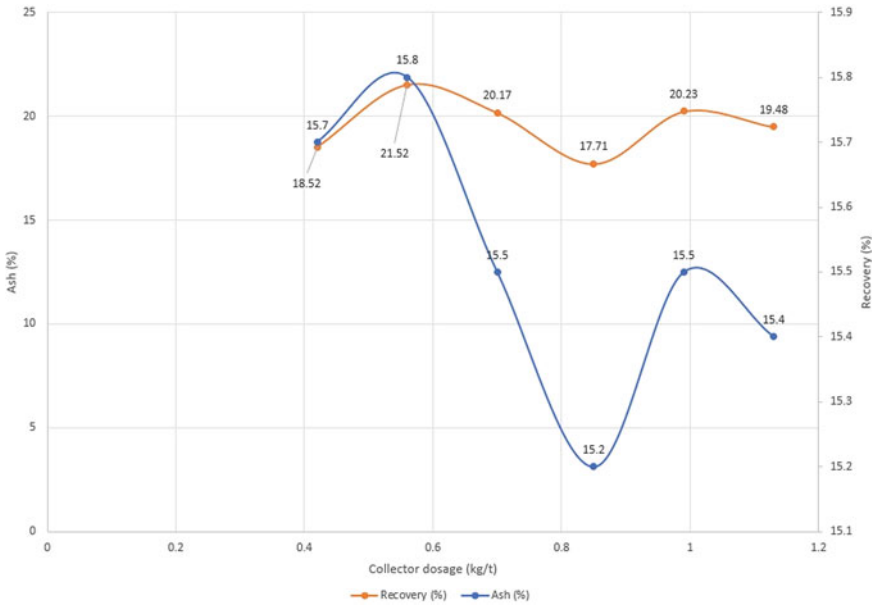


Fig. 6 Effect of Collector (diesel) on yield% and ash%

3.5.3 Optimization of Frother (MIBC) Dosage

The collector dosage was kept constant at 0.85 kg/t, and flotation tests were carried by varying frother dosages of 0.07, 0.11, 0.15, 0.19 kg/t. From the graph, it can be concluded that the lowest ash value of 17.71% was achieved with a recovery of 15.23% in concentrate (rougher concentrate) when 0.85 kg/t of diesel as collector with 0.07 kg/t of MIBC as frother was used. It also shows that high dosages of frother couldn't decrease the ash percentage but increased. The froth produced becomes more stable at higher froth dosages which carrying of gangue particles into float leading to high ash percentages in float. As the ash content was observed to be high, further cleaning of the rougher concentrate was carried out. After two-stage cleaning, a final concentrate was obtained with 12.66% weight recovery with 8.70% ash content (Fig. 7).

3.5.4 Optimization of Collector (Collector PE) Dosage

Collector PE dosage was optimized by varying the dosage (0.42, 0.57, 0.7, 0.85, 1.13 kg/t) and maintaining a constant frother dosage of 0.07 kg/t. Three stage cleanings were done to improve the grade of the concentrate. It can be observed from the graph that the lowest ash value of 8.9% with the highest recovery of 13.04% was achieved when treated with 0.57 kg/t of collector PE and 0.07 kg/t of MIBC (Fig. 8).

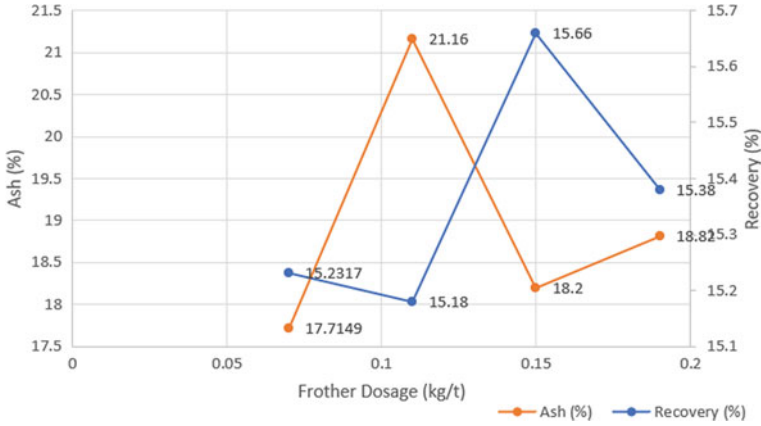


Fig. 7 Effect of Frother (MIBC) on yield% and ash%

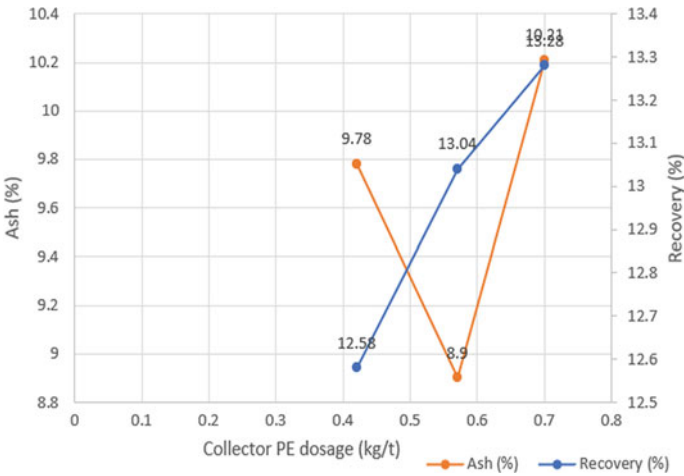


Fig. 8 Effect of Collector PE on yield% and ash%

3.5.5 Optimization of Frother (MIBC) Dosage

At fixed collector PE dosage (0.57 kg/t), MIBC frother dosage was optimized by varying dosage of 0.03, 0.07, 0.11 kg/t. It can be concluded from the graph that a yield of 13.04% with 8.90% ash was achieved with two-stage cleaning, when treated with 0.57 kg/t of collector PE and 0.07 kg/t of MIBC (Fig. 9).

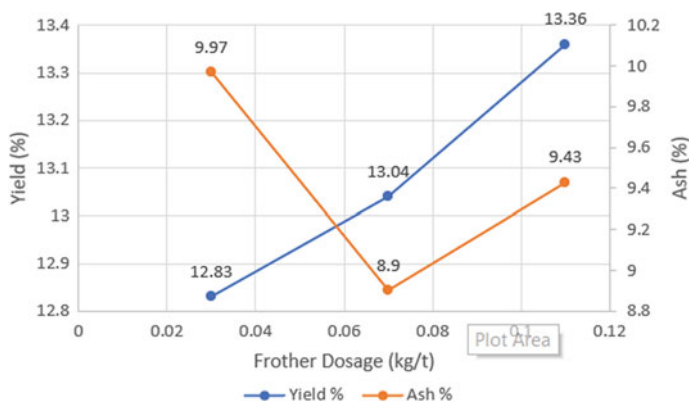


Fig. 9 Effect of Frother (MIBC) on yield% and ash%

4 Conclusion

The flotation studies of low-grade graphite carried out using the newly derived collector PE from the LDPE wastes and diesel indicates that the flotation efficiency of the collector PE is comparable with that of diesel and would be economical when used in large-scale industrial graphite flotation as the consumption amount of collector PE is also less than that of diesel. This would pave way for effective waste utilization of LDPE wastes and also to reduce the operational costs due to rapid cost escalation of diesel proving beneficial for graphite processing industries.

References

1. Graphite: Donald W. Olson, 2012 Minerals yearbook. United States Geological Survey, 2013
2. Chehreh S, Chelgani S, Rudolph M, Kratzsch R, Sandmann D, Gutzmer J (2016) A Review of graphite beneficiation techniques. *Miner Process Extr Metall Rev* 37(1):58–68
3. Yuan XM, Palsson BI, Forsberg KSE (1996) Statistical interpretation of flotation kinetics for a complex sulphide ore. *Miner Eng* 429–442
4. Sripriya R, Rao PVT, Choudhury RB (2003) Optimisation of operating variables of fine coal flotation using a combination of modified flotation parameters and statistical techniques. *Int J Miner Process* 68:109–127
5. Kawatra S (2011) Fundamental principles of froth flotation. *SME mining engineering handbook*, pp 1517–1532
6. Bulatovic SM (2007) Handbook of flotation reagents: chemistry, theory and practice: volume 1: flotation of sulfide ores. Elsevier, p 119
7. Li C, Li X, Xu M, Zhang H (2020) Effect of ultrasonication on the flotation of fine graphite particles: nanobubbles or not? *Ultrasonics sonochemistry*, p 105243
8. Barma SD, Baskey PK, Rao DS, Sahu SN (2019) Ultrasonic-assisted flotation for enhancing the recovery of flaky graphite from low-grade graphite ore. In: *Ultrasonics sonochemistry*, vol 56, pp 386–396. ISSN 1350-4177

9. Jianping X, Xin Z, Lingyan Z (2015) Experimental research on beneficiation of aphanitic graphite ore from Jilin area by flotation. *China Non-Met Miner Ind* 5:19–22
10. Florena FF, Syarifuddin F, Hanam ES (2016) Floatability study of graphite ore from Southeast Sulawesi (Indonesia) AIP conference proceedings, vol 1712, p 050005
11. Salgado MR (2001) Upgrading graphite by flotation at Bogala Mines in Sri Lanka. *J Cent South Univ Technol* 8:193–196
12. Chander S, Nagaraj DR (2007) FLOTATION | flotation reagents. Academic Press, Encyclopedia of Separation Science, pp 1–14
13. Nagaraj DR, Ravishankar SA (2005) Flotation reagents - a critical overview from an industry perspective, pp 375–424
14. Vasumathi N, Vijaya Kumar TV, Ratchambigai S, Subba Rao S, Bhaskar Raju G (2015) Flotation studies on low grade graphite ore from Eastern India. *Int J Min Sci Technol*
15. Wakamatsu T, Numata Y (1991) Flotation of graphite. *Minerals Eng* 4
16. Xia Y, Xing Y, Gui X, Cao Y (2022) Probing the interactions between collector molecules and hydrophobic graphite surfaces using chemical force microscopy. *Appl Surf Sci* 597:153760. ISSN 0169-4332
17. Oney O, Samanli S, Celik H, Tayyar N (2015) Optimization of operating parameters for flotation of fine coal using a box-behken design. *Int J Coal Prep Util* 35(5):233–246
18. Zhou H, Wang X, Bu X, Shao H, Hu Y, Alheshibri M, Li B, Ni C, Peng Y, Xie G (2020), Effects of emulsified kerosene nanodroplets on the entrainment of gangue materials and selectivity index in aphanitic graphite flotation. *Miner Eng* 158:106592
19. Weng X, Li H, Song S, Liu Y (2017) Reducing the entrainment of gangue fines in low grade microcrystalline graphite ore flotation using multi-stage grinding-flotation process. *Minerals* 7(3):38

Material Processing

Micromorphology and Pore Size Evaluation of Biomass Chars During Pyrolysis



R. Shivakumar and Samita Maitra

1 Introduction

The utilization of solar energy by plants for photosynthesis results in the generation of food energy and is used as one of the primary energy sources for other needs of humans apart from nutrition [1]. Presently biomass contributes 6–10 % of global energy needs by low-efficiency methods. Hence is critical that we improve the efficiency of biomass conversion. Reduce the environmental impacts caused due to biomass conversion [2]. Improvement can be adapted by understanding the properties of biomass and their burning behavior in a closed circuit in a different gaseous environment. Renewable energy sources are recurring in nature, and they need an efficient energy storage system for reliable and continuous supply for applied applications. Hence biomass chars can be one of the most reliable and cost-effective porous carbon materials applied in energy storage devices and sensors [3]. Most of the research works carried out in the past aimed to understand the structural changes in biomass after pyrolysis. Investigate the applications of bio-chars in electrochemical energy storage devices and sensors [4]. The present work discusses on micromorphology of the coconut shell, coconut fiber, sugarcane bagasse, and maize stalk chars during pyrolysis. The pyrolysis was carried out in a Conventional Thermogravimetric analyzer (C-TGA). The C-TGA equipment was developed indigenously. The morphological changes, developed surface area, pore size, and porosity of the bio-chars after pyrolysis are critical parameters for electrochemical energy storage devices and sensors applications. Hence the resulting chars are characterized using Scanning Electron Microscope (SEM) and Nitrogen adsorption and desorption analysis to evaluate the critical parameters.

R. Shivakumar (✉) · S. Maitra
Chemical Engineering Department, B.M.S. College of Engineering, V.T.U, Bengaluru,
Karnataka 560 019, India
e-mail: shivakumarr.che@bmsce.ac.in

© The Author(s), under exclusive license to Springer Nature Singapore Pte Ltd. 2023
E. Chinthapudi et al. (eds.), *Sustainable Chemical, Mineral and Material Processing*,
Lecture Notes in Mechanical Engineering,
https://doi.org/10.1007/978-981-19-7264-5_17

227

2 Material and Methods

The materials selected and methodology followed for pyrolysis experiments for the present experimental investigations are reported in this section. The biomass materials selected for the present study are based on their availability in surplus in India [5].

2.1 Materials

Coconut shell and coconut fiber biomass samples were collected from coconut oil processing agroindustry, Tumkur district, Karnataka, India. Sugarcane bagasse and Maize stalks was collected from sugar industry and agricultural fields in Mandya district, Karnataka, India.

2.2 Methods

The experimental procedure adopted for pretreatment of biomass samples, pyrolysis procedure, and different analytical instruments used for characterization of biomass samples after pretreatment and pyrolysis are discussed in detail in this section.

2.2.1 Characterization of Biomass Samples

The selected biomass samples are dried till the weight of the samples were constant in a muffle furnace at 120 °C. The samples are milled after complete drying and sieved. The particle size of the biomass samples is less than 500 microns. The prepared samples are stored in airtight containers for further experiments. The sieved samples are characterized for particle size analysis (Malvern AIMIL, UK), proximate analysis (ASTM D3172-TA Instruments, Newcastle), ultimate analysis (ASTM D3176-Thermo Scientific FLASH 2000 Elemental Analyzer, Italy), and calorific values (LECO, USA, AC350). The proximate and ultimate analysis results are shown in Table 1. Particle size and calorific values are reported in Table 2.

2.2.2 Pyrolysis of Biomass Samples

Non-isothermal pyrolysis experiments were carried out in a muffle furnace with nitrogen gas purging. The nitrogen gas flow was maintained around 20 L/min. Initially around 20 g of biomass samples were taken in ceramic crucibles and heated to the maximum temperature of 950 °C at a rate of 10 °C per minute. After the temperature reaches 950 °C the furnace temperature was kept constant till the weight loss of the

Table 1 Proximate and ultimate analysis for samples

Sample name	Proximate analysis				Ultimate analysis				
	Percentage as-received basis				Percentage as-received basis				
	Moisture	Volatile	Fixed carbon	Ash	C	H	N	O	S
Coconut fiber	10	66	21	3	50	7.07	0.16	42.62	0.15
Sugarcane bagasse	8	77	13	2	65.5	4.16	0.14	30.2	–
Coconut shell	6	36	64	9	47.1	6.1	0	38.3	8.5
Maize stalk	6	38	50	6	51.3	4.3	0.4	42.2	1.8

Table 2 Particle size analysis and calorific value

Sample name	Average mean diameter ($D_{V0.9}$, μm)	Calorific value HHV (MJ/kg)
Coconut Fiber	480	17
Sugarcane Bagasse	460	18
Coconut Shell	350	21
Maize Stalk	450	20

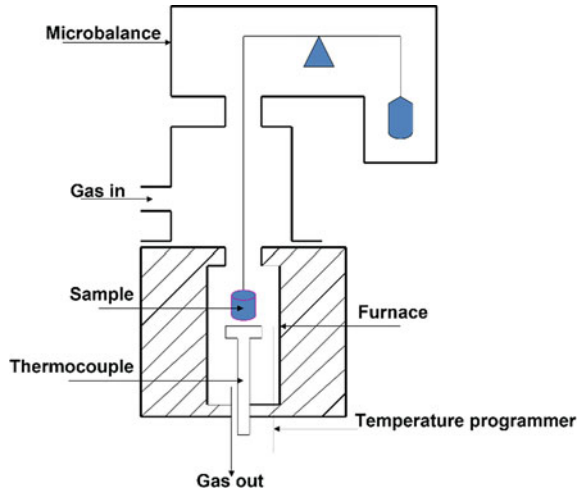
samples was constant. The nitrogen gas purging was continued in all three stages of pyrolysis experiment. The schematic diagram of the experimental setup is shown in Fig. 1. The resulting char samples were grounded and stored in airtight containers. The resulting biomass chars were characterized using Scanning Electron Microscope (Tescan-Vega3 LMU, Czech Republic) and Nitrogen adsorption–desorption analysis using micromeritics BET analyzer (BELSORP-max, Microtrac BEL, Japan).

3 Results and Discussion

3.1 Micromorphology of Biomass Char Samples

Surface morphology of biomass char samples are shown in Figs. 2 and 3. Coconut fiber and coconut shell chars surface morphology images from Fig. 2, indicate that the surface has cracks. The breakage of cellulosic structure and layers overlapping was observed for coconut fiber as depicted by Fig. 2a. The small pore opening developed after devolatilization are clearly visible on the surface of coconut fiber and coconut shell char samples. Figure 2a indicate that the coconut fiber char particles shrink in size and get fragmented followed by agglomeration of particles after devolatilization [6, 7]. Coconut shell char surface images from Fig. 2b reveals presence of pores

Fig. 1 Schematic diagram of pyrolysis setup



on the surface due to break out of lignin, cellulose, and hemicellulose components during devolatilization [8].

Sugarcane bagasse and maize stalks char samples surface morphology is shown in Fig. 3. Both sugarcane bagasse and maize stalk chars surface morphologies depicts the cracked fiber tissues on the surface. Bio-chars surface images show that they are irregular flake like structures. Sugarcane bagasse and maize stalk chars show complex pore structure. Sugarcane bagasse chars resulted in smaller pore size complex pore structure. However maize stalk chars resulted in bigger pore size complex pore structure.

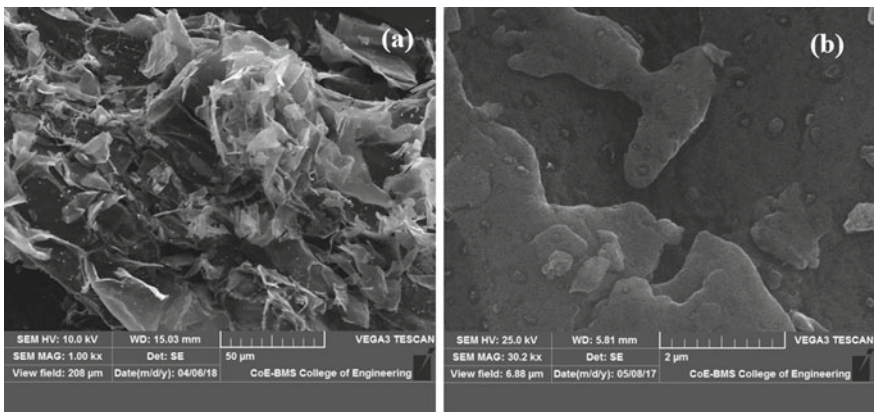


Fig. 2 Micromorphology of **a** coconut fiber and **b** coconut shell chars

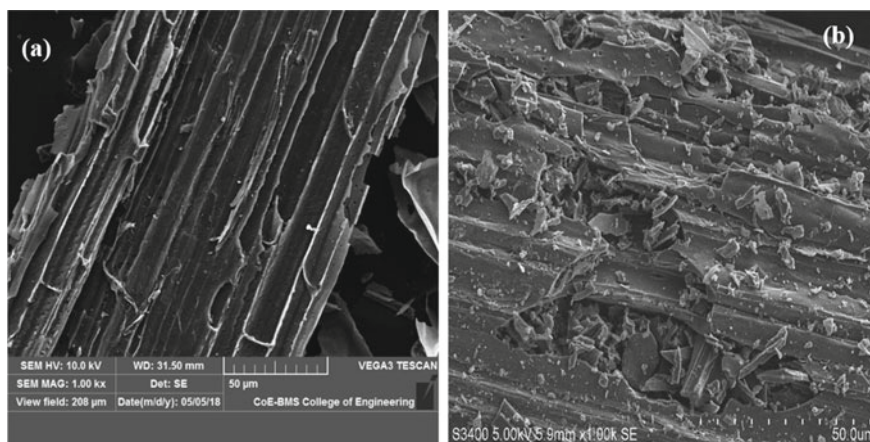


Fig. 3 Micromorphology of **a** sugarcane bagasse and **b** maize stalks

3.2 Nitrogen Gas Adsorption and Desorption Isotherms

Adsorption–desorption isotherms for coconut fiber, coconut shell, sugarcane bagasse, and maize stalk samples are shown in Figs. 4, 5, 6, and 7. In nitrogen gas adsorption studies the nitrogen gas molecules diffuse into the micropores particularly at low relative pressure. Adsorption initially occurs in a monolayer state with initial micropore filling. Later, multilayer adsorption occurs on the mesopore walls, followed by pore condensation [9]. Figure 4 shows that adsorption and desorption isotherm for coconut fiber char resulted in strong open loop hysteresis behavior. Volume of nitrogen gas adsorbed at STP conditions is least compared to other biomass char samples this can be attributed to the absence of macropores. Figure 5 evince that adsorption and desorption isotherm for coconut shell char resulted in less open loop hysteresis behavior. Volume of nitrogen gas adsorbed at STP conditions is around 500 cm³/g STP. The Adsorption–desorption isotherms clearly indicate the presence of macropores in the sample and absence of micropores.

Fig. 4 Isotherms for coconut fiber

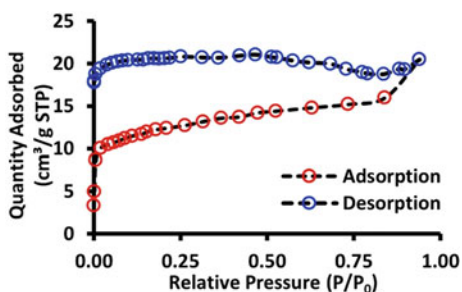


Fig. 5 Isotherms for coconut shell

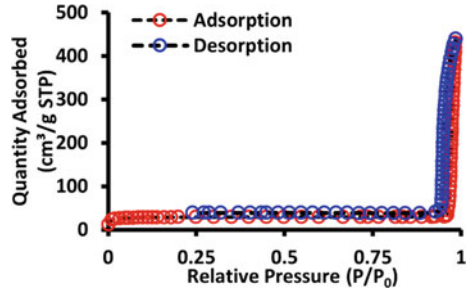


Fig. 6 Isotherms for sugarcane bagasse

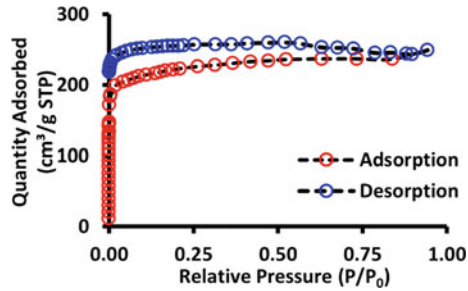


Fig. 7 Isotherms for maize stalk

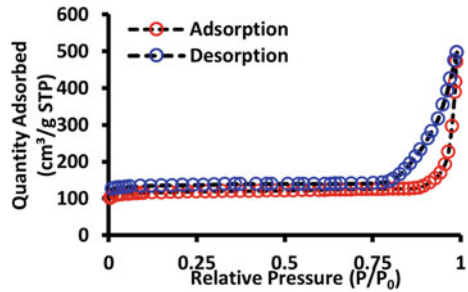


Figure 6 indicates that adsorption and desorption isotherm for sugarcane bagasse char resulted in less open loop hysteresis behavior similar to other three biomass chars. Volume of nitrogen gas adsorbed at STP conditions is around 220 cm³/g STP. The Adsorption–desorption isotherms clearly indicate the absence of macropores in the sample. Figure 7 depicts that volume of gas adsorbed at STP conditions for maize stalk char sample is maximum at high relative pressure values compared to coconut fiber, coconut shell, and sugarcane bagasse char samples. Adsorption–desorption results evince that the volume of gas adsorbed by coconut fiber, coconut shell and sugarcane bagasse chars was decreased by 27, 1.2, and 2 times respectively, compared to maize stalk char. Adsorbed gas volume for maize stalk char increased due to increase in number of pores compared to other three bio-chars. Sharp rise in the adsorbed gas volume at low relative pressure indicate the presence micropores

for coconut fiber and sugarcane bagasse char samples. Coconut shell and maize stalk chars do not show a sharp rise in adsorbed gas volume at low relative pressure indicating a smaller number of micropores on the surface compared to coconut fiber and sugarcane bagasse chars [10].

Results infers that coconut shell and maize stalk chars are microporous, mesoporous, and macro-porous in nature. However, coconut fiber and sugarcane bagasse chars are microporous and mesoporous in nature [11]. Difference in the pore volume developed during pyrolysis in chars can be attributed to their cellulose, hemicellulose, and lignin structure degradation during pyrolysis. Adsorption-desorption isotherms for all bio-chars are of Type IV with open loop hysteresis behavior [12]. The hysteresis loop for coconut fiber and sugarcane bagasse chars follows H4 type as shown in Figs. 4 and 6 respectively. Coconut shell and maize stalk chars follows H3 type hysteresis loop as shown in Figs. 5 and 7. The distinctive feature of H4 type hysteresis loop is absence of macropore in the pore network, but distinctive feature of H3 type hysteresis loop is presence of macropore in the pore network [13].

3.3 Macropore, Mesopore and Micropore Distributions

The Barrett, Joyner, and Halenda approach (BJH) and T-plot analysis were carried out to evaluate the macropore, mesopore, and micropore ranges. The results are shown in Fig. 8. Figure 8 depicts the presence of macropores, mesopores, and micropores in coconut shell and maize stalk chars. However, the coconut fiber and sugarcane bagasse samples were mesoporous and microporous in nature. Macropores were absent in both coconut fiber and sugarcane bagasse chars [14].

Fig. 8 Macropore, mesopore and micropore volume for bio-chars

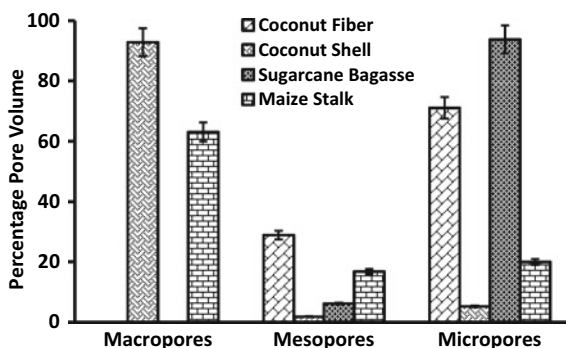


Table 3 Porosity and BET surface area

Sample name	Porosity (ϵ_0)	BET surface area, m^2/g
Coconut fiber	0.57	441
Sugarcane bagasse	0.61	838
Coconut shell	0.91	91
Maize stalk	0.99	360

3.4 BET Surface Area

Brunauer–Emmett–Teller (BET) surface area and porosity results for all the bio-chars are tabulated in Table 3. From Table 3, results infer that increase in micropore volume results in increase in BET surface area. Hence, sugarcane bagasse char resulted in higher surface area value around $800 \text{ m}^2/\text{g}$. The percentage of micropore volume in sugarcane bagasse char is around 94 % as shown in Fig. 8. Coconut fiber char sample surface area was around $441 \text{ m}^2/\text{g}$. The percentage of micropore volume for coconut fiber was around 71 % as indicated in Fig. 8. Maize stalk char resulted surface area around $360 \text{ m}^2/\text{g}$ and coconut shell char resulted in the lower surface area value compared to other three bio-chars around $91 \text{ m}^2/\text{g}$ [15, 16].

4 Conclusion

The present paper has discussed the micro-morphological changes and evaluation of pore size, surface area and porosity of biomass chars during pyrolysis. These factors are critical for their applications in electrochemical devices and sensors. SEM images shows the structural changes occurred in bio-char samples due to pyrolysis. These changes resulted highly microporous, mesoporous, and microporous carbonaceous materials. Adsorption–desorption isotherms results conclude that the bio-chars have good adsorption and desorption capacity. The isotherms for all four bio-chars are of a type-IV with open loop hysteresis behavior. Surface area and the porosity of the bio-chars were high enough to be used as electrode materials and other catalytic applications. The major properties for carbonaceous materials applied for electrochemical applications surface area, porosity, and pore size. The present carbonaceous materials resulted after pyrolysis of biomass samples are highly meso and micro porous in nature with high surface area. This property is one crucial while considering these materials as electrode materials and other sensor applications.

Acknowledgements The authors wish to acknowledge the partial funding by TEQIP-II, MHRD, Govt. of India. The authors wish to acknowledge the support for BET surface area analysis by Central Salt and Marine Chemicals Research Institute, CSIR, Bhavnagar, India.

References

1. Jenkins BM (1998) Combustion properties of biomass. *Fuel Process Technol* 54:17–46
2. Haykiri-Acma H (2003) Combustion characteristics of different biomass materials. *Energy Convers Manage* 44:155–162
3. Bhat VS, Supriya S, Hegd G (2020) Review-biomass derived carbon materials for electrochemical. *J Electrochem Soc* 167(3):037526
4. Li R, Zhou Y, Li W, Zhu J, Huang W (2020) Structure engineering in biomass-derived carbon materials for electrochemical energy storage. *Research* 2020:1–27
5. Kumar A (2007) Electrification and bio-energy options in rural India, Italy
6. Yang H, Yan R, Chen H, Lee DH, Zheng C (2007) Characteristics of hemicellulose, cellulose and lignin pyrolysis. *Fuel* 86:1781–1788
7. Shivakumar R, Maitra S (2020) Evaluation of pore size and surface morphology during devolatilization of coconut fiber and sugarcane bagasse. *Combust Sci Technol* 192(12):2326–2344
8. Biagini E, Narducci P, Tognotti L (2008) Size and structural characterization of lignin-cellulosic fuels after the rapid devolatilization. *Fuel* 87:177–186
9. Thommes M, Kaneko K, Neimark AV, Olivier JP, Rodriguez-Reinoso F, Rouquerol J, Sing KS (2015) Physisorption of gases, with special reference to the evaluation of surface area and pore size distribution. *Pure Appl. Chem* 87:9–10, 1–19
10. Kenneth S (2001) The use of nitrogen adsorption for the characterisation of porous materials. *Colloids Surf A: Physicochemical Eng Asp* 187–189:3–9
11. Gleysteen VR, Deitz Leland F (1945) Hysteresis in the physical adsorption of Nitrogen on bone char and other adsorbents. *J Res Natl Bur Stand* 35(4):285–307
12. Barrett EP, Joyner LG, Halenda PP (1951), The determination of pore volume and area distributions in porous substances. I. Computations from nitrogen isotherms. *J Am Chem Soc* 73:373–380
13. Qi L, Tang X, Wang Z, Peng X (2017) Pore characterization of different types of coal from coal and gas outburst disaster sites using low temperature nitrogen adsorption approach. *Int J Min Sci Technol* 27(2):371–377
14. Satya Sai PM, Krishnaiah K (2005) Development of the pore-size distribution in activated carbon produced from coconut shell char in a fluidized-bed reactor. *Ind Eng Chem Res* 44:51–60
15. Wen-yue LI, Shi-yong WU, You-qing WU, Sheng HUANG, Jin-she GAO (2019) Pore structure characterization of coconut shell char with narrow microporosity. *J Fuel Chem Technol* 47(3):297–309
16. Everson RC, Hennie Coetzee GS, Sakurovs R, Neomagus HWJP, Mathews JP, Bunt JR (2017) Particle size influence on the pore development of nanopores in coal gasification chars: From micron to millimeter particles. *Carbon* 112:37–46

Characterization of Indigenous Clay-Based Ceramic Water Purifiers Mostly Available in Tripura and Its Performance Evaluation



Aritrika Saha, Harjeet Nath, and Rahul Das

1 Introduction

The importance of some essential nutrients in clean water plays important role in the existence of life on our earth which is well known to us [1–3]. All of us require water each and every day because each and every system in our body is made up of tissue and cells which form different important organs that need water to function properly. Water also serves as the sustainable media for plants, animals, and aquatic organisms [4]. Humans used to depend mainly on surface water during the ancient times. With the increase in human population, the demand for water is skyrocketing and human race started to explore water from underground sources too. Now with the rise of industries and the discharge of industrial effluents along with domestic and hospital discharges sometimes untreated along with various other anthropogenic activities, the quality of water has started to degrade. India is in the list of 3rd worst water quality as per NITI Aayog reports where India stands at 120 out of 122 in the chronology of water quality Index. India is also reported to extract almost 25% of its water needs from underground sources and if the trend goes like this the day is not far when there will be a scarcity of underground water [5].

In north-eastern India, Tripura is a small hilly land-locked state and rich in biodiversity reservoir. Aggressive civilization, rapid growth in the industries may result in pollution and may also cause different species loss from our earth thereby causing danger to our biodiversity. Different tribes in Tripura still depend on river and stream water as a drinking water source and for ritual ceremonies also [4]. Various reports have indicated that most of the areas from where samples have been collected

A. Saha · H. Nath (✉) · R. Das

Waste Utilization Lab, Department of Chemical and Polymer Engineering, Tripura University (A Central University), Agartala 799022, Tripura, India

e-mail: harjeetnath@gmail.com

throughout the state, the problem of excessive iron content especially in ground-water has been observed which requires the usage of Iron Removal Plants (IRP) for making the water potable and further make it suitable for drinking [6]. Moreover, there are various other reasons which make the water unsuitable for drinking and one such reason is that the water obtained is found to be mostly acidic in nature [7]. In a hilly state like Tripura, there is a lack of safe water. Tripura is hampered by a lack of financial resources, which is exacerbated during natural calamities. As a result, efficient low-cost systems for point-of-use water treatment are required. Ceramic filtration has a high pedigree for drinking water treatment, size of the pores are made enough small that it can remove all protozoa and bacteria by size of $0.2 \mu\text{m}$ referred to in the range of microfiltration [8]. Ceramic membranes are also enhanced with different types of microbial amendments such as silver [9] coating that is painted over the surface, impregnated with ceramic components either before or after firing. Colloidal solution of silver or solution of silver nitrate is used for that purpose. This practice was started from twentieth century to control the bacterial growth problem in ceramic household filter [3].

The advantages of ceramic filters which are produced locally are easy to make, lightweight, portable, comparatively inexpensive, and low maintenance. It mostly removes suspended particles from raw water by gravity filtration using porous type ceramic membrane, with 1–3 liter/hour rate of flow thereby reducing turbidity. Filters have a stable function and have one moving part (tap) and don't need any external source of energy such as pumps, etc. They are said to last about 5 + years with proper maintenance and care but all implementers and manufacturer recommend replacing the filter element regularly every 1–2 years. To avoid slow filtration rates scrubbing, the surface of the ceramic filter periodically is being carried out. With no scientific study currently available for such purifiers, it's high time to crosscheck the efficiency of such filters and make the entire process of preparation of such filters more scientific and hygienic in addition to checking the operation limit of using such filters keeping in mind drinking water quality parameters.

The objective of the study is to determine the properties of various raw materials used in the manufacture of indigenous clay-based ceramic water filters, which are often housed in a cement structure and are extensively used by the rural population of northeastern India, particularly Tripura. To get a clearer idea of how the system works, the purifier's performance was assessed. Multiple characterization techniques such as FESEM-EDAX, FFTIR, and XRD were employed to analyze the feed material and ceramic filter in order to determine their morphological properties, numerous elements, groups of functions, and phases which is essential to check if any harmful constituent is present in the candle or its cement structure. Analysis of pH, TDS, turbidity, and microbial analysis was used to determine the ceramic filter's performance and efficacy.

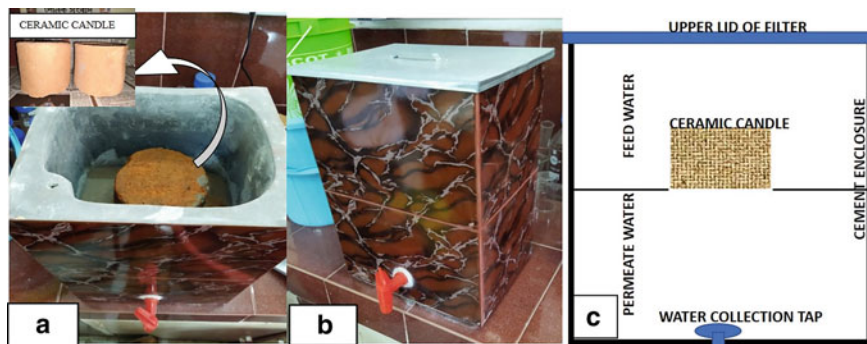


Fig. 1 a–c Top view, side view, and schematic diagram of the indigenously developed filter with ceramic candle

2 Materials and Methods

2.1 Raw Materials

The ceramic filter unit is primarily obtained from the local manufacturer. One small calcined filter is used throughout the arrangement, which is housed inside a cement container. It has a single water channel tap. The ceramic candle's primary raw materials are clay, sand, and rice husk. Figure 1 a–c shows the picture and schematic diagram of the assembly.

2.2 Preparation of Ceramic Filter Candle

After the raw materials have been collected from various locations, they are mixed in a specific ratio in the local industry. Afterwards, it is poured into the molds to create the desired shape for the candles. The wet candles are then dried in natural sunlight until they turn white. Sintering is processed in a traditionally designed kiln for nearly 48 h after one or two days. The ceramic filter preparation process is illustrated in the following flowchart (Fig. 2a, b). The sintering kiln/oven unit is shown in Fig. 3.

2.3 Methodology

The filtration unit can hold 4 liters of water at a time which requires approx. 4 h to get completely permeated. The feed water is subjected to certain preliminary physical parameter testing before being fed into the filter. The physical parameters are TDS, pH, conductivity, and turbidity. Deionized water was used as the feed

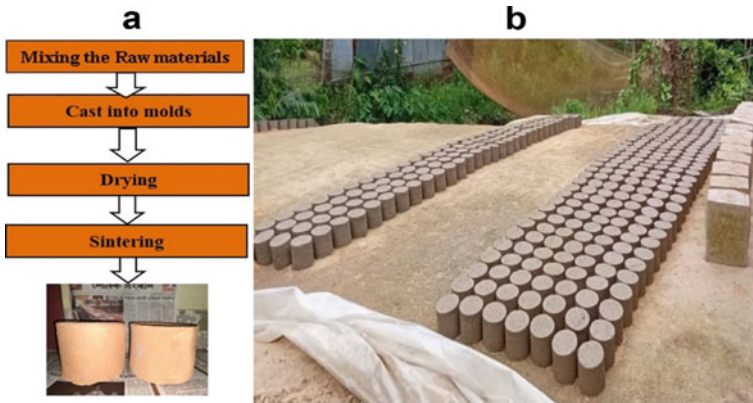


Fig. 2 Flowchart and drying method for preparing candles

Fig. 3 Traditionally designed sintering kiln/oven for preparing the candles



solution for the ceramic filter setup. The permeate samples were collected at a time interval of 2, 4, and 24 h and were analyzed again by using a portable TDS meter, pH meter, conductivity meter, turbidity meter, and at room temperature, all physical parameters are analyzed. To prevent unwanted changes in water quality, samples were collected in a clean 50 ml centrifuge tube and were further analyzed. Ceramic filter characterization was also carried out in this work. Clay, sand, rice husk, as well as the candle and cement container samples were powdered and dried in an oven overnight at 75 °C. The samples were then crushed and sent for FESEM-EDAX, FTIR, and XRD analysis. *E.coli* samples were collected from Biotech Hub of Tripura University and the prepared raw water containing *E.coli* and the filtrate/permeate water was analyzed using portable *E.coli* detection kit.

Analysis

The pH was measured using EUTECH pH 700 Ph/mv/°C/°F Bench meter. The TDS and electrical conductivity were measured using EUTECH CON 700 conductivity/°C/°F Bench Meter. To measure the turbidity of feed and permeate water, EUTECH Waterproof Portable Turbidity meter (TN100) was used. For FESEM and EDX, Carl ZEISS Sigma 300 instrument was used to characterize the candle and the raw materials. SHIMADZU IR Spirit FTIR Spectrophotometer was used to analyze the functional groups of the raw materials of the candle and ceramic candle. XRF, XRD, and compressive strength of the samples have been done by Malvern Panalytical Model Zetium 4.0 KW, Panalytical x'pert3 powder instrument and Aimil, AIM-314E-DG-1 machines, respectively. The permeate water sample has been examined using a RAKIRO-BACTASLYDE-Microbe detection setup.

3 Results and Discussion

3.1 Performance Evaluation Study by Physical Parameters

3.1.1 Electrical Conductivity and TDS Measurements

Electrical conductivity (EC) measurements provide an assessment of a solution's total ionic content, and conductivity is directly related to total dissolved solids (TDS) [10]. From Table 1, it can be observed that the EC and TDS of the permeate water increased after filtration. Maximum EC was found to be 285 $\mu\text{S}/\text{cm}$ and maximum TDS was found to be 143 ppm which can be observed for the samples collected at 24 h. Some carbonates or bicarbonates may have leached from the filter system that may be the reason for increased EC and TDS.

3.1.2 PH Measurements

The use of water can be harmed by pH levels that are unusually high or low. The allowable pH range for drinking water, according to BIS guidelines, is 6.5 to 8.5 [11]. The pH of the permeate water increased with filtration time, as can be seen in Table 2. After filtering, the pH of water was found to have risen to around 10.417, indicating that the water was found to have increased to a more alkaline side. This increase in pH also relates to the addition of ions in the permeate similar to the method which led to increased conductivity and TDS thereby again making it unfit for drinking (Tables 3, 4, 5 and 6).

Table 1 Analysis of physical parameters of indigenous water filter (F₁, F₂, F₃, and F₄ relate to feed and P₁, P₂, P₃, P₄ relate to filtrate/permeate parameters for each batch in different time duration 2 h, 4 h, and 24 h, respectively)

Filtrate (2 h)	Physical parameters	F ₁	P ₁	F ₂	P ₂	F ₃	P ₃	F ₄	P ₄
	Conductivity (μS/cm)	69.6	160	49.5	216	52.8	148.6	48.8	114
	TDS (ppm)	34.7	80	24.7	109	26.4	74	24.5	57.1
	pH	6.89	9.86	6.81	10.28	6.59	9.57	6.8	9.33
	Turbidity (NTU)	3.76	0.27	0.16	0.02	0.05	0.05	0.02	0.01
Filtrate (4 h)	Conductivity (μS/cm)	69.6	156	48.8	119.8	51.2	112.3	49.4	111.4
	TDS (ppm)	34.7	78.1	24.5	60	25.2	56	24.8	55.6
	pH	6.89	9.81	6.8	9.4	6.7	8.46	6.64	8.9
	Turbidity (NTU)	3.76	0.86	0.02	0.04	0.05	0.01	0.06	0.04
Filtrate (24 h)	Conductivity (μS/cm)	69.6	285	57	160.4	51.2	159.2	49.4	145.5
	TDS (ppm)	34.7	143	28.6	80.1	25.2	80.3	24.8	72.5
	pH	6.89	10.75	6.78	10.42	6.7	10.26	6.64	10.24
	Turbidity (NTU)	3.76	0.19	0.1	0.03	0.05	0.05	0.06	0.41

3.1.3 Turbidity Measurements

The optical property of water is investigated via turbidity parameter analysis, which looks at how light is scattered in the sample due to the presence of inorganic suspended particulate matter. The turbidity of the feed water is reduced after filtering, as shown in Table 1. This indicates that the filter is effective for removing suspended particles.

3.2 Characterization of Filter Media

3.2.1 FESEM and EDAX Analysis

The morphology of the clay, sand, rice husk, candle, and cement container are shown in Figs. 4, 5, 6, 7, and 8, respectively. The flake-like structure of clay and the crystalline structure of sand are shown in Figs. 4 and 5, respectively. Figure 7 depicts the porous morphology of a ceramic candle.

EDAX analysis produces spectra with peaks corresponding to the components that make up the real composition of the samples. Figure 9a–e shows the EDAX elemental analysis of clay, sand, rice husk, filter candle, and filter interior, respectively. In the clay sample, silica and oxygen weights are higher, particularly silica at 27.88% and oxygen at 43.83% as shown in Table 2. Heavy metal, specifically lead (Pb) and arsenic (As) can be found in the clay. The most predominant elements in the rice husk sample are silica, oxygen, and carbon. Where 35.47% is carbon, 10.82% is silicon, and 49.42% is oxygen which is shown in Table 4. Table 5 illustrates the elemental

Table 2 Chemical composition of the clay sample determined by XRF analysis

Composition of clay sample	Na ₂ O	MgO	Al ₂ O ₃	SiO ₂	P ₂ O ₅	SO ₃	K ₂ O	CaO	TiO ₂	MnO	Fe ₂ O ₃
Weight percentage	0.600	1.277	18.372	63.845	0.117	0.171	2.304	0.425	1.064	0.127	6.378

Table 3 Chemical composition of the sand sample determined by XRF analysis

Composition of sand	Co ₃ O ₄	Fe ₂ O ₃	TiO ₂	CaO	K ₂ O	SO ₃	P ₂ O ₅	SiO ₂	Al ₂ O ₃	MgO	Na ₂ O
Weight percentage	0.154	0.552	0.158	0.184	0.520	0.105	0.023	95.555	1.714	0.113	0.101

components of the filter candle. The candle has some lead residues; however, the candle does not contain any arsenic. The elements of the interior portion of the filter unit are shown in Table 6. It shows the major constituents of cement from which it can be concluded that the interior portion of the filter unit is truly made up of cement.

3.2.2 XRF and XRD Analysis

By using XRF analysis, all of the constituents of the raw clay, sand, rice husk, filter candle, and interior of the cement filter are determined in their oxide state. Tables 2, 3, 4, 5, and 6 show the composition of the raw material by their weight percentage.

The XRD spectra of clay, sand, rice husk, and filter revealed significant variances which are shown in Figure 10. The clay sample showed characteristic peaks for quartz at 2θ values of 26.7° , 21° , 39.5° , 50.2° [12–14], for kaolinite at 20.9° , 44.7° and for muscovite at 39.59° [15]. The crystalline phase of silica is the more dominant in sand, and the characteristics peaks of quartz are at 21.01° , 26.6° , 36.5° , 39.4° , 42.4° , 50.3° , 60.1° , 68.3° [16]. The XRD analysis was carried out on raw rice husk. A broad peak of amorphous silica ranging from 15° to 30° can be observed in raw rice husk [17–19]. In the XRD analysis of the candle, the major quartz phases are matched with sand and soil samples, and the major characteristic peaks are 20.9° and 26.7° . Cristobalite is a crystalline form of silica in ceramics that is created at high temperatures. The sintered candle may contain these phases which indicate that the sintering temperature of the candle are may be from 1000°C to 1400°C [8, 20, 21].

3.2.3 FTIR Analysis

According to the results of the FTIR study (Fig. 11), there is a clear match between the peak of the filter candle and the constituents of the filter as well as a wavenumber that spans between 775 and 2925 cm^{-1} . The FTIR peak of filter candle is a match for every major Si–O stretching in raw materials. All the major groups of raw materials and filter candle are shown in Table 7 [22–25].

Table 4 Chemical composition of the rice husk sample determined by XRF analysis

Composition of rice husk	Na ₂ O	MgO	Al ₂ O ₃	SiO ₂	P ₂ O ₅	SO ₃	Cl	K ₂ O	CaO	MnO	Fe ₂ O ₃	C ₃ O ₄	ZnO
Weight percentage	0.119	1.611	0.455	82.280	5.734	2.024	0.345	3.623	0.980	0.336	1.995	0.257	0.047

Table 5 Chemical composition of the candle sample determined by XRF analysis

Composition of candle	Na ₂ O	MgO	Al ₂ O ₃	SiO ₂	P ₂ O ₅	SO ₃	K ₂ O	CaO	TiO ₂	MnO	Fe ₂ O ₃
Weight percentage	0.762	1.402	18.384	67.005	0.174	0.118	2.468	0.473	1.118	0.102	6.944

3.3 Microbial Analysis

To validate the microbiological quality of the water produced by the micro-porous ceramic filters, the ceramic candle was tested with water inoculated with specified strains of bacteria, specifically *E.coli*. 0.3 ml of *E.coli* stock (Fig. 12a) was mixed with 3 liters of distilled water, and then the feed water was taken after two hours. An immediate bacterial analysis kit was used to examine the growth in the spiked water. Figure 12b depicts the rapid growth of *E.coli* bacteria in the feed sample after it has been incubated for 24 h. After a period of 24 h, a sample of the filtrate water is collected. After that, a filtration sample is inoculated with *luria–bertani* agar media, disseminated with a spreader, and then placed in an incubator for twenty-four hours. The spread plate method is used to examine the development of microorganisms. Figure 12c illustrates the growth of the microorganisms. In the event of microbial infection, this candle's growth indicates that it is ineffective against providing microbial protection.

3.4 Compressive Strength

The length and diameter of the candles taken are 12 cm and 13 cm, respectively. The compressive strength of the filter candle is less than 1 MPa and, more precisely, it is 0.6 MPa.

4 Conclusion

In the present study, the EDAX analysis revealed that Pb and As were present in small amounts in the filter candle, which if gets leached into water may be harmful to human health. The XRF analysis however could not trace Pb and As thereby indicating their very negligible presence in oxide form, but another heavy metal, cobalt, was found in some samples. This is due to the fact that the raw materials source may vary and moreover no standard method is generally followed to ensure the raw material is free of any toxins. Also, it has been found from the various water parameter analysis that the sample collected after 24 h has a high TDS level as compared to the samples collected at 2 h and 4 h, which may be due to the reason that

Table 6 Chemical composition of the cement container sample determined by XRF analysis

Composition of cement container	Na ₂ O	MgO	Al ₂ O ₃	SiO ₂	P ₂ O ₅	SO ₃	K ₂ O	CaO	TiO ₂	Fe ₂ O ₃
Weight percentage	0.184	0.888	5.361	58.184	0.111	1.560	0.789	20.645	0.803	2.105

Fig. 4 FESEM image of cay sample

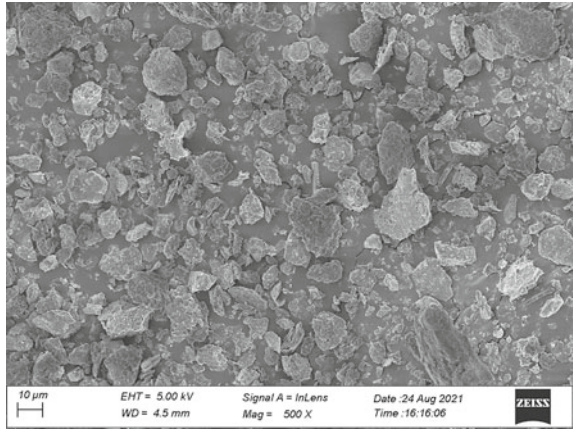


Fig. 5 FESEM image of sand sample



Fig. 6 FESEM image of rice husk sample

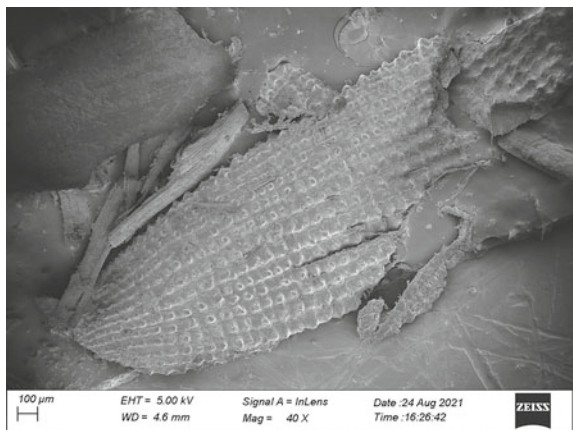


Fig. 7 FESEM image of candle sample

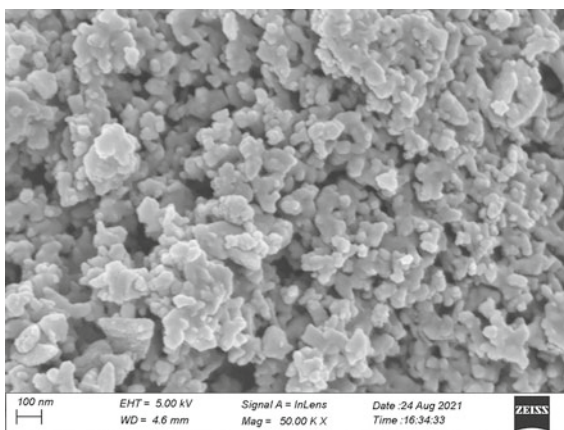
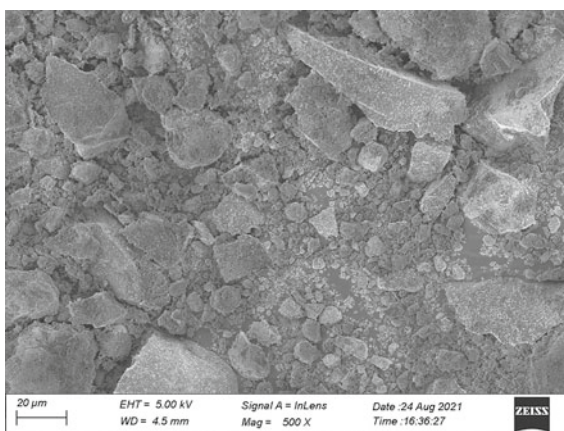


Fig. 8 FESEM image of cement container



some of the elements present in the water filter might have leached into the permeate, which may even include the harmful heavy metals in case its amount is high in the candle. The pH was also found to have been enhanced above the permissible limit of drinking water. Because of the occurrence of crystalobite phase of silica in the candle, the sintering temperature of the candle may be 1000–1400 °C, according to XRD analysis. Microbial analysis shows that this kind of indigenous filter candle is not suitable for the removal of microbial contaminated water especially *E.coli*. Overall it is thus recommended to undertake a more scientific approach in preparing of such filters in today's time as random selection of any raw material sample may lead to harmful consequences in terms of both chemical contaminant risk as well as microbial risk.

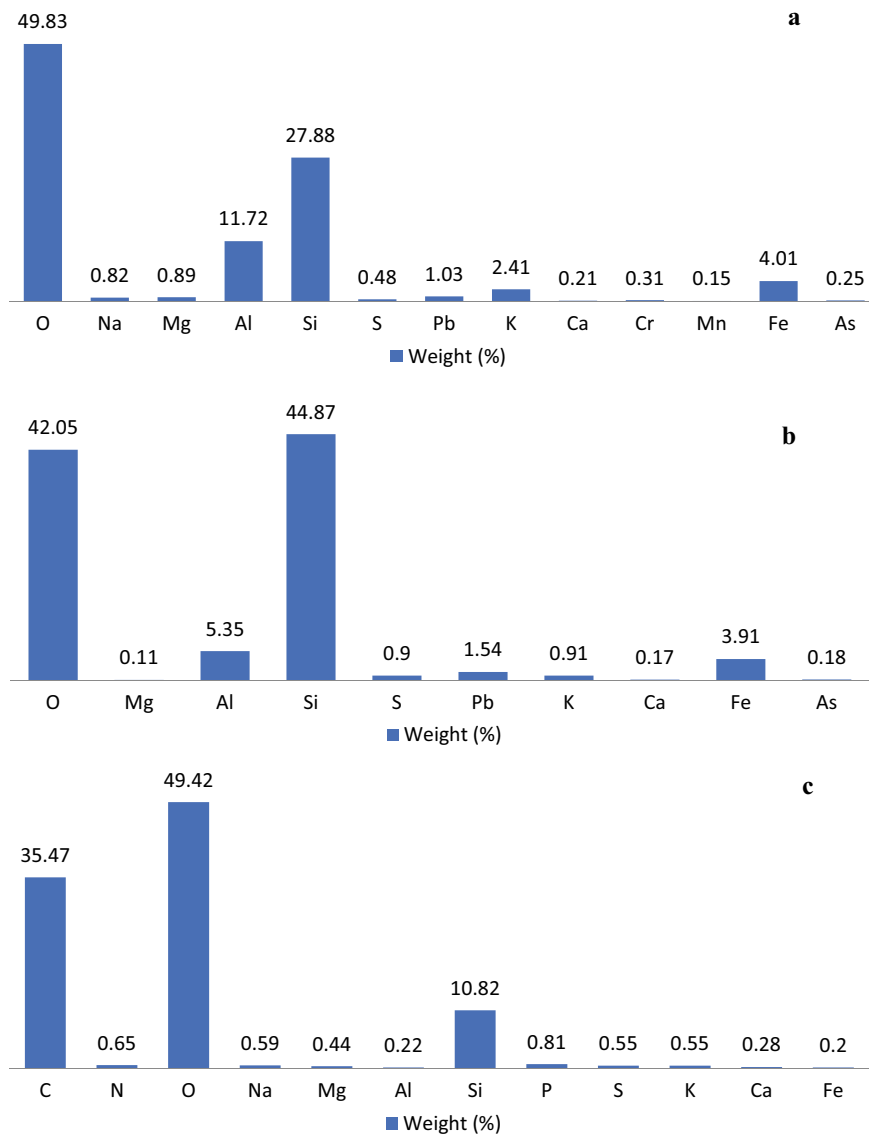


Fig. 9 a–e is the graphical representation of the elements present in the clay, sand, rice husk, candle, and cement container, respectively, by EDAX analysis

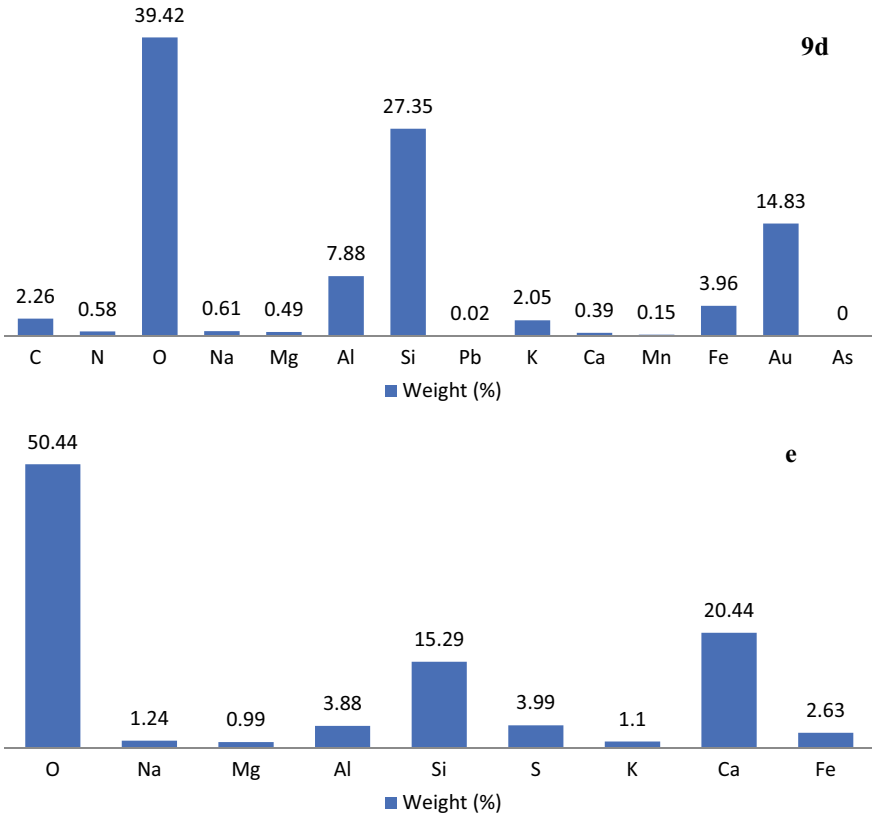


Fig. 9 (continued)

Fig. 10 XRD analysis of clay, sand, rice husk, filter material

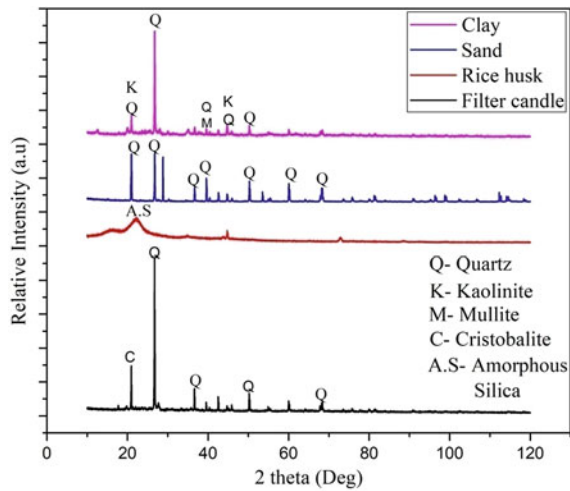


Fig. 11 FTIR analysis of sand, clay, rice husk, and candle

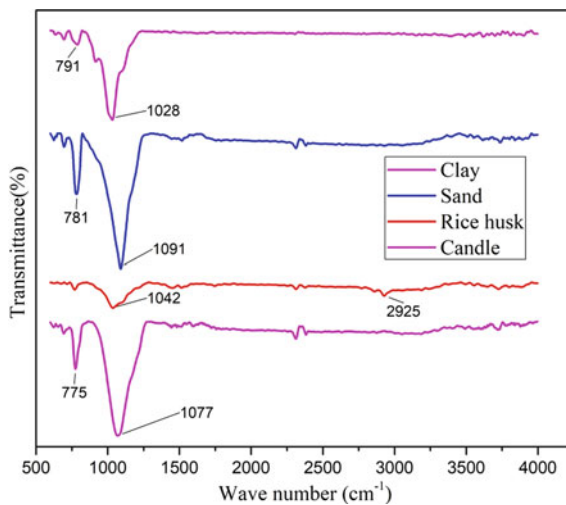


Table 7 FTIR analysis of Clay, sand, rice husk, and candle

Components	Wave number (cm^{-1})	Groups
Clay	791	Si-O Stretching Vibration
	1028	Si-O
Sand	781, 1091	Si-O Stretching
Rice husk	1042	Si-H stretching
	2925	C-H stretching of alkanes
Candle	775	Si-O
	1077	Si- O stretching

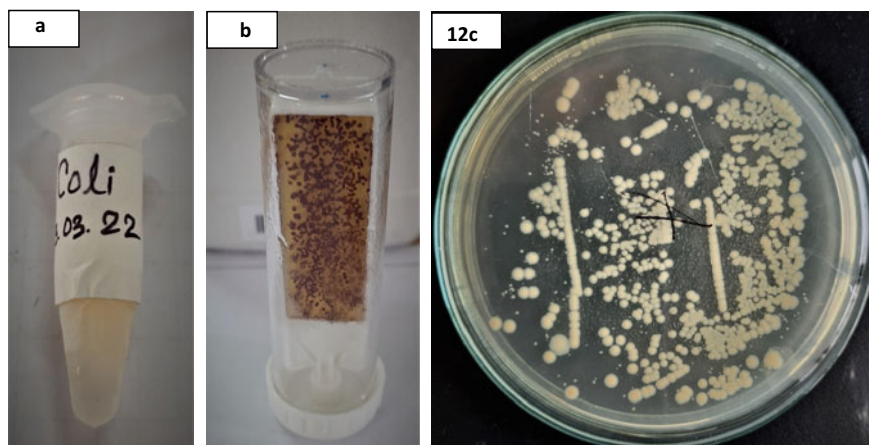


Fig. 12 a *E.coli* stock sample, b, c shows the growth of the bacteria in the feed water and filtrate water, respectively

Acknowledgements The authors would like to thank the Vice Chancellor of Tripura University for providing the necessary facilities. The authors would also like to thank Central Instrumentation Facility and Biotech Hub of Tripura University for providing FESEM facility and *E.coli* samples, NIT Silchar for providing XRD facility and CSIR IMMT Bhubaneswar for providing XRF facility.

References

1. De B, Debbarma T, Sen S, Chakraborty R (2010) Tribal life in the environment and biodiversity of Tripura, India. *Curr World Environ* 5:59–66. <https://doi.org/10.12944/cwe.5.1.08>
2. Das J, Debnath C, Nath H, Saxena R (2019) Antibacterial effect of activated carbons prepared from some biomasses available in North East India. *Energy Sources Part A Recover Util Environ Eff* 0, 1–11. <https://doi.org/10.1080/15567036.2019.1656305>
3. Sophia AC, Nath H, Praneeth NV (2016) Synthesis of nano-porous carbon from cellulosic waste and its application in water disinfection Synthesis of nano-porous carbon from cellulosic waste and its application in water disinfection. *Curr Sci* 111:1377–1382. <https://doi.org/10.18520/cs/v111/i8/1377-1382>
4. Banerjee S, Das B, Umlong IM, Devi RR, Kalita H, Saikia LB, Borah K, Raul PK, Singh L (2011) Heavy metal contaminants of underground water in Indo Bangla border districts of Tripura, India, vol 3, pp 516–522
5. NITI Ayog: research study on composite water resources management index for Indian States conducted by Dalberg Global Development Advisors Pvt. Ltd_New Delhi, <https://niti.gov.in/sites/default/files/2019-06/Final>; Report of the research study on composite water resources management index for Indian states conducted by Dalberg Global Development Advisors Pvt. Ltd_New Delhi.pdf. Accessed 08 Feb 2021
6. Ren L, Lu H, He L, Zhang Y (2014) Enhanced electrokinetic technologies with oxidation-reduction for organically-contaminated soil remediation. *Chem Eng J* 247:111–124. <https://doi.org/10.1016/j.cej.2014.02.107>

7. Chowdhury SR, Yanful EK (2010) Arsenic and chromium removal by mixed magnetite-maghemite nanoparticles and the effect of phosphate on removal. *J Environ Manage.* <https://doi.org/10.1016/j.jenvman.2010.06.003>
8. Youmou M, Fongang RTT, Sofack JC, Kamseu E, Melo UC, Tonle IK, Leonelli C, Rossignol S (2017) Design of ceramic filters using Clay/Sawdust composites: effect of pore network on the hydraulic permeability. *Ceram Int* 43:4496–4507. <https://doi.org/10.1016/j.ceramint.2016.12.101>
9. Sondi I, Salopek-Sondi B (2004) Silver nanoparticles as antimicrobial agent: a case study on *E.coli* as a model for Gram-negative bacteria. *J Colloid Interface Sci* 275:177–182. <https://doi.org/10.1016/j.jcis.2004.02.012>
10. Ahmad J, EL-Dessouky H (2008) Design of a modified low cost treatment system for the recycling and reuse of laundry waste water. *Resour Conserv Recycl* 52:973–978. <https://doi.org/10.1016/j.resconrec.2008.03.001>
11. Islam R, Faysal SM, Amin R, Juliana FM, Islam MJ, Alam J, Hossain MN, Asaduzzaman M (2017) Assessment of pH and Total Dissolved Substances (TDS) in the commercially available bottled drinking water. *IOSR J Nurs Heal Sci Ver IX* 6:35–40. <https://doi.org/10.9790/1959-0605093540>
12. Xavier KCM, Dos Santos MDSF, Santos MRMC, Oliveira MER, Carvalho MWNC, Osajima JA, Da Silva Filho EC (2014) Effects of acid treatment on the clay palygorskite: XRD, surface area, morphological and chemical composition. *Mater Res* 17:3–8. <https://doi.org/10.1590/S1516-14392014005000057>
13. Belibi Belibi P, Nguemtchouin MMG, Rivallin M, Ndi Nsami J, Sieliechi J, Cerneaux S, Ngassoum MB, Cretin M (2015) Microfiltration ceramic membranes from local Cameroonian clay applicable to water treatment. *Ceram Int* 41:2752–2759. <https://doi.org/10.1016/j.ceramint.2014.10.090>
14. Phonphuak N, Saengthong C, Srisuwan A (2019) Physical and mechanical properties of fired clay bricks with rice husk waste addition as construction materials. *Mater Today Proc* 17:1668–1674. <https://doi.org/10.1016/j.matpr.2019.06.197>
15. Liu X, Jiang J, Zhang H, Li M, Wu Y, Guo L, Wang W, Duan P, Zhang W, Zhang Z (2020) Thermal stability and microstructure of metakaolin-based geopolymer blended with rice husk ash. *Appl Clay Sci* 196:105769. <https://doi.org/10.1016/j.clay.2020.105769>
16. Tiwari D, Laldanwngliana C, Choi CH, Lee SM (2011) Manganese-modified natural sand in the remediation of aquatic environment contaminated with heavy metal toxic ions. *Chem Eng J* 171:958–966. <https://doi.org/10.1016/j.cej.2011.04.046>
17. Yuzer N, Cinar Z, Akoz F, Biricik H, Gurkan YY, Kabay N, Kizilkanat AB (2013) Influence of raw rice husk addition on structure and properties of concrete. *Constr Build Mater* 44:54–62. <https://doi.org/10.1016/j.conbuildmat.2013.02.070>
18. Krishnarao RV, Godkhindi MM (1992) Distribution of silica in rice husks and its effect on the formation of silicon carbide. *Ceram Int* 18:243–249. [https://doi.org/10.1016/0272-8842\(92\)90102-J](https://doi.org/10.1016/0272-8842(92)90102-J)
19. Johari I, Said S, Jaya RP, Bakar BHA, Ahmad ZA (2011) Chemical and physical properties of fired-clay brick at different type of rice husk ash. *Environ Sci Eng* 8:171–174
20. Haslinawati MM, Matori KA, Wahab ZA, Sidek HAA, Zainal AT (2009) Effect of temperature on ceramic from rice husk ash. *Int J Basic Appl Sci* 9:1985–1988
21. Sembiring S, Simanjuntak W, Situmeang R, Riyanto A, Sebayang K (2016) Preparation of refractory cordierite using amorphous rice husk silica for thermal insulation purposes. *Ceram Int* 42:8431–8437. <https://doi.org/10.1016/j.ceramint.2016.02.062>
22. Madejov J (2003) FTIR techniques in clay mineral studies. *Vib Spectrosc* 31:1–10. [https://doi.org/10.1016/S0924-2031\(02\)00065-6](https://doi.org/10.1016/S0924-2031(02)00065-6)
23. Branca C, D’Angelo G, Crupi C, Khouzami K, Rifici S, Ruello G, Wanderlingh U (2016) Role of the OH and NH vibrational groups in polysaccharide-nanocomposite interactions: a FTIR-ATR study on chitosan and chitosan/clay films. *Polymer (Guildf)* 99:614–622. <https://doi.org/10.1016/j.polymer.2016.07.086>

24. Daffalla SB, Mukhtar H, Shaharun MS (2010) Characterization of adsorbent developed from rice husk: effect of surface functional group on phenol adsorption. *J Appl Sci* 10:1060–1067. <https://doi.org/10.3923/jas.2010.1060.1067>
25. Naiya TK, Singha B, Das SK, Ftir K, Vi C (2011) FTIR study for the Cr (VI) removal from aqueous solution using rice waste 10:114–119

Magnetic and LPG Sensing Properties of Nickel Ferrite Nanoparticles Derived from Metallurgical Wastes



K. J. Sankaran, U. Balaji, and R. Sakthivel

1 Introduction

Spinel-type ferrite nanomaterials have gained attention in numerous applications such as microwave devices, recording media, high-density information storage, catalysts, gas sensors, magnetic- and ferrofluids, and so on [1]. Particularly, ferrites conquer a noteworthy place in sensing devices since they are a choice for economical and robust detection systems. Ferrites display superior chemical and thermal stability, better surface reactivity, and high selectivity than metal oxide semiconductors, especially for the detection of gases [2, 3]. They are also capable to attain high oxygen ion mobility that exemplifies exceptional catalytic characteristics in oxidation reactions. For instance, CuFe_2O_4 nanoparticles were prepared by co-precipitation method and observed an enhanced H_2S gas sensing characteristics [4]. MgFe_2O_4 and CdFe_2O_4 sensors were fabricated for the detection of LPG and C_2H_2 gases [5]. Moreover, $\text{CuCdFe}_2\text{O}_4$ [6], $\text{ZnMnFe}_2\text{O}_4$ [7], and $\text{NiCuFe}_2\text{O}_4$ [8] nanoparticles were also utilized as sensors to sense various toxic gases. From the above-mentioned studies, it is clear that ferrites are the suitable materials to fabricate devices for sensing several gases. Among gas sensors, particularly, the development of an LPG sensor is currently a major requirement for domestic use. LPG is flammable because it is a mixture of propane and butane. Leakage of LPG consequences numerous accidents and material loss. Therefore, it is highly required to develop an efficient sensor material for the detection of LPG.

Though spinel-type ferrites have been synthesized using numerous methods such as laser ablation, sol-gel, hydrothermal, and ball milling [9, 10], these methods necessitate high synthesizing temperature, longer duration, and high energy. A practicable

K. J. Sankaran · U. Balaji · R. Sakthivel (✉)

Advanced Materials Technology Department, CSIR-Institute of Minerals and Materials Technology, Bhubaneswar, Odisha 751013, India

e-mail: rsakthivel@immt.res.in

and forthright synthesizing method is greatly looked for. Moreover, readily available chemicals are generally utilized as the preliminary materials to synthesize ferrites, followed by multistep methods.

Generally, synthesizing nanomaterials from metallurgical wastes is a potential way to motivate “waste to wealth” perception, which would be beneficial for society and industries [11, 12]. In this work, using simple chemical co-precipitation method nickel ferrite (NiFe_2O_4) nanoparticles were synthesized from metallurgical wastes such as nickel scrap and mill scale. The LPG sensing characteristics of the obtained ferrite nanomaterials were evaluated and observed that NiFe_2O_4 -based LPG sensor showed a high sensitivity and better reproducibility at low temperatures.

2 Materials and Methods

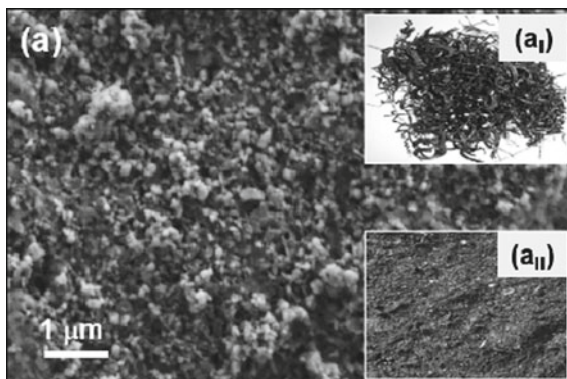
2.1 *Synthesis of Nickel Ferrite Nanoparticles from Metallurgical Wastes*

Nickel scrap (Fig. 1aI) and mill scale (Fig. 1aII) were the preliminary materials for the synthesis of nickel ferrite. First, nickel scrap was dissolved in diluted hydrochloric acid (solution A). Second, mill scale was refluxed in hydrochloric acid at 95 °C for the preparation of ferrous and ferric chloride solution. After cooling down to room temperature, the acid-insoluble portion was separated by filtration and total iron content in the acid leached iron chloride solution (solution B) was estimated by standard chemical method. Then both A and B solutions were mixed to sustain the Fe:Ni molar ratio of 2:1. Subsequently, potassium oxalate was mixed to Fe and Ni solution, and by slow addition of aqueous KOH solution its pH was raised to 12 to form mixed metal oxalate precipitate. The obtained mixed metal oxalate precipitate was aged in its mother liquor overnight, filtered, and washed with hot distilled water to remove chloride. Then, the precipitate was oven-dried at 110 °C for 8 h and ground into a fine powder. The acquired mixed metal oxalate was finally calcined at 900 °C for 4 h to attain NiFe_2O_4 nanoparticles [12].

2.2 *Characterization*

The phase analysis of NiFe_2O_4 nanoparticles was performed using X-ray diffraction (XRD) analysis technique in an XRD instrument (Panalytical Instrument-Model: X'pert Pro, Netherlands) using Cu $K\alpha$ radiation ($\lambda = 1.54056 \text{ \AA}$). The morphologies of the nanoparticles are characterized using a field emission scanning electron microscope (FESEM; Zeiss SUPRA55). The bonding characteristics of the nanoparticles were characterized using Raman spectroscopy (Renishaw; $\lambda = 532 \text{ nm}$). Fourier

Fig. 1 FESEM micrograph of nickel ferrite nanoparticles. The insets show the photographs of nickel scrap (**aI**) and mill scale (**aII**)



transform infrared spectroscopies were carried out using FTIR spectrometer (spectrum GX Perkin Elmer) from the ranges of 400 cm^{-1} – 4000 cm^{-1} with the resolution of 4 cm^{-1} .

The magnetic properties of NiFe_2O_4 nanoparticles were characterized using a vibrating sample magnetometer (VSM) (VSM; PAR155). All the NiFe_2O_4 nanoparticles were filled in acrylic cups followed by fixing it to quartz rods for mounting on the VSM. Before the magnetic measurement, the samples were A.C. demagnetized with a demagnetization factor of 0.9 for removing any stray magnetization from the samples. The magnetic properties such as saturation magnetization (M_s), remanent magnetization (M_r), and coercivity (H_c) at room temperature were calculated. The same measurement conditions were used for the respective background corrections.

2.3 Gas Sensing Measurements

NiFe_2O_4 nanoparticles in pellet form (10 mm in diameter) were used as a gas sensor. The pellets were made using polyvinyl alcohol (PVA) as a binder, and the pellets were calcined at $450\text{ }^\circ\text{C}$ to remove PVA. The LPG sensing measurements were carried out at operating temperatures between RT to $400\text{ }^\circ\text{C}$. A thermocouple is used to monitor the operating temperature. LPG gas concentration of 5000 ppm in air was then injected into the gas sensing chamber through mass flow controllers. The gas sensing characteristics was recorded by using a source meter. Using Eq. 1, the sensitivity (S) is calculated from the resistance of the samples, which is measured before and after supply of air and LPG,

$$S(\%) = (|\Delta R|/R_a) \times 100\% \quad (1)$$

ΔR is $R_a - R_g$, where R_a signifies the resistance of sensor when exposed to air, and R_g signifies the resistance of sensor when exposed to LPG gas [13]. After each gas

sensing measurement, the samples were heated at 400 °C for 30 min to get rid of any adsorbed species above the sample surface in order to achieve for high sensitivity and better reproducibility.

3 Results and Discussion

3.1 Materials Characteristics

Figure 1 shows the FESEM micrograph of NiFe₂O₄ nanoparticles, which have a uniform particle size of 50 nm and because of their magnetic nature the particles are agglomerated. The particle size of around 50 nm indicates the enhancement of solid–gas contact properties. Figure 2 shows the XRD pattern of NiFe₂O₄ nanoparticles that indicates the nanoparticles are of face-centered cubic spinel-type structure with Bragg reflections are (111), (220), (311), (222), (400), (422), (511), (440), (620), (533), (444), (642), (553), and (800), respectively [13], which are in good accord with the JCPDS file no. 10-0325 (#742,081 for NiFe₂O₄). Using Debye–Scherrer equation, the crystallite size from the XRD pattern is calculated and found to be around 55 nm and by using the equation: $d_{hkl} = a/\sqrt{(h^2 + k^2 + l^2)}$, the calculated lattice constant value is 8.36 Å for NiFe₂O₄, respectively.

The room temperature FTIR spectrum of NiFe₂O₄ nanoparticles shown in Fig. 3 reveals the Fe–O absorption at 584–610 cm⁻¹, which is at the tetrahedral site. The octahedral site Ni–O band is observed at the range of 385–450 cm⁻¹. The other absorption bands such as carbonyl (CO³⁻) group, O–H groups (bending), and hydroxyl groups (stretching) are evidenced around 1050 cm⁻¹, 1500–1700 cm⁻¹, 3100–3700 cm⁻¹, respectively [14]. The inset of Fig. 3 shows the Raman spectrum of NiFe₂O₄ that reveals bands around 470 cm⁻¹ representing tetrahedral site (Fe⁺³ at A) and the bands around 690 cm⁻¹ representing the octahedral (Ni⁺², Fe⁺³ at B) sites, confirming the inverse spinel structure AB₂O₄ ferrites [15].

Fig. 2 XRD diffraction studies of nickel ferrite nanoparticles

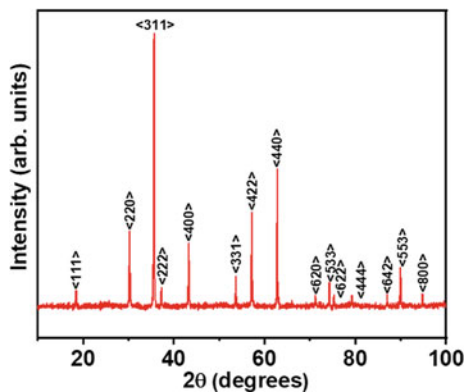
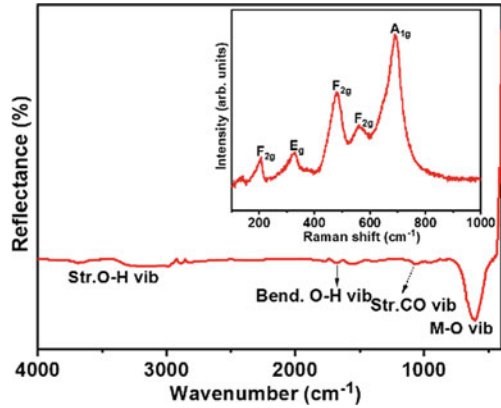


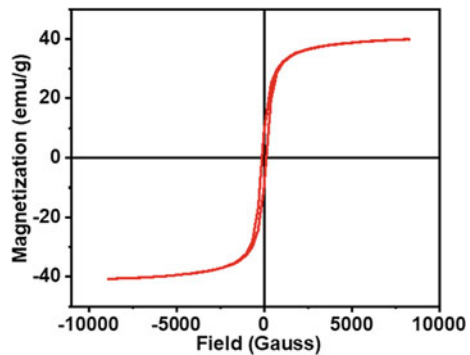
Fig. 3 FTIR and Raman spectra (inset) of nickel ferrite nanoparticles



3.2 Magnetic Properties

The hysteresis loop obtained from VSM measurements for NiFe_2O_4 nanoparticles recorded at room temperature displayed in Fig. 4 shows a typical soft magnetic property of low coercivity of 160 O_e [16–18]. In superparamagnetic materials, responsiveness to an applied magnetic field without retaining any magnetism after removal of the magnetic field is observed. This behavior is an important property for magnetic targeting carriers [19]. Moreover, the particle size of 50 nm confirms the superparamagnetic behavior of NiFe_2O_4 nanoparticles [18, 20]. The M-H plot reveals the saturation magnetization and magnetic retentivity values of 40 emu/g and 15 emu/g , respectively.

Fig. 4 VSM curves of nickel ferrite nanoparticles



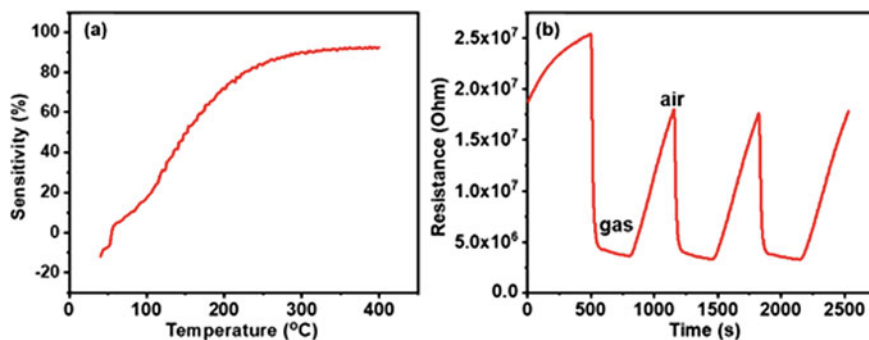


Fig. 5 **a** Sensitivity (%) to LPG at different operating temperatures and **b** the response time and recovery time of nickel ferrite nanoparticles for the gas concentrations of 5000 ppm

3.3 LPG Sensing

Figure 5a displays the gas sensing response of NiFe₂O₄ nanoparticles for LPG with respect to the operating temperature between 50 and 400 °C at LPG gas concentration of 5000 ppm in air. The gas sensing studies reveal that the optimum LPG response of NiFe₂O₄ nanoparticles is around 200°C and superior sensitivity of 92% at 400 °C. Moreover, the response and recovery of NiFe₂O₄ nanoparticles with exposure of 5000 ppm of LPG at 200 °C are signified in Fig. 5b. Here, the response time achieved is only 15 s for NiFe₂O₄ nanoparticles. As the LPG gas was turned off, the response of the same material fell rapidly, indicating that an excellent recovery time of 85 s was achieved.

The gas sensing mechanism for NiFe₂O₄ nanoparticles is correlated with the change in resistance of the nanoparticles supported by the oxygen adsorption on the nanoparticles. The smaller particle size and the large surface area of these nanoparticles result in the more adsorption of LPG on the surface of the nanoparticles, ensuing the high sensitivity of these NiFe₂O₄ nanoparticles.

4 Conclusions

In this work, NiFe₂O₄ nanoparticles were synthesized from metallurgical wastes and achieved a superior LPG gas sensing properties. The gas sensing behavior of these nanoparticles is correlated with the morphology and the magnetic properties of the nanoparticles. The gas sensing measurements of these nanoparticles were carried out at a constant LPG concentration of 5000 ppm in air. The NiFe₂O₄ nanoparticles responded, sensed, and recovered faster, which makes it a possible material for LPG sensing. The resistance of nanoparticles and the oxygen adsorption on the surface of the nanoparticles determined the gas sensing mechanism of NiFe₂O₄ nanoparticles.

Consequently, the approach to synthesizing NiFe₂O₄ nanoparticles from metallurgical waste is a good pathway for the conversion of waste to wealth and utilizing the nanoparticles as a LPG sensor with steady and fast-reacting gas sensing properties.

Acknowledgements The authors would acknowledge the financial support of the Ministry of Steel, New Delhi [File Number: S20021/5/2022-TECH-45(i)]. The authors are grateful to Central Characterization Department, CSIR-IMMT for providing analytical facilities.

References

1. Valenzuela R (2012) Novel applications of ferrites. *Phys Res Inter* 591839
2. Koli PB, Kapadnis KH, Deshpande UG (2019) Nanocrystalline modified nickel ferrite films: an effective sensor for industrial and environmental gas pollutant detection. *J Nanostruct Chem* 9:95
3. Prasad PD, Hemalatha J (2019) Enhanced magnetic property of highly crystalline cobalt ferrite fibers and their application as gas sensor. *J Magn Magn Mater* 484:225
4. Ayesb AI, Haija MA, Shaheen A, Banat F (2017) Spinel ferrite nanoparticles for H₂S gas sensing. *Appl Phys A* 123:682
5. Chen NS, Yang XJ, Liu ES, Huang JL (2000) Reducing gas sensing properties of ferrite compounds MFe₂O₄ (M=Cu, Zn, Cd, Mg). *Sensors Actuat B* 66:178
6. Ebrahimi HR, Usefi H, Emami H, Amiri GR (2018) Synthesis, characterization, and sensing performance investigation of copper cadmium ferrite nanoparticles. *IEEE Trans Mag* 54:4000905
7. Ebrahimi HR, Amini AR (2017) Synthesis of Mg_{0.5}Zn_{0.5}Fe₂O₄ nanoparticles via co precipitation method and study of its sensitivity properties. *J Adv Manuf Tech* 10:129
8. Ebrahimi HR, Heydari M, Bahraminejad B (2015) Highly sensitive Ni_{0.5}Cu_{0.5}Fe₂O₄ nanoparticles as an ethanol gas sensor. *Sens Lett* 13(1)
9. Kumari N, Kour S, Singh G, Sharma RK (2020) A brief review on synthesis, properties and applications of ferrites. *AIP Conf Proc* 2220:020164
10. Jauhar S, Kaur J, Goyal A, Singhal S (2018) Tuning the properties of cobalt ferrite: a road towards diverse applications. *RSC Adv* 6:97694
11. Corder GD, Golev A, Giurco D (2015) Wealth from metal waste: translating global knowledge on industrial ecology to metals in Australia. *Minerals Eng* 76:2
12. Sankaran KJ, Suman S, Sahaw A, Balaji U, Sakthivel R (2021) Improved LPG sensing properties of nickel doped cobalt ferrites derived from metallurgical wastes. *J Magn Magn Mater* 537:168231
13. Cherpin C, Lister D, Dacquait F, Liu L (2021) Study of the solid-state synthesis of nickel ferrite (NiFe₂O₄) by X-ray diffraction (XRD), scanning electron microscopy (SEM) and Raman spectroscopy. *Materials* 14:2557
14. Singh HS, Sangwa N (2017) Structural and magnetic properties of nickel ferrite nanoparticles synthesized by ball milling. *Inter J Eng Sci Invent* 6:36
15. Lazarevic ZZ, Jovalekic C, Milutinovic A, Sekulic D, Ivanovski VN, Recnik A, Cekic B, Romcevic NZ (2013) Nanodimensional spinel NiFe₂O₄ and ZnFe₂O₄ ferrites prepared by soft mechanochemical synthesis. *J Appl Phys* 113:187221
16. Nathani H, Gubbala S, Misra RDK (2005) Magnetic behavior of nanocrystalline nickel ferrite: Part I. The effect of surface roughness. *Mater Sci Eng B* 121:126
17. Kodama RH, Berkowitz AE, McNiff JEJ, Foner S (1996) Surface spin disorder in NiFe₂O₄ nanoparticles. *Phys Rev Lett* 77:394

18. Manova E, Tsoncheva T, Estournes C, Paneva D, Tenchev K, Mitov I, Petrov L (2006) Nano-sized iron and iron-cobalt spinel oxides as catalysts for methanol decomposition. *Appl Catal A* 300:170
19. Li G-y, Jiang Y-r, Huang K-l, Ding P, Chen J (2008) Preparation and properties of magnetic Fe₃O₄-chitosan nanoparticles. *J Alloys Compd* 466:451
20. Zhi J, Wang Y, Lu Y, Ma J, Luo G (2006) In situ preparation of magnetic chitosan/Fe₃O₄ composite nanoparticles in tiny pools of water-in-oil microemulsion. *Reac Funct Polym* 66:1552

Catalytic Behavior of Noble Metal Nanoparticle-Metal Oxide Assemblies: An Effect of Interfacial Ligands



Simantini Nayak and Yatendra S. Chaudhary

1 Introduction

The surface plasmonic resonance and catalytic properties exhibited by noble metal nanoparticles have allured great attention for their application, particularly in the catalysis [1–3]. Gold nanoparticles (Au NPs) exhibit high catalytic activity in contrast to bulk gold and hence are being exploited to catalyze various reactions such as propylene oxidation, water gas shift reaction, olefin epoxidation, and CO oxidation, etc [4–8]. However, the noble metal NPs are not stable and tend to collapse over a short period of time (a few hours) due to their high surface energy [22, 23]. An alternative approach developed to improve stability while retaining their catalytic activity is based on the dispersion of NPs on support materials. For example, Au NPs have been dispersed in both reducible oxides (TiO_2 , ZnO , Fe_2O_3 , CeO_2 , ZrO_2 , etc.) [9–11] and inert oxides (MgO , Al_2O_3 , SiO_2) [12, 13]. Such Au NPs supports are conventionally synthesized from single-atom gold precursors using aqueous chemistry: by co-precipitation or deposition–precipitation methods [24]. Nonetheless, these approaches do not offer precise control over the size, size distribution, and degree of dispersion of Au NPs on the support.

The improved catalytic activity exhibited by such Au NPs–metal oxide support materials has been attributed to the size of Au NPs, NPs–metal oxide support interface and the surface defects of the support. Although the literature suggest that NPs–metal oxide support interface is the most active site for catalytic reactions, but, the role

S. Nayak · Y. S. Chaudhary (✉)
Materials Chemistry Department, CSIR-Institute of Minerals and Materials Technology,
Bhubaneswar, Odisha 751013, India
e-mail: yschaudhary@immt.res.in

Y. S. Chaudhary
Academy of Scientific and Innovative Research (AcSIR), Ghaziabad 201 002, India

© The Author(s), under exclusive license to Springer Nature Singapore Pte Ltd. 2023
E. Chinthapudi et al. (eds.), *Sustainable Chemical, Mineral and Material Processing*,
Lecture Notes in Mechanical Engineering,
https://doi.org/10.1007/978-981-19-7264-5_20

265

of interfacial interactions between NPs-metal oxide support has not been explored extensively.

To investigate the role of interfacial ligands/interactions between NPs-oxide support, the Au NPs were grafted on silica spheres using various kinds of interfacial functionalities such as amine, polyelectrolyte, and CTABr. These functionalities offer different nature of interfacial interactions ranging from electrostatic to coordination. SiO₂ is known to be a less active support for catalysis; however, we used SiO₂ in this study as support so that the catalytic activity is predominantly influenced by the interfacial interactions rather than the inherent activity of the support. Herein, the detailed results on the structural and CO oxidation activity of Au NPs-SiO₂ samples studied using TEM, FTIR, TPR, XPS, etc. are presented.

2 Material and Methods

2.1 Materials

Reagents used for the synthesis of silica spheres included TEOS (tetraethylorthosilicate) (98.0%, Aldrich), ethanol (99.9%, SDF Chem.), ammonia solution, and H₂O (deionized, milli Q). For the synthesis of Au nanoparticles, Gold chloride trihydrate (ACS, Aldrich), Sodium citrate (Merck), Sodium borohydride (Merck), Cetyltrimethylammonium bromide (CTABr) (SDF Chem.), Ascorbic acid (Merck), and Sodium hydroxide (Merck) were used. All reagents were used as supplied.

2.2 Methods

2.2.1 Synthesis of Hydrolyzed Spherical Silica Spheres

Silica spheres were synthesized using Stober's process [14]. The obtained product was then calcined at 500 °C for 1 h. Since the calcinations lead to condensation of silanol groups, the calcined silica sphere samples were hydrolyzed to introduce hydroxyl groups for better functionalization. For this 1 g of the calcined powder was boiled with water in a 100 ml beaker with gentle stirring for 2 h. The obtained product was then centrifuged at 4000 rpm for 10 min and washed with deionized water for 3 times.

2.2.2 Synthesis of Au Nanoparticles

The citrate-stabilized and CTABr-capped Au NPs were synthesized by following the procedures reported in literature [15, 16]. Citrate stabilized Au precursor solution

was prepared by using HAuCl_4 and sodium citrate. CTABr-capped Au nanoparticle precursor solution was prepared by using the above Au precursor solution and a growth solution containing CTABr, HAuCl_4 , and ascorbic acid and which was then kept for 12 h aging. After synthesis, CTABr-capped Au nanoparticles were centrifuged at 8000 rpm for 10 min and washed with deionized water for complete removal of the surfactant. The washing procedure was repeated for 4 times. The product obtained from 180 ml gold NP solution was resuspended in 5 ml of deionized water.

2.2.3 Anchoring of Au Nanoparticles onto Silica Spheres

To graft Au NPs, the hydrated silica spheres were functionalized with different functionalities. Using APTES (0.002 mol), silica sphere samples were functionalized with $-\text{NH}_2$ functionality. The other set of silica samples was functionalized with cationic polyelectrolyte (PE), using 1 ml of Poly(diallyldimethylammonium chloride). 3 mg of $-\text{NH}_2$ and PE functionalized silica spheres were mixed with 6 ml of citrate-stabilized Au NP solution and allowed under equilibrium for 1 h which was followed by washing with deionized water and centrifugation. The Au NPs grafted silica sample having the functionalities of $-\text{NH}_2$ and PE are referred to as S- NH_2 -Au and S-PE-Au, respectively, in the following text.

The grafting of CTABr-capped Au NPs onto silica spheres was carried out by the method reported by us by dispersing 50 mg of silica spheres in 5 ml of Au NP solution and sonicated for 1 min [17]. It was consequently stirred gently for 30 min at RT and allowed to stand for overnight at RT. The Au NP-silica spheres composites were recovered by centrifuging and washing with deionized water to ensure the absence of any unabsorbed Au NP solution. The completion of loading was confirmed by the absence of the absorption peak in the UV-Vis absorbance spectra taken for the supernatant solution. This sample is referred as S-CTABr-Au in the following text.

2.2.4 Characterization

The absorption spectra of Au nanoparticles and metal NP-functionalized silica spheres composites were recorded using a UV-Vis spectrophotometer (Shimadzu UV-2450). The morphology and size of silica spheres was examined by scanning electron microscope (Hitachi S-3400 N). The TEM analysis was done using a FEI Technai G2 20 microscope operated at 200 kV to determine the size and anchoring of Au NPs onto silica supports. The presence of different functional groups in the metal NP-silica sphere hybrids was confirmed using Fourier transform infra-red spectroscopy (Varian).

X-ray photoelectron spectroscopy (XPS) spectra were recorded by a VG Microtech ESCA 2000 Multilab spectrometer, equipped with a standard Mg $K\alpha$ excitation source ($h\nu = 1253.6$ eV), and a hemispherical analyzer operating at constant pass energy of 20 eV. The binding energy (BE) scale calibration was done

by measuring C 1 s peak (BE = 284.6 eV) from the surface contamination and the accuracy was ± 0.9 eV. The differential surface charging of samples was ruled out by repeated scans under different X-ray exposures. All XPS data were fitted using the program of VGX-900, based on Gaussian peak shape after background subtraction.

The most reducing conditions of these Au-silica catalysts were examined by the analysis of temperature programmable reduction (TPR). Then the sample was subjected to heat treatment from RT to 700 °C under the 5% H₂/Ar (vol %) with a constant flow rate of 50 ml min⁻¹.

2.3 Catalytic Activity Evaluation

The catalytic activity of samples towards the oxidation of carbon monoxide was explored using a fixed bed flow reactor. 80 mg of samples were diluted with quartz and placed in the reactor. The reactant gas mixture consisting of CO (10%), O₂ (5%), and He (85%) at a flow rate of 40 ml min⁻¹ was passed through the reactor. Analysis of effluent gases from the reactor was carried out using gas chromatography.

3 Results and Discussion

3.1 TEM Analysis

The silica sample synthesized using Stobers process lead to the formation of white powder which turned into light pink in color when grafted with Au NPs. To ensure the anchoring of Au NPs, the extent of surface coverage, and their structural details, TEM analysis was performed for all samples. The silica sample consists of monodisperse spheres of 320 ± 15 nm as can be seen in Fig. 1a, also SEM image is shown in supplementary information, Figure S1. The grafting of pre-fabricated Au NPs on silica spheres using different ligands is shown in Fig. 1b–d. The CTABr-capped Au nanoparticles are bigger in size, as expected, due to further growth of Au NPs while allowing them to age for longer time to ensure complete surface coverage by CTABr—as it was confirmed by FTIR spectrum (supporting information, Figure S2). The –NH₂ and PE functionalized silica spheres were found to have better coverage with Au NPs as compared to that achieved by CTABr-capped Au NPs onto silica spheres. In general, the grafted Au NPs were sturdily anchored onto silica spheres in case of all samples, as can be seen in the inset of Fig. 1b–d.

Fig. 1 TEM image of **a** silica spheres, **b** S-CTABr-Au, **c** S-NH₂-Au, **d** S-PE-Au, and inset shows their high magnification image of Au NP—support interface

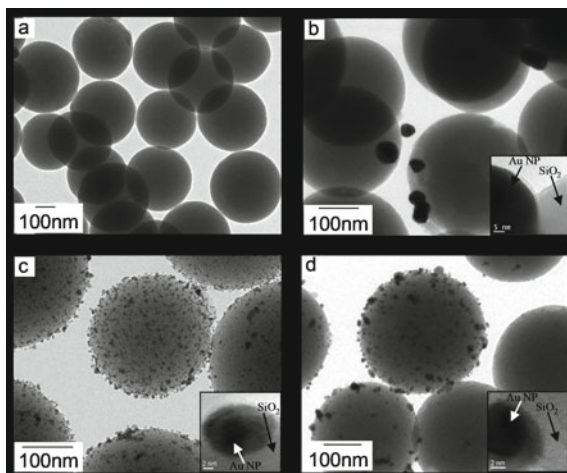
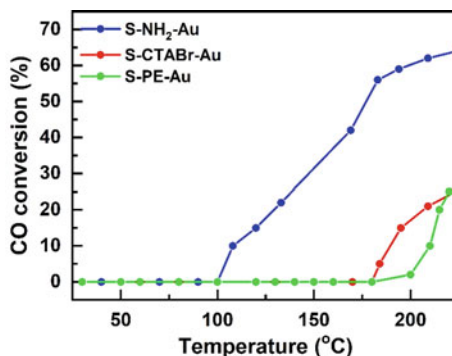


Fig. 2 CO oxidation as a function of temperature for Au NPs anchored silica sphere samples



3.2 CO Oxidation

To examine the catalytic activity and the effect of interfacial ligands of Au NPs grafted SiO₂ samples, CO oxidation was undertaken. The S-NH₂-Au shows CO oxidation at much lower temperature (starts at 100 °C) than that of reported in literature on non-reducing silica supports (ca ~ 270 °C) and lead to overall ~63% CO oxidation at 225 °C, Fig. 2. Whereas, in the case of both S-CTABr-Au and S-PE-Au, the CO oxidation starts at ca 180 °C and lead to ~25% CO oxidation at 225 °C, Fig. 2.

3.3 X-ray Photoelectron Spectroscopy (XPS)

In order to get an insight in such variation shown in the catalytic activity of these samples, XPS and TPR measurements were undertaken. XPS measurements were

performed for S-CTABr-Au, S-NH₂-Au, S-PE-Au catalysts to obtain further information about chemical state of Au species on the surface of the catalyst. All binding energy values given here have been charge corrected using the C1s line, Fig. 3. The binding energy (BE) values shown at 84.5 and 88.2 eV for S-CTABr-Au correspond to Au 4f_{7/2} and Au 4f_{5/2}, thus suggesting the presence of Au⁰ species [18, 19]. Whereas, two 4f_{7/2} components (at BE values of 86.6 and 90.1 eV) and two 4f_{5/2} components (at BE values 87.7 and 90.3 eV) observed for S-NH₂-Au indicate the presence of both, Au⁺¹ and Au⁺³ species [18, 19]. The calculations done to determine the fractions of Au³⁺ and Au¹⁺ present show that only 17.84% of the total gold present on S-NH₂-Au corresponds to Au³⁺ species. In the case of S-PE-Au, the BE values were observed at 85.7 and 89.3 eV which correspond to Au 4f_{7/2} and Au 4f_{5/2} and thus indicating the presence of Au¹⁺ species.

Fig. 3 XPS curve fitting of the Au 4f photoelectron peak in Au nanoparticle-silica samples

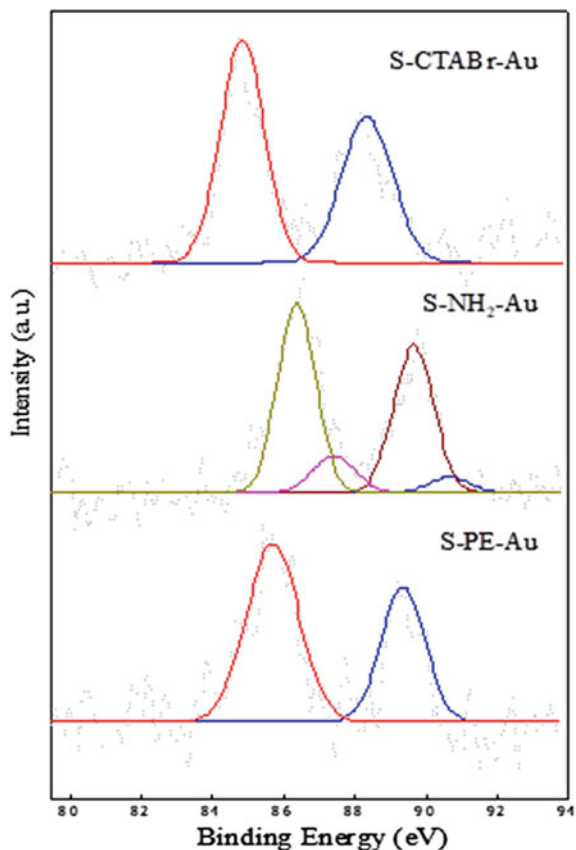
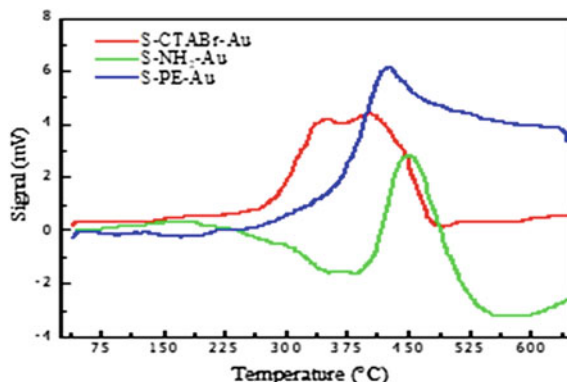


Fig. 4 Hydrogen TPR profile of Au NPs anchored silica sphere samples



3.4 Temperature Programmable Reduction (TPR)

The TPR profile of S-CTABr-Au demonstrates that the reduction of Au NPs initiated at lower temperature ca 259 °C than that of S-NH₂-Au (392 °C) samples, Fig. 4. The maximum reduction for these samples was observed at 346–403, 424, and 450 °C, respectively. The reduction taking place at higher temperature for S-NH₂-Au suggests strong binding of Au on silica spheres. Whereas, the S-CTABr-Au seems to have weakly bound Au NPs. The reduction taking place at moderate temperature 307 °C observed for S-PE-Au sample suggest weaker binding of Au NPs than that of S-NH₂-Au and stronger than that of S-CTABr-Au.

The CO oxidation observed at lower temperature for S-NH₂-Au is possibly due to better interaction of Au NPs with silica sphere supports which forms active interface. The presence of Au⁺¹ species, as suggested by XPS data, plays an important role. It appears that it forms AuO⁻ species at the interface which subsequently leads to significantly improved catalysis at lower temperature. The strong interfacial interaction between the Au NPs and the SiO₂ supports is also in compliance with the TPR data. The formation of such AuO⁻ and consequently improved catalytic activity has also been observed with other oxide supports [20, 21]. The catalytic activity initiation at higher temperature that is 180 °C for S-CTABr-Au and S-PE-Au may be ascribed to weak interactions (as suggested by TPR data). S-CTABr exhibits very low catalytic activity at 180 °C which increases gradually till 200 °C and then increases exponentially. Such dual catalytic activity rate exhibited by S-CTABr-Au is complementary to the reduction behavior as shown by a broad peak having two maxima at 347 and 403 °C in TPR profile and may be attributed to the Au NPs shape effect. The synthesis of CTABr-Au NPs leads to elongated nanoparticles, as shown by the appearance of weak shoulder along with prominent peak in the absorption spectrum of CTABr-Au NPs (supporting information Figure S4). Therefore, Au NPs with such elongated shape may anchor in two different orientations and thus may exhibit different interface activity and consequently different catalytic activity.

4 Conclusion

In brief, the TPR study reveals that Au NPs exhibit the ascending interaction affinity order from S-CTABr-Au < S-PE-Au < S-NH₂-Au and interestingly the catalytic activity follows the same trend for all these samples. The CO oxidation observed at lower temperature for S-NH₂- is due to higher degree of the intimate interaction of Au NPs with silica sphere supports as compared to that of other S-PE-Au and S-CTABr. Furthermore, the dual catalytic activity rate observed in the case of S-CTABr-Au elongated nanoparticles enables the difference in the degree of the interaction between two different facets of nanoparticles. The CO oxidation, TPR, and XPS findings show that the interactions and the chemical state of the Au at the Au-support interface greatly influence the overall catalytic activity. These results on the interface tuning might have great implications on designing the catalysts for various commercially viable reactions.

Supporting Information

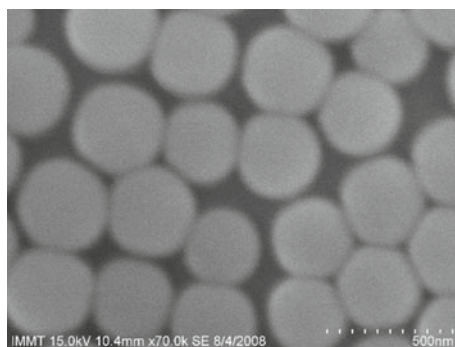


Figure S1 SEM image of silica spheres

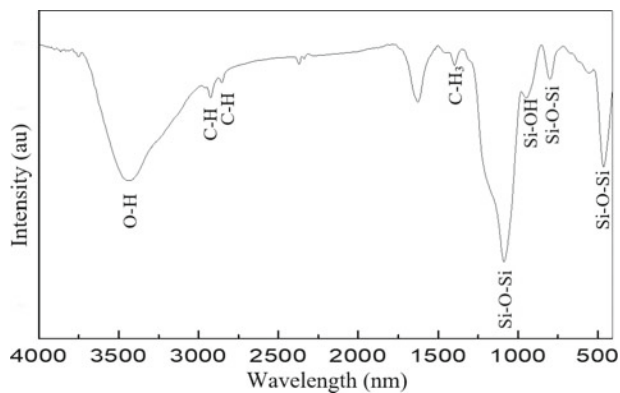


Figure S2 FTIR spectra S-CTABr-Au

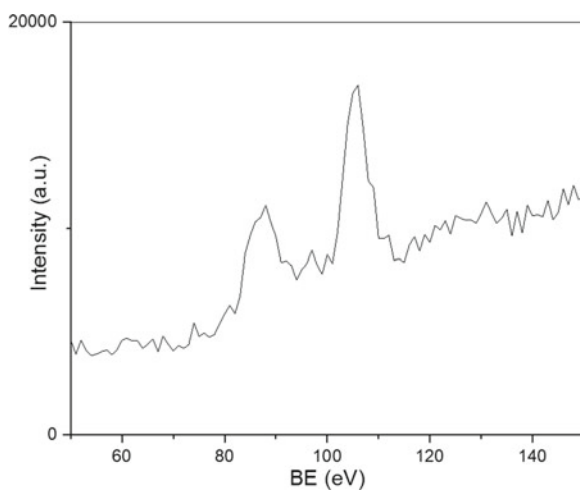


Figure S3 XPS Full survey spectrum of S-NH₂-Au

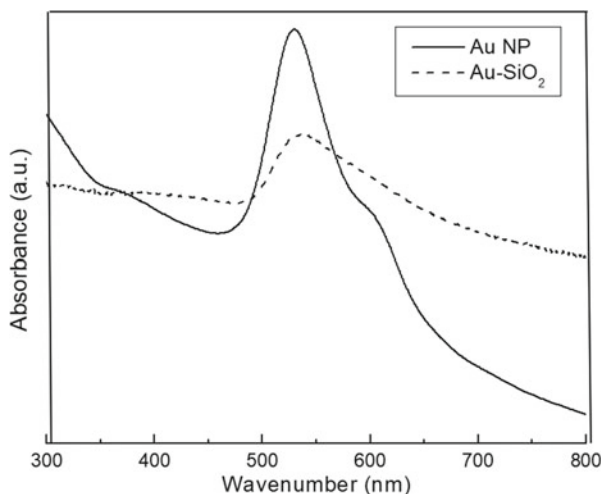


Figure S4 UV-Vis absorbance spectra of Au NP (capped with CTABr) before and after assembling steps

References

1. Warren SC, Thimsen E (2012) Plasmonic solar water splitting. *Energy Environ Sci* 5:5133
2. Haruta M, Daté M (2001) Advances in the catalysis of Au nanoparticles. *Appl Catal A* 222:427–437
3. Kim SH (2018) Nanoporous gold: preparation and applications to catalysis and sensors. *Curr Appl Phys* 18:810–818
4. Haruta M, Kobayashi T, Sano H, Yamada N, Novel (1987) Gold catalysts for the oxidation of carbon monoxide at a temperature far below 0 °C. *Chem Lett* 16:405–408
5. Haruta M, Yamada N, Kobayashi T, Iijima S (1989) Gold catalysts prepared by coprecipitation for low-temperature oxidation of hydrogen and of carbon monoxide. *J Catal* 115:301–309
6. Giorgi PD, Elizarov N, Antonioti S (2017) Selective oxidation of activated alcohols by supported gold nanoparticles under an atmospheric pressure of O₂: batch and continuous-flow studies. *ChemCatChem* 9:1830–1836
7. Lomello-Tafin M, Chaou AA, Morfin F, Caps V, Rousset J (2005) Preferential oxidation of CO in H₂ over highly loaded Au/ZrO₂ catalysts obtained by direct oxidation of bulk alloy. *Chem Commun* 41:388–390
8. Reina TR, Ivanova S, Centeno MA, Odriozola JA (2016) The role of Au, Cu & CeO₂ and their interactions for an enhanced WGS performance. *Appl Catal B* 187:98–107
9. Ha H, Yoon S, An K, Kim HY (2018) Catalytic CO oxidation over Au nanoparticles supported on CeO₂ nanocrystals: effect of the Au–CeO₂ interface. *ACS Catal* 8:11491–11501
10. Kim HY, Lee HM, Henkelman G (2012) *J Am Chem Soc* 134:1560–1570
11. Han M, Wang X, Shen Y, Tang C, Li G, Smith RL Jr (2010) Preparation of highly active, low Au-loaded, Au/CeO₂ nanoparticle catalysts that promote CO oxidation at ambient temperatures. *J Phys Chem C* 114:793
12. Zhang Y, Zhang J, Zhang B, Si R, Han B, Hong F, Niu Y, Sun L, Li L, Qiao B, Sun K, Huang J, Haruta M (2020) Boosting the catalysis of gold by O₂ activation at Au-SiO₂ interface. *Nat Commun* 11:558

13. Hernández WY, Aliç F, Navarro-Jaen S, Centeno MA, Vermeir P, Voort PVD, Verberckmoes A (2017) Structural and catalytic properties of Au/MgO-type catalysts prepared in aqueous or methanol phase: application in the CO oxidation reaction. *J Mater Sci* 52:4727–4741
14. Stöber W, Fink A, Bohn E (1968) Controlled growth of monodisperse silica spheres in the micron size range. *J Colloid Interf Sci* 26:62–69
15. Petkov N, Stock N, Bein T (2005) Gold electroless reduction in nanosized channels of thiol-modified SBA-15 material. *J Phys Chem B* 109:10737–10743
16. Busbee BD, Obare SO, Murphy CJ (2003) An improved synthesis of high-aspect-ratio gold nanorods. *Adv Mater* 15:414–416
17. Chaudhary YS, Ghatak J, Bhatta UM, Khushalani D (2006) One-step method for the self-assembly of metal nanoparticles onto faceted hollow silica tubes. *J Mater Chem* 16:3619–3623
18. Casaletto MP, Longo A, Martorana A, Prestianni A, Venezia AM (2006) XPS study of supported gold catalysts: the role of Au⁰ and Au^{+δ} species as active sites. *Surf Interf Anal* 38:215–218
19. Fu Q, Saltsburg H, Flytzani-Stephanopoulos M (2003) Active nonmetallic Au and Pt species on ceria-based water-gas shift catalysts. *Science* 301:935–938
20. Pestryakov AN, Lunin VV, Kharlanov AN, Kochubey DI, Bogdanchikova N, Stakheev AY (2002) Influence of modifying additives on electronic state of supported gold. *J Mol Struct* 642:129–136
21. Pestryakov AN, Lunin VV (2000) Physicochemical study of active sites of metal catalysts for alcohol partial oxidation. *J Mol Catal A* 158:325
22. Bachenheimer L, Elliot P, Stagon S et al (2014) Enhanced thermal stability of Ag nanorods through capping. *Appl Phys Lett* 105:213104
23. Sheng WC, Lee SW, Crumlin EJ, Chen S, Shao-Horn Y (2011) Synthesis, activity and durability of Pt nanoparticles supported on multi-walled carbon nanotubes for oxygen reduction. *J Electrochem Soc* 158:B1398–B1404
24. Priece P, Salami HA, Padilla RH, Zhong ZY, Lopez-Sanchez JA (2016) Anisotropic gold nanoparticles: preparation and applications in catalysis. *Chin J Catal* 37:1619–1650

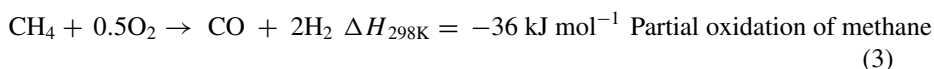
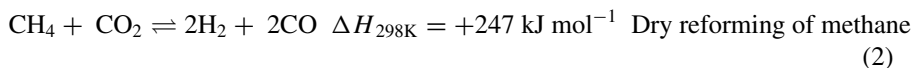
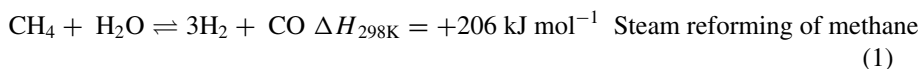
Optimization of Nickel Loading of Ni-Al₂O₃ Catalyst for Syngas Production by Tri-Reforming of Methane



Satyam Gupta and Goutam Deo

1 Introduction

The major anthropogenic sources of CO₂ are flue gases from fossil fuel-based electricity generation plants. Separating CO₂ from flue gas is an energy-intensive process, which reduces a power plant's net electricity output by approximately 20% [1]. In addition to CO₂, flue gas contains N₂, oxygen, moisture, and trace amounts of SO_x, NO_x, and particulate matter [2]. Recently, there has been an interest in the direct conversion of flue gases into syngas (CO + H₂) by co-feeding methane. The resulting process is called the Tri-reforming of methane (TRM). The TRM process combines mainly three reactions, which are dry reforming of methane (DRM), Eq. (1), steam reforming of methane (SRM), Eq. (2), and partial oxidation of methane (POM), Eq. (3). As can be seen, the TRM process does not require separating CO₂ from flue gas.



S. Gupta · G. Deo (✉)

Department of Chemical Engineering, Indian Institute of Technology Kanpur, Kanpur 208016, India

e-mail: goutam@iitk.ac.in

G. Deo

Department of Sustainable Energy Engineering, Indian Institute of Technology Kanpur, Kanpur 208016, India

Previous studies have shown that the TRM is a more energy-efficient technique for syngas production and high CO₂ conversion than steam reforming and CO₂ reforming of methane [2, 3]. Furthermore, by adjusting the feed molar ratios, a desired H₂/CO ratio can be achieved, which is needed for further utilization of syngas. Coke deposition on the catalyst surface is significantly reduced since O₂ and H₂O are present in the feed stream, increasing catalytic stability [2].

The metal loading significantly affects the physicochemical characteristics of a catalyst, such as dispersion and reducibility. Consequently, the activity and stability of the catalyst are affected [1, 4–6]. Rezaei et al. [7] examined the auto-thermal reforming of methane over a Ni–MgO catalyst and showed that the catalytic activity improved as Ni loading increased up to 15 wt.%. The loading was not increased further. Furthermore, Singha et al. [1] reported MgCeZr-supported Ni catalysts with 2.5, 5, and 10 wt.% of Ni. The 5Ni–MgCeZr catalyst showed superior activity due to its improved reducibility and a large number of active sites present on the surface. Singha et al. [4] also examined Ni–ZrO₂ catalysts with 2.3, 4.8, and 9.5 wt.% Ni for the TRM. The 4.8Ni–ZrO₂ catalyst exhibited the highest catalytic performance among the prepared catalysts due to the presence of highly dispersed nickel particles and strong metal-support interaction. Thus, an optimum Ni loading was achieved. Pino et al. [5] examined Ni–La–CeO₂ catalysts containing 1.7, 3.6, 7.8, and 10.2 wt.% Ni in TRM and reported high Ni dispersion at low Ni loading, resulting in increased activity at low metal loading in the catalyst. However, for the TRM reaction, the optimum metal loading for the catalysts possessing strong metal-support interactions, such as those existing in traditional Ni–Al₂O₃ catalysts calcined at high temperatures, appears to be less investigated.

To determine the optimum metal loading, Ni–Al₂O₃ catalysts with different Ni wt.% were prepared, characterized, and employed in the TRM reaction. γ -Al₂O₃ as a support for catalysts was chosen because of its large surface area, high thermal stability, and low cost. To impart a strong metal-support interaction and its associated advantages, the catalysts were calcined at 850 °C. The amount of CO₂, steam, and oxygen in the feed for the TRM experiment was equivalent to that of flue gas composition from coal-fired power plants. Based on the characterization and reactivity results, directions toward the development of a suitable catalyst for TRM are suggested.

2 Material and Methods

2.1 Catalyst Synthesis

A series of Ni–Al₂O₃ catalysts with a nickel content from 5 wt.% to 22.5 wt.% were prepared using the incipient wetness impregnation method [8, 9]. Nickel (II) nitrate hexahydrate (Sigma-Aldrich) salt was used as a precursor. Initially, the pre-treated support was impregnated with the required amount of an aqueous nitrate solution.

During synthesis, single impregnation was used for metal loadings up to 15 wt.%, and double impregnation was used for > 15 wt.%. Multiple impregnations were needed because the precursor solution volume required for loadings higher than 15 wt.% was greater than the incipient wetness volume of support. After impregnation, the mixture was dried in an oven for 12 h, followed by calcination at 850 °C for 5 h. For loadings > 15 wt.%, the drying was done twice and high-temperature calcination once. The prepared catalysts were referred to as xNi-Al. Here 'x' refers to the nickel amount (w/w) in the catalyst. The prepared catalysts were denoted as 5Ni-Al, 7.5Ni-Al, 15Ni-Al, and 22.5Ni-Al. To obtain the reduced form used for characterization and reaction, the 850 °C calcined xNi-Al catalysts were reduced at the corresponding reduction temperatures (T_{\max}) from H₂-TPR results for 2 h.

2.2 Catalyst Characterization

N₂-physisorption analysis was performed on a Quantachrome AutosorbIQ instrument to measure surface area and total pore volume. A Diffuse reflectance UV–vis instrument (DR-UV–vis), Cary 5000 (Harrick Scientific), was used to obtain the spectra of fresh xNi-Al catalysts. The reduction characteristics of the prepared catalysts were examined by H₂-TPR using an Altamira AMI-200 instrument. The H₂-TPR profile was generated by heating the sample from 50–1000 °C in a reducing gas stream of 10% H₂/Ar. The XRD patterns of fresh and reduced catalysts were obtained using a PANalytical X'Pert PRO Diffractometer. The crystallite size of the metallic-Ni in the reduced catalysts was calculated from the Debye–Scherrer equation. Furthermore, The dispersions (%) of Ni, D, in different xNi-Al catalysts were measured from the XRD patterns of the reduced catalysts by using Eq. (4) given by [10, 11]

$$D(\%) = \frac{101}{d_{\text{Ni}}} \quad (4)$$

where d_{Ni} is the crystallite size of metallic-Ni in nm.

2.3 Catalytic Activity Test

Activity measurements of the TRM process were carried out in a continuous down-flow tubular fixed-bed quartz reactor (8 mm i.d.) under atmospheric pressure at 600 °C. A catalyst bed with 0.05 g catalyst was placed in the middle of the reactor, supported on the quartz wool. The reactor was placed in a furnace equipped with a temperature controller. The catalysts were reduced in the quartz reactor at their respective T_{\max} temperatures from H₂-TPR results for 2 h in a flow of pure H₂ just before they were used for the reaction. Premixed reactant gases with a molar ratio of CH₄: CO₂: H₂O: O₂: N₂ = 1: 0.5: 0.5: 0.1: 14.6 were passed through the reactor. A

set of calibrated mass flow controllers (MFCs) was used to control the gas flow. The vapor pressure of H₂O at the gas sparger temperature (25 °C) was used to control the water content in the feed mixture for the tri-reforming experiments. For this purpose, N₂ gas was bubbled through a gas sparger filled with water. To prevent condensation, all lines downstream of the gas sparger were insulated. The gas hourly space velocity (GHSV) of the total gas mixture was fixed at 1,20,000 ml g⁻¹ h⁻¹.

The composition of the exit gas stream from the reactor was analyzed by a gas chromatograph (GC) (Nucon 5765) equipped with a Carbosphere column and a thermal conductivity detector (TCD) using Ar as the carrier. The TRM reactions were performed for 4 h for time-on-stream (TOS) analysis. Each reaction was repeated at least three times with a calcined catalyst, and the average values were reported. Errors were less than 5% of the average values.

CH₄ and CO₂ conversions, Eq. (5), H₂ yields, Eq. (6), CO yields, Eq. (7), and H₂/CO molar ratios, Eq. (8), were used to evaluate the catalytic performances.

$$X_i(\%) = \frac{F_{i, \text{in}} - F_{i, \text{out}}}{F_{i, \text{in}}} \times 100; \quad i = \text{CH}_4 \text{ and } \text{CO}_2 \quad (5)$$

$$Y_{\text{H}_2}(\%) = \frac{F_{\text{H}_2, \text{out}}}{2F_{\text{CH}_4, \text{in}} + F_{\text{H}_2\text{O}, \text{in}}} \times 100 \quad (6)$$

$$Y_{\text{CO}}(\%) = \frac{F_{\text{CO}, \text{out}}}{F_{\text{CH}_4, \text{in}} + F_{\text{CO}_2, \text{in}}} \times 100 \quad (7)$$

$$\frac{\text{H}_2}{\text{CO}} \text{ ratio} = \frac{F_{\text{H}_2, \text{out}}}{F_{\text{CO}, \text{out}}} \quad (8)$$

where $F_{i, \text{in}}$ and $F_{i, \text{out}}$ are the molar flow rates of gas species at the reactor inlet and outlet, respectively. Furthermore, X_i and Y_j are conversion of reactant i and yield of product j .

3 Results and Discussion

Some of the different techniques described in the material and methods section were used to characterize the calcined and reduced catalysts. For example, the surface area and the total pore volume of calcined catalysts were examined by N₂-physisorption, the phases present by UV-vis and XRD, and their reducibility by H₂-TPR. Similarly, the reduced catalysts were characterized for their dispersion and the crystallite size of metallic-Ni by XRD analysis.

3.1 Characterization of Calcined Catalysts

The surface areas of support and calcined xNi-Al catalysts were measured by N₂-adsorption, and the values are reported in Table 1. It was observed that the surface areas of all the catalysts were lower than the support. Furthermore, with an increase in Ni amount, the surface area monotonically decreased. The total pore volume of the supported catalysts also decreased with an increase in Ni amount. A reduction in the surface area was previously reported and was attributed to the partial blockage of the pores of the support at higher loadings [9, 12].

To confirm the presence of the nickel oxide species in the calcined samples, the DR-UV-vis spectra were obtained and are shown in Fig. 1. Bands between 550 nm–650 nm are usually associated with tetrahedral Ni²⁺ species that are present in NiAl₂O₄ [8, 9]. Indeed, all spectra show peaks between 550–650 nm, which suggests the presence of these tetrahedral Ni²⁺ species. Furthermore, with an increase in Ni loading, the bands due to tetrahedral Ni (II) became more prominent. A peak at around 370 nm was also observed. However, the band at 370 nm was not clearly assigned, which may be due to the formation of NiAl₂O₄ [9].

Table 1 Structural properties of support and xNi-Al catalysts with different Ni loadings

Sample	BET surface area (m ² /g)	Total pore volume (cm ³ /g)	Metal oxide reduction (%)
γ-Al ₂ O ₃	136	0.20	–
5Ni-Al	106	0.19	92.4
7.5Ni-Al	104	0.15	95.2
15Ni-Al	100	0.14	97.4
22.5Ni-Al	94	0.11	94.3

Fig. 1 DR-UV-vis spectra of calcined xNi-Al catalysts for various metal loadings: x = a 5, b 7.5, c 15, and d 22.5

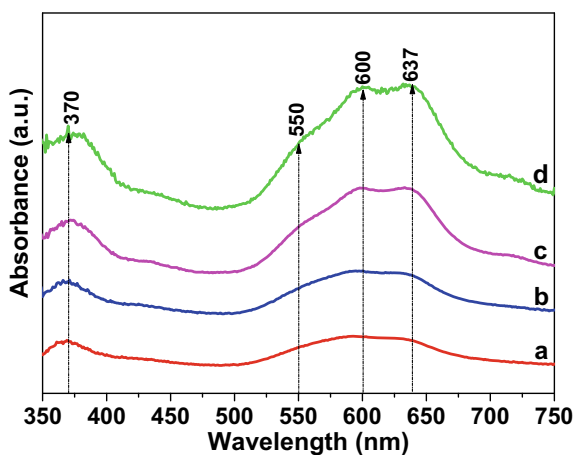
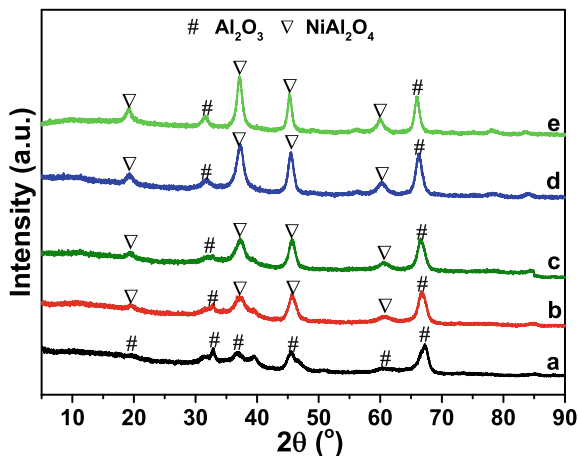


Fig. 2 XRD patterns of calcined xNi–Al catalysts for various metal amount (wt.%): **a** γ - Al_2O_3 , **x = b** 5%, **c** 7.5%, **d** 15%, and **e** 22.5%



The XRD patterns of the γ - Al_2O_3 support and the calcined xNi–Al catalysts were also obtained and are shown in Fig. 2. The diffraction peaks corresponding to NiO species were absent in all XRD patterns. In contrast, the diffraction peaks assigned to the NiAl_2O_4 phase were observed at $2\theta = 19.3^\circ, 37^\circ, 45.1^\circ,$ and 60.2° [8, 13]. The NiAl_2O_4 phase was present in all the calcined samples of Ni–Al, and the intensity of this peak increased with an increase in metal amount, indicating the increase in the degree of crystallinity of NiAl_2O_4 with an increase in loading [4]. The presence of NiAl_2O_4 is consistent with the UV–vis spectra results discussed above. Therefore, NiO interacts with γ - Al_2O_3 during calcination at 850°C to form NiAl_2O_4 , and the amount (DR–UV–vis) and crystallinity (XRD) of the aluminate increase with nickel loading.

The reduction profiles of catalysts calcined at 850°C show a single reduction peak between 800°C to 900°C for all catalysts. This single reduction peak was referred to as T_{max} and was attributed to the reduction of NiAl_2O_4 to metallic-Ni [13]. Further, the peak intensity increases with an increase in metal loading; the increase in intensity reflects the larger amount of NiAl_2O_4 undergoing reduction, as is expected from the other characterization studies. The metal-oxide reduction% for xNi–Al catalysts is given in Table 1. Increasing the nickel loading increases the percentage reduction of NiAl_2O_4 from 92.4% for the 5Ni–Al catalyst to 97.4% for the 15Ni–Al catalyst. However, with a further increase in the metal loading, metal-oxide reduction % slightly decreased to 94.3% for 22.5Ni–Al. The maximum of the major reduction peak (T_{max}) of xNi–Al are reported in Table 2. With an increase in the metal loading, the reduction peak initially shifted toward a lower temperature, reached the lowest temperature of 820°C for 15Ni–Al, and then shifted toward a higher temperature of 850°C for 22.5Ni–Al, indicating a decrease in the metal-support interaction with an increase in the loading up to 15 wt.% followed by an increase in the metal-support interaction in 22.5Ni–Al.

Table 2 Characterization information about the Ni-metal in the reduced xNi-Al catalyst (x = 5–22.5%)

xNi-Al x =	Reduction temperature (T _{max})	Crystallite size from XRD (nm)	Dispersion (%)
5	870	24.1	4.2
7.5	840	14.3	7.1
15	820	11.8	8.6
22.5	850	13.8	7.3

3.2 Characterization of Reduced Catalysts

The XRD patterns of reduced samples of xNi-Al (Fig. 3) show reflections corresponding to cubic Ni. The XRD pattern of γ -Al₂O₃ was also included for comparison. Peaks due to metallic-Ni appeared at $2\theta = 44.5^\circ$, 51.8° , and 76.2° [8, 13]. The formation of metallic-Ni by reducing the NiAl₂O₄ phase present in the calcined sample has been observed previously [13]. Based on the metallic-Ni peak at 51.8° , the crystallite size of the nickel was calculated and tabulated in Table 2. With an increase in the metal amount, the crystallite size of metallic-Ni decreased, reached a minimum for the 15Ni-Al catalyst, and then increased for the 22.5Ni-Al catalyst.

The dispersions (%) of Ni in different xNi-Al catalysts were measured from the XRD patterns of the catalysts reduced at their respective T_{max} temperatures as reported in Table 2. A comparison between the crystallite size and dispersion (%) revealed that they were inversely related. The dispersion increased with an increase in Ni loading, reached a maximum for the 15Ni-Al catalyst, and then decreased for higher loading of Ni. 15Ni-Al showed the highest dispersion of 8.6% due to the smallest crystallite size of metallic-Ni obtained in the 15Ni-Al catalyst. The variation of dispersion values with the metal amount implied the non-monotonic change in the number of surface Ni sites.

Fig. 3 XRD profile of reduced xNi-Al catalysts for various metal amount: **a** γ -Al₂O₃, x = **b** 5, **c** 7.5, **d** 15, and **e** 22.5

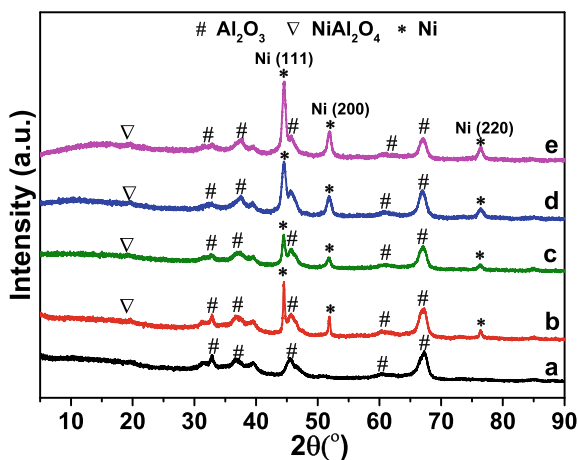


Table 3 Effect of metal amount on conversions, yields, and H₂/CO ratios for the TRM reaction. Reaction conditions: Molar feed ratio CH₄: CO₂: H₂O: O₂: N₂ = 1: 0.5: 0.5: 0.1: 14.6, pressure = 1 atm, temperature = 600 °C, and GHSV = 1,20,000 ml g⁻¹ h⁻¹. Data averaged over 4 h of TOS

xNi-Al x =	Conversion (%)		Yield (%)		H ₂ /CO ratio
	CH ₄	CO ₂	H ₂	CO	
5	70.5 ± 2.8	10.2 ± 1.9	71.4 ± 1.5	31.6 ± 2.4	3.8 ± 0.2
7.5	76.8 ± 1.5	15.9 ± 1.7	73.1 ± 2.6	37.7 ± 1.8	3.5 ± 0.1
15	82.4 ± 1.9	19.7 ± 2.1	78.6 ± 1.5	41.8 ± 2.9	3.2 ± 0.2
22.5	78.9 ± 1.4	16.8 ± 1.9	75.3 ± 1.8	41.4 ± 1.5	3.0 ± 0.1

3.3 Catalytic Performance

The effect of metal loading on the catalytic activity of Ni-Al₂O₃ catalysts was examined for TRM at 600 °C. The conversions, yields, and H₂/CO molar ratios of the TRM are reported in Table 3. At 600 °C, the equilibrium conversions of CH₄ and CO₂ for the given feed composition are 90.7% and 34.6%, respectively.

It was observed that the CH₄ and CO₂ conversions increased with an increase in the metal amount and were highest for 15Ni-Al and then decreased for 22.5Ni-Al. Thus, the optimum metal loading for the xNi-Al catalyst is 15 wt.%. Comparing the conversion data in Table 3 with the crystallite size data given in Table 2 revealed that the CH₄ and CO₂ conversions are inversely related to the crystallite size. The complete conversion of O₂ was achieved with all catalysts due to the O₂ affinity for the surface nickel sites [14]. The H₂ and CO yields, in general, followed similar trends in CH₄ and CO₂ conversions, both of which were directly related to the crystallite size. Furthermore, a H₂/CO ratio of > 3 was obtained for all the catalysts. However, the molar H₂/CO ratio decreased with an increase in the metal amount, and an optimum metal loading that maximizes the H₂/CO ratio is the catalyst with the lowest metal content.

The active metal dispersion increased with an increase in Ni amount from 5 wt.% to 15 wt.%. However, an additional increase in Ni content decreased the dispersion, as shown in Table 2. Consequently, the conversions and yields also increased, reached a maximum for 15Ni-Al, and then decreased. Earlier studies suggest that the catalytic performance depends on the active metal particle diameter, dispersion, reducibility, and metal-support interaction [4, 6, 13]. The present study shows that the changes in the activity of the xNi-Al catalysts are directly correlated with the number of surface Ni sites present. Among the four prepared catalysts, the superior activity of 15Ni-Al was attributed to the well-dispersed Ni-particles present in the catalysts.

In comparison, the optimum loading 5Ni-MgCeZr catalyst of Singha et al. [1], showed a CH₄ and CO₂ conversion of 70% and 3% and a H₂/CO ratio of ~2.3 at 600 °C using a GHSV of 20,000 ml g⁻¹ h⁻¹ and a molar feed ratio of CH₄: CO₂: H₂O: O₂: He = 1.0: 0.2: 0.4: 0.2: 3.6. The optimum loading 4.8Ni-ZrO₂ catalyst of Singha et al. [4], showed a CH₄ and CO₂ conversion of 38.2% and 31.4% and

a H₂/CO ratio of 2.1 at 600 °C using a GHSV of 80,000 ml g⁻¹ h⁻¹ and the same molar feed ratio of CH₄: CO₂: H₂O: O₂: He.

A higher or comparable CH₄ and CO₂ conversions and H₂/CO ratios were achieved with the optimum 15Ni-Al catalyst of the present study when compared with the other reported catalysts. However, the optimum 4.8Ni-ZrO₂ catalyst of Singha et al. [4] reveals higher CO₂ conversion at 600 °C than those reported in the present study. Specific catalyst properties have an influence on CO₂ conversions. For example, the use of supports with basic nature and high oxygen storage capacity facilitates CO₂ adsorption over the catalyst surface and enhances CO₂ conversion [1, 2, 4]. The combined effect of these factors appears to be the reason behind the high conversion of CO₂ for the 4.8Ni-ZrO₂ catalyst. Thus, the xNi-Al catalysts used in the present study need to be examined in more detail and suitably modified to further enhance their catalytic performance, especially with respect to CO₂ conversions.

4 Conclusion

The TRM reaction was studied over nickel-alumina catalysts containing 5, 7.5, 15, and 22.5 wt.% Ni. Characterization results revealed that with an increase in the metal amount, the crystallite size of metallic-Ni and metal-support interaction reached a minimum for the 15Ni-Al catalyst, and then increased for the 22.5Ni-Al catalyst. The active metal dispersion reached a maximum of 8.6% by increasing metal loading from 5 wt.% to 15 wt.%, then reduced by further increasing the metal loading to 22.5Ni-Al. The CH₄ and CO₂ conversions increased with an increase in the metal amount till 15 wt.% loading and then decreased for 22.5 wt.% loading. The H₂/CO ratio was greater than 3 for all catalysts and decreased with Ni loading. Unfortunately, only a few previous studies have addressed the optimum metal loading required for a series of catalysts containing the same support. The present investigation shows that loading of 15 wt.% Ni in the xNi-Al catalyst calcined at high temperatures provided the maximum conversions and yields for the TRM reaction. Thus, in the future, due importance should be given to determine the optimum metal loading for a series of catalysts containing the same support so that the most effective catalyst for the TRM can be developed.

References

1. Singha RK, Das S, Pandey M et al (2016) Ni nanocluster on modified CeO₂-ZrO₂ nanoporous composite for tri-reforming of methane. *Catal Sci Technol* 6:7122–7136. <https://doi.org/10.1039/c5cy01323b>
2. Song C, Pan W (2004) Tri-reforming of methane: a novel concept for catalytic production of industrially useful synthesis gas with desired H₂/CO ratios. *Catal Today* 98:463–484. <https://doi.org/10.1016/J.CATTOD.2004.09.054>

3. Jardine CN (2003) Environmental challenges and greenhouse gas control for fossil fuel utilization in the 21st century. In: Mercedes Maroto-Valer M, Song C, Soong Y (Eds) Kluwer Academic Publishers/Plenum Press, New York, 450 pp., Hardback, ISBN 0-306-47336-4. Environmental Science & Policy 6:395–396. [https://doi.org/10.1016/S1462-9011\(03\)00062-5](https://doi.org/10.1016/S1462-9011(03)00062-5)
4. Singha RK, Shukla A, Yadav A et al (2016) Energy efficient methane tri-reforming for synthesis gas production over highly coke resistant nanocrystalline Ni-ZrO₂ catalyst. Appl Energy 178:110–125. <https://doi.org/10.1016/j.apenergy.2016.06.043>
5. Pino L, Vita A, Cipiti F et al (2011) Hydrogen production by methane tri-reforming process over Ni-ceria catalysts: effect of La-doping. Appl Catal B 104:64–73. <https://doi.org/10.1016/j.apcatb.2011.02.027>
6. Rahbar Shamskar F, Rezaei M, Meshkani F (2017) The influence of Ni loading on the activity and coke formation of ultrasound-assisted co-precipitated Ni–Al₂O₃ nanocatalyst in dry reforming of methane. Int J Hydrogen Energy 42:4155–4164. <https://doi.org/10.1016/j.ijhydene.2016.11.067>
7. Rezaei M, Meshkani F, Ravandi AB et al (2011) Autothermal reforming of methane over Ni catalysts supported on nanocrystalline MgO with high surface area and plated-like shape. Int J Hydrogen Energy 36:11712–11717. <https://doi.org/10.1016/J.IJHYDENE.2011.06.056>
8. Chaudhary PK, Koshta N, Deo G (2020) Effect of O₂ and temperature on the catalytic performance of Ni/Al₂O₃ and Ni/MgAl₂O₄ for the dry reforming of methane (DRM). Int J Hydrogen Energy. <https://doi.org/10.1016/J.IJHYDENE.2019.12.053>
9. Sengupta S, Ray K, Deo G (2014) Effects of modifying Ni/Al₂O₃ catalyst with cobalt on the reforming of CH₄ with CO₂ and cracking of CH₄ reactions. Int J Hydrogen Energy 39:11462–11472. <https://doi.org/10.1016/J.IJHYDENE.2014.05.058>
10. Asencios YJO, Rodella CB, Assaf EM (2013) Oxidative reforming of model biogas over NiO–Y₂O₃–ZrO₂ catalysts. Appl Catal B 132–133:1–12. <https://doi.org/10.1016/J.APCATB.2012.10.032>
11. Bartholomew CH, Pannell RB (1980) The stoichiometry of hydrogen and carbon monoxide chemisorption on alumina- and silica-supported nickel. J Catal 65:390–401. [https://doi.org/10.1016/0021-9517\(80\)90316-4](https://doi.org/10.1016/0021-9517(80)90316-4)
12. Asencios YJO, Assaf EM (2013) Combination of dry reforming and partial oxidation of methane on NiO–MgO–ZrO₂ catalyst: effect of nickel content. Fuel Process Technol 106:247–252. <https://doi.org/10.1016/J.FUPROC.2012.08.004>
13. Kumar R, Kumar K, Pant KK, Choudary NV (2019) Tuning the metal-support interaction of methane tri-reforming catalysts for industrial flue gas utilization. Int J Hydrogen Energy. <https://doi.org/10.1016/j.ijhydene.2019.11.111>
14. Walker DM, Pettit SL, Wolan JT, Kuhn JN (2012) Synthesis gas production to desired hydrogen to carbon monoxide ratios by tri-reforming of methane using Ni–MgO–(Ce, Zr)₂O₃ catalysts. Appl Catal A 445–446:61–68. <https://doi.org/10.1016/J.APCATA.2012.08.015>

Preparation of SiC from Rice Husk: Past, Present, and Future



Saroj Kumar Singh, Sudarsan Raj, and Debiduta Debasish

1 Introduction

At present, rice husk is generated in million tonnes per year by milling of paddy. The rice husk is always considered an agricultural waste which is primarily utilized in combustion as a source of heat energy for producing par boiled rice. Rice husk usually contains around 20% ash with 92% to 95% porous and high surface area silica [1]. Burning of rice husk can be dangerous as it contains silica which is very fine and can affect the atmosphere thereby causing health hazards. Hence, burning in open air is not at all suitable and this leads to the accumulation of a huge amount of husk on the roadside which causes soil pollution.

Silicon carbide (SiC) is widely known for its high strength, hardness, stiffness, good wear, corrosion resistance, high thermal conductivity, low thermal expansion, and high thermal shock resistance. SiC is commercially produced by the Acheson process, where carbothermal reduction of quartz (silica) by petroleum coke (carbon) is carried out. The formation of silicon carbide is associated with large agglomerates of different sizes. This SiC is not suitable for advanced ceramic applications.

The main problems of the Acheson process are the particle size of the reactants and the need for an intimate contact among them. In an attempt to resolve these problems, attention has been paid to the use of alternative starting materials for the production of SiC. The intimate mixture of SiO₂ and C in the rice husk provides an ideal platform for SiC synthesis. Since the pioneering work of Lee and Cutler [2, 3], many studies have been reported on the preparation of SiC from rice husk [4–11].

In a novel approach, one of the authors produced fine and ultrafine SiC from rice husk using thermal plasma [6–11], an advanced ceramic material. The plasma produced SiC, after suitable processing, was further used as nano-fluids [12], applied

S. K. Singh (✉) · S. Raj · D. Debasish
CSIR-IMMT, Bhubaneswar, Odisha 751013, India
e-mail: sarojksingh@gmail.com

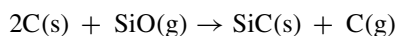
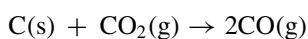
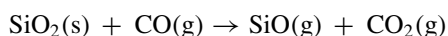
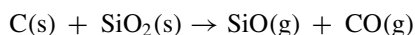
in catalysis [13–17], polymer-SiC composites [18], and the development of SiC magnetic materials [19–22].

However, there are specific problems that still exist in the preparation of silicon carbide from rice husk. The considerable amount of volatiles present in the rice husk has not been utilized by any of the methods including our own method mentioned above. The silicon carbide made from rice husk is usually a mixture of silicon carbide powder/whisker, free carbon, and unreacted silica. The free carbon (in the form of fine and nano graphite/graphene) and fine silica need to be recovered as valuable by-products to make the process attractive.

The present manuscript compares the work carried out in the past and suggests a few solutions to overcome the associated problems for preparing silicon carbide from rice husk in the future. The main objective here is to bring out a possible solution where the volatiles, free carbon, and unreacted silica are present during the processing of rice husk for silicon carbide production.

2 Comparison of Different Methods for the Preparation of SiC

Both Acheson process and rice husk process follow the carbothermal reduction of silica with carbon. The reaction mechanism may follow a multi-step reaction as given below [23].



resulting in the overall reaction.

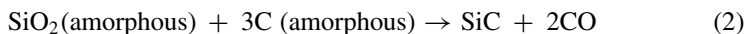


To make the process efficient, the following points need to be considered:

1. Particle size of the reactants: Smaller particle size of the reactants reduces the reaction time thereby increasing the yield.
2. Processing temperature: Higher temperature decreases the reaction time.

Rice husk mainly contains silica in hydrated amorphous form and cellulose. Thermal treatment of rice husk mainly results in a by-product that mainly contains

silica and carbon with a high surface area. In case of rice husk, Eq. (1) may be written as [23]



Consequently, the formation of silicon carbide occurs at a lower temperature range (1200–1500 °C) in case of rice husk as compared to the reactions (1200–2000 °C) between quartz and petroleum coke in case of the Acheson process [5].

2.1 *The Conventional Process of Processing Rice Husk*

In the conventional process [1–5] of producing silicon carbide from rice husk where rice husk is kept in a pot and energy in the form of heat or any other form is provided from outside. Since the raw rice husk is a thermally insulating material, the process becomes inefficient and requires a long processing time. In certain cases, high vacuum has been employed to reduce the reaction time. All these processes are batch processes, and only a small quantity of mater is processed. Employing high vacuum increases the processing cost.

2.2 *Thermal Plasma Process*

A single step was adopted to prepare SiC directly from raw rice husk in an indigenously developed pot-type extended arc plasma reactor using graphite electrodes. The details of the experimental conditions and characterization of the products are described elsewhere [6, 23]. However, the plasma processing and results are briefly described here for a better understanding of the process. The bottom electrode comprises of the graphite crucible containing the charge. There is an axial hole in the top electrode which is made of graphite in order to pass the plasmagen gas into the crucible. The arc was generated subsequently by vertical movement of the top electrode into the crucible. Experiments were carried out in batch operations and experimental conditions such as power and time were varied. The plasma treated sample was found to be fragile in nature, and thus could easily be ground. The plasma-produced powder was further heat treated at 800 °C for 2 h to remove excess carbon and subsequently acid leached with HF to remove unreacted silica. The process flow sheet is depicted below (Fig. 1).

Formation of beta-Silicon carbide could be established by the appearance of green colour just after 5 min of synthesis. It has been seen that the reaction is more or less complete around 20 min of plasma operation. The particle size of the powder is found to be in the micron range from the SEM studies. By suitably grinding the plasma-synthesized powder, the particle size could be reduced to a few nanometres (Figs. 2 and 3).

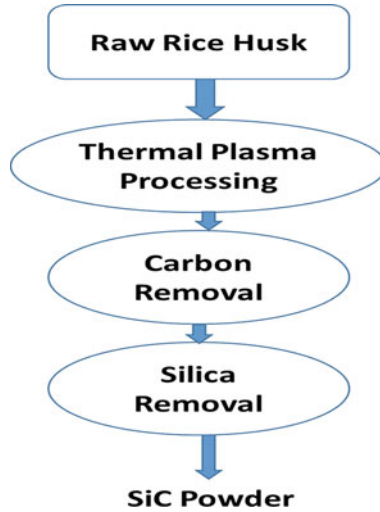


Fig. 1 Flow sheet of the process

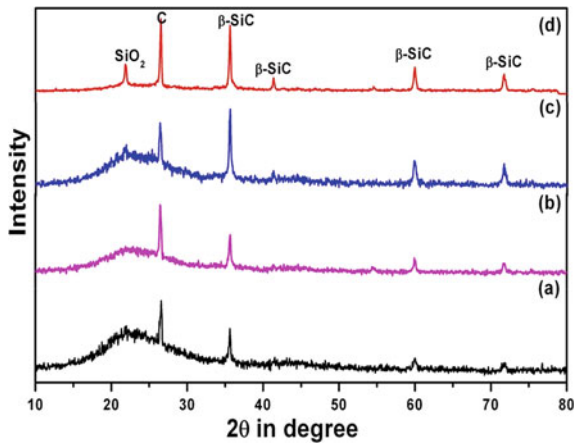


Fig. 2 Comparison of XRD peaks of plasma-treated rice husk at various time intervals of processing—a 5 min, b 10 min, c 15 min, d 20 min [23]

2.3 Comparison of Thermal Plasma Process and Conventional Process for Rice Husk Processing

Figure 4 shows the schematic of the conventional and thermal plasma process. The disadvantage of rice husk being thermally insulating material becomes advantageous in case of thermal plasma process as depicted in Fig. 4. The heat is retained here. High temperature ($\sim 10^4$ K) associated with thermal plasma induces a fast reaction

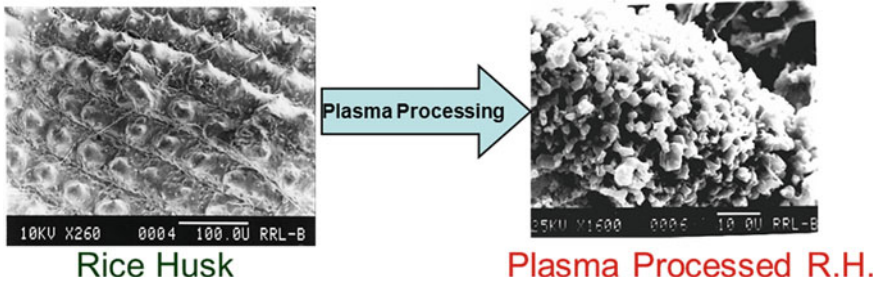


Fig. 3 SEM micrograph of the outer surface of the raw rice husk and plasma-produced powder [23]

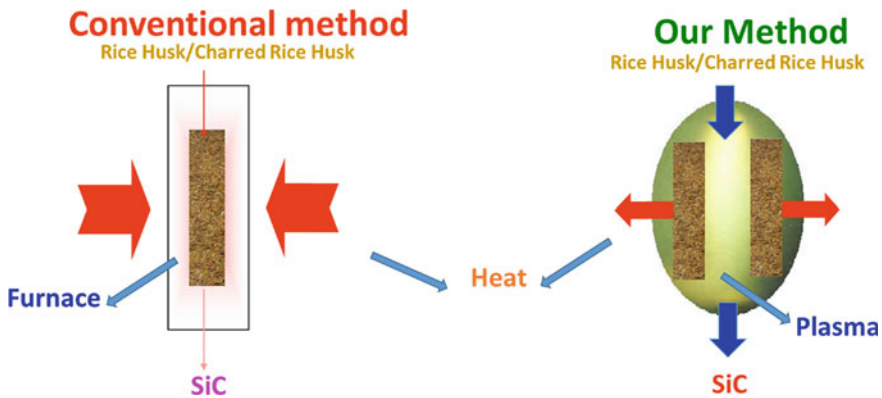


Fig. 4 Schematic of conventional and thermal plasma process for rice husk processing

[23]. Suitably designing the reactor, the rice husk can be processed in a continuous manner.

However, the plasma reactors using conventional DC and RF torches are expensive. In our case, the plasma setup is considerably cheaper as we are using graphite electrodes (top electrode and crucible) and the plasma processing is carried out in transferred arc mode. Since the rice husk process is a carbothermal process, contamination from the electrodes is not a problem here. We also do not require any vacuum in our system.

The plasma-processed rice husk primarily contains SiC with some unreacted SiO₂ and free C. The powder was oxidized to remove free carbon. The removal of silica was affected by treatment with HF.

The problem associated with the above work is as follows:

1. Raw rice husk contains 50–60% volatiles.
2. The free carbon is removed by oxidation.
3. The unreacted SiO₂ is removed by HF leaching.

The possible solutions are the following:

1. The volatiles may be treated appropriately to generate energy. It has been possible to generate energy even hydrogen by gasification of rice husk [24–26]. However, no attempt has been made so far to integrate this approach with silicon carbide preparation of rice husk.
2. The free carbon may be separated by adopting froth flotation or any other suitable technique to obtain extremely fine carbon particles in the form of nano graphite or graphene, a valuable product. Previously, the main objective was to recover silicon carbide from processed rice husk [27] by flotation technique. In our earlier work, we observed the presence of fine graphite/graphene along with the SiC [28]. However, the recovery of graphite/graphene was never considered seriously.
3. Nano silica has been produced by the chemical treatment of rice husk by NaOH [29, 30]. Instead of using HF, NaOH may be used to remove unreacted SiO₂ in the form of nano-silica in the plasma-processed rice husk.

In this way, three valuable products, namely fine SiC, C, and nano SiO₂ will be obtained from agricultural waste. The proposed flow sheet is depicted in Fig. 5.

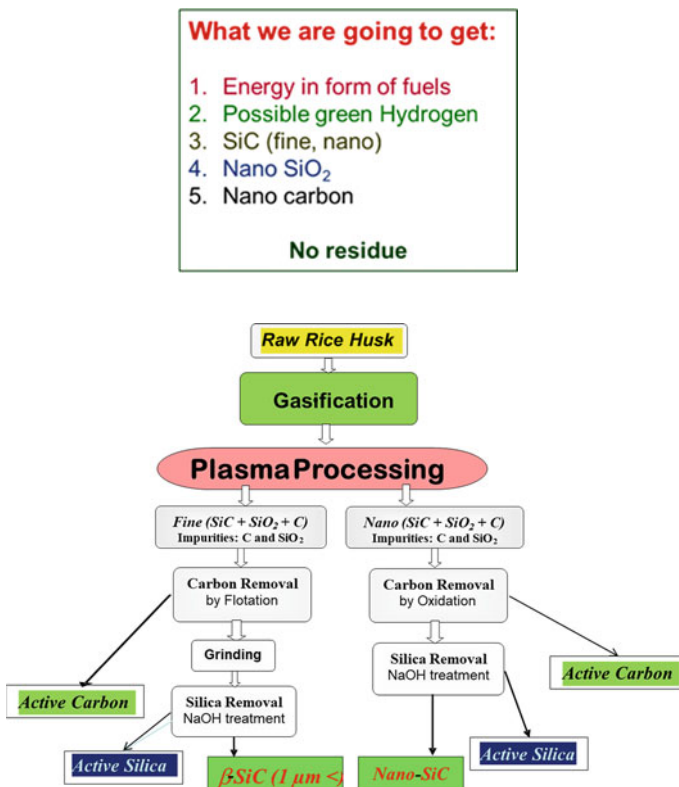


Fig. 5 Flow diagram of the proposed process

3 Conclusion

Silicon carbide has been produced by thermal plasma from rice husk in a very short time period. The process can be upgraded to operate in a continuous manner. Once the appropriate techniques as proposed are adopted, energy, nano-silica and carbon (graphite or graphene) may also be produced. Capturing the energy in form of fuel gas is a promising area that has immense applications. The carbon nanoparticles have very good application in the area of biomedical sciences. It can act as biosensors in biomedical imaging as well as in cancer therapy. Silicon carbide, nano-silica have applications in various automobile, steel, abrasive sectors, etc. Utilization of agricultural waste for value-added products can be achieved through various routes of processing.

Acknowledgements The authors would like to acknowledge the Ministry of Steel, New Delhi for funding this work through a Grant-In-Aid Project bearing No. GAP-339.

References

1. Jongpradist P, Kongkitkul W, Sukkarak R, Kongkitkul W, Jamsawang P (2018) Efficiency of rice husk ash as cementitious material in high-strength cement-admixed clay. *Adv Civil Eng* 4:1–11
2. Cutler IB (1973) Production of silicon carbide from rice hulls, US patent no. 3,754,076
3. Lee JG, Cutler IB (1975) Formation of silicon carbide from rice hulls. *Am Ceram Soc Bull* 54(2):195–198
4. Sun L, Gong K (2001) Silicon-based materials from rice husks and their applications. *Ind Eng Chem Res* 40:5861–5877
5. Pereira MLG, Figueira DSS, Girolamo BR, Vernilli F (2020) Synthesis of silicon carbide from rice husk. *Cerâmica* 66:256–261
6. Singh SK, Basu S, Mohanty BC. An improved process for the production of silicon carbide from rice husk, Indian Patent No. IN242140-B
7. Singh SK, Sahu AK. A method for production of fine and ultra-fine powders of electrically conducting and non-conducting precursor materials and equipment. Indian Patent No. IN262343
8. Singh SK, Stachowicz L, Girshick SL, Pfender E (1993) Thermal plasma synthesis of SiC from rice hull (husk). *J Mater Sci Lett* 12:659–660
9. Stachowicz L, Singh SK, Pfender E, Girshick SL (1993) Synthesis of ultrafine SiC from rice hull (husk) a plasma process. *Plasma Chem Plasma Process* 13:447–461
10. Singh SK, Mohanty BC, Basu S (2002) Synthesis of SiC from rice husk in a plasma reactor. *Bull Mater Sci* 25:561–563
11. Nayak BB, Mohanty BC, Singh SK (1996) Synthesis of silicon carbide from rice husk in a dc arc plasma reactor. *J Am Ceram Soc* 79(5):1197–1200
12. Manna O, Singh SK, Paul G (2012) Enhanced thermal conductivity of nano-SiC dispersed water based nanofluid. *Bull Mater Sci* 35(5):707–712
13. Singh SK, Parida KM, Mohanty BC, Rao SB (1995) High surface area silicon carbide from rice husk: a support material for catalysts. *React Kinet Catal Lett* 54:29–34
14. Mishra G, Behera GC, Singh SK, Parida KM (2012) Liquid phase esterification of acetic acid over WO₃ promoted β -SiC in a solvent free system. *Dalton Trans* 41:14299–14308

15. Mishra G, Parida KM, Singh SK (2014) Solar light driven Rhodamine B degradation over highly active β -SiC-TiO₂ nanocomposite. *RSC Adv* 01(4):12918–12928
16. Mishra G, Parida KM, Singh SK (2015) Facile fabrication of S-TiO₂/ β -SiC nanocomposite photocatalyst for hydrogen evolution under visible light irradiation, *ACS Sustain Chem Eng* 3:245–253
17. Mishra G, Behera GC, Singh SK, Parida KM (2020) Facile synthesis and synergetic interaction of VPO/ β -SiC composites toward solvent-free oxidation of methanol to formaldehyde. *ACS Omega* 5:22808–22815
18. Satapathy A, Jha AK, Mantry S, Singh SK, Patnaik A (2010) Processing and characterization of jute-epoxy composites reinforced with SiC derived from rice husk. *J Reinf Plast Compos* 29(18):2869–2878
19. Moharana GP, Kothari R, Narayanan HK, Singh SK (2019) Role of spin, phonon and plasmon dynamics on ferromagnetism in Cr doped 3C-SiC. *J Magn Magn Mater* 491:165505
20. Moharana GP, Singh SK, Babu PD, Narayanan HK (2018) Investigation of magnetic order and spin dynamics in Mn doped 3C-SiC. Investigation of magnetic order and spin dynamics in Mn doped 3C-SiC. *J Alloy Compd* 765:314–323
21. Moharana GP, Kothari R, Narayanan HK, Singh SK (2021) Ferromagnetism in Mn doped 3C-SiC: a variable temperature ESR study. *J Magn Magn Mater* 527:167707
22. Moharana GP, Kothari R, Singh SK, Babu PD, Narayanan HK (2022) F⁺ center exchange mechanism and magnetocrystalline anisotropy in Ni-doped 3C-SiC. *J Magn Magn Mater* 555:169358
23. Singh SK (2003) Thermal plasma synthesis of SiC powder and characterization. PhD thesis, IIT, Kharagpur
24. Li Z, Jiang E, Xu X, Sun Y, Wu Z (2017) The complete utilization of rice husk for production of synthesis gas. *RSC Adv* 7:33532–33543
25. Aytenuw G, Nigus G, Bedewi B (2018) Improvement of the energy density of rice husk using dry and chemical treated torrefaction. *Adv Chem Eng* 8(1):1000185
26. Xu X, Li Z, Tu R, Sun Y, Jiang E (2018) Hydrogen from rice husk pyrolysis volatiles via non-noble Ni-Fe catalysts supported on five differently treated rice husk pyrolysis carbon supports. *ACS Sustain Chem Eng* 6(7):8325–8339
27. Singh SK, Biswal SK, Mohanty BC (1995) Recovery of fine sized silicon carbide from plasma treated rice husk. In: Mehrotra SP, Sankar R (ed) *Mineral processing: recent advances and future trends*. Allied Publishers Ltd. pp 834–836. (International Conference on Mineral Processing: Recent Advances and Future Trends, Dec 11–15, 1995)
28. Gorzkowski EP, Qadri SB, Rath BB, Singh SK (2011) Nano-dimensional structures of 3C-SiC formed from rice husk. In: 2011 international semiconductor device research symposium (ISDRS). <https://doi.org/10.1109/isdrs.2011.6135304>
29. Yuvakkumar R, Elango V, Rajendran V, Kannan N (2014) High-purity nano silica powder from rice husk using a simple chemical method. *J Exp Nanosci* 9(3):272–281
30. Guo W, Li G, Zheng Y, Li K (2021) Nano-silica extracted from rice husk and its application in acetic acid steam reforming. *RSC Adv* 11:34915–34922

Synthesis and Characterization of a Novel Nanocarbon Derived Nanoporous Al₂O₃ Powder as a Potential Adsorbent for Treatment of Wastewater



K. Sarath Chandra, D. Suharika, Debasish Sarkar, G. V. S. Sarma, and K. V. Ramesh

1 Introduction

There is no need to emphasize the acute hazardous effects of pollutants on human health. There are ample cases reported globally in this regard [1]. It is widely established that the adsorption technique would be both effective and economical in treating polluted wastewaters [2]. In this regard, scientists worldwide employed both natural and synthetic materials as adsorbents, and to realize better removal efficiencies, these materials were also subjected to different combinations of physical, thermal as well as chemical treatments [3–8]. However, to facilitate successful industrial adoption, adsorbents with better removal efficiencies should be developed. It is well-established in the ceramic literature that the nanostructured porosity features of alumina adsorbent powder particles play a predominant role in improving the adsorption capacity [9]. So, to gain the enhanced adsorption capacity, the current study uses 32 nm size nanocarbon powder particles as a pore-forming agent to create the nanostructured porosity in all parts of the in-house synthesized alumina adsorbent powder particles.

K. S. Chandra · D. Sarkar
Laboratory for Materials Processing and Engineering, Department of Ceramic Engineering, NIT,
Rourkela, Odisha, India

D. Suharika · G. V. S. Sarma (✉) · K. V. Ramesh
Department of Chemical Engineering, Andhra University, Visakhapatnam, India
e-mail: gvssarma@gmail.com

D. Sarkar
Center for Nanomaterials, National Institute of Technology, Rourkela, Odisha, India

2 Material and Methods

2.1 Adsorbent Synthesis

A facile chemical precipitation synthesis route was used for the bulk-scale preparation of nanoporous alumina adsorbent powders with nanocarbon as the pore-forming additive. High-purity commercially available $\text{Al}(\text{NO}_3)_3 \cdot 9\text{H}_2\text{O}$ (Rankem chemicals, 99% purity), NH_4HCO_3 (Rankem chemicals, 99% purity), NH_4OH (Rankem chemicals), and nanocarbon powder (Birla Carbon, N220, 98% Fixed Carbon, Particle size ~ 2 nm) were taken as the starting materials. A stock solution of 0.15 M $\text{Al}(\text{NO}_3)_3 \cdot 9\text{H}_2\text{O}$ was prepared in distilled water. An ultrasonicated dispersion of nanocarbon particles (pore-former) was prepared in alcoholic media. The amount of nanocarbon was 5000 ppm. Reverse-strike chemical precipitation was performed by the simultaneous addition of metal nitrate solution as well as nanocarbon dispersion to the NH_4HCO_3 (3 M) precipitant solution. During the precipitation process, 0.3 g of ammonia water (2 M NH_4OH) was added to maintain the pH of the reaction system between 9 and 9.5. The aging period was 30 min. The nanocarbon loaded alumina precursor particles were collected from the precipitant solution and washed in distilled water using a research centrifuge (Sigma 3k15, Germany). These washed powder particles were dried under a heat lamp overnight. It can be noted that the dried precursor particles were of amorphous nature.

2.2 Adsorbent Characterization

The morphology, as well as composition details of alumina adsorbent powder loaded with and without nanocarbon, were studied with scanning electron microscopy (Nova NanoSEM 450, FEI Make). The crystallography features were determined by X-ray diffraction. The diffractograms were recorded with the use of a Rigaku X-ray diffractometer equipped with Copper (Cu) target ($\lambda_{\text{Cu-K}\alpha} \sim 1.54 \text{ \AA}$). The scanning range (2θ) was $20\text{--}60^\circ$. The scan rate was $10^\circ \text{ min}^{-1}$. The crystallite size (τ) was estimated for the diffraction peaks corresponding to (104), (113), and (116) family of planes of α -alumina by the application of X-ray line broadening technique using Scherrer's formula, which is given as

$$\tau = \frac{0.89\lambda}{B \cos\theta} \quad (1)$$

where B is known as full-width at half maximum (FWHM) and θ as Bragg angle. The surface area, as well as porosity characteristics, were measured from N_2 sorption isotherms of alumina adsorbent powders. It can be noted that the N_2 adsorption-desorption isotherms were recorded using a surface area analyzer (Autosorb x 1, Quantachrome) at 77 K in the relative pressure (P/P_0) range between 0.05 and 0.99.

The degassing temperature was 200 °C. The specific surface area was estimated with the application of the BET (Brunauer–Emmet–Teller) model. From the BET specific surface area measurements (S_{BET}), the average particle size (a) of alumina adsorbent powder was estimated as per the given formula [10].

$$a = \frac{6}{\rho S_{BET}} \quad (2)$$

where ρ is known as the theoretical density of α -alumina (3.98 g cm⁻³). The average pore size was computed by the application of the Barret–Joyner–Halenda (BJH) model.

3 Results and Discussions

3.1 Adsorbent Synthesis

The nanocarbon powder (pore-forming additive) was constituted with ~32 nm sized amorphous carbon particles. These nanocarbon particles were homogeneously distributed throughout the chemically precipitated alumina adsorbent precursor powder, as can be seen from its low-resolution SEM–EDX composition map (cf. Fig. 1). The nanocarbon loaded alumina adsorbent precursor powder particles were calcined at 1000 °C for 1 h in air. The calcined adsorbent particles, however, were pure phase alumina powders with a significant amount of open porosity, as can be seen from the low-resolution SEM image (cf. Fig. 2a). The localized microstructures (as seen as high-resolution images, cf. Fig. 2b–g) indicated that such class of open porosity was constituted by inter- as well as intra-particulate pores, which were created in each and every portion of alumina adsorbent particle surfaces due to oxidative loss of nanosized carbon during the various stages of calcination in oxygen-containing air atmosphere. The intra-particulate porosity (identified as white colored arrows, cf. Fig. 2b–g) was composed of a combination of lenticular/spherical-shaped isolated pores with sizes ranging from 10–50 nm. The inter-particulate porosity (identified as yellow-colored arrows, cf. Fig. 2b–g) was constituted predominantly of slit-shaped interconnecting pores with sizes ranging from 100–300 nm. Such features of spherical shaped isolated/intra-particulate porosity (spot ‘X’), as well as slit shaped interconnecting/inter-particulate porosity (spot ‘Y’), in almost all surface portions of the alumina adsorbent particles, can be further evidenced from the localized SEM–EDX microstructure map (cf. Fig. 3). The powder adsorbent morphology can be best described as a collection of hierarchically distributed wider-sized spherical/lenticular shaped intra-particulate (isolated) pores as well as slit shaped inter-particulate (inter-connecting) pores in such a way as a continuous integrated pore network in all surface portions of the alumina powder particles. It is observed that the diffraction peak positions (2θ) and the corresponding intensity (I) values are consistent with the JCPDS

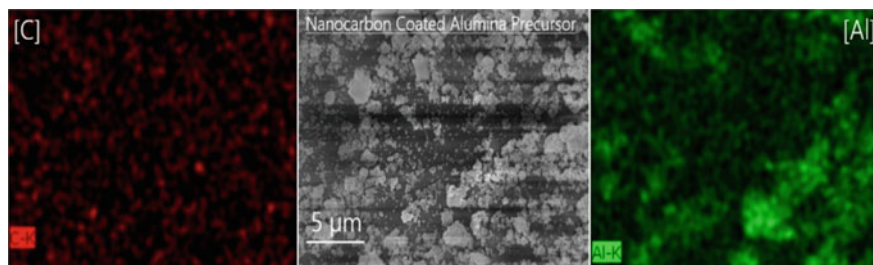


Fig. 1 SEM–EDX composition map showing the homogeneous distribution of nanocarbon (as seen in red color) in all parts of the chemically precipitated alumina precursor

Card file no. 10–0473, corroborating that the chemical precipitation route produces pure phase α -alumina (Al_2O_3) adsorbent powders (cf. Fig. 4). The calculations based on Scherrer's formula (cf. Eq. 1) indicated that the crystallite size (τ) was 50 nm. N_2 sorption isotherms showed a visible area of hysteresis between both adsorption and desorption branches, indicating that the adsorbent powder particles have a significant amount of mesoporosity (cf. Fig. 5). The BET specific surface area of the alumina adsorbent powder was $10 \text{ m}^2 \text{ g}^{-1}$. The average particle size (a) calculated based on the surface area measurements (cf. Eq. 2) was 150 nm, which is almost three times the estimated crystallite size of the alumina adsorbent. This feature characterizes that the synthesized alumina adsorbent powders were with soft agglomerated morphology, which is in agreement with the SEM images. The calculations based on BJH pore model indicated that the average pore size of the alumina adsorbent powder was 30 nm. Analysis based on the various nanometric characteristic features of the adsorbent morphology indicated that the nanocarbon derived alumina is a nanoporous powder adsorbent. It is anticipated that such a class of nanostructured porous surfaces drive fast mass transfer kinetics, which may directly result in significant enhancement of adsorption capacity for nanocarbon derived nanoporous alumina adsorbent prepared in-house than many of the commercially available alumina-based powder adsorbents.

Few works [11] were reported in the literature on the successful application of alumina as an adsorbent for the treatment of wastewaters. The alumina synthesized in the present study is utilized as an adsorbent in some preliminary experiments from which it was found that this synthesized alumina would have potential applications as an adsorbent, especially in wastewater treatment. The present article is limited to the synthesis of alumina only. However, a systematic study on the application of alumina to adsorption will be taken up in near future.

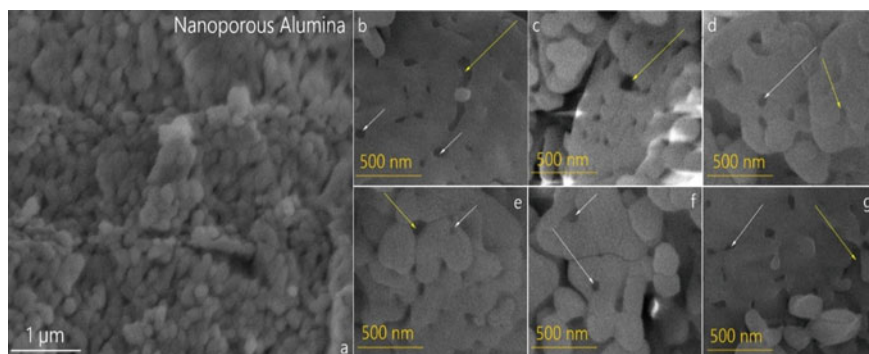


Fig. 2 Scanning electron microscopy of nanoporous alumina adsorbent. **a** Low-resolution image showing the alumina adsorbent particles with a significant amount of open porosity generated from the oxidative loss of nanocarbon in an oxygen-containing air atmosphere during calcination. **b–g** High-resolution images indicating the appearance of intra-particulate porosity as lenticular/spherical shaped isolated pores (as seen as white color) and inter-particulate porosity as slit shaped interconnecting pores (as seen as yellow color) in almost all surface portions of the alumina adsorbent particles

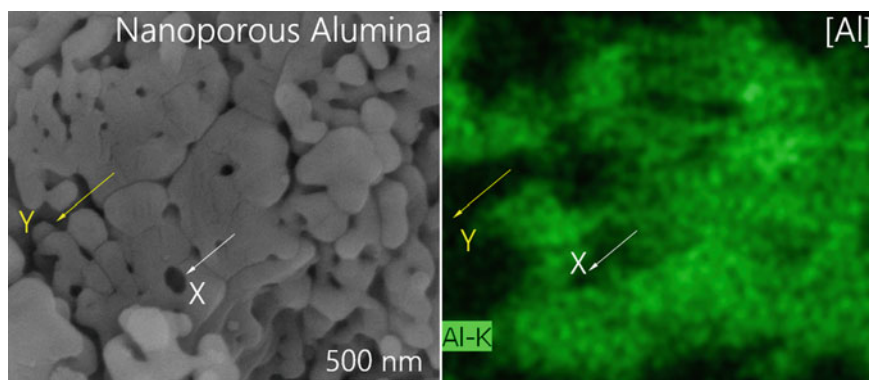


Fig. 3 SEM–EDX microstructure map indicating the intra-particulate/isolated porosity (spot ‘X’) as well as inter-particulate/interconnecting porosity (spot ‘Y’) in almost all surface portions of the alumina adsorbent powder particles

4 Conclusions

A novel alumina adsorbent has been synthesized in the present work. Since adsorption is highly dependent on the porosity of the adsorbent, the alumina was loaded with nano carbon powder and was subjected to calcination at a temperature of 1000 °C for a duration of one hour. The powder that resulted has been characterized for its morphology and crystallography using SEM–EDX and X-ray diffraction techniques.

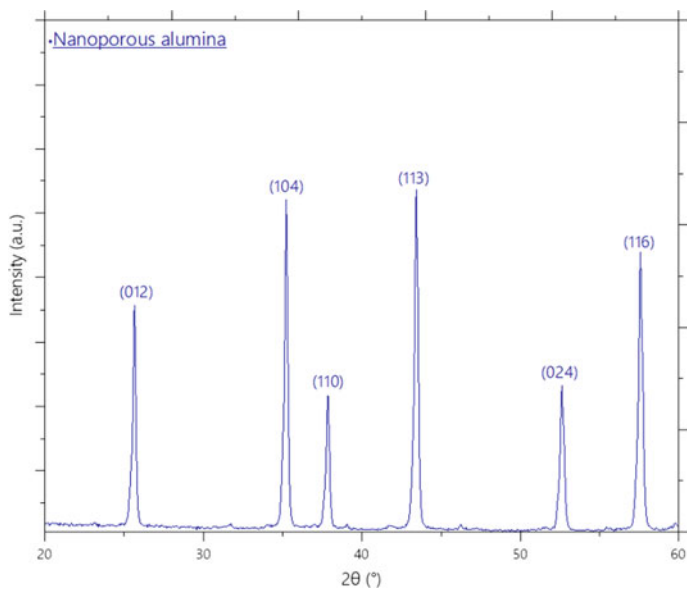


Fig. 4 X-ray diffraction pattern of nanoporous alumina

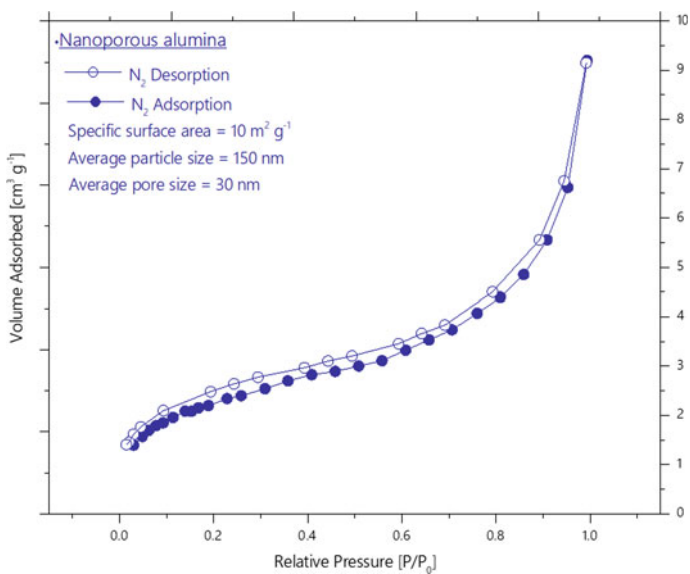


Fig. 5 N₂ adsorption and desorption isotherms of nanoporous alumina at 77 K

The porosity was determined by BET and BJH methods. It was found that the alumina thus synthesized has the potential to be an efficient adsorbent for treating wastewaters.

References

1. Ramesh KV, Sasibhushan B, Gouru Naidu K, Mohan Kumar S (2011) The renal failure in Uddanam region of Srikakulam district, Andhra Pradesh: areas identified for further investigations. *IUP J Chem Eng* 3(2):68–71
2. Fu F, Want Q (2011) Removal of heavy metal ions from waste waters: a review. *J Environ Manag* 92:407–418
3. Sudha Rani K, Ashok Kumar K, Gouru Naidu K, Ramesh KV (2016) Removal of phosphate ions from water by using paper pulp as an adsorbent. *Pollut Res* 35(4):757–763
4. Sudha Rani K, Srinivas B, Gouru Naidu K, Ramesh KV (2018) Removal of copper by adsorption on treated laterite. *Mater Today: Proc* 5:463–469
5. Sudha Rani K, Sarma GVS, Gouru Naidu K, Ramesh KV (2019) Adsorptive removal of chromium by modified laterite. *Mater Today: Proc* 18(7):4882–4892
6. Sudha Rani K, Sarma GVS, Gouru Naidu K, Ramesh KV (2020) Modified laterite adsorbent for cadmium removal from waste water. *J Inst Eng (India) Series D* 101(2):197–203
7. Sarma GVS, Sudha Rani K, Sarath Chandra K, Kishore Babu B, Ramesh KV (2020) Potential removal of phenol using modified laterite adsorbent. *Indian J Biochem Biophys* 57(5):613–619
8. Rohini Kumar P, Sarath Chandra K, Durga Prasad C, Ramesh KV (2021) Removal of fluorides from ground waters of coastal Andhra Pradesh in a fixed bed column by using alumina loaded nanoporous Mn-Ce oxide powder adsorbent. *Mater Today Proc* 46(P1):198–201
9. Suharika D (2019) Synthesis, characterization and application of α -Al₂O₃. M.Tech dissertation, Andhra University, Visakhapatnam, India
10. Sarath Chandra K, Sarkar D (2021) Oxidation resistance, residual strength, and microstructural evolution in Al₂O₃-MgO-C refractory composites with YAG nanopowder. *J Eur Ceram Soc* 41(6):3782–3797
11. Barbara KH (2004) Chemistry of alumina, reactions in aqueous solution and its application in water treatment—A review. *Adv Colloid Interf Sci* 111(1–2):19–47

Rice Husk-Derived Silica Nanoparticles Using Optimized Titrant Concentration for the One-Step Nanofluid Preparation



Prashant Kumar and Sudipto Chakraborty

1 Introduction

Rice, a prime staple for half of the world population, contributes to agricultural waste generation during paddy processing to rice; about 20% of paddy weight forms agricultural by-product—rice husk (RH) [1]. Over the years, RH has found numerous applications; in addition to cattle feeding, energy generation, landfills, and conventional usage, the scientific usage of silica has emerged. Most organic fiber contains cellulose, lignin, hemicellulose, lignin, and silica [2]; however, owing to the enormity of RH during milling, its proper utilization can reduce environmental pollution and result in value generation from waste. RH constituents have about 20% silica, which has found applications in various fields such as catalyst support, dental filler, cement additives, plastic fillers, waste-water treatment, solar cells, nano-medicine, CO₂ capture, semiconductor industry, composites, anti-corrosive agents, photo-catalyst, rubber compounding, cosmetics, thin-film coating, and nanofluid, usage depicted in Fig. 1. However, silica application as nanofluid in heat transfer is comparatively new, which is used in fields like micro-channel [3], heat exchangers [4], heat sinks [5], solar collectors [6], etc. The nano-silica economical and bulk synthesis ease can suit heat transfer applications when an enormous nanofluid is required, in applications such as ultrafast cooling in steel processing [7].

Interestingly, naturally occurring silica in RH is present uniformly over kernel microstructure matrix [8]; this crystalline inbound silica in RH, upon processing and chemical treatment, changes to an amorphous state, a reactive form of silica. Although silica has limited solubility; however, sonication [9] and further stabilizer

P. Kumar · S. Chakraborty (✉)
Department of Chemical Engineering, Indian Institute of Technology Kharagpur,
Kharagpur 721302, India
e-mail: sc@che.iitkgp.ac.in

Fig. 1 Diverse uses of silica in numerous fields

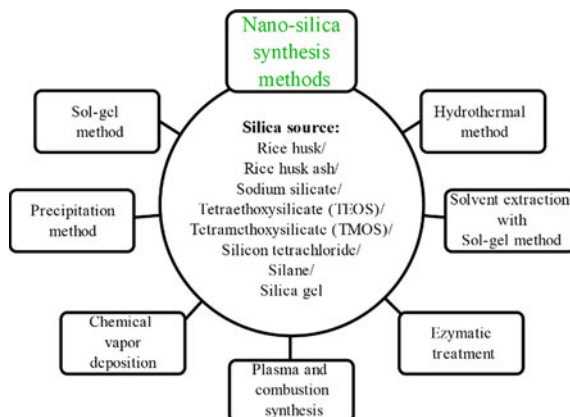


inclusion [10] can increase the suspension stability. Silica also has moderate thermal conductivity, depicting temperature dependency [11].

Over the years, various nano-silica synthesis methods have been developed, such as the sol–gel method [12], precipitation method [13], chemical vapor deposition [14], plasma and combustion method [15], enzymatic treatment method [16], solvent extraction based sol–gel method [12], the hydrothermal method [17], shown schematically with various precursors in Fig. 2. Among all nano-silica preparation methods, the sol–gel method is the most prevalent and economical; therefore, this method has received tremendous attention. During the nano-silica preparation with the sol–gel method, the optimum base concentration in the sol step is established in the literature [18]; however, the optimum acid concentration required in the gel step remains a new research domain. The acid concentration optimization can serve two purposes: establish the least-titrant concentration needed for gel formation and minimize the water usage involved in the gel-washing stage.

In the current work, incorporated novelties are optimized titrant concentration usage in the gel formation step, followed by silica nanofluid preparation using the one-step method. The silica nanoparticle prepared via the sol–gel method is characterized using FTIR, XRD, FESEM, XRF, and EDS techniques. The nanofluid is characterized visually through settling and Tyndall effect observation. Moreover, thermophysical properties, particle size distribution, and stability of nanofluid are determined.

Fig. 2 Nano-silica synthesis methods



2 Materials and Methods

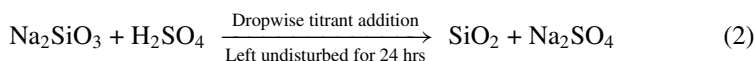
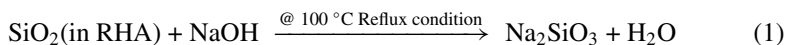
2.1 Materials

The RH was procured from a local rice mill. For nano-silica extraction from RHA, emplura grade sodium hydroxide pellets (NaOH), sulfuric acid (H_2SO_4), and emparta grade hydrochloric acid (HCl) were obtained from Merck. Deionized water (DIW) has been used throughout the nanoparticle and nanofluid preparation stages.

2.2 Method

In SiO_2 nanoparticle preparation, RH as the silica precursor in the Sol-gel method was employed, following the method reported in the literature [11], with slight modification as RH pre-acidic treatment and optimum titrant utilization. The process starts with RH treatment with HCl (0.10 % HCl at 80 °C) for metallic impurities reduction, longer chain hydrocarbon decomposition, and high surface area generation [19], resulting in leached RH formation. After that, multiple DIW washing is followed for pH neutrality of leached RH; air-dried leached RH undergoes 4 h incineration at 600 °C inside the furnace, resulting in the ash, 1-RHA, formation. The mortar pestle grounded fine RHA is sieved using a 400 mesh sieve to get uniform fine 1-RHA powder. In the next sol-formation step, in reaction 1, obtained fine 1-RHA is treated with 1M NaOH solution in reflux condition at 100 °C for 4 h, followed by sol cooling and filtration. In the next gel formation step, in reaction 2, the filtrate is titrated with an optimized 0.2% H_2SO_4 concentration, which is the optimum titrant concentration required for gel formation. The formed gel undergoes 24 h aging, followed by defragmentation, stirring, and DIW dilution; thick broken liquid-gel is sieved,

and DIW-washed multiple times for possible remnants removal, resulting in semi-gel-like mass formation. The overnight gel refrigeration facilitates gel deformation, resulting in liquidation in the open environment. Instead of drying and subsequent mixing for stable suspension preparation as followed in two-step nanofluid preparation, the nanofluid is prepared via the single-step method, attained with 7 h prolonged ultrasonic dual mixing (UDM) application, resulting in nanofluid formation. For one-step nanofluid preparation, prolonged UDM application is employed on similar lines with nanoparticle dispersion in the polymer matrix [20, 21] for effective cluster size reduction and uniform suspension. Furthermore, for nanoparticle suspension stabilization, optimized SDS surfactant concentration has been used [22] as suitable in bulk application.



The steps from RH cleaning to nanofluid preparation are depicted in Fig. 3. For nanoparticle characterization, a certain nanofluid amount is hot-dried at 80 °C.

3 Results and Discussion

3.1 Titrant Concentration Optimization

In the gel formation step, titrant H_2SO_4 concentration is varied in four levels (2, 5, 10, 15) %, revealing that silica gel forms even at the lowest titrant concentration. Therefore, 2% H_2SO_4 is used to obtain silica gel, lessening the titrant consumption and DIW washing requirements in the gel-cleaning stage.

3.2 Characterization of Nano-Silica

3.2.1 FTIR Analysis

Through FTIR analysis, the available functional groups in prepared unleached RH, leached RH, and silica nanoparticles are assessed, evaluating characteristic bond-induced vibrations, as shown in Fig. 4. Using FTIR instrument (Make: PerkinElmer, Model: Spectrum 100, USA), with 4000–400 cm^{-1} wavenumbers, and KBr disk characteristic bond is identified; in which, OH stretching vibration around 3400 cm^{-1} is owed to silanol or adsorbed water molecules; asymmetric siloxane bond vibration is at 1072 cm^{-1} ; Si–O–Si bending vibration is around 466 cm^{-1} . Moreover, the

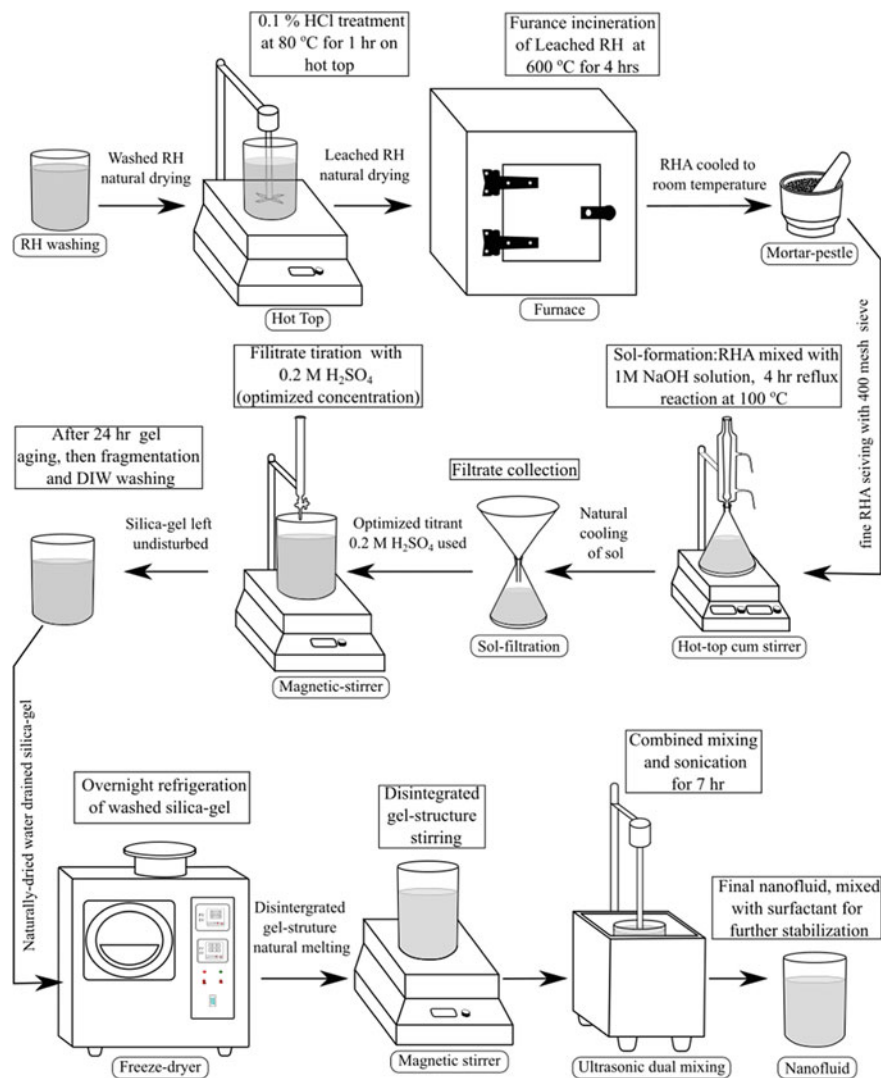
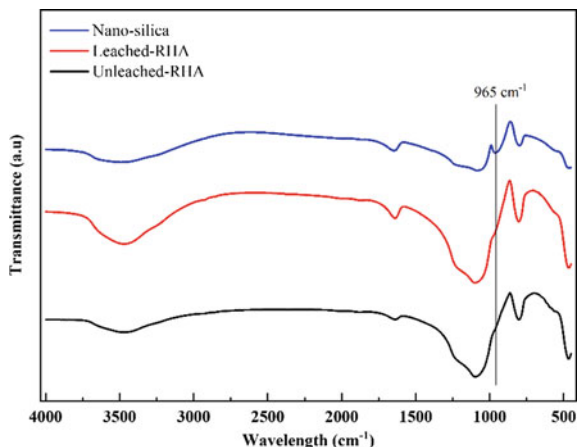


Fig. 3 Complete steps involved in silica nanofluid preparation

additional peak at 965 cm^{-1} is observed compared to unleached RH and leached RH, which denotes silanol group presence, conveying the additional solubility tendency of the prepared nano-silica.

Fig. 4 FTIR spectra of unleached RHA, leached RHA, and nano-silica



3.2.2 XRD Analysis

The XRD analysis was performed using X-ray Diffractometer (Make: PANalytical X'pert3 Pro Model: PW-3050/60; UK) equipped with nickel filtered Cu K α radiation ($\lambda = 1.54059 \text{ \AA}$), with a scan range of 10° – 90° , step size of 0.02, the time step of 0.20, generator voltage of 40 kV and tube current of 3 mA settings, to assess the silica state. XRD analysis was performed for unleached RHA, leached RHA, and nano-silica, as depicted in Fig. 5. The peak around 22° for nano-silica and other RH cases indicates amorphous silica presence.

Fig. 5 Diffractogram of unleached RHA, leached RHA, Nano-silica

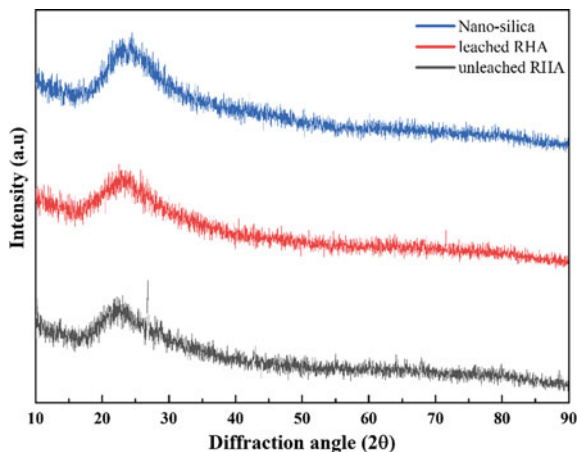
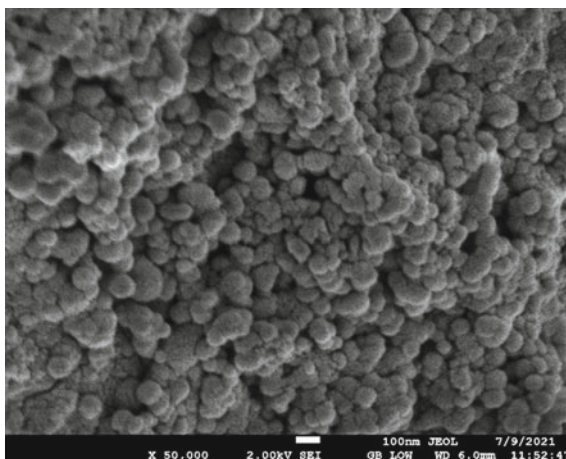


Fig. 6 FESEM micrographs of nano-silica



3.2.3 FESEM Analysis

In the morphology assessment of prepared nanoparticles, FESEM analysis was performed using the FESEM instrument (Make: JEOL, Model: JSM-7610F, Japan). The micrograph of nano-silica is depicted in Fig. 6, from which near-spherical nature is evident, with present micrograph similarity with literature reported nano-silica micrograph [17]. Additionally, the average diameter of nanoparticles comes around 97 nm, which is determined using micrograph analysis through the ImageJ software. Thus, particle length-scale conveys nanoparticles formation below 100 nm, which is supported later by other analyses.

3.2.4 XRF Analysis

XRF analysis determines the elemental constituents using the XRF instrument (Make: PANalytical, Model: AXIOS, Netherlands). This analysis becomes pertinent for metallic and non-metallic constituents determination with silica in various stages. The constituents of unleached RH, leached RH, and nano-silica are presented in Table 1. The percentage analysis of compounds also reveals that nano-silica contains the highest percentage of silica oxide and the lowest percentage of metal impurities than ul-RHA and l-RHA, which is in agreement with the literature [19, 23]. Owing to the lowest metallic and non-metallic impurities, leached RHA is used in the sol-gel method for nano-silica preparation.

Table 1 Elemental constituents of unleached RHA, leached RHA, and nano-silica

Compound, %	u-RHA	l-RHA	Nano-silica
SiO ₂	78.29	96.97	97.65
P ₂ O ₅	9.88	0.935	0.52
MgO	4.92	0.28	0.42
K ₂ O	2.96	0.06	0.03
CaO	1.39	0.05	0.05
Fe ₂ O ₃	0.68	0.54	0.33
SO ₃	0.62	0.33	0.09
Na ₂ O	0.51	0.54	0.81
MnO	0.46	0.03	0.01
Al ₂ O ₃	0.21	0.18	0.03
TiO ₂	0.04	0.04	0.03
Cl	0.03	0.03	0.02
ZrO ₂	0.01	0.01	0.01

3.2.5 EDS Analysis

This analysis is used for nanoparticle surface elemental constituents determination, shown in Fig. 7. The current elemental analysis is performed in addition to XRF analysis, which supports the SiO₂ compound in the sample, constituents shown in Table 2. Additionally, literature verification support SiO₂ formation [24].

Fig. 7 EDS spectrum of SiO₂ nanoparticles

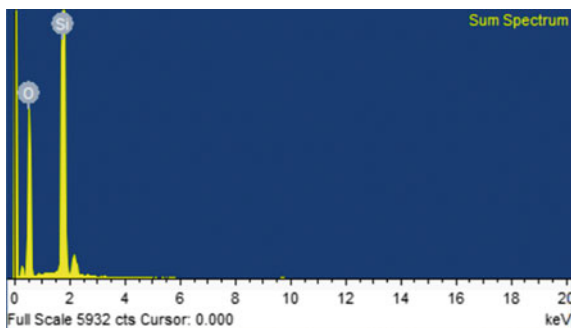


Table 2 Weight and atomic distribution of SiO₂

Component	Weight (%)	Atomic (%)
Si K	50.33	36.60
O K	49.67	63.40

3.3 *Silica Nanofluid Characterization*

3.3.1 Visual Analyses

Two fundamental visual analyses, Settling and Tyndall effect analysis, are performed.

Setting Observation

The bare silica nanofluid is prepared in four concentration levels (100, 500, 1000, and 10,000 ppm), and their visual analysis is performed up to 36 h, as shown in Fig. 8. It is observed that nanoparticle loading greater than 1000 ppm has significant silica deposition at the test tube bottom after 24 h observation. Therefore, concentration up to 1000 ppm has been considered in further analysis.

Tyndall Effect Analysis

Another basic test to confirm nanoparticle presence is through the Tyndall effect analysis. For 1000 ppm highest concentration, the effect is visualized for bare silica nanofluid at different time intervals; nanoparticles appear suspended firmly in the fluid even after 36 h, as depicted in Fig. 9.

3.3.2 Thermo-Physical Property Analysis

The thermophysical properties of utmost significance for heat transfer, such as thermal conductivity, surface tension, and viscosity, are assessed.

Thermal Conductivity Measurement

The thermal conductivity enhancement indicates possible improvement in heat transfer performance, which is determined using the thermal property analyzer (Make: Decagon devices, Model: KD2, USA) (%). The variation of thermal conductivity for both bare silica and surfactant-added silica is presented in Fig. 10. In the case of bare silica nanofluid, we observed a 5.94% maximum improvement in thermal conductivity at 1000 ppm and about 6.62% enhancement in thermal conductivity for surfactant-supported silica. Due to exposure to high sonication time and surfactant inclusion, an enhancement in thermal conductivity is observed with particle loading [25]. Therefore, improvement in thermal conductivity with nanoparticle loading and surfactant addition can improve the performance of silica nanofluid in heat transfer enhancement.

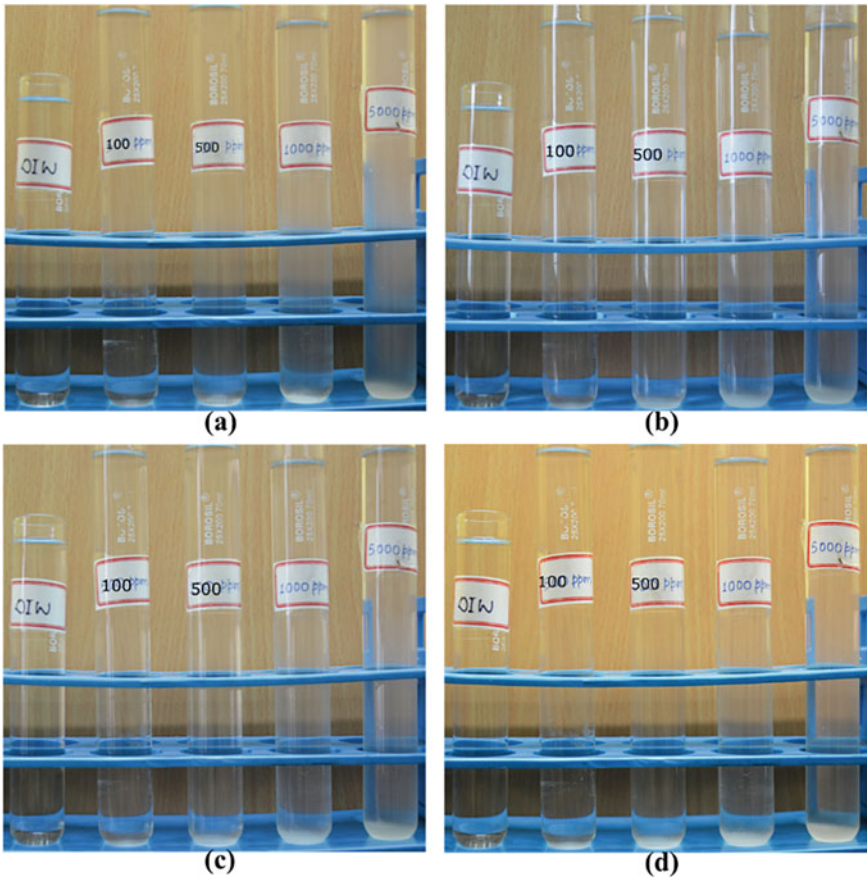


Fig. 8 Silica nanofluid at different concentration visual observation at time intervals: **a** 0 h, **b** 12 h, **c** 24 h, and **d** 36 h

Fig. 9 Tyndall effect observation in 1000 ppm silica nanofluid: **a** 0 h, **b** 12 h, **c** 24 h, and **d** 36 h

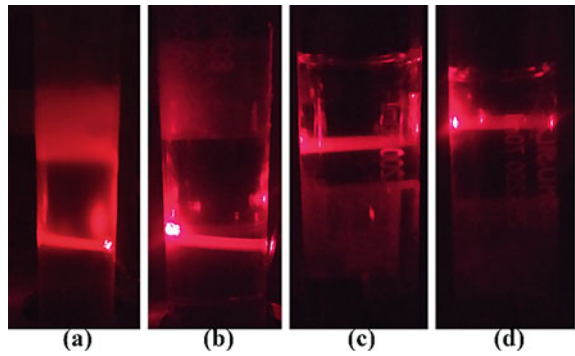
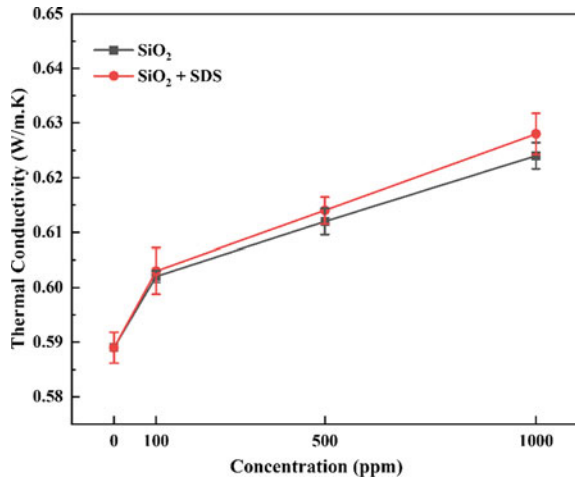


Fig. 10 Thermal conductivity variation of silica nanofluid with and without surfactant



Surface Tension Measurement

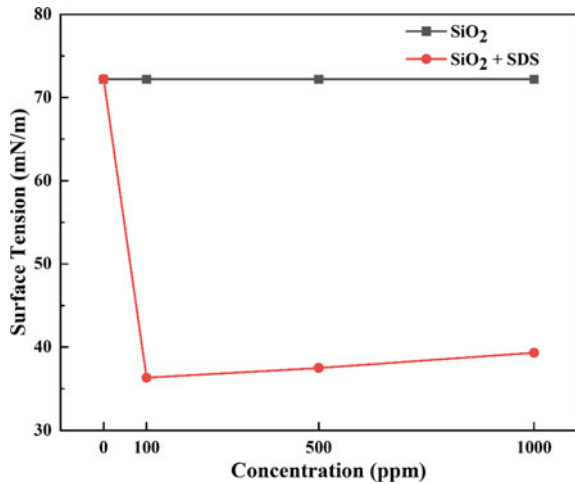
Nanofluid spreading and wetting nature on the surface can be determined from surface tension determination, measured using a Du-Nouÿ ring surface tensiometer (Make: Testing Instrument, India). A reduction in surface tension positively influences heat transfer performance improvement, as established in the literature [26–29]. The surface tension variation with SiO₂ nanofluid with and without surfactant addition is presented in Fig. 11. For bare silica, the surface tension is unaffected by concentration change; however, with surfactant inclusion, surface tension reduction is highest at low concentration and lowest at the highest nanoparticle concentration. Therefore, surfactant inclusion in nanofluid causes a reduction in surface tension, which can enhance heat transfer.

Viscosity Measurement

Likewise, the surface tension, nanofluid spreading, and wetting nature are influenced by viscosity. An enhancement in viscosity is detrimental to heat transfer performance, as it leads to a surge in pumping cost and pipeline clogging; therefore, viscosity decrement is desirable. The current work employs the Cannon–Fenske viscometer for kinematic viscosity assessment. Researchers have used this viscometer for nanofluids owing semi-transparent and opaque nature [30, 31]. For viscosity measurement, the viscometer is placed inside a constant temperature water bath, and flow time from one bulb to another is recorded, which is used in Eq. (1) for viscosity calculation

$$v = C_1 t_1 - \left(\frac{C_2}{t_2^2} \right) \tag{1}$$

Fig. 11 Surface tension variation of silica nanofluid with and without surfactant



where t_1 , t_2 , C_1 , and C_2 are for lower bulb flow time, upper bulb flow time, lower bulb constant, and upper bulb constant, respectively.

The variation in viscosity in both with and without surfactant nanofluids is presented in Fig. 12. With an increment in silica loading, monotonous enhancement in viscosity is observed; however, with surfactant addition, viscosity enhancement is suppressed at all considered concentrations. The viscosity enhancement with concentration is on similar lines with literature findings [32], and viscosity reduction with surfactant addition is also on similar lines with literature findings [33]. With only bare silica, at the highest 1000 ppm loading, 4.14% enhancement in viscosity is observed, while with the surfactant case, 3.03% enhancement in viscosity is observed compared to plain water. Thus, surfactant inclusion appears beneficial for viscosity reduction, which can improve heat transfer performance.

3.3.3 DLS Analysis

Dynamic light scattering (DLS) analysis is performed using a DLS instrument (Model: Zeta Sizer Nano-ZS; Make: Malvern Instrument, USA) to assess the particle size distribution in a nanofluid. This analysis helps identify nanoparticle aggregation through average agglomerated particle size distribution, shown in Fig. 13. Tian et al. [34] assessed the particle size distribution of SiO₂ nanofluid in terms of number distribution and diameter, confirming its suitability for particle size distribution. The SiO₂ particle size ranges from 60 to 450 nm; however, most particles are below 100 nm, few are above 100 nm, and most are centered around 79 to 82 nm. Thus, particle size distribution confirms successful nano-silica preparation.

Fig. 12 Kinematic viscosity variation of silica nanofluid with and without surfactant

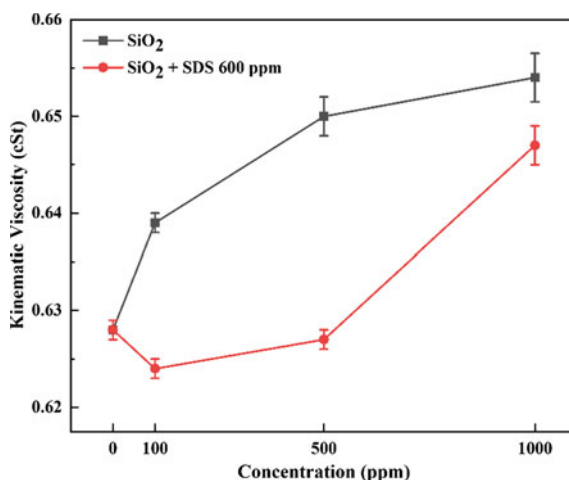
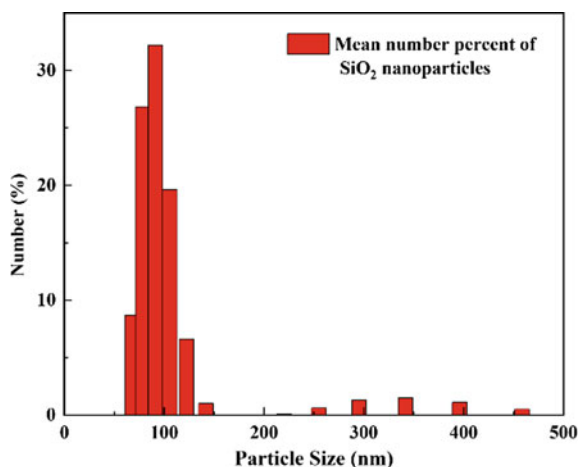


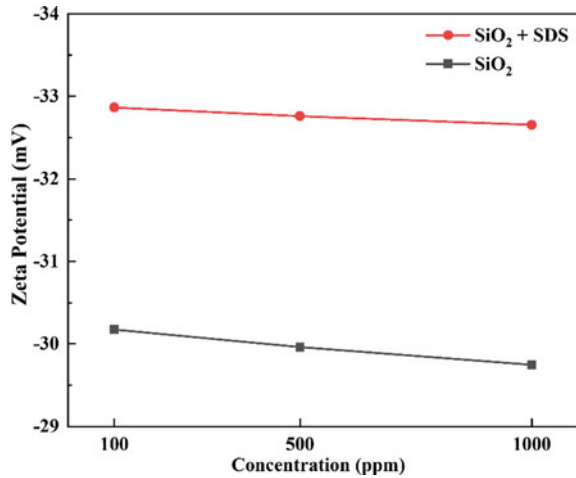
Fig. 13 Number (%) distribution of nano-silica with size



3.3.4 Zeta Potential Analysis

The quantitative determination of stability is crucial for prolonged suspension storage, which is determined using the Zeta potential instrument (Make: Malvern Instrument, Model: Zeta Sizer Nano-ZS; USA). In zeta potential analysis, the surrounding charge of the surface of the nanoparticles is measured, which gives nanoparticles electrophoretic mobility [35]. The greater the zeta potential value, the better the nanofluid's stability. With bare silica only, zeta potential varies from -30.17 to -29.74 mV for 100 ppm to 1000 ppm concentration, respectively; however, with added dispersant, Zeta potential increases, as shown in Fig. 14. The obtained zeta potential value of surfactant added is above the moderate stability range of bare silica. The bare silica has low inherent zeta potential, which can be enhanced by

Fig. 14 Zeta potential of silica nanofluid with and without dispersant



prolonged sonication [9] and surfactant inclusion [10]. Therefore, stability enhancement with sonication and surfactant can enable silica nanofluid suitability in heat transfer applications.

4 Conclusion

The modified sol–gel method is used in nano-silica preparation and the resultant nanoparticle is used in one-step nanofluid synthesis. The gel formation step uses the optimized titrant 2% H₂SO₄ concentration. The functional group imparting SiO₂ solubility is evident from FTIR analysis. Silica’s amorphous nature is apparent from XRD analysis. The SiO₂ FESEM analysis confirms the presence of nanometric-scale particles. The visual study through settling confirms that up to 1000 ppm nanofluid is stable for over 24 h, and the Tyndall effect confirms nanometric particles. The thermal conductivity enhances with concentration for both bare and surfactant-added SiO₂, with a slight increment in surfactant-supported nanofluid. Only silica nanofluid surface tension is unaffected by concentration enhancement; surface tension reduction is observed with surfactant-added silica, followed by slight enhancement with concentration. The surfactant-added SiO₂ nanofluid shows viscosity decrement, followed by slight viscosity enhancement at high concentrations. The particle size distribution depicts that most particles are below 100 nm. The stability of surfactant-added SiO₂ increases compared to bare nanofluid. Thus, the prepared silica nanofluid with moderate thermophysical properties, size, and stability provides its prospects in nanofluid applications, especially in bulk usage.

References

1. Chandra S (1996) Waste materials used in concrete manufacturing. Noyes Publications, Westwood, New Jersey
2. Le VH, Thuc CNH, Thuc HH (2013) Synthesis of silica nanoparticles from Vietnamese rice husk by sol-gel method. *Nanoscale Res Lett* 8(1):58
3. Anoop K, Sadr R, Yu J, Kang S, Jeon S, Banerjee D (2012) Experimental study of forced convective heat transfer of nanofluids in a microchannel. *Int Commun Heat Mass Transf* 39(9):1325–1330
4. Darzi AAR, Farhadi M, Sedighi K, Shafaghath R, Zabihi K (2012) Experimental investigation of turbulent heat transfer and flow characteristics of SiO₂/water nanofluid within helically corrugated tubes. *Int Commun Heat Mass Transf* 39(9):1425–1434
5. Fazeli SA, Hosseini Hashemi SM, Zirakzadeh H, Ashjaee M (2012) Experimental and numerical investigation of heat transfer in a miniature heat sink utilizing silica nanofluid. *Superlattices Microstruct* 51(2):247–264
6. Yan S, Wang F, Shi Z, Tian R (2017) Heat transfer property of SiO₂/water nanofluid flow inside solar collector vacuum tubes. *Appl Therm Eng* 118:385–391
7. Chakraborty S, Sarkar I, Ashok A, Sengupta I, Pal SK, Chakraborty S (2018) Synthesis of Cu-Al LDH nanofluid and its application in spray cooling heat transfer of a hot steel plate. *Powder Technol* 335:285–300
8. James J, Rao MS (1986) Silica from rice husk through thermal decomposition. *Thermochim Acta* 97:329–336
9. Jafari V, Allahverdi A, Vafaei M (2014) Ultrasound-assisted synthesis of colloidal nanosilica from silica fume: effect of sonication time on the properties of product. *Adv Powder Technol* 25(5):1571–1577
10. Bajpai S, Shreyash N, Sonker M, Tiwary SK, Biswas S (2021) Investigation of SiO₂ nanoparticle retention in flow channels, its remediation using surfactants and relevance of artificial intelligence in the future. *Chemistry (Easton)* 3:1371–1380
11. Ranjbarzadeh R, Moradikazerouni A, Bakhtiari R, Asadi A, Afrand M (2019) An experimental study on stability and thermal conductivity of water/silica nanofluid: eco-friendly production of nanoparticles. *J Clean Prod* 206:1089–1100
12. Adam F, Chew TS, Andas J (2011) A simple template-free sol-gel synthesis of spherical nanosilica from agricultural biomass. *J Sol-Gel Sci Technol* 59:580–583
13. Jal PK, Sudarshan M, Saha A, Patel S, Mishra BK (2004) Synthesis and characterization of nanosilica prepared by precipitation method. *Colloids Surf A Physicochem Eng Asp* 240:173–178
14. Lumen D et al (2021) Investigation of silicon nanoparticles produced by centrifuge chemical vapor deposition for applications in therapy and diagnostics. *Eur J Pharm Biopharm* 158:254–265
15. Hong R, Ding J, Zheng G (2004) Thermodynamic and particle-dynamic studies on synthesis of silica nanoparticles using microwave-induced plasma CVD. *China Particuology* 2(5):207–214
16. Conradt R, Pimkhaokham P, Leela-Adisorn U (1992) Nano-structured silica from rice husk. *J Non Cryst Solids* 145(C):75–79
17. Mor S, Manchanda CK, Kansal SK, Ravindra K (2017) Nanosilica extraction from processed agricultural residue using green technology. *J Clean Prod* 143:1284–1290
18. Foletto EL, Gratieri E, de Oliveira LH, Jahn SL (2006) Conversion of rice hull ash into soluble sodium silicate. *Mater Res* 9(3):335–338
19. Bakar RA, Yahya R, Gan SN (2016) Production of high purity amorphous silica from rice husk. *Procedia Chem* 19:189–195
20. Goyat MS, Ray S, Ghosh PK (2011) Innovative application of ultrasonic mixing to produce homogeneously mixed nanoparticulate-epoxy composite of improved physical properties. *Compos Part A Appl Sci Manuf* 42(10):1421–1431
21. Goyat MS et al (2019) Superior thermomechanical and wetting properties of ultrasonic dual mode mixing assisted epoxy-CNT nanocomposites. *High Perform Polym* 31(1):32–42

22. Ravikumar SV, Jha JM, Sarkar I, Mohapatra SS, Pal SK, Chakraborty S (2013) Achievement of ultrafast cooling rate in a hot steel plate by air-atomized spray with different surfactant additives. *Exp Therm Fluid Sci* 50:79–89
23. Hincapié-Rojas DF, Rosales-Rivera A, Pineda-Gomez P (2018) Synthesis and characterisation of submicron silica particles from rice husk. *Green Mater* 6(1):15–22
24. Joni IM, Nulhakim L, Vanitha M, Panatarani C (2018) Characteristics of crystalline silica (SiO₂) particles prepared by simple solution method using sodium silicate (Na₂SiO₃) precursor. *J Phys Conf Ser* 1080:1–6
25. Li Z, Kalbasi R, Nguyen Q, Afrand M (2020) Effects of sonication duration and nanoparticles concentration on thermal conductivity of silica-ethylene glycol nanofluid under different temperatures: an experimental study. *Powder Technol* 367:464–473
26. Jha JM, Ravikumar SV, Tiara AM, Sarkar I, Pal SK, Chakraborty S (2015) Ultrafast cooling of a hot moving steel plate by using alumina nanofluid based air atomized spray impingement. *Appl Therm Eng* 75:738–747
27. Ravikumar SV, Jha JM, Sarkar I, Pal SK, Chakraborty S (2014) Mixed-surfactant additives for enhancement of air-atomized spray cooling of a hot steel plate. *Exp Therm Fluid Sci* 55:210–220
28. Chakraborty S, Sarkar I, Roshan A, Pal SK, Chakraborty S (2019) Spray cooling of hot steel plate using aqueous solution of surfactant and polymer. *Therm Sci Eng Prog* 10:217–231
29. Chakraborty S, Sarkar I, Behera DK, Pal SK, Chakraborty S (2017) Experimental investigation on the effect of dispersant addition on thermal and rheological characteristics of TiO₂ nanofluid. *Powder Technol* 307:10–24
30. Yalçın G, Öztuna S, Dalkılıç AS, Wongwises S (2021) Measurement of thermal conductivity and viscosity of ZnO–SiO₂ hybrid nanofluids. *J Therm Anal Calorim* 1–17
31. Nair V, Parekh AD, Tailor PR (2019) Experimental investigation of thermophysical properties of R718 based nanofluids at low temperatures. *Heat Mass Transf Stoffuebertragung* 55(10):2769–2784
32. Mukherjee S, Mishra PC, Chaudhuri P (2018) Stability of heat transfer nanofluids—A review. *Chem Bio Eng Rev* 5(5):312–333
33. Chakraborty S, Sengupta I, Sarkar I, Pal SK, Chakraborty S (2019) Effect of surfactant on thermo-physical properties and spray cooling heat transfer performance of Cu-Zn-Al LDH nanofluid. *Appl Clay Sci* 168(October 2018):43–55
34. Tian Z, Etedali S, Afrand M, Abdollahi A, Goodarzi M (2019) Experimental study of the effect of various surfactants on surface sediment and pool boiling heat transfer coefficient of silica/DI water nanofluid. *Powder Technol* 356:391–402
35. Bhattacharjee S (2016) DLS and zeta potential—What they are and what they are not? *J Contr Release* 235:337–351